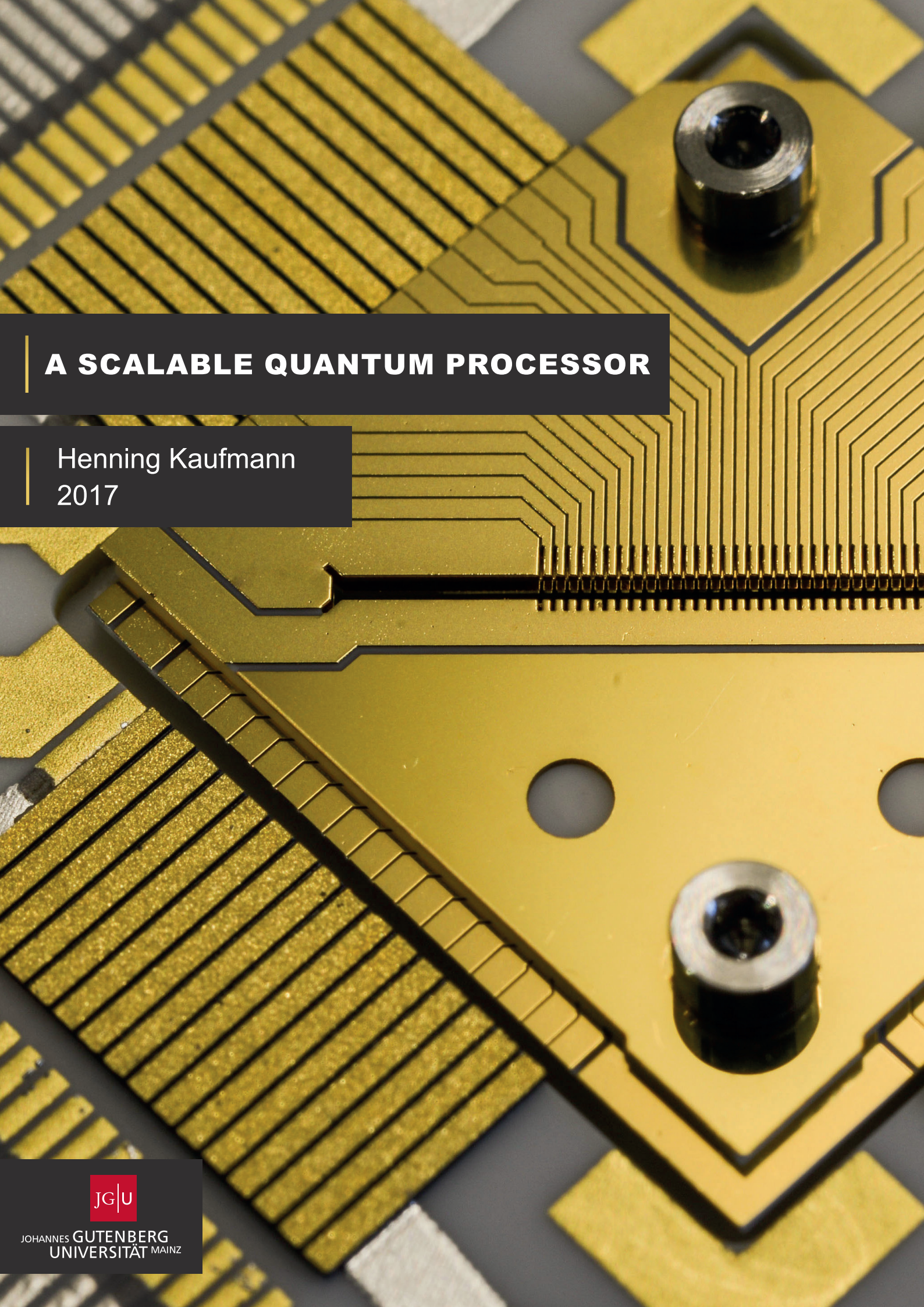

A SCALABLE QUANTUM PROCESSOR

Henning Kaufmann

2017

JOHANNES GUTENBERG UNIVERSITÄT MAINZ

A Scalable Quantum Processor

Dissertation

zur Erlangung des akademischen Grades

„Doktor der Naturwissenschaften“

am Fachbereich Physik, Mathematik und Informatik

der Johannes Gutenberg-Universität

in Mainz

vorgelegt von

Henning Kaufmann

geboren in Koblenz

JOHANNES GUTENBERG
UNIVERSITÄT MAINZ

Mainz, August 2017

Abstract

In this work, the construction and operation of a scalable trapped-ion quantum logic processor is presented. Quantum information is stored in Zeeman sublevels $|\uparrow\rangle$ and $|\downarrow\rangle$ of $^{40}Ca^{+}$ ions and operated by laser Raman interactions. Central part of the processor is a segmented micro-structured linear Paul trap, which is also referred to as *quantum charge-coupled device* (QCCD). Single ions are shuttled along the trap axis between memory zones and a processing zone, where single- and two-qubit logic gates are driven with lasers.

Single-qubit gates are performed with a fidelity of 99.9949(2)% and we achieve a qubit state preparation and measurement rate of 99.923(3)%. For two-qubit entangling gates a fidelity of 99.5(1)% is accomplished. High fidelity entangling gates require the ions to be close to the motional ground state, which imposes stringent requirements on coherent excitation from shuttling operations and anomalous heating of the ion trap. We achieve a low heating rate of three motional quanta per second at a radial mode frequency of $2\pi\times4.6\,\mathrm{MHz}$. We actively stabilize this mode frequency to better than $2\pi\times20\,\mathrm{Hz}$.

Three different shuttling operations suffice for QCCD operation – transport, rotation and separation of ion crystals. Since suppressing motional excitation along the axial shuttling direction is experimentally challenging, we use a radial mode, as a bus mode for the entangling gate. Ion transport is performed with a motional excitation of 0.028(2) phonons on this mode within 30 µs, two-ion separation with 0.03(1) phonons (80 µs) and two-ion rotation with 0.02(1) phonons (42 µs).

The experimental building blocks are combined to implement a scalable quantum logic circuit. We generate a maximally entangled four-qubit Greenberger-Horne-Zeilinger state $|\psi\rangle = \frac{1}{\sqrt{2}}(|0000\rangle + |1111\rangle)$, which is an important resource for measurement-based quantum computing and quantum error correction. The constituent entangled ions are spatially separated over a distance of 1.8 mm and full quantum state tomography yields a state fidelity of 94.4(3)%. A dynamical decoupling technique is employed to maintain 69(5)% coherence at a storage time of 1.1 seconds.

Aside from probing the QCCD approach to scalable quantum computing, we demonstrate gate operations with a planar ion crystal: ground state cooling of a *zigzag mode* in a planar ion crystal is performed. For the first time, we realize the application of a spin-dependent optical dipole force on this mode, which is an important step towards an analog quantum simulator in a two-dimensional geometry.

Zusammenfassung

Diese Arbeit beschreibt den Aufbau und den Betrieb eines skalierbaren Ionen-Quantenprozessors. In Diesem wird Quanteninformation in den Zeeman-Zuständen $|\uparrow\rangle$ und $|\downarrow\rangle$ von $^{40}Ca^{+}$-Ionen gespeichert und durch lasergetriebene Raman-Übergänge gesteuert. Das Herzstück des Prozessors ist eine segmentierte, mikrostrukturierte, lineare Paul-Falle, welche auch als *quantum charge-coupled device* (QCCD) bezeichnet wird. Einzelne Ionen werden entlang der Fallenachse zwischen Speicherzonen und einer Prozessorzone bewegt, wo Ein- und Zwei-Qubit-Logikgatter mit Lasern durchgeführt werden.
Für Ein-Qubit-Gatter wurde eine *Fidelity* von 99.9949(2)% erzielt, wobei eine Erfolgsrate von 99.923(3)% für die Präparation und Messung des Qubit-Zustands erreicht werden konnte. Verschränkende Zwei-Qubit-Gatter wurden mit einer Fidelity von 99.5(1)% realisiert und setzen voraus, dass sich die Ionen nahe am Grundzustand der Bewegung befinden. Daher müssen die kohärente Anregung, welche durch Ionen-Verschiebeoperationen entsteht, und das anomale Aufheizen der Ionen möglichst gering sein. Die *Heizrate* der Ionenfalle ist niedrig. Sie beträgt drei Phononen pro Sekunde bei einer radialen Fallenfrequenz von $2\pi\times4.6\,\mathrm{MHz}$, die aktiv auf eine Frequenzabweichung von weniger als $2\pi\times20\,\mathrm{Hz}$ stabilisiert wird.
Für einen QCCD werden drei unterschiedliche Ionen-Verschiebeoperationen benötigt: Transport-, Rotations- und Trennoperationen von Ionenkristallen. Da die Unterdrückung von Bewegungsanregung entlang der axialen Verschiebungsrichtung eine experimentelle Herausforderung ist, wird das verschränkende Quantengatter mittels einer radialen Schwingungsmode realisiert. Die Anregung dieser Mode betrug für Ionentransporte 0.028(2) Phononen bei einer Transportdauer von 30 µs. Trennoperationen von Zwei-Ionenkristallen wurden innerhalb von 80 µs bei einer Anregung von 0.03(1) Phononen realisiert, Rotationsoperationen innerhalb von 42 µs (0.02(1) Phononen).
Die vorgestellten experimentellen Techniken wurden kombiniert, um mit vier Qubits einen skalierbaren Quantenlogikschaltkreis auszuführen, welcher einen maximal verschränkten Greenberger-Horne-Zeilinger-Zustand $|\psi\rangle = \frac{1}{\sqrt{2}}(|0000\rangle + |1111\rangle)$ erzeugt. Dieser stellt eine wichtige Ressource für messungsbasierte Quantencomputer und Quantenfehlerkorrekturverfahren dar. Die vier verschränkten Ionen waren räumlich über eine Distanz von 1.8 mm verteilt und mittels Quantenzustandstomographie wurde eine Zustands-Fidelity von 94.4(3)% gemessen. Mithilfe einer dynamischen Entkopplungssequenz konnte eine Zustandskohärenz von 69(5)% bei einer Speicherzeit von 1.1 Sekunden aufrechterhalten werden.
Neben der Erforschung des QCCD-Ansatzes zur Realisierung eines skalierbaren Quantencomputers wurden Gatteroperationen mit einem planaren Ionenkristall demonstriert: Auf einer *Zickzack-Mode* wurde Grundzustandskühlen und zum ersten Mal eine Spinabhängige Dipolkraft realisiert. Dies stellt einen wichtigen Schritt in Richtung eines analogen Quantensimulators in einer zweidimensionalen Geometrie dar.

Contents

1

Motivation

Quantum computing might become one of the most disruptive technologies of the twenty-first century. Information storage and processing in a quantum computer are performed on the single-atom level, where physics is governed by the laws of quantum mechanics. Phenomena, such as entanglement, are required and harnessed for the operation of a quantum computer. A universal quantum computer offers the potential to solve important problems in the fields of information science, solid state physics, chemical processes and health care substantially more efficient than a classical computer [Fey82; Nie00; Lad10]. A high degree of experimental control is required to construct and operate such a device, which implies the use of cutting edge technology. The field of quantum technologies is growing quickly and commercial development of this key technology is advancing [Tou16; Moh17; Cas17].
In this thesis, the design and construction of a trapped-ion quantum logic processor is presented. Ions are stored in a segmented micro-structured linear Paul trap and are shuttled along the trap axis between memory zones and a processing zone, where quantum logic gates are driven with lasers. The device is characterized and its suitability for scalable quantum computing is investigated by performing a multi-qubit quantum logic circuit. In this introductory chapter, a brief historical overview of quantum computing and its basic ideas are presented. Furthermore, quantum information experiments are reviewed and experimental platforms for the realization of a universal quantum computer are compared.

1.1. The quantum computer

The invention of digital computers has led to groundbreaking success in research and fundamentally changed our society. First steps towards the quantum computing age

were made in 1980, when Yuri Manin discovered the potential of a quantum computer to efficiently simulate quantum systems and Paul Benioff proposed a quantum Turing machine [Man80; Ben80; Man99]. Richard Feynman independently developed the quantum simulator approach in more detail [Fey82; Fey86]. Quantum turing machines were further developed by Deutsch [Deu85], Yao [Yao93] and Bernstein and Vazirani [Ber97].

Information in a quantum computer is stored in quantum bits (qubits), which are the analogue to bits in a classical computer. However, a qubit can be in the two computational basis states $|0\rangle$ and $|1\rangle$ at the same time. Such a quantum mechanical superposition is described by the wave function $|\psi\rangle = \alpha\,|0\rangle + \beta\,|1\rangle$, where α, β are complex amplitudes with the constraint $|\alpha|^2 + |\beta|^2 = 1$. Therefore, the smallest unit of information can take infinitely many different states and thus, in principle, store an infinite amount of information. However, if a superposition state is measured, the wave function collapses to the state $|0\rangle$ or $|1\rangle$ with probability $|\alpha|^2$ or $|\beta|^2$.
Quantum information, that is stored in a qubit, is manipulated by *quantum logic gates*. Logic gates are executed either on single qubits or multiple qubits. A concatenation of multiple quantum logic gates constitutes a *quantum logic circuit*.
To unleash the potential of qubits in a quantum computer, it is necessary to create entanglement between multiple qubits. The simplest example is a maximally entangled Bell state $|\psi\rangle = 1/\sqrt{2}(|00\rangle + |11\rangle)$ [Ein35; Bel64; Asp82]. This state can be created from the separable two-qubit state $|\psi\rangle = |0\rangle \otimes |0\rangle \equiv |00\rangle$ by the application of a Hadamard quantum logic gate [Nie00] on the first qubit, followed by a controlled-NOT gate on both qubits [SK03]. The corresponding quantum circuit is sketched in figure 1.1.

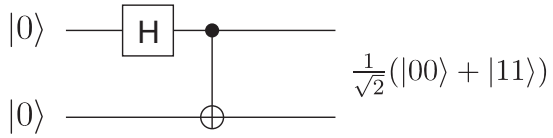

Figure 1.1.: Quantum logic circuit for the creation of a Bell state. The single-qubit Hadamard gate creates a superposition state $1/\sqrt{2}(|0\rangle + |1\rangle)$ for the first qubit. A subsequent C-NOT gate flips the second qubit, depending on the state of the first qubit. Since the first qubit is in a superposition state, a maximally entangled Bell state is created.

It has been shown, that any quantum circuit can be constructed from only single- and two-qubit gates, which makes such a set of gates universal [DiV95]. The power of

a quantum computer arises from a property called *quantum parallelism*. It enables the device to evaluate a function $f(x)$ for many different input states x at the same time [Nie00]. However, in a single experimental realization, only one measurement result is acquired. In *Deutsch's algorithm* [Deu85] for instance, quantum parallelism is combined with *interference*, to obtain output information for two different inputs with a single evaluation. A classical algorithm would require at least two evaluations for the same task.

A combination of creating entanglement between qubits and manipulating them in parallel is used in *quantum algorithms*, such as Shor's factorization algorithm [Sho94]. The algorithm finds the prime factors of a given integer number. It is based on a quantum Fourier transform and features an exponential speedup over classical factorization algorithms, which poses a threat to many of today's encryption systems. Another class of quantum algorithms is based on Grover's quantum search algorithm for unsorted data bases [Gro97]. It is an attractive candidate for implementation, as it features a quadratic speedup over classical search algorithms, which are a bottleneck in many of today's algorithms. A recent overview on quantum algorithms is provided in [Mon16a].

Besides the circuit model of quantum computation [Deu89], there exist other promising approaches, such as the one-way quantum computer [Rau01; Lan13] and adiabatic quantum computing [Far01; Miz07]. It is not clear which of these approaches will prevail in the future. In our research, we focus on the circuit model of quantum computation. The approach requires the qubits to be well protected from the outside world in order to prevent decoherence. Despite this challenge, remarkable realizations in the field of quantum computing were made, such as the first realization of the Grover [Chu98] and Shor [Van01] algorithms, using nuclear magnetic resonance. Today, advanced few-qubit trapped-ion [Sch13; Deb16] and solid state [Kel15] quantum processors have been realized. The realization of a *useful* scalable quantum computer is a great challenge and it is unclear, which physical platform will succeed in this open race.

1.2. Quantum computing platforms

A physical system, which might serve as a platform for a quantum computer, needs to fulfill requirements, known as the DiVincenzo criteria [DiV00]. In a nutshell, the device needs to be scalable to a large number of well characterized qubits without an excessive use of resources. Relevant coherence times have to be long and a universal set of logic

gates has to be available to manipulate the qubits. Error correction [Sho95; Ste96] is necessary, as undesired qubit-environment interaction cannot be entirely prevented. The need for error correction implies efficient qubit state initialization and readout. These requirements are experimentally challenging and currently, researchers aspire to fulfill them using various candidate platforms.

Trapped atomic ions

One of the most promising platforms for quantum information processing are trapped atomic ion qubits. The idea behind this approach was put forward in 1995 by Cirac and Zoller [Cir95]. Ions are stored as a chain in a Paul trap [Pau90] and qubits are encoded using long-lived electronic states. Qubit transitions are driven with laser beams, focused at the ions, as sketched in figure 1.2. Common vibrational modes of the

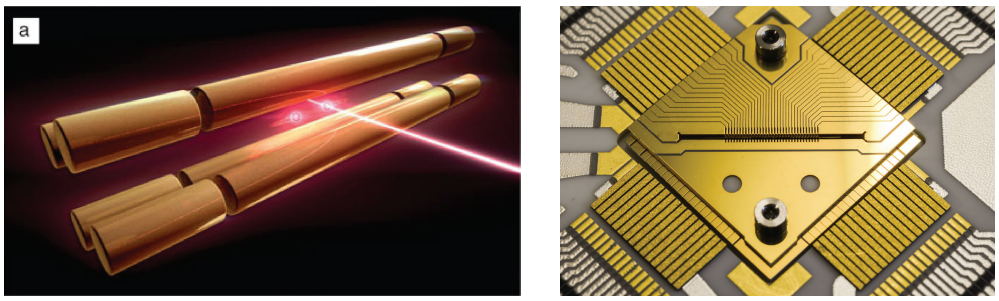

Figure 1.2.: Left: Sketch of laser beam addressing of a trapped ion in a linear Paul trap. Image taken from [Hit13]. **Right:** Photograph of the trapped-ion quantum processor at Mainz university, which is presented in this thesis.

ion string are used as *bus* modes for laser-driven entangling operations between ions. Entanglement between two [Tur98], four [Sac00], eight [Häf05a] and 14 [Mon11a] ions has been demonstrated experimentally. The first quantum logic C-NOT gate, which is based on the Cirac-Zoller idea, was realized with a single ion [Mon95a] and later between two ions [SK03; Lei03a]. Logic operations between trapped ions were then used to teleport quantum information [Rie04; Bar04] and led to the development of few-qubit programmable quantum computers [Mon16b; Deb16], that feature quantum error correction operations [Nig14].
Trapped ions also offer the possibility to couple qubits between distant locations via photon transfer [Mon14]. Entanglement between two ions, which are separated by

one meter, was demonstrated [Moe07] and quantum teleportation between distant ions was realized [Olm09]. A long-term goal is the construction of a quantum repeater with this technique, that would allow for secure quantum communication over large distances [Dür99; Pfi16; Zwe17].
The success story of trapped ions for quantum information processing is based on some key properties:

- Qubit preparation and readout can be performed with near unity efficiency [Har14].
- Complex quantum algorithms require high-fidelity quantum logic operations, that are significantly above the threshold for fault-tolerant quantum computation. Today such gates exist for trapped ions, which can be driven with lasers [Bal16; Gae16] or microwaves [Har16].
- Qubit coherence times in the seconds regime have been demonstrated, which are orders of magnitude higher than the required time for single-qubit operations. High coherence times can be achieved by storing qubits in hyperfine *atomic clock states* [Bol85; Har14], in a decoherence free subspace [Kie01] or by applying shielding techniques to combat ambient magnetic field noise [Rus16].
- Sympathetic recooling of ions allows for cooling of the quantum register without affecting the qubit coherence [Kie00].

Entangling logic gates require the ions to be close to the ground state of motion, which can be compromised by anomalous heating [Des06]. This noise effect can be suppressed by in-situ cleaning of the trap surface [All11; Hit12] or by operating the trap at cryogenic temperatures [Des06]. The challenge for trapped ions in quantum computing is to extend the high quality of deterministic few-qubit algorithms, to more complex algorithms, that feature error correction schemes [Ber17]. Furthermore, it is necessary to reduce the duration of quantum logic gates [Cam10], while maintaining a high gate fidelity.

Superconducting circuits

Superconducting materials feature electric currents without resistance at cryogenic temperatures. This effect is caused by electrons, that form Cooper pairs [Coo56; Bar57]. Cryogenic electric resonator circuits exhibit an anharmonic potential with discrete energy

levels, that can be used as qubits [Lad10]. A circuit model for a superconducting qubit is shown in figure 1.3.

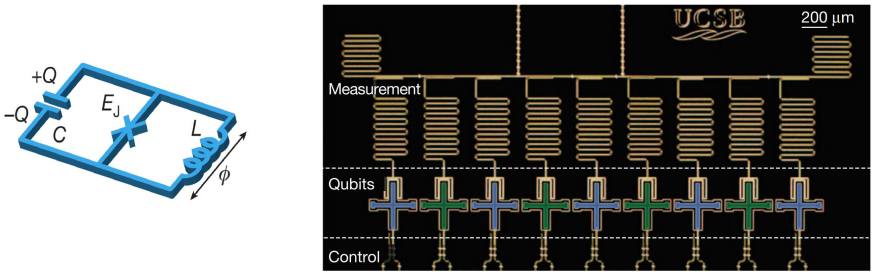

Figure 1.3.: Left: Circuit model of a superconducting qubit – the blue X denotes a Josephson junction [Jos74]. Image taken from [Lad10]. **Right:** Microscope image of a linear array of nine superconducting Xmon [Bar13] transmon qubits, which feature individual control and measurement, as well as nearest-neighbor coupling. Image taken from [Kel15].

Qubits are either manufactured as charge [Nak99], flux [Chi03], or phase qubits [Mar02], depending on the choice of circuit components and the resulting potential shape. Recent developments include transmon [Koc07] qubits and three-dimensional resonator qubits [Pai11].
Qubit manipulation is accomplished via electronic radio frequency and microwave signals. Each qubit requires electric connections, which is challenging for the scalability of the devices. Superconducting qubits are analogous to chip devices and thus benefit from decades of fabrication technique optimization. Atomic ion qubits are identical, whereas superconducting qubits differ from each other, due to fluctuations in the fabrication process. State preparation and readout for superconducting qubits has been improved [Wal17] but does not match the quality in trapped-ion systems [Har14]. Therefore, the realization of quantum error correction schemes is aggravated for superconducting qubits.
Superconducting qubit logic gates have been advanced [Bar14] and allow for the execution of complex quantum algorithms [Bar16]. Currently, experimental efforts are made [Cho14; Kel15; Cór15], to implement the two-dimensional *surface code* quantum error correction scheme [Fow12]. Qubit logic gates are usually carried out within tens of nanoseconds, which is considerably faster than typical gate times in trapped ion systems. However, this is not central to quantum computing – the number of logic gates within the coherence time is comparable for both platforms. Superconducting qubits are more prone to decoherence than trapped ions, due to the large number of participating conduction

electrons. However, technical development has continuously improved coherence times to around one millisecond [Rea16], which is still considerably less than in trapped-ion systems. Qubit circuits are manufactured next to each other on chips and couple either inductively or capacitively. To operate a deterministic quantum computer, it is necessary to have full control over inter-qubit couplings. For this purpose, tunable interactions between qubits have been demonstrated [Nis07], but interaction between distant qubits still remains challenging. An experimental comparison between two five-qubit quantum computers – trapped-ion and superconducting qubits – is provided in [Lin17].
Creating photonic interconnects between distant quantum processors is much harder than for trapped ions. A proposal for coupling of optical photons to superconducting qubits is based on interaction with an organic molecule [Das17].

Other platforms

Pioneering experiments in quantum computing were performed with nuclear spins in molecules, using magnetic resonance technology [Chu98; Van01]. However, this approach is considered to be not scalable as precise control of larger molecules in liquid solutions becomes difficult. Other viable platforms are photons, quantum dots, dopants in solids, neutral atoms and Rydberg atoms. A comprehensive overview over these technologies and their advantages and disadvantages is provided in [Lad10]. At the present day, trapped ions and superconducting circuits are the most promising candidates for a universal quantum computer, while many other experimental platforms have contributed to the field and continue to do so.

1.3. Trapped-ion quantum computing architectures

Various architectures have been proposed and realized for quantum computation and simulation with trapped ions. The earliest experiments were performed using one-dimensional ion crystals [Cir95; SK03; Lei03a]. Entanglement of up to 14 has been demonstrated, by using a common vibrational mode of an ion crystal [Mon11a]. Addressing of individual qubits is realized by tightly focused laser beams, see figure 1.4.

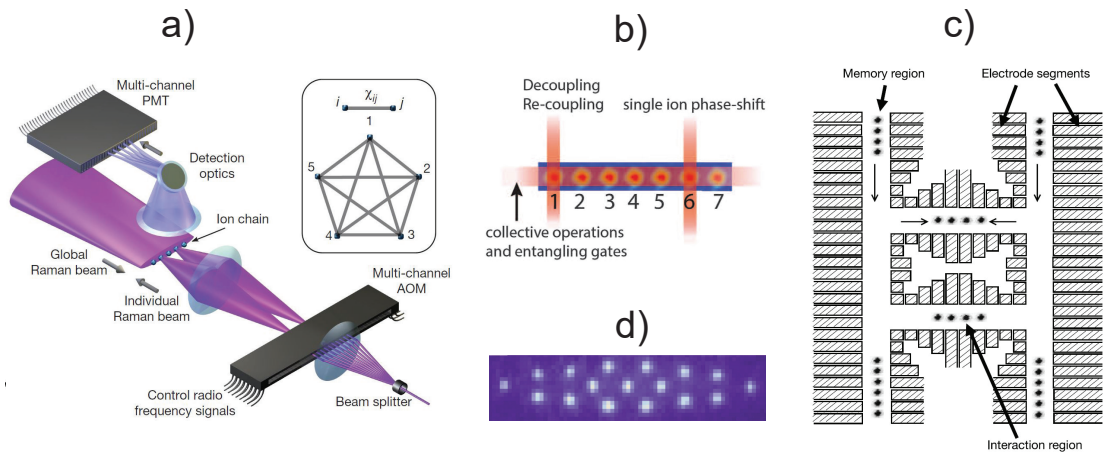

Figure 1.4.: Trapped-ion architectures for quantum computation and simulation. (a): Sketch of a linear five-ion chain quantum processor. Qubit-selective gates are performed with a multi-channel acousto-optic modulator, which can simultaneously address multiple individual ions. Image taken from [Deb16]. (b): Linear ion chain quantum processor. Qubit-selective gates are performed via spectroscopic decoupling operations of individual ions. Image taken from [Nig14]. (c): Proposal for a quantum charge-coupled device, where ions are shuttled between memory and processing zones. Image taken from [Kie02]. (d): Fluorescence image of a 17-ion planar ion crystal for quantum simulation of quantum spin magnetism. Image taken from [Ber12].

For larger ion chains however, the inter-ion distances shrink and the laser beam crosstalk to adjacent qubits significantly affects the performance of quantum logic operations. Furthermore, individual qubit readout is challenging for larger numbers of closely positioned ions. It is thus rather likely, that a large-scale trapped-ion quantum processor will require a reconfigurable quantum register, enabled via ion shuttling operations [Mon14; Lek17]. This approach is discussed in detail in section 1.4.

Planar ion crystals are a promising architecture for the realization of an analog quantum simulator [Ber12; Sch12]. They also allow for the study of structural phase transitions [Kau12b; Ulm13; Mie13] and solitons [Lan14; Bro17]. Ion crystals are either stored in three-dimensional [Pau90] or surface ion traps [Sei06]. The latter are easier to fabricate on a microscopic scale with conventional integrated circuit manufacturing techniques and offer high optical access for laser beams. However, the ions are stored closer to the trap surface, which leads to pronounced anomalous heating. Due to the deeper and less anharmonic trapping potentials, three-dimensional ion traps are better suited for storing large ion crystals.

1.4. Quantum CCD

A quantum charge-coupled device (QCCD) is an array of interconnected Paul traps, that allows for shuttling operations of ions between memory zones and processing zones [Kie02]. Analogously to a CCD, charges are transported, by changing control electrode voltages, and thus moving electrostatic potential wells. Scalability of this architecture was first demonstrated as a realization of a programmable two-qubit quantum processor [Hom09; Han10]. It is desirable to perform shuttling operations within a duration comparable to logic gate operations (10 – 100 µs). The relevant timescale is given by the secular trap frequencies, which are typically around $2\pi\times1$ MHz in the axial direction and about $2\pi\times3$ MHz in the radial direction. Any quantum register in a QCCD can be reconfigured by three basic shuttling operations – ion transport, ion crystal separation and ion crystal rotation, see figure 1.5.

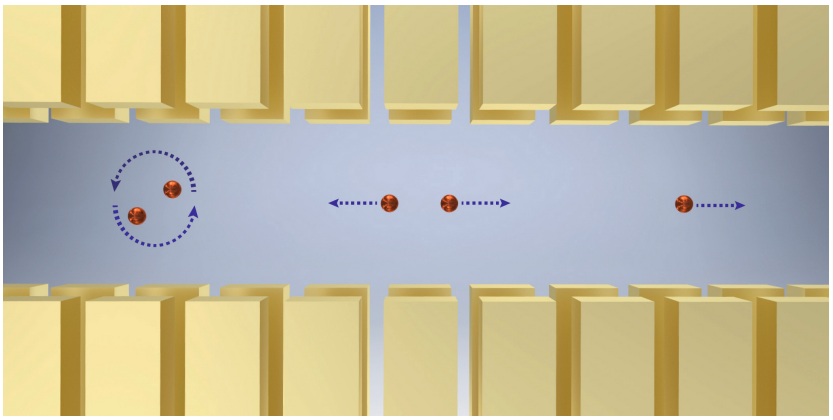

Figure 1.5.: Three fundamental shuttling operations in a quantum QCCD. **From left to right**: ion crystal rotation, ion crystal separation and ion transport operation. The operations are performed by applying well-tailored DC supply voltages to the individual trap electrodes.

The performance of ion shuttling operations is crucial to the operation of a QCCD, since high-fidelity quantum gates require the ions to be close to the motional ground state. Therefore, ion shuttling operations ought to be operated with low motional excitation. Ions are trapped in a harmonic potential well and sudden changes of the trapping voltages will lead to coherent excitation. Careful timing calibrations allow for fast transport operations without significant coherent excitation [Bow12; Wal12]. The ion crystal separation imposes additional challenges, since the trapping potential becomes

shallow during the transition from a single well to a double well potential [Kau14]. This operation can also be carried out with only a few motional quanta of excitation [Bow12; Rus14]. A fast ion crystal rotation reconfigures the quantum register, such that initially non-adjacent ions can interact. During this operation, the ions are tightly confined in a single well potential, which allows for fast execution with negligible motional excitation [Kau17a].
The architecture was originally proposed with X,T-or Y-junctions to store ions in memory zones. However, design and fabrication of such junctions is challenging, as the radio frequency potentials need to be carefully calculated and the resulting electrode geometries are complex [Hen06; Moe11]. Shuttling operations through these junctions are harder to control and in general lead to motional excitation of a few quanta [Bla09]. Our QCCD is manufactured without junctions, as we can achieve comparable functionality by fast ion crystal rotations.

The thesis is structured as follows: In chapter 2, the theoretical concepts for our trapped-ion qubits are presented. Emphasis is laid on the laser-ion interaction, that is used for single- and two-qubit quantum logic gates. The construction of the trapped-ion processor is described in detail in chapter 3. It requires hardware for operation, such as lasers and electrical supply voltages, which are described in chapter 4. In chapter 5, a detailed theoretical analysis of fast ion crystal separation is provided. The experimental performance of our apparatus is assessed in chapter 6. In chapter 7, the realization of a fast and cold two-ion crystal rotation is presented. We demonstrate the capability of our programmable QCCD in chapter 8. A quantum logic circuit is performed on a reconfigurable four-qubit register, to create a four-ion entangled Greenberger-Horne-Zeilinger state. In chapter 9, we turn to a different subject and present experimental results from measurements on a static two-dimensional ion crystal. We realize sideband cooling of a zigzag motional mode and demonstrate the application of a spin-dependent optical dipole force on this mode, which is an important step towards an analog quantum simulator in a two-dimensional geometry. An outlook on future experiments in our quantum device is provided in chapter 10.

2

Theoretical Elements

In this chapter, the theoretical foundations for ion trap operation are summarized. We focus on considerations, which are relevant for our particular implementation of a quantum processor.

2.1. The $^{40}Ca^{+}$ spin qubit

We use trapped $^{40}Ca^{+}$ ions to store and process quantum information. In this section, laser cooling, qubit initialization and qubit readout are described. In figure 2.1, the relevant atomic transitions of calcium ions are sketched.

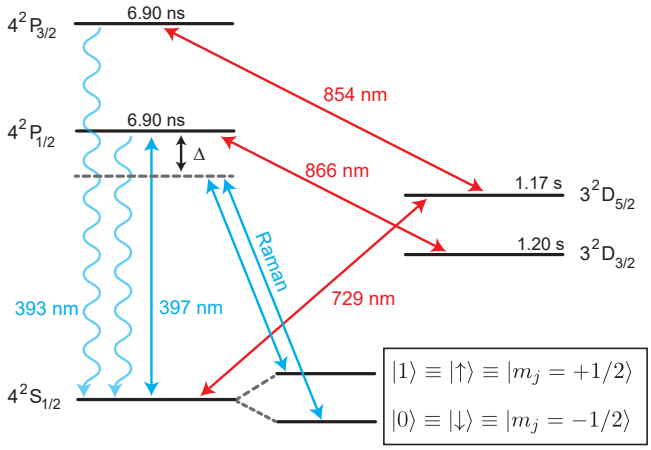

Figure 2.1.: Relevant atomic levels of $^{40}Ca^{+}$. Wavy arrows indicate spontaneous decay from the short-lived P-states and solid arrows indicate laser-driven transitions. The spin quantum bit $|0\rangle, |1\rangle$ is encoded in the ground state of the Zeeman sublevels, which are split by around $2\pi\times10\,\mathrm{MHz}$. Qubit transitions are realized by stimulated Raman transitions near 397 nm, which are typically detuned by $\Delta \approx -2\pi\times3\,\mathrm{THz}$.

2.1.1. Doppler cooling

Doppler cooling of trapped ions is performed on the $2S_{1/2} \leftrightarrow 2P_{1/2}$ transition (hereafter referred to as *cycling* transition) with laser light near 397 nm. The light is red detuned from the atomic resonance by a few tens of MHz. In the reference frame of an ion, which moves towards the laser source, the light is resonant. Thus, a photon is absorbed and the ion is excited to the short-lived $P_{1/2}$ state. The state decays by spontaneous photon emission with 94% probability [Het15] to the ground state $S_{1/2}$ and with 6% probability to the metastable $D_{3/2}$ state, from where it is transferred back to the P-state with laser light near 866 nm. Emitted photons apply a recoil on the ion in all directions, whereas the initial absorption of photons occurs in one direction and thus reduces the ion motion in that particular direction. As a result, a net force arises, which reduces the ion motion in one direction. Since the ion is trapped in a three-dimensional harmonic oscillator potential, it is necessary to cool the oscillatory motion along the principal trap axes x, y, z. This is achieved by a single laser beam, that projects on all of the axes by around 45°. Due to the stochastic nature of the absorption and emission processes, the ion cannot cool down to zero energy. The ion motion is thus reduced to a thermal state. For calcium ions, a Doppler cooling limit temperature of $T = \hbar/(2k_B\gamma) \approx 550\,\mu\text{K}$ is calculated [Win87], where k_B is the Boltzmann constant and $\gamma = 6.9\,\text{ns}$ is the lifetime of the $2P_{1/2}$ state. At a motional frequency of around $\omega = 2\pi\times 1.5\,\text{MHz}$ in our trap, this temperature corresponds to a theoretical minimum mean phonon occupation number of $\bar{n} = 1/(e^{(\hbar\omega/k_BT)} - 1) \approx 7$.

2.1.2. Qubit initialization

For our experiments, we initialize an ion to the $|\uparrow\rangle$-state. This is achieved by optical pumping with light near 397 nm and 729 nm. Pumping near 397 nm is an incoherent process – a laser beam with σ^+ polarization drives exclusively the transition $|\downarrow\rangle \leftrightarrow |P_{1/2}, m_j = +1/2\rangle$. The P-state decays into both ground states $|\downarrow\rangle$ and $|\uparrow\rangle$. Since no excitation from the $|\uparrow\rangle$-state is driven, ultimately all population from the $|\downarrow\rangle$-state is transferred to the $|\uparrow\rangle$-state.
Additionally, coherent optical pumping near 729 nm is performed. A laser pulse with a pulse area of about π is executed to drive the transition $|\downarrow\rangle \rightarrow |D_{5/2}, m_j = +3/2\rangle$. In the experiment, the optical frequency of the laser beam is calibrated to this transition with a precision of a few kHz. To transfer the population from the metastable D-state to the

short-lived $P_{3/2}$-state, light near 854 nm is applied. The P-state decays to the ground states $|\downarrow\rangle$ and $|\uparrow\rangle$, from where only the $|\downarrow\rangle$-state is excited by subsequent repetitions of the scheme. Thus, the ion is initialized to the $|\uparrow\rangle$-state.
Incoherent σ-pumping near 397 nm is simpler to implement, than coherent optical pumping. Selectivity for the driven atomic transitions is given by the polarization of the laser beams, which is subject to small imperfections in the experiment. Thus, the preparation success rate for this method is typically around 98% to 99%. For coherent optical pumping near 729 nm, selectivity is provided by the optical frequency of the laser beam. Thus, a higher preparation success rate of >99% is typically achieved in the experiment. However, 729 nm pumping exhibits an increased duration compared to σ-pumping. We use a combination of both methods as a compromise between duration and efficiency.

2.1.3. Qubit readout

To determine, whether the ion is in the qubit state $|\uparrow\rangle$ or $|\downarrow\rangle$, we use state-selective electron shelving and fluorescence detection. If the ion is in the $|\uparrow\rangle$-state, a frequency-selective laser pulse near 729 nm will transfer it, via a robust rapid adiabatic passage on the narrow quadrupole transition [Pos09], to the metastable $D_{5/2}$-state. Specifically, we transfer the population to the states $|D_{5/2}, m_j = +5/2\rangle$ and $|D_{5/2}, m_j = -3/2\rangle$. Subsequently, light near 397 nm and 866 nm is applied for fluorescence detection, to drive the cycling transition $4^2S_{1/2} \leftrightarrow 4^2P_{1/2}$. If no photons are scattered, the ion was shelved to the metastable D state, thus initially in the state $|\uparrow\rangle$. If photon scattering is observed, the ion was initially in the state $|\downarrow\rangle$. After the fluorescence detection, a laser near 854 nm transfers population in the metastable D-state to a P-state, from where it decays to the S-state. Readout is performed by collecting fluorescence light for about 0.7 ms and a state discrimination rate above 99% is achieved.

2.2. Segmented linear Paul trap

We trap single $^{40}Ca^{+}$ ions in a segmented linear Paul trap [Pau90] in three dimensions x, y, z by applying direct current (DC) and radio frequency (RF) electric fields. The RF field generates a rapidly oscillating quadrupole field, that provides confinement in the radial directions, whereas the DC field provides confinement along the trap axis.

A sketch of the ion trap geometry, which we use in our experiments, is shown in figure 2.2.

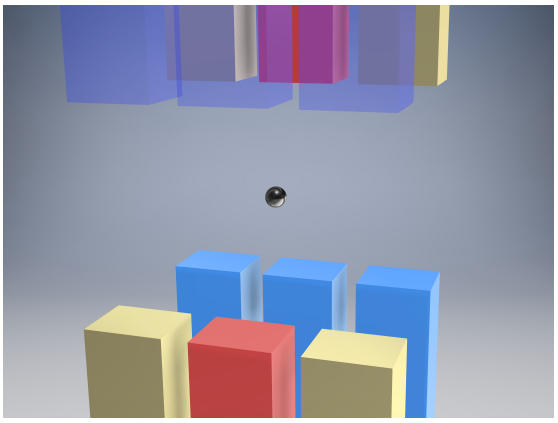

Figure 2.2.: Sketch of a segmented linear Paul trap and a single ion, which is located in the center of the trap. Red electrodes are supplied with DC voltage for axial confinement, blue electrodes with RF voltage for radial confinement and yellow electrodes are on ground potential.

2.2.1. Ion motion

In the following, we consider the motion along the axial x-direction of a single trapped ion – the other directions can be treated analogously. The potential energy for a single ion is given by

$$V(x,t) = \frac{1}{2} m W(t) x^2 \tag{2.1}$$

with the ion mass m and the ion position x. The ion is trapped in a harmonic oscillator potential with time-dependent curvature

$$W(t) = \frac{\Omega_{RF}^2}{4}[a_x + 2q_x \cos(\Omega_{RF} t)] \tag{2.2}$$

where Ω_{RF} is the frequency of the applied radio frequency electric field. The dimensionless parameters a, q for a singly charged ion are given by [Pau90]

$$a_x = \frac{4|e|\alpha U_{DC}}{m\Omega_{RF}^2}, \quad q_x = \frac{2|e|\alpha' U_{RF}}{m\Omega_{RF}^2} \tag{2.3}$$

where e is the elementary charge, U_{DC} is the applied static voltage, U_{RF} is the radio frequency voltage and α, α' are geometry parameters of the ion trap.

The ion position along the x-axis is given for ($|a_x|, q_x^2 \ll 1$) by

$$x(t) \approx 2AC_0 \cos\left(\beta_x \frac{\Omega_{RF}}{2} t\right)\left[1 - \frac{q_x}{2}\cos(\Omega_{RF} t)\right] \tag{2.4}$$

with $\beta_x \approx \sqrt{a_x + q_x^2/2}$, where A is an arbitrary constant and C_0 is a real coefficient from a series expansion, see [Lei03b] for details. The ion motion is comprised of a harmonic oscillation at the frequency $\omega_x = \beta_x \Omega_{RF}/2 \ll \Omega_{RF}$ and a fast oscillation at the trap drive frequency Ω_{RF}, which is denoted as *micromotion*. This motion is enhanced, if the ion is displaced from the node of the RF quadrupole field. Excess micromotion is undesirable in the experiment, since it impairs operations such as coherent laser manipulations. We compensate for the micromotion by displacing the ion with compensation electrodes and minimizing the ion fluorescence on the Doppler cooling transition, for details see [Pos10a].

2.2.2. Ion trap potentials

The ion trap, which is presented in this thesis, is typically operated at an axial electrode voltage of $-6\,\mathrm{V}$. This results in a depth of the trapping potential of around 1.1 eV. The mean kinetic energy of laser-cooled trapped ions is four to five orders of magnitude lower, thus the ions are strongly confined in the trapping potential. The trap features 32 individual segment pairs, which are equally spaced along the x-direction – the calculated electric potentials are shown in figure 2.3 and the technical details of the ion trap are provided in chapter 3.
The electrostatic force feed-through between adjacent segments is high. In the minimum of a single potential well, the slope of an adjacent potential well is almost maximum, which is beneficial for transport operations. The total axial potential is given by

$$\Phi(x) = \sum_i V_i \Phi_i(x), \tag{2.5}$$

where V_i is the voltage at electrode pair i and $\Phi_i(x)$ is the potential, which corresponds to this electrode pair. Each minimum of the total axial potential constitutes an individual

ion trap. The trap frequency of a potential minimum is given by $\omega = \sqrt{\frac{e}{m}\Phi''(x_{min})}$, where x_{min} is the potential minimum position.

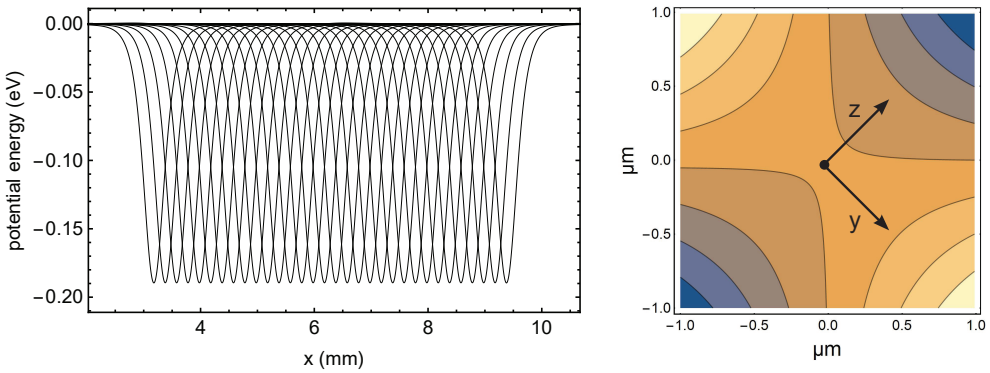

Figure 2.3.: Calculated electrostatic potentials of our ion trap. **Left:** Axial potential wells of the 32 individual Paul traps along the x-direction of the ion trap. In order to calculate the individual axial potential wells, all electrodes are set to ground potential, except for a pair of two opposing DC electrodes, which are set to $-1\,\mathrm{V}$. **Right:** A single ion is located in the center of the static radial potential. Darker colors indicate a higher potential. For this calculation a static voltage is applied to all RF electrodes, which are located along the z-direction. The DC electrodes – located along the y-direction – are set to ground potential. Since the trap geometry in the radial direction is not symmetric, the confinement in the z-direction is stronger, compared to the y-direction. The numerical calculation of the electrostatic potentials is performed with a boundary element method [Sin10].

2.2.3. Ion crystals

We extend the single-ion description to N ions, trapped in the same harmonic potential. The ions $n = 1, ..., N$ repel each other due to the Coulomb force and form *ion crystals* [Jam98; Enz00; Mar03]. A fluorescence image of a six-ion crystal, which is located in our trap, is shown in figure 2.4.

The effective potential for singly charged ions of identical mass is given by

$$V = \frac{m}{2}\sum_{n=1}^{N}\sum_{i=x,y,z}\omega_i^2 x_{n,i}^2 + \frac{e^2}{8\pi\varepsilon_0}\sum_{\substack{n,m=1\\ m\neq n}}^{N}\left[\sum_{i=x,y,z}(x_{n,i}-x_{m,i})^2\right]^{-\frac{1}{2}} \tag{2.6}$$

where $x_{n,i}$ denotes the position of each ion and ε_0 is the vacuum permittivity. For small displacements from the equilibrium position, the dimensionless equilibrium positions

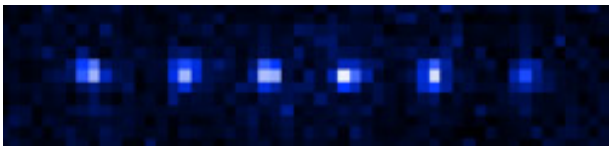

Figure 2.4.: Fluorescence image of a six-ion crystal in our trap. The distance between the ions is around 12 µm and the axial confinement is $2\pi\times0.15$ MHz

of the ions $u_{n,i} = \bar{x}_{n,i}/l$, with $l = [e^2/(4\pi\varepsilon_0 m\omega_x)]^{1/3}$, are obtained by solving the equation [Jam98]

$$\left(\frac{\omega_i}{\omega_x}\right)^2 u_{n,i} + \sum_{\substack{m=1\\m\neq n}}^{N} \frac{u_{m,i} - u_{n,i}}{\left[\sum_{i=1}^{3}(u_{n,i} - u_{m,i})^2\right]^{3/2}} = 0 \tag{2.7}$$

The equation can be solved analytically for $N = 2$ and $N = 3$ in one dimension.
Since the ions are trapped in a common harmonic potential and coupled via the Coulomb force, common motional modes of the ions ω_i arise. Expanding equation 2.6 around the equilibrium positions to second order and neglecting the constant term yields

$$V \approx \frac{1}{2l^2}\sum_{s,t}^{3N} q'_s q'_t D_{s,t} \ . \tag{2.8}$$

where D is the $3N \times 3N$ Hessian matrix of V and $q'_{iN+n} = q_{n,i} \approx x_{n,i} - \bar{x}_{n,i}$ are the displacements from the equilibrium positions $\bar{x}_{n,i}$. Equation 2.8 is now in the form of a harmonic oscillator potential with eigenfrequencies

$$\omega_r = \omega_x\sqrt{\mu_r} \quad \text{with} \quad r = (1, ..., 3N) \tag{2.9}$$

where μ_r are the eigenvalues of the Hessian matrix D [Mar03]. The relevant two-ion modes, for the experiments performed in this thesis, are shown in figure 2.5. Ion crystals align in a chain along the direction of the weakest confinement, which is usually the trap axis x. If the ratio of axial to radial confinement is increased, linear ion crystals undergo the phase transition to a *zigzag* ion crystal. A detailed study of the equilibrium positions and motional modes of these crystals is provided in [Kau12a; Kau12b]. In chapter 9 of this thesis, the realization of a spin-dependent force on a three-ion zigzag crystal is presented.

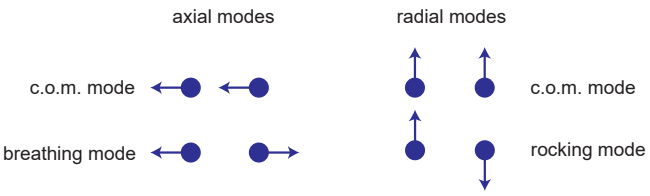

Figure 2.5.: Common motional modes of a two-ion crystal. The motional frequency of the axial breathing mode is $\sqrt{3} \cdot \omega_x$, where ω_x is the axial secular frequency, that corresponds to the center-of-mass mode. The rocking mode frequencies are $\sqrt{\omega_r^2 - \omega_x^2}$, where $\omega_r = \omega_{y,z}$ is one of the radial secular frequencies.

2.3. Light-motion coupling

In the following, quantization of the ion motion is used to describe the coupling to a light field. The ion motion in the one-dimensional harmonic oscillator potential along the x-direction, from equation 2.1, is described in the Heisenberg picture by the Hamilton operator

$$\hat{H}_m = \hbar\omega_x(\hat{a}^\dagger\hat{a} + 1/2) \tag{2.10}$$

with the ladder operators $\hat{a}^\dagger$ and $\hat{a}$, that act on the eigenstates $|n\rangle$ of the harmonic oscillator at frequency ω_x. The position operator is given in this picture by $\hat{x} = \sqrt{\hbar/(2m\omega_x)}(\hat{a}^\dagger + \hat{a})$.
We treat the ion as a two-level system for the light-matter interaction following [Lei03b]. The ground state $|g\rangle$ and the excited state $|e\rangle$ are separated by the energy $\hbar\omega_0 = \hbar(\omega_e - \omega_g)$. The Hamiltonian, which describes this system is given by

$$\hat{H}_e = \hbar(\omega_g |g\rangle \langle g| + \omega_e |e\rangle \langle e|) = \hbar\frac{\omega_0}{2}\sigma_z, \tag{2.11}$$

where σ_z is the Pauli z-matrix. A single ion, coupling to a running wave light field, is described by the total Hamiltonian

$$\hat{H} = \hat{H}_m + \hat{H}_e + \hat{H}_i. \tag{2.12}$$

The interaction Hamiltonian is given by

$$\hat{H}_i = \frac{\hbar}{2}\Omega(\sigma_+ + \sigma_-)[e^{i(k\hat{x}-\omega t+\phi)} + e^{-i(k\hat{x}-\omega t+\phi)}], \tag{2.13}$$

where $|g\rangle\langle e| = \sigma_- = 1/2(\sigma_x - i\sigma_y)$ and $|e\rangle\langle g| = \sigma_+ = 1/2(\sigma_x + i\sigma_y)$, Ω is the resonant Rabi frequency, k is the wave number, ω is the effective light frequency and ϕ is the phase of the light field.
The *Lamb-Dicke* parameter is defined as $\eta = kx_0 = k\sqrt{\hbar/(2m\omega_x)}$. It is the product of the extension of the ground state wave function and the wave number of the driving laser field – a large η results in a strong coupling of the ion motion to the driving laser field. We now consider ions, which are near the motional ground state – that is in the Lamb-Dicke regime, where $\eta \ll 1$ and the mean phonon occupation number $\bar{n}$ is small.

The Hamiltonian from equation 2.13 is transformed to the interaction picture with respect to the free Hamiltonian $\hat{H}_m + \hat{H}_e$. Subsequently, a rotating wave approximation and an expansion to the lowest order in η are applied. Finally, the Hamiltonian takes the following form in the Lamb-Dicke regime [Lei03b]:

$$\hat{H}_i^{(LD)} = \frac{\hbar}{2}\Omega_0\sigma_+[1 + i\eta(\hat{a}e^{-i\omega_x t} + \hat{a}^\dagger e^{i\omega_x t})]e^{i(\phi-\delta t)} + h.c., \tag{2.14}$$

where Ω_0 is the bare Rabi frequency and $\delta = \omega - \omega_0$ is the detuning of the effective light frequency to the atomic transition. Three important transitions between atomic levels are described by this Hamiltonian:

- carrier transitions for $\delta = 0$ of the type $|n\rangle|g\rangle \leftrightarrow |n\rangle|e\rangle$ with Rabi frequency Ω_0 are used for spin flips.

- red sideband transitions for $\delta = -\omega_x$ of the type $|n\rangle|g\rangle \leftrightarrow |n-1\rangle|e\rangle$ with Rabi frequency $\Omega_{n,n-1} \approx \Omega_0\eta\sqrt{n}$ are used for resolved sideband cooling.

- blue sideband transitions for $\delta = +\omega_x$ of the type $|n\rangle|g\rangle \leftrightarrow |n+1\rangle|e\rangle$ with Rabi frequency $\Omega_{n,n+1} \approx \Omega_0\eta\sqrt{n+1}$ are used for spectroscopic measurements.

Beyond the Lamb-Dicke regime, the Rabi frequencies for the transitions are given by

$$\Omega_{n,n+\Delta n} = \Omega_{n+\Delta n,n} = \Omega_0 e^{-\eta^2/2}\eta^{|\Delta n|}\sqrt{\frac{n_<!}{n_>!}}L_{n_<}^{|\Delta n|}(\eta^2), \tag{2.15}$$

where L is the generalized Laguerre polynomial [Lei03b] and $n_<$ is the lesser of $n + \Delta n$ and n.

2.4. Stimulated Raman transitions

We use two laser beams near 397 nm to drive transitions between the qubit states $|\uparrow\rangle$ and $|\downarrow\rangle$, via two-photon stimulated Raman transitions [Mon95b] – the scheme is sketched in figure 2.6.

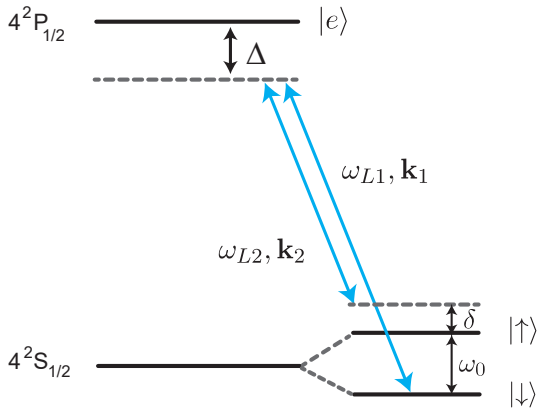

Figure 2.6.: Scheme of stimulated Raman transitions in $^{40}Ca^+$ ions. The secular frequencies are not shown here – the detuning δ can be tuned to $-\omega_x$, for instance, to adress the first red sideband. Typically, coupling of the individual laser beams via electric dipole transitions is considered [Win98].

The beams have the optical frequencies ω_{L1} and ω_{L2}, respectively. The effective wave vector, that couples to the internal states of the ion, is the difference of the individual laser beam wave vectors $\mathbf{k} \equiv \mathbf{k}_1 - \mathbf{k}_2$. The effective detuning δ from the transition $|\uparrow\rangle \leftrightarrow |\downarrow\rangle$ is given by $\omega_0 + \delta = \omega_{L1} - \omega_{L2}$. Both beams are detuned from the cycling transition by a single photon detuning Δ, which is typically more than four orders of magnitude larger than its natural linewidth of about $2\pi\times22$ MHz. The effective coupling strength between the states $|\uparrow\rangle$ and $|\downarrow\rangle$ is then given by [Lei03b]

$$(\hbar/2)\Omega = -\hbar\frac{|\Omega_{L1}\Omega_{L2}|}{\Delta}e^{-i\Delta\phi}, \tag{2.16}$$

with the dipolar Rabi frequencies Ω_{L1} and Ω_{L2}, that pertain to resonant driving of the cycling transition for each of the two beams. The phase $\Delta\phi$ corresponds to the difference phase between the two laser beams.

2.5. Entangling quantum gate

In order to create entanglement between the spins of two trapped ions, we employ a geometric phase gate – specifically the light-shift gate [Lei03a]. The explanation of the gate mechanism in the following is based on [Lee05; Roo08].

2.5.1. Forced harmonic oscillator

We consider a single ion harmonic oscillator at frequency ω_x, which is driven by a force at frequency ω_f and coupling strength Ω, and we neglect the two-level structure of the trapped ion qubit. The Hamiltonian describing this system has the form $\hat{H} = \hat{H}_m + \hat{H}_i = \hbar\omega_x(\hat{a}^\dagger\hat{a} + 1/2) + \hbar\Omega i(\hat{a}^\dagger e^{i\omega_f t} - \hat{a}e^{-i\omega_f t})$, where we neglect the wave vector and the phase of the driving laser field. In the interaction picture, with respect to $\hat{H}_m$, the Hamiltonian takes the form

$$\hat{H}_{int} = \hbar\Omega i(\hat{a}^\dagger e^{i\delta_f t} - \hat{a}e^{-i\delta_f t}), \tag{2.17}$$

with $\delta_f = \omega_f - \omega_x$ and where $|\delta_f| \ll \omega_x$. If the interaction Hamiltonian is applied for a time t, a displacement operator is realized

$$\hat{D}(\alpha) = e^{\alpha\hat{a}^\dagger - \alpha^*\hat{a}}, \tag{2.18}$$

where $\alpha(t) = \int_0^t dt'\Omega e^{i\delta_f t'}$. The operator translates motional states in position-momentum phase space without distortion. It acts on the motional ground state by creating a coherent state $\hat{D(\alpha)}\,|0\rangle = |\alpha\rangle = e^{-1/2|\alpha|^2}\sum_{n=0}^{\infty}\frac{\alpha^n}{\sqrt{n!}}\,|n\rangle$, where $|n\rangle$ are Fock states of the harmonic oscillator.
After an interaction time t with the driving force, the time evolution operator is given by

$$\hat{U}(t) = e^{i\Phi(t)}\hat{D}(\alpha(t)) \quad \text{with} \quad \Phi(t) = \mathrm{Im}\left(\int_0^t d\alpha(t')\alpha(t')^*\right), \tag{2.19}$$

where an integration over infinitesimal displacements in time and the Baker-Campbell-Hausdorff relation $\hat{D}(\alpha)\hat{D}(\beta) = \hat{D}(\alpha+\beta)e^{i\mathrm{Im}(\alpha\beta^*)}$ were used [Lee05; Roo08]. The

geometric phase Φ is accumulated over the entire path in phase space and the following relations are obtained for the displacement and the geometric phase

$$\alpha(t) = i\frac{\Omega}{\delta_f}(1 - e^{i\delta_f t}) \quad \text{and} \quad \Phi(t) = \left(\frac{\Omega}{\delta_f}\right)^2 (\delta_f t - \sin(\delta_f t)). \tag{2.20}$$

After an interaction time $\tau = 2\pi K/|\delta_f|$, where K is an integer, K loops in phase space are closed ($\alpha(\tau) = 0$) and the initial motional state is retained. However, a phase of $\Phi(\tau) = 2\pi K \left(\frac{\Omega}{\delta_f}\right)^2 \text{sign}(\delta_f)$ is imprinted on the state. Entanglement between the spins of two ions can be created by making this phase spin-state dependent, as explained in the following section.

2.5.2. The $\sigma_z \otimes \sigma_z$ gate on two ions

In order to create entanglement, we trap two ions in a potential well and apply a harmonic driving force with two superposed laser beams, as shown in figure 2.7. The beams form a beat pattern with the frequency $\omega_L \equiv \omega_{L1} - \omega_{L2}$ and the effective wave vector $\mathbf{k} \equiv \cos(\Theta)(\mathbf{k}_{\mathrm{L1}} - \mathbf{k}_{\mathrm{L2}})$ in the radial z-direction. An AC Stark shift is exerted on the spin states $|\uparrow\rangle, |\downarrow\rangle$, which depends on the polarization of the light and is different for each state [Sch16]. This corresponds to a spin-dependent displacement force [Mon96; Lei03a]. The beat pattern is essentially a moving periodic spin-dependent potential, which gives rise to a near-resonant force on both ions in the radial direction. The beat pattern is moving, since the two laser beams are detuned. This system can be treated similarly to the forced harmonic oscillator, where only a single ion is considered, see section 2.5.1. By extending equation 2.17, the resulting Hamiltonian describing the interaction is then

$$\hat{H}_{int} = \hbar\Omega i(\hat{a}^\dagger e^{i\delta_f t} - \hat{a}e^{-i\delta_f t})(\hat{\sigma}_z \otimes \mathrm{I} + \mathrm{I} \otimes \hat{\sigma}_z) \tag{2.21}$$

where I is the 2×2 identity matrix, and unimportant global and single qubit phases are disregarded. In our case, the detuning is $\delta_f = \omega_L - \omega_z$, with the radial c.o.m. mode ω_z of the two ions, which is used as a bus mode for the gate. Excitation of other radial modes can be ignored in first order, as they are sufficiently separated in frequency space.

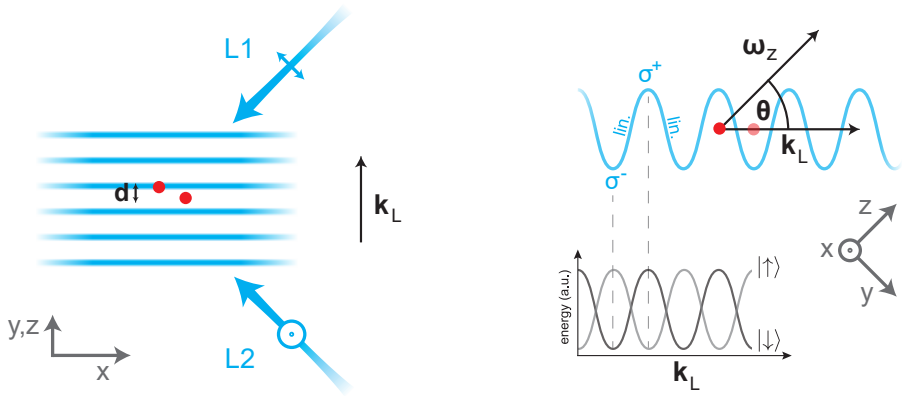

Figure 2.7.: Raman laser beam configuration for the light shift gate on a radial secular mode. **Left:** Top-view of two ions in the trap. Two laser beams L1 (horizontal polarization) and L2 (vertical polarization) are focused on the ions. A polarization standing wave is formed, which is perpendicular to the trap axis (x-direction). Blue stripes indicate zones of σ^+-polarized light and white areas indicate zones of σ^--polarized light. The effective wave vector of this wave is given by $\mathbf{k}_\mathrm{L} = \mathbf{k}_\mathrm{L2} - \mathbf{k}_\mathrm{L2}$. **Right:** View from the x-direction on the ions and the polarization standing wave. One ion is opaque for better visibility. The radial trap axis z forms an angle Θ with the effective wave vector. Thus, the effective wave vector, for the coupling to the gate mode ω_z, is reduced by $\cos(\Theta)$. Due to the linear $\perp$ linear polarization configuration of the beams, the resulting polarization is space-dependent [Cou92; Sch16]. Specifically, it varies from σ^- to linear to σ^+. The circular components give rise to a Stark shift, which depends on the spin state. In the lower panel, the resulting energy shift to the spin states is sketched. As a result, a space- and spin-dependent potential is formed.

The relative ion distance $\mathbf{d}$, in the moving periodic potential, corresponds to the Raman phase difference between the ions and determines which of the four spin states are driven by the near resonant force [Bal14]. If the distance is chosen to be $\mathbf{k} \cdot \mathbf{d} = \pi + n2\pi$, where $n = 0, \pm1, \pm2, ...$, only the states $|\downarrow\uparrow\rangle, |\uparrow\downarrow\rangle$ are driven by the force for maximum gate efficiency.

Two ions, which are initialized to the state $|\uparrow,\downarrow\rangle\,|n = 0, n = 0\rangle$, are driven along a closed circle in phase space, when exposed to the gate laser pulse for duration $\tau = 2\pi/|\delta_f|$. Spin and motion of each individual ion are entangled during the phase space trajectory, but separable once the loop is closed. After the closed trajectory in phase space, the two ions are in the separable state $e^{-i\Phi(\tau)}\,|\uparrow\downarrow\rangle\,|n = 0, n = 0\rangle$. The laser intensities, the gate

detuning and the beam polarizations can be adjusted, such that the geometric phase is $\Phi(\tau) = -\pi/2$. In this situation, the time evolution operator is given by

$$\hat{U}(\tau) = \hat{G} \equiv \begin{pmatrix} 1 & & & \\ & i & & \\ & & i & \\ & & & 1 \end{pmatrix}. \tag{2.22}$$

This phase gate can be used in combination with single-qubit rotations [Nie00] to produce a maximally entangled Bell state $1/\sqrt{2}(|\uparrow\uparrow\rangle + i\,|\downarrow\downarrow\rangle)$, which is demonstrated in section 8.4. In the experiment, the gate operator will feature a global phase, which does not play a role, as long as the phase difference between the states $|\uparrow\uparrow\rangle, |\downarrow\downarrow\rangle$ and $|\downarrow\uparrow\rangle, |\uparrow\downarrow\rangle$ is $\pm\pi/2$.

3

Ion Trap

The centerpiece of cold ion experiments is the ion trap, which needs to meet stringent design requirements. Within the scope of the work leading to this thesis, a micro-structured ion trap was designed, manufactured, characterized and used to conduct state-of-the-art quantum information processing experiments. The goal was to produce a trap, that features low motional heating and good optical access and allows for fast ion shuttling operations. In this chapter, the design of the trap and the *filter board* as well as the fabrication and the ultra high vacuum assembly procedure of these parts are described. The entire trap is displayed in figure 3.1 – it is an advancement of a former version of a microchip ion trap [Sch07; Sch09] with significantly improved performance.

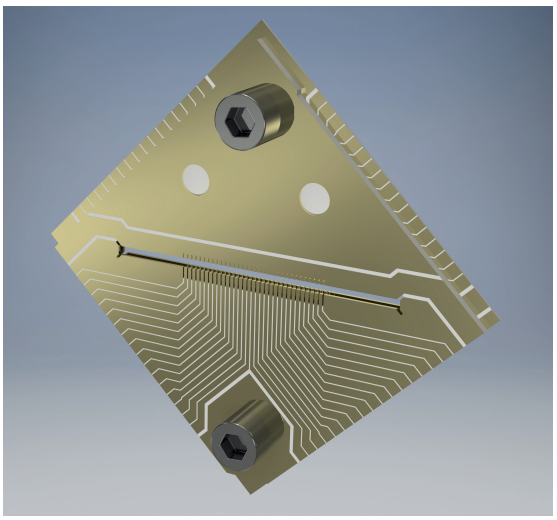

Figure 3.1.: Technical drawing of the linear segmented micro-structured ion trap. The trap consists of three layers, which are mounted by two titanium screws. The outside dimensions of the trap are around 15 mm x 15 mm.

3.1. Micro-structured ion trap design

Three-dimensional segmented Paul traps typically consist of two chips with a conducting coating, which constitute the trap electrodes and feature a slit that defines the center of the trap. The two trap chips are separated by an insulating spacer layer. A close-up view of the trapping region of our ion trap is shown in figure 3.2.

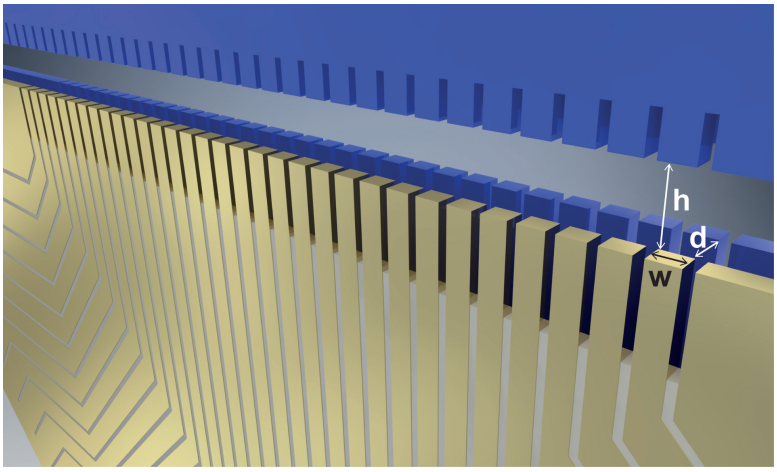

Figure 3.2.: Close-up view of the trapping region of the segmented ion trap showing all 32 trapping zones. The gold-colored electrodes, are individually supplied with programmable voltage waveforms. Between the electrodes, 50 µm wide white isolation trenches are located. The RF electrodes are colored blue in this drawing for clarity. They are segmented in the same fashion to make the trap geometry symmetric. The effective trap dimensions are initially chosen to be $h = 400\,\mu m$, $d = 254\,\mu m$ and $w = 150\,\mu m$. After an electroplating procedure, the thickness of all gold surfaces is increased by around 8 µm. Therefore, the trap dimensions are changed to $h = 384\,\mu m$ and $w = 166\,\mu m$. Another DC electrode array, identical to the electrode array on the bottom, resides behind the blue top RF electrode. Ions are trapped in the center of the trap slit and are transported between individual electrodes.

The trap features 32 independent DC electrodes, which are supplied from a fast multichannel arbitrary waveform generator, thus enabling fast ion transports along the trap axis. The geometry parameters are chosen to facilitate separation and merging operations for ion crystals, see section 5.2. The overall dimensions result from a trade-off between small dimensions for large electric fields for tight confinement and fast shuttling, and large dimensions for sufficient optical access. Thus, a trap slit of $h = 400\,\mu m$ is chosen as well as a thickness of $d = 254\,\mu m$ for the spacer between the trap chips. The width of the electrodes was chosen to be $w = 150\,\mu m$ as this maximizes the quartic

confinement during a separation operation and also features a sufficiently high trap frequency [Kau14].
The trap slit is elongated to 12.84 mm to suppress axial micromotion. The isolation trenches between all gold surfaces are at least 50 µm wide, since about 8 µm of gold are added to the thickness of the gold layers in a consecutive electroplating process. A thick gold layer is empirically known to reduce anomalous heating of the ions for comparable traps [Bla10; Kie15].
Two screws ensure a precise and sturdy assembly of the trap chips. Similar ion traps were assembled in our research group with glue. However, this comes with the disadvantage of potential outgassing, which could lead to increased overall background pressure in the UHV apparatus, increases local pressure in the back volume, and undesired contamination of the trap surfaces. Furthermore, the glue does not allow for minor corrections of the trap chip alignment once it has become solid.

3.2. Ion trap fabrication

The ion trap was fabricated in cooperation with Christian S.[1] (mainly responsible for electroplating and trap chip cutting) and Marco D.[2] (filter board design) and Max H.[2] (wire bonding). The main parts of the ion trap are two gold-coated alumina chips, which form the trap electrodes, see figure 3.3. The manufacturing process of these chips consists of five steps. In the first step, the chips are laser machined – cuts which penetrate the wafer are carried out, for instance the trap slit. In the second step, the chips are coated with gold in an evaporation process. Since all electrodes are shorted after this step, in the third step a further laser machining run removes gold, such that a set of electrically isolated electrodes is obtained. On the outer edge of the chips, the electrodes are still connected, which is necessary for the fourth step: an electroplating procedure creates a thick gold layer on top of the first rather thin gold layer. In a last step, the chips are diced along their sides in order to isolate all electrodes. This section contains a description of the five steps in the manufacturing process of the trap chips.

[1] Present address: .....
[2] Present address: .....

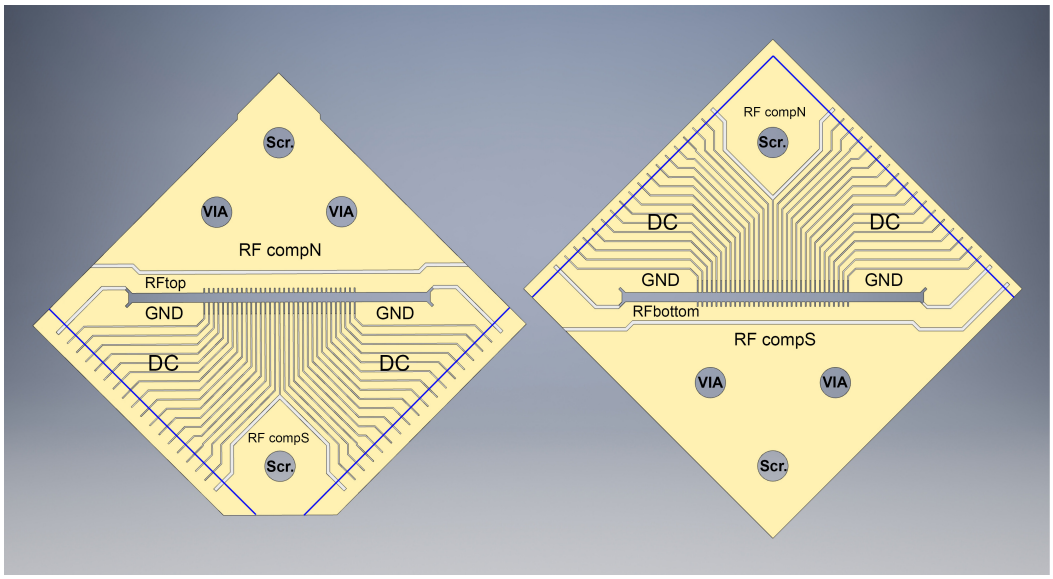

Figure 3.3.: Top (left) and bottom (right) chip of the ion trap. All electrodes are labeled, the acronym 'Scr.' denotes the 1.3 mm wide holes for the two titanium screws. Additionally, for micromotion compensation in the direction of the DC electrodes, the electrodes RF compN and RF compS feature compensation in the direction of the RF electrodes. The back side of each chip is symmetric with respect to its front side. After the electroplating procedure, the chips are cut along the blue lines in order to isolate the conducting surfaces.

First step – laser machining: The trap chips are made from 5.08 cm x 5.08 cm polished alumina wafers[3] (aluminum oxide, Al_2O_3) of 127 µm thickness. A femtosecond laser is capable of cutting well defined structures in this material with a precision of a few µm – the process is executed by a specialized company[4]. The dimensions of the wafers allow for placing eight trap chips on a single wafer, which allows for a better handling of the fragile trap chips and a production of several identical chips within one fabrication run for a selection of the best samples. The laser machining and gold evaporation process are carried out on all chips on the same wafer. In the first laser machining step, all cuts which penetrate the chip are laser machined: the trap slit, including the segmented electrode geometry, as well as the holes for the vertical interconnect accesses (VIAs). The trap electrodes are cut from only one side with the ablation laser, which results in a slightly conical shape. Thus, the sharp well-defined edges are the sides of the trap chips which face the ions in the assembled trap.

[3]Coors ADS996-polished / Al2O3 99,6%
[4]Micreon GmbH, Garbsener Landstraße 10, 30419 Hannover, Germany

After the laser machining, the wafers experience a thorough cleaning procedure to ensure a perfectly clean surface for the subsequent gold coating. At first, the wafers are cleaned in an ultra sonic bath at 40 °C of isopropyl alcohol (C_3H_8O, purity grade $\geq$ 99.8%) and afterwards rinsed with de-ionized water. A successive cleaning with the aggressive *piranha solution* removes organic, reactive and many other materials from the alumina wafers. The piranha solution is made by slowly adding one part of hydrogen peroxide (H_2O_2, 30% dilution) to four parts of concentrated sulfuric acid (98% H_2SO_4). After a waiting period of 30 minutes, which serves to cool from the exothermic mixing procedure, the wafers are slowly dipped into the solution. The submerging needs to be carried out slowly to prevent damage to the thin alumina wafers from a thermal shock. The wafers spend ten minutes in the piranha solution and are then submerged in de-ionized water (purity grade: lab grade) and ultimately in isopropyl alcohol (purity grade $\geq$ 99.8%). After this wet cleaning procedure, the wafers are dried for at least one hour, suspended inside a beaker and covered by aluminum foil to prevent contamination. Subsequently, the wafers are packaged and prepared for the gold coating process.

Second step – gold coating: In the next step, the wafers are coated by an electron beam physical vapor deposition procedure with an adhesive titanium layer of 50 nm, followed by a 500 nm layer of gold to create an inert conducting surface. The process is performed at the university of Ulm[5]. In the procedure, the wafers are rotated and turned to ensure a homogenous coating around corners and edges. One example of the wafers after this fabrication step is shown in figure 3.4.

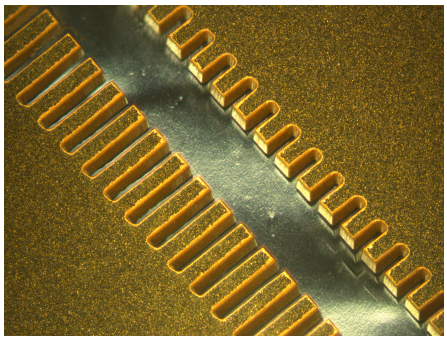

Figure 3.4.: Microscope image of the trapping region after gold coating. Small grains of gold are visible. From a distance, the wafers resemble a mirror-like surface.

[5]Universität Ulm, Institut für Optoelektronik, Albert-Einstein-Allee 45, 89081 Ulm. Contact person: R. R.

Third step – isolating the electrodes: The gold-coated wafers experience a second run of laser machining at a specialized company[6] similar to the first step. Here, the deposited gold is removed precisely along tracks to provide isolation and thus creating the trap electrodes. Finally, the individual trap chips are removed from the wafer – one of the chips is shown in figure 3.5. On the outside of the chips, all electrodes are connected to allow for the subsequent electroplating procedure. On the top chip, we leave 1 mm excess material on the outside and on the bottom chip, we leave 0.5 mm excess material.

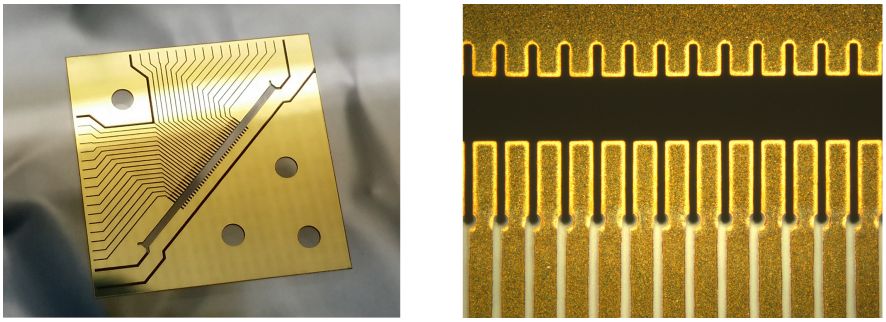

Figure 3.5.: Left: Photograph of a gold-coated ion trap chip after the second laser machining run. On the outside of the chip all electrodes are still electrically connected for the subsequent electroplating procedure. **Right:** Microscope image of the trapping region. The exposed alumina between the electrodes serves as electrical isolation.

Fourth step – electroplating: In this procedure, the 500 nm gold layer on the chip surface is increased with an electrochemical deposition technique to around 8 µm. After the last, step all electrodes on the chip are still electrically connected, thus only one electrical connection per chip is required to set all electrodes on the same electrical potential for the procedure.

The electroplating procedure was carried out similarly to [Bla10]. The solution, which was used for the gold deposition, is a sulphite-based gold bath[7]. Before the electroplating, the chips are cleaned in an ultra sonic bath of isopropyl alcohol (purity $\geq$ 99.8%) at 40 °C for 15 minutes. The basic principle of the electroplating procedure is to place the trap chip in the gold bath next to a platinum[8] electrode. This electrode is set to a positive voltage and acts as the anode, whereas the trap chip is wired to ground and acts as a cathode. Gold is then deposited on the cathode and increases the surface

[6] Micreon GmbH, Garbsener Landstraße 10, 30419 Hannover, Germany
[7] Gold-SF-bath, Metakem GmbH, Achtzehnmorgenweg 3, 61250 Usingen, Germany
[8] beaker glass anodes - platinized titanium 0.5l, Metakem GmbH

thickness of the original layer. The ideal current density on the surface is specified to be $10\,\mathrm{mA/cm^2}$, which results in a deposition rate of $38\,\mu\mathrm{m}$ per hour. The setup for the electroplating process is shown in figure 3.6.

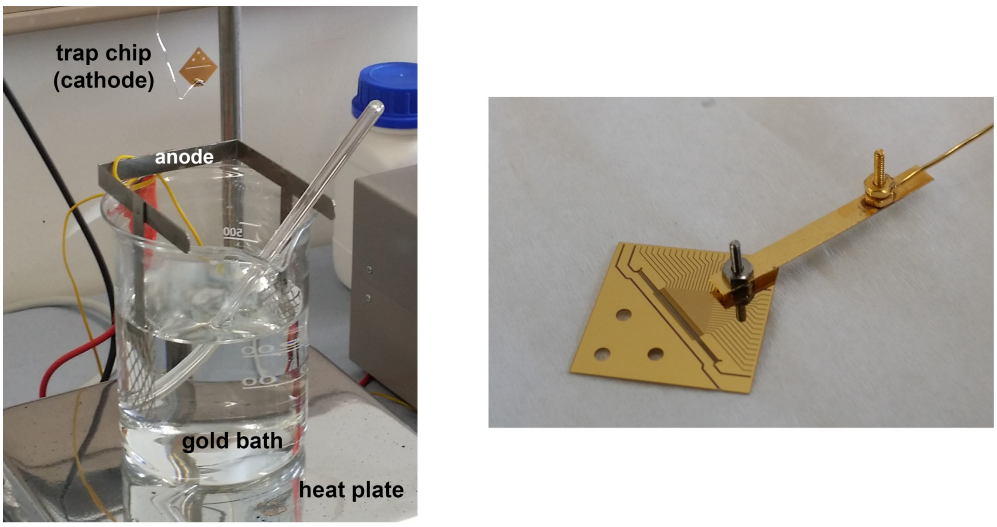

Figure 3.6.: Left: Setup for the electroplating procedure. The gold bath, a platinum anode, a manual stirring rod and a magnetic stirrer reside in a 500 ml beaker. The trap chip is submerged in the gold bath for electroplating. A current supply is connected to the anode and the cathode. **Right:** The screw holes, which are used for assembling the multi-layered trap, serve as an electrical connection for a single trap chip during the electroplating procedure. The screw, which connects the thin metal sheet to the trap chip, is a conventional stainless steel M1.2 screw. Between the metal sheet and the trap chip, as well as on top of the metal sheet, a stainless steel nut is placed. The contact between the metal sheet and the conducting wire is established similarly – the wire is tightened between two M1.2 nuts. Tightening of the screws is executed by hand without a defined torque.

The voltage drop between cathode and anode as well as the current are monitored with two multimeters. The heat plate is used stabilize the gold bath at 60 °C and the magnetic stirrer is set to 600 rpm. Before placing the trap chip into the gold bath, the anode is set to $-0.1\,\mathrm{V}$ to prevent detrimental effects on the surface quality from an uncontrolled start of the process. Once the trap chip is submerged in the gold bath, the anode is switched to a positive voltage and ramped to $+0.6\,\mathrm{V}$. It is stabilized at this setting, by the constant voltage mode of the power supply, throughout the process. In test procedures for the electroplating process it was found, that stabilizing the voltage – rather than the current – yields a satisfying result. In principle, the current should

be stabilized to reach the ideal current density of $10\,\mathrm{mA/cm^2}$, however this relies on having precise knowledge of the surface that is being electroplated. Since the trap chip is contacted by a wire, a metal sheet, a screw and nuts, calculating the precise surface resulted in a current density which deviated from the expected value by 20% to 50%. The voltage is a monotonous function of the applied current and thus a working procedure was found where the voltage is stabilized and the current density is monitored, to be in the region of the expected value. The trap surface, which is electroplated, is $4.5\,\mathrm{cm^2}$ and the contacting chip holder and wire has a combined surface of around $1.5\,\mathrm{cm^2}$. Thus, the current is monitored to be around 60 mA to reach the ideal current density.
The chips spend about 15 minutes in the gold bath, which results in a layer thickness of about 8 µm. The process is paused several times for an inspection of the chips, where the chips are removed from the solution. There is no evidence that this might be detrimental to the surface quality. During the process, a manual stirring rod is used in addition to the magnetic stirrer, in order to enhance the mixing of the solution and to prevent a well defined flow of the gold particles. Once the desired layer thickness is reached, the current is turned off and the chips are taken out of the gold bath. After the electroplating process, the trap chips are cleaned in de-ionized water, isopropyl alcohol (purity $\geq$ 99.8%) and acetone (C_3H_6O). A fully coated trap chip is shown in figure 3.7.

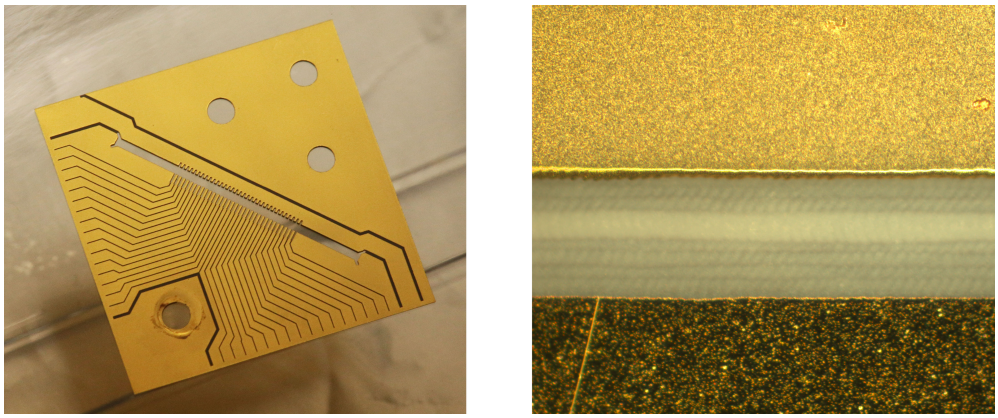

Figure 3.7.: Left: Photograph of an electroplated trap chip. The surface is slightly less reflective than after the initial gold evaporation. In the bottom corner, the surface shows traces of the electrical contact during the procedure. **Right:** Microscope image of a region with and without electroplating. The top region was contacted during the deposition process and the gold layer is thus about 8 µm thicker than the region at the bottom, which only features the evaporated gold layer. The two regions are separated by an isolation trench.

During the electroplating process, small nuggets of gold are observed in the gold bath. For future procedures it is thus advisable to filter the solution. It will also be helpful to put the beaker, that contains the gold bath in a larger beaker which contains tap water and is already heated to 60 °C. This heat bath setup ensures a quicker heating process and a more stable temperature for the gold bath. Furthermore, for a more accurate voltage and current control during the electro plating procedure, the surface of the wires, which hold the trap chips in the solution, should be accounted for in the calculation.

Fifth step – cutting off the trap chips: After the trap chips are electroplated, they need to be diced along the blue lines in figure 3.3 to isolate the electrodes. The trap chips are cut individually with a dicing saw. To prepare the trap chips for the cutting procedure, they are glued to the surface of a 5 cm x 5 cm x 1 cm slab of plastic with a special wax[9], which can be completely dissolved in acetone later on. It is advisable to apply a thin bubble-free layer of wax between the trap chip and the plastic slab – we inspect the wax layer by eye and do not observe bubbles. The plastic slab is then sturdily mounted in the diamond wire saw[10]. The saw wire has a thickness of 220 µm and a diamond grain size of 40 µm. It moves up and down along the trap chip surface and cuts through the alumina wafer along the desired lines. The wire changes its direction every 5 s and the velocity of the wire is estimated to be around 2 m/s. The precision of the cuts is sufficient, it is measured to be around 200 µm since the sawing was guided by eye. However, the described cutting procedure causes a complication which is illustrated in figure 3.8.

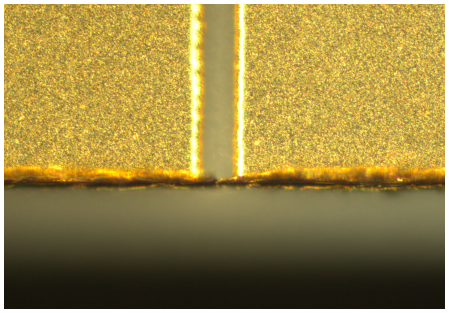

Figure 3.8.: Microscope image of a sawed off edge of a trap chip. The cutting wire is moved along the surface along the horizontal direction to cut through the alumina. As a side effect, the movement drags gold from the soft gold surface into the isolation trench between the electrodes.

[9] Crystalbond™ Type 509
[10] model 3500, Diamond WireTec GmbH & Co.KG, Südliche Bergstraße 14, 69469 Weinheim, Germany

Gold from the surface is dragged into the isolation trenches and needs to be removed in a subsequent filing procedure, to prevent short-cuts between the electrodes. The trap chip is glued on the plastic slab, with both cut-off sides coinciding with the edges of the plastic slab. The slab is clamped to a simple holder and mounted under a 45° angle with respect to the table. We then file across the cut-off side carefully with diamond-coated paper[11] in parallel to the table. An inspection under the microscope reveals that using this procedure the gold in the isolation trenches is reliably removed.
The trap chips are then removed from the plastic slab, by dissolving the wax in acetone and afterwards thoroughly cleaned in de-ionized water (evaporation residue < 1 ppm, total organic carbon < 10 ppb) and isopropyl alcohol (purity $\geq 99.8\%$) in an ultra sonic bath. This step finalizes the fabrication of the ion trap chips, which are then ready for assembly.

3.3. Filter board

The voltage supply for each DC electrode is filtered in two steps to reduce electrical noise near the trapped ions. The DC voltage is first filtered by an external low-pass filter outside the vacuum chamber, which has a cutoff frequency of around $2\pi\times50\,\mathrm{kHz}$, as described in section 4.1. A second step of filtering is done inside the vacuum chamber close to the ion trap. It serves mostly to suppress the pick-up of the RF supply at a frequency of $2\pi\times33\,\mathrm{MHz}$. This second filter is a simple RC low-pass filter with a cutoff frequency of $f_c = 2\pi\times8\,\mathrm{MHz}$. Since each of the 32 DC electrode pairs needs to be equipped with a filter, a total amount of 64 low-pass filters is assembled close to the trap. This is achieved by arranging the electronic components around the trap on a filter board as depicted in figure 3.9. The board is made of alumina and features a laser machined opening in the center for the placement of the ion trap. The conducting tracks are printed and sintered on the alumina[12].

[11] polishing sheets for optical fibers
[12] fabricated at the Technische Universität Dresden: Fakultät Elektrotechnik und Informationstechnik. Institut für Aufbau und Verbindungstechnik der Elektronik. Contact person: M. L.

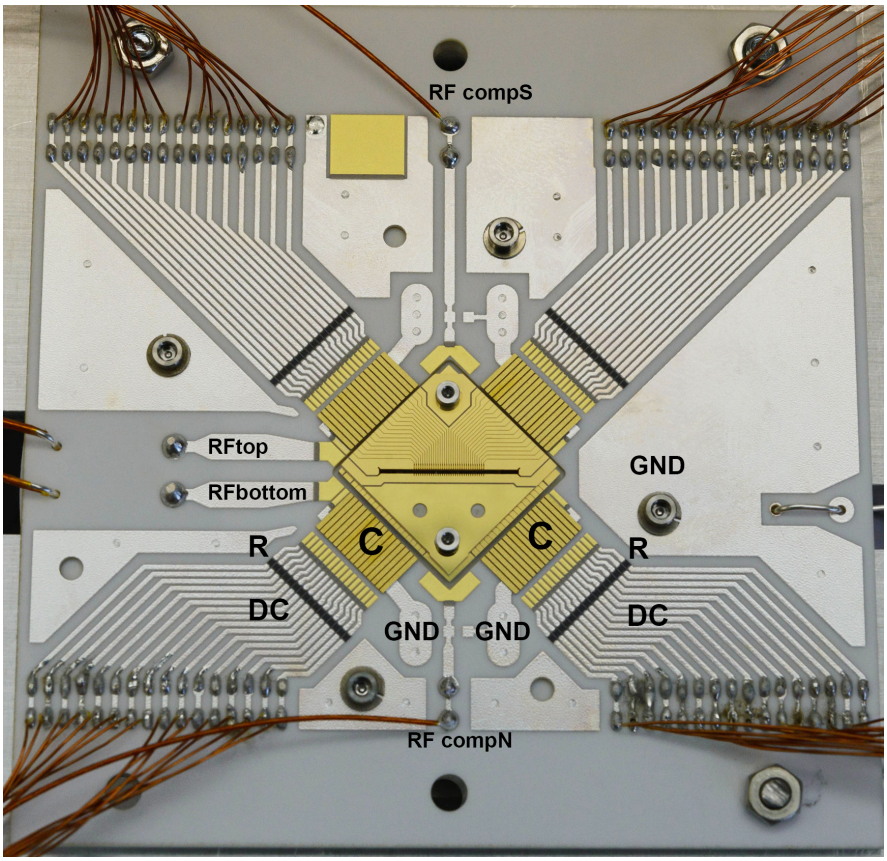

Figure 3.9.: Photograph of the filter board with the ion trap mounted in its center and labels for all relevant electrodes. The outer dimensions of the board are 79.9 mm x 78.3 mm x 630 µm. Each of the four DC track arrays, which encompasses 16 individual lines, is wired to a D-sub connection, that is mounted to the vacuum flange in the final assembly. The RF electrodes of the top chip RFtop and the bottom chip RFbottom are wired individually with cables of the exact same length – the wires are visible in the very left of the image. On the right side of the filter board, a similar wire is used to supply a large ground plane, which covers almost the entire backside of the filter board. VIAs are fabricated to supply ground potential for the capacitances from this backside ground plane – three VIAs are fabricated next to each other, close to the capacitances. Next to the VIAs, a small square is placed – it provides the option to supply ground potential to the electrodes RF compS and RF compN. However, we opted for supplying these electrodes with individual wires. In the RF compS conducting track, a narrowing is fabricated, which can absorb excess solder if the connection to the adjacent square were chosen to be soldered. In the top region of the image, a gold pad is placed, which is used for practicing of the wire bonding procedure.

A printed resistance of 10 Ω and 2 nF row capacitors[13] form the low-pass filter. The row capacitors are connected to a ground electrode on the filter board with reflow soldering. Wire bonding is later used to connect the gold surface of the row capacitors to the gold surface on the ion trap. In order to simplify the wire bonding from the DC lines to the row capacitors, the end of the DC conducting tracks feature small gold pads, where the gold wire forms a durable connection to the gold surface.

3.4. Vacuum assembly

In this section, the assembly of the trap chips and the filter board is described as well as the attachment of the filter board to the vacuum flange. The arrangement for the trap chips is shown in figure 3.10, a cross section is provided in figure 3.11.

In a first step, the trap chips are assembled on the support layer using two titanium M1 screws[14] with a thread diameter of 1 mm and a screw head diameter of 2.2 mm. Titanium is chosen because magnetizable materials are to be avoided close to the magnetically sensitive trapped ions. The screws are countered by titanium nuts[15], which are placed in a trench below the setup, such that they cannot move. The trench is part of a trap assembly tool, which assists in the assembly and wire bonding procedure, see appendix D. An earlier test procedure revealed, that the fragile chips can withstand a torque of at least 3 N cm applied to the screws. This first assembly step is the most critical and requires the most diligence, since the quality of chip alignment affects the symmetry of the resulting trapping potentials and the amount of residual micromotion. Thus, the alignment procedure is performed under a microscope while observing the trap chips from the top. The precisely structured trap electrodes and the long trap slit are good references for the procedure. As long as the screws are loose, it is helpful to block the movement of the bottom trap chip. This is accomplished by carefully pushing against the bottom chip from each of the four rims with fixed alumina spacer layers. Once this situation is established, one of the screws can be tightened quite thoroughly, such that the top trap chip can only move in the region of the second screw. Soft plastic pliers are employed to move the top trap chip in the desired position. Once precise alignment is

[13] Compex row capacitor, CR/CM series: CR16-200-344.2X178X10-3-G-202-Z
[14] DIN912, inside hex head, scarce special dimensions, available at 'Der Schraubenladen', Villingen, Max-Planck-Straße 39, 78052 Villingen-Schwenningen, Germany
[15] DIN934

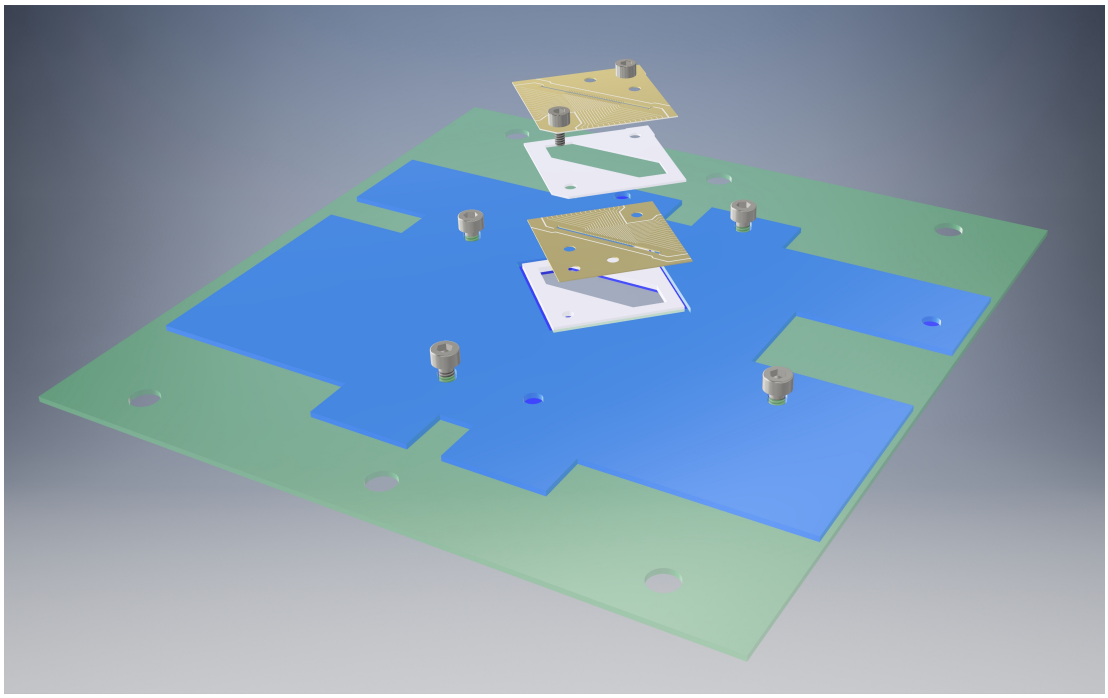

Figure 3.10.: Technical drawing of the ion trap assembly. The ion trap consists of the two gold-coated ion trap chips, which are separated by a spacer layer with a thickness of 254 µm. Below the green transparent layer, which illustrates the filter board, an additional alumina support layer is mounted with screws. In this drawing the layer is colored blue for better visibility, its function is to allow for a modular assembly process. On top of this layer resides another alumina layer right below the ion trap. The thickness of this layer is the same as of the filter board. This arrangement positions the bottom layer at the same height as the filter board, which facilitates the wire bonding procedure.

achieved under the microscope, both screws are tightened.

In the next step, the filter board is mounted on top of the support alumina layer with four titanium M1.6 screws. The trap needs to be in the center of the opening, to allow for good wire bonding from all sides. The assembly procedure is followed by thorough cleaning of the whole filter board and ion trap in an ultra sonic bath at 40 °C of iospropanol (purity $\geq$ 99.8%) for 15 minutes.

A ball bonding machine is then employed to create electrical connections between the trap electrodes and the row capacitors as well as between the row capacitors and the filter board DC tracks. Prior to wire bonding, the trap is heated to approximately 170 °C. At the increased temperature, a small amount of foam is observed to protrude from the surface of the row capacitors, which was not observed in earlier heat up procedures.

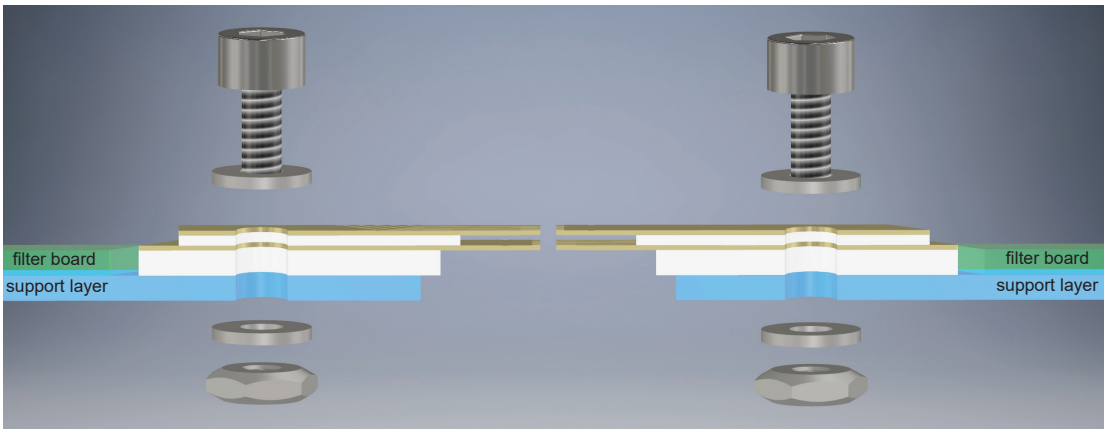

Figure 3.11.: Cross section of the ion trap assembly. The gold-coated ion trap chips are separated by an alumina spacer. The support alumina layer is colored blue in the sketch for better visibility. The washers adjacent to the nuts feature a small slit, in order to vent the screw hole. All screws, nuts and washers are made of titanium. The thickness of each assembled part is: support layer (630 µm), filter board (630 µm), alumina layer between filterboard an bottom trap chip (630 µm), trap chips (143 µm), spacer (254 µm).

The setup is cooled down, the foam is rinsed with isopropyl alcohol (purity $\geq 99.8\%$) and the setup is heated again until no further change is observed.
At least two wire bonds are made for each electrical connection, to make them fail-safe. After the bonding procedure, all relevant electrical connections are measured using an LCR meter[16]. The capacitances of the 64 DC connection pins at the attached D-sub connector to the ground electrode of the filter board are measured[17] to be around 2.5 nF and the impedances are determined[18] to about 200 Ω. The values are higher than from the parts used for the low pass filter on the filter board, due to the attached cable connections. It is desirable, that all of the 64 connections exhibit similar electrical characteristics. Additionally, the capacitance between the RF electrodes to the ground electrodes on the filter board is measured[19] to be 26 pF for the RFtop and 25 pF for the RFbottom electrode. Using the same measurement settings, the capacitance between a random pin of a DC electrode at the D-sub connector and the RFtop electrode was measured to be 25 pF and to the RFbottom electrode to be 22 pF. The similar values for the RF and DC electrodes indicate decent electrical connections, such that the trap

[16] Hameg HM 8118
[17] measurement setting: C-D mode at 1 kHz
[18] measurement setting: R-X mode at 1 kHz
[19] measurement setting: C-D mode at 200 kHz

is ready for vacuum assembly. In a final cleaning procedure, the wire-bonded trap and filter board are cleaned in ultra sonic baths of isopropyl alcohol (purity $\geq 99.8\%$) and finally ultra pure de-ionized water.
The filter board is mounted to an aluminum frame and the vacuum flange as shown in figure 3.12. All electrodes are wired with kapton-coated copper cables to ultra high vacuum compatible feedthroughs on the vacuum flange, the connections are shown in appendix D.
Calcium ions are produced in the trap by ionizing a vapor of neutral atoms with a laser beam, see section 4.2. The atomic vapor is generated by electric heating of calcium granules in a small tube, which is denoted as the *calcium oven* [Rot03]. The particular oven has been used in an ion trap setup before, thus the remaining calcium inside the oven tube is carefully poured out. Calcium oxidizes when exposed to air and thus new calcium granules are loosely filled in the oven tube. It is not advisable to use force when filling the granules into the tube, as this can cause sudden eruptions of calcium onto the sensitive ion trap surface.

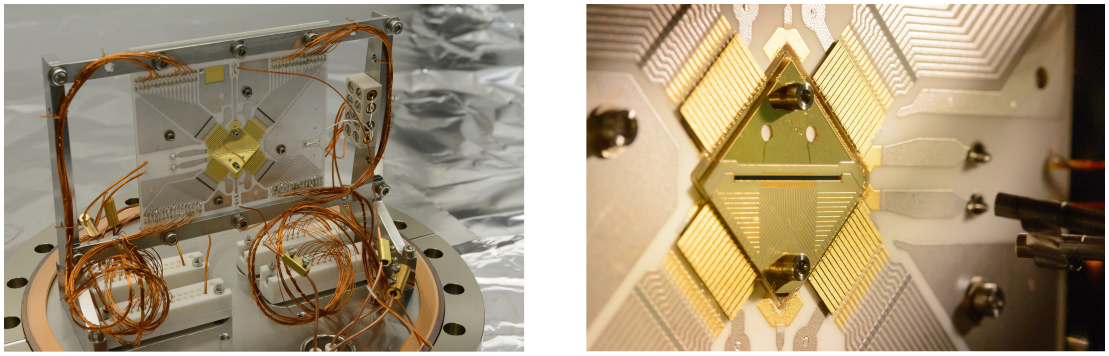

Figure 3.12.: Left: Photograph of the filter board and the ion trap assembled to the vacuum flange. The luster terminal serves as a star point ground for the ion trap. **Right:** Photograph of the ion trap mounted inside the vacuum chamber. The thin wirebonds are visible in this image on the outside of the ion trap chip. On the right the calcium oven is mounted and points at a distance of about 1 cm at the ion trap.

The entire vacuum chamber is then exposed to a bake-out process in order to achieve ultra high vacuum. At a rate of not more than 15 °C per hour, the chamber is heated to 180 °C and kept at this temperature for two weeks. The heat detaches contaminants from the chamber walls, which are then removed by a temporarily attached vacuum pump. Two permanent vacuum pumps are installed in the chamber: a passive getter

pump[20] and an ion pump[21], which additionally contains a similar passive getter element. Before the bake-out procedure, both getter elements are activated, which involves heating them to around 500 °C for one hour. During the bake-out procedure, this activation is repeated once per day at only 30% of the electrical power, which was used in the initial activation. Once the bake-out is finished, another full activation is performed at a temperature of around 90 °C during cooling down. It is also important, to supply the calcium oven with current for a few hours during the bake-out process to remove contaminants from the oven tube. The pressure inside the chamber needs to be carefully monitored during these operations. At the end of the process, the ion pump is turned on. Finally, a pressure on the order of 10^{-12} mbar is achieved after a few days, which results in storage times of several days for the ions in the trap.
After the bake-out procedure, the surface of the trap chips changed visibly, a comparison is shown in figure 3.13.

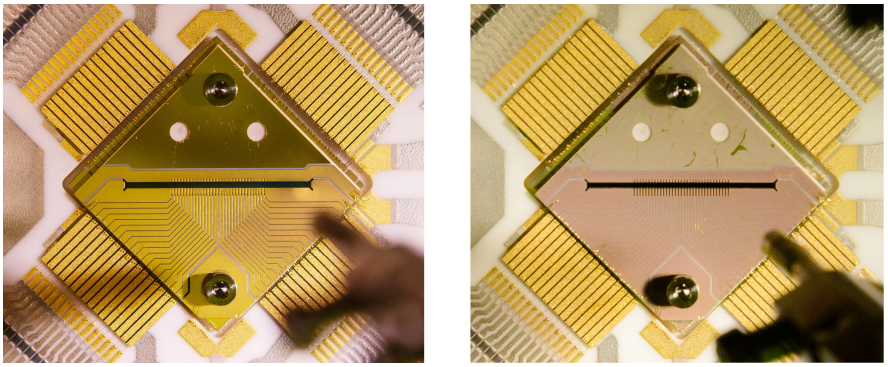

Figure 3.13.: Left: Photograph of the ion trap inside the vacuum chamber before bake-out. The large RF compensation electrode was not electroplated, since it is far away from the trapping region and thus looks different from the other electrodes. Near the two VIAs, scratches are visible on this electrode which originate from the alignment process of the trap chips with soft pliers. **Right:** Ion trap after the bake-out procedure. Both the electroplated and the evaporated gold surface on the trap visibly changed surface color. This transformation is found to be not detrimental to the performance of the ion trap.

It is unclear what the origin of this change is. The trap was covered in wax in the fabrication process which might have left residues. Furthermore, a getter pump was activated close to the ion trap for the first time, possibly this first activation spilled contaminants over the chip surface. We exclude the calcium oven to be responsible,

[20] CapaciTorr® D 100, SAES Advanced Technologies SpA, Viale Italia, 77 20020 Lainate, Milan - Italy
[21] NEXTorr® D100-5, SAES Advanced Technologies SpA

since the surface also changed its color on the backside of the trap chips. The surface of the trapping zone however is still in a supreme condition, since the motional heating of the ions in the trap is low, see section 6.1.

4

Apparatus

In this chapter, our apparatus for quantum information experiments is described. The complete experimental setup including lasers and electronics to operate the ion trap is shown in figure 4.1.

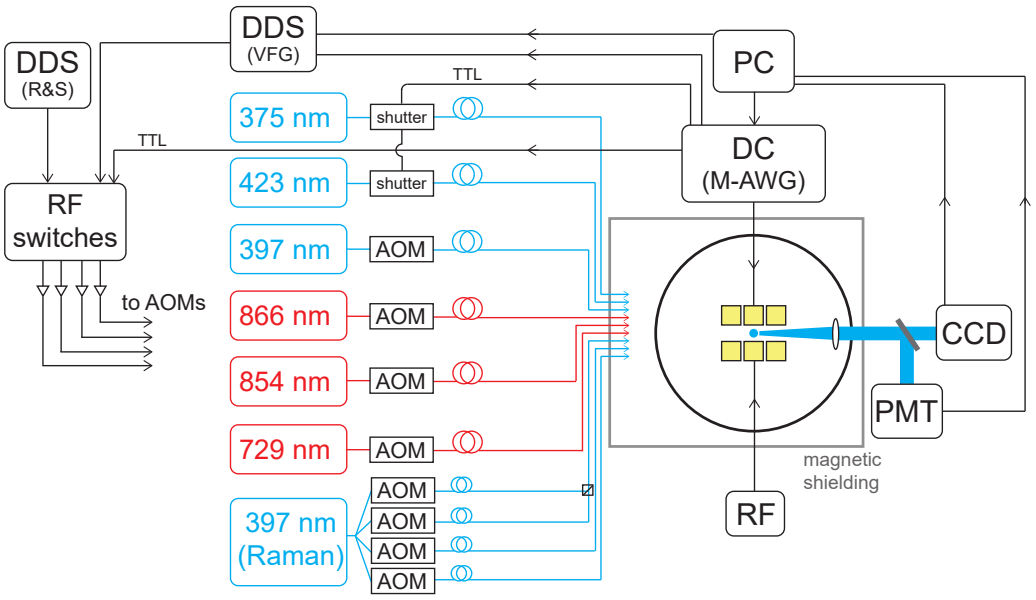

Figure 4.1.: Experimental setup for the operation of the segmented ion trap. The trap resides in the center of a shielded spherically-shaped vacuum chamber. DC and RF supplies are necessary to confine the ion. A photo-multiplier tube (PMT) and a CCD camera detect ion fluorescence. Seven laser sources are steered to the vacuum chamber with optical fibers for laser cooling of the ions as well as performing quantum logic operations. Except for the four acousto-optic modulators (AOMs) in the laser beam path for the Raman transitions, all other AOMs are set up in a double-pass configuration.

The diameter of the vacuum chamber is around 25 cm and the magnetic shielding enclosure measures 51 cm x 62.5 cm x 62.5 cm . It is made of three layers: 2 mm μ-metal – 6 mm aluminum – 2 mm μ-metal and provides attenuation factors in the range between 20 and 30 dB for signal frequencies between 50 Hz and 100 kHz [Rus16]. The enclosure also provides passive thermal stability for the vacuum vessel and the optical elements which guide the laser beams to the ion trap as well as the electric circuit that stabilizes the RF trap drive. The pressure inside the vacuum vessel is determined to be on the order of 10^{-12} mbar, which provides ion storage times of several days.

4.1. Experimental control

The experiments are controlled by a C++ program from the experimental control computer (PC) which is connected to various devices. Data acquisition is typically achieved by 100 experimental repetitions. Fluorescence detection is performed with the PMT module[1] within an exposure time of about 700 µs. A CCD camera[2] is mainly employed to observe the ions between the experiments.
Experimental sequences are transfered via ethernet to a FPGA-based fast multichannel arbitrary waveform generator (M-AWG) [Wal12; Rus14]. The device supplies the DC trap electrodes for ion shuttling operations and triggers laser pulses to conduct quantum logic experiments. Digital outputs drive multiple RF switches via TTL logic and thus switch the AOMs, respectively the laser beams, within a few hundred nanoseconds. One source for the RF is a direct digital synthesizer[3] (DDS), which is set to a frequency of 110 MHz. A second source is a versatile frequency generator[4] (VFG) which is connected to the control computer via USB and stores pulse sequences in an internal memory. Upon an TTL trigger from the M-AWG the RF pulses are generated and fed to the AOMs. The device is capable of phase coherent switching between multiple RF frequencies, which is crucial for the quantum logic operations. The network for the RF switches is shown in figure 4.2. Only the Raman and 729 nm laser beams – which coherently drive atomic transitions – are controlled by this scheme. The AOMs for all other lasers are supplied by voltage controlled oscillators and switched in a similar fashion.
In the experimental sequences, which are looped on the M-AWG, DC voltage updates

[1] Photon counting head H10682-210, Hamamatsu Photonics K.K.
[2] Andor iXon, Model No. DV860DCS-UVB
[3] R&S SML 01, ROHDE & SCHWARZ GmbH & Co. KG
[4] VFG-150, TOPTICA Photonics AG

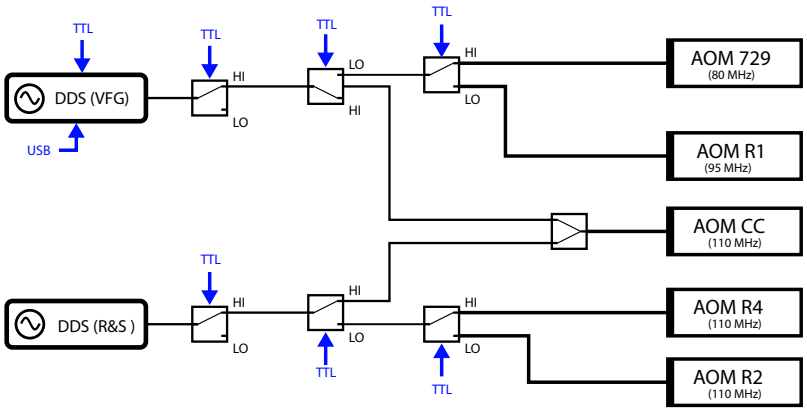

Figure 4.2.: RF switch network for the control of the Raman laser beams CC, R1, R2 and R4 and the 729 nm laser beam, which coherently drive atomic transitions. All TTL signals are supplied by the M-AWG, the frequency at each AOM denotes the typical operation frequency.

are supplied within 400 ns by the M-AWG in the range of ± 10 V. The voltage supply features low noise ($10\,\mathrm{nV} \lesssim /\sqrt{\mathrm{Hz}}$ at the trap frequency [Wal12]), which is filtered by a low-pass filter on the vacuum flange and a low-pass filter inside the vacuum chamber, see section 3.3. The low-pass Π-type filter on the vacuum flange features a cutoff frequency of $2\pi \times 50$ kHz and is comprised of two capacitances[5] (47 nF) and one inductance[6] (220 µH) which is built in series with a precision resistor[7] (69.8 Ω). The inductance is electromagnetically shielded to reduce crosstalk to nearby signal wires.

4.2. Laser setup

The ion trap resides in a stainless steel vacuum chamber that features ultra high vacuum. To interact with the atomic levels of the trapped calcium ions multiple lasers are employed and described in this section. All laser beams, which interact with the ion, as well as the imaging system are shown in figure 4.3. The ion trap resides in the center of the chamber and the ion fluorescence light at 397 nm is split in two paths and detected by

[5] AVX 06035C473KAT2A, MLCC, X7R, 47NF, 50V
[6] Coilcraft 1812PS-224JLB 220UH, 0.47A, 5%, 7MHZ
[7] TE Connectivity 5-1879222-5, 69R8, 0.1%

a PMT (90 %) and a CCD camera (10 %). A dichroic mirror (DM) and a specialized imaging objective[8] allow for the focusing of a 729 nm laser beam on the ion.

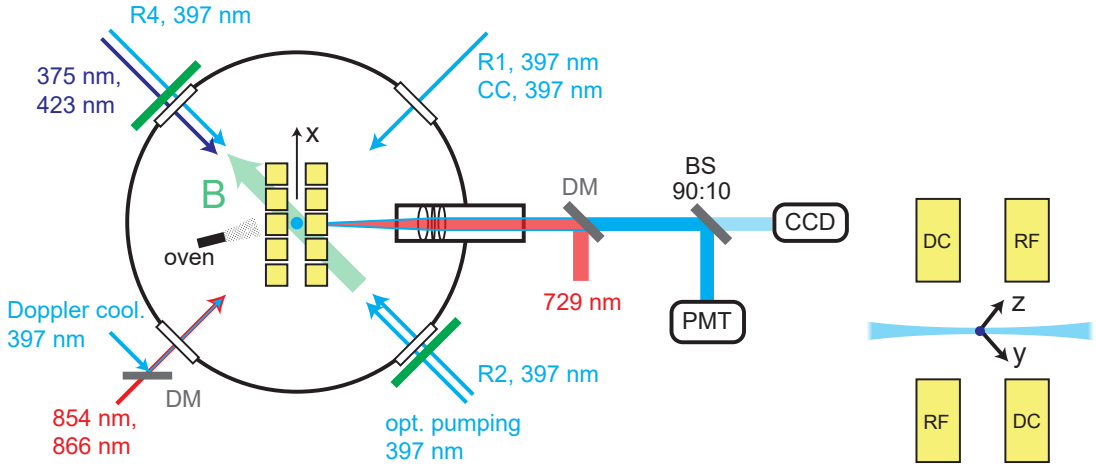

Figure 4.3.: Left: Top view of the vacuum vessel and the laser beams, which are focused on the ion. Beams which are represented by a single arrow are guided to the chamber in a single optical fiber. Lenses outside the chamber are used to focus the laser beams to a waist of a few tens of µm on the ion position as indicated in the sketch on the right. The beams enter the chamber through anti-reflection coated glass view ports. A magnetic field of 0.37 mT is generated at the ion position by two green colored permanent magnets, which are mounted on aluminum rings [Rus16]. **Right:** The two principle axes of the trap in the radial y- and z-direction are orthogonal to the trap axis, which is denoted as the x-direction.

The laser beams at 375 nm and 423 nm are utilized to **ionize the atomic vapor**, that is generated by the calcium oven in a two step photo-ionization process. The first excitation step from the 4^1S_0 state to the 4^1P_1 state in neutral calcium is driven by a single mode laser[9], which is stabilized to a wavemeter[10] at around 422.7912 nm. A subsequent excitation to the continuum is achieved by a free running laser[11] at 375 nm. The optical power of the 423 nm beam is typically around 1 mW, and the power of the 375 nm beam is set to 200 - 300 µW.

Doppler cooling and fluorescence detection of the trapped ions on the $4^2S_{1/2} \leftrightarrow 4^2P_{1/2}$ cycling transition is established by a single mode laser[12] at a wavelength of

[8] $f \approx 67$ mm, S6ASS2241/045 SILL 132177, Sill Optics GmbH & Co. KG
[9] DL 100 Pro, TOPTICA Photonics AG
[10] Type WSU, HighFinesse Laser and Electronics Systems GmbH
[11] DL 100, TOPTICA Photonics AG
[12] DL 100 pro, TOPTICA Photonics AG

397 nm. The laser is stabilized to 396.95900 nm by a Pound-Drever-Hall locking scheme [Dre83; Pos10a]. An AOM is facilitated in a double-pass configuration to control the intensity and frequency of the beam – it is red detuned with respect to the atomic resonance by around 30 MHz and the optical power is typically around 40 µW.

The same laser source is used for **optical pumping** with a separate beam, which enters the vacuum chamber in parallel to the magnetic field. The polarization of the beam is set to circular polarization (corresponds to σ^+) by a $\lambda/4$ wave plate. Thus, only the $|4^2S_{1/2}, m_J = -1/2\rangle \equiv |\downarrow\rangle$ to $4^2P_{1/2}$ transition is driven by this beam, which is controlled by an AOM in a double-pass configuration. Typically 50 µW of optical power are used for this beam.

Repumping on the $3^2D_{3/2} \rightarrow 4^2P_{1/2}$ transition is realized by a single mode laser[13] at a wavelength of 866 nm. The laser is stabilized by the same scheme as the 397 nm laser to a wavelength of 866.45160 nm. The typical laser intensity for this beam is around 20 µW and the polarization is set to be linear. An AOM in a double-pass configuration controls the beam intensity.

Quenching on the $3^2D_{5/2} \rightarrow 4^2P_{3/2}$ transition is achieved by a single mode laser[14] at a wavelength of 854 nm. The laser is stabilized to the wavemeter at around 854.4434 nm and the laser intensity is controlled by an AOM in a double-pass configuration – typically it is set to around 20 µW. We set the polarization of the beam to be linear. The repumping laser and the quenching laser are coupled to the same optical single mode fiber and guided to the vacuum vessel.

Electron shelving and optical pumping on the quadrupole $4^2S_{1/2} \leftrightarrow 3^2D_{5/2}$ transition are implemented by a single mode laser source[15] near 729 nm. It is stabilized to an ultra-stable cavity at 729.34730 nm and features a linewidth around 1 kHz [Mac12]. An AOM in a double-pass configuration is utilized to control the power and frequency of the light, the laser intensity is usually in the range of a few mW. The polarization is linear and is set to be in the plane of the optical table. Consequently, the coupling to the $\Delta m_j = \pm 2$ transitions is enhanced [Roo00].

[13] DL 100, TOPTICA Photonics AG
[14] DL 100, TOPTICA Photonics AG
[15] Matisse TX, Sirah - Lasertechnik GmbH

Qubit manipulation and ground state cooling are realized by stimulated Raman transitions with a single mode laser[16] near 397 nm, which drives the transition $4^2S_{1/2} \leftrightarrow 4^2P_{1/2}$ respectively the transition between the Zeeman sublevels: $|\downarrow\rangle \leftrightarrow |\uparrow\rangle$, see section 2.4. The laser is comprised of an amplified near-infrared laser diode, which is sent to a bowtie cavity for second harmonics generation with an lithium triborate (LBO) crystal. The cavity is used to stabilize the laser at a wavelength of around 397.12 nm, which corresponds to a detuning of about $\Delta = -2\pi \times 290\,\text{GHz}$ from the atomic resonance. The detuning from the atomic resonance requires an increased optical power – the laser is capable of producing 80-100 mW of light near 397 nm. The optical setup for the control of the laser beams is displayed in figure 4.4. Initially, the light passes through an EOM, which rotates the polarization of the beam depending on the supplied high voltage. Subsequently, the light passes through a polarizing beam splitter and is coupled to an optical fiber which guides the light to an interferometric setup. A photo diode measures the intensity of the light after the fiber. The signal is fed back to a PID controller[17] and a fast high voltage amplifier[18], which act on the EOM by adjusting the supplied high voltage and thus stabilize the light intensity inside the interferometric setup. The beam intensity is well stabilized, see results in section 6.5. In principle one expects to observe an impeded coupling to the optical fibers from frequency i.e. beam position changes in the AOM single-pass configuration. However, the effect is rather small and since we only change the AOM frequencies within a few tens of kHz we do not observe any disadvantage in the experiments. We use AOMs[19], which feature a high beam pointing stability and small turn-on effects. The diffraction efficiency of the AOMs is around 65 % and the subsequent fiber coupling efficiency is about 70 %. Typically frequencies around $2\pi \times 100\,\text{MHz}$ at an input power of 2 W are used to drive the devices. The radio frequency is generated by a direct digital synthesizer (DDS) and amplified by a water-cooled RF power amplifier[20].

At the ion trap position, the beams denoted by R1, R2 and R4 are horizontally polarized with respect to the optical table and the beam denoted by CC is vertically polarized.

To drive **coherent rotations between the qubit states** $|\downarrow\rangle \leftrightarrow |\uparrow\rangle$, without coupling to the ion motion, the beams R1 and CC are employed, which both propagate orthogonally to the magnetic field. Thus, the beam R1 is π-polarized and drives $\Delta m_J = 0$

[16] TA-SHG, TOPTICA Photonics AG
[17] NoiseEater 3V2, TEM Messtechnik GmbH
[18] HVA-F, TEM Messtechnik GmbH
[19] e.g. I-M110-3C10BB-3-GH27, Gooch & Housego
[20] ZHL-5W-1, Mini-Circuits®

transitions whereas the beam CC features equally σ^+ and σ^- polarization component and drives $\Delta m_J = \pm 1$ transitions.

Resolved sideband cooling is established by coupling to the ion motion with an effective k-vector of two superimposed Raman beams. Cooling the axial mode of vibration requires the beams R1 and R2 to be focused on the ion to form an effective k-vector along the x-direction, i.e. the trap axis. The horizontally polarized R2 beam propagates along the magnetic field and is thus equally composed of σ^+ and σ^- components. The same holds for the R4 beam that propagates in the opposite direction. It is used to form an effective k-vector orthogonal to the trap axis which couples to the radial y- and z-direction when superimposed with the R1 or CC beam.

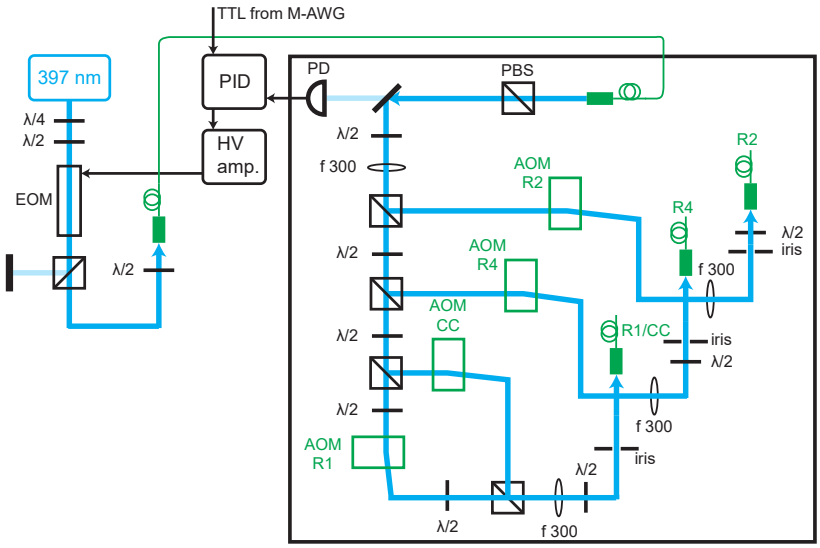

Figure 4.4.: Beam path of the Raman laser setup, which is used for qubit manipulation and ground state cooling. The beam is split into four individual beams, that are controlled by AOMs in a single pass configuration. Only the first diffracted order is sketched here, which is coupled to an optical fiber and guided to the ion trap. Each AOM is placed in the focal plane of two lenses with a focal length of $f = 300\,\mathrm{mm}$. This configuration ensures a robust coupling with respect to frequency adjustments in the AOM. Vertically polarized light is supplied to each AOM by means of polarizing beam splitters or $\lambda/2$ wave plates. A wave plate before each fiber ensures alignment to the polarization maintaining direction of the single mode fibers. The beams R1 and CC are coupled to the same fiber and are orthogonally polarized with respect to each other. A small fraction of light passes through the first mirror in the enclosed setup and is detected by a photo diode to stabilize the intensity. A TTL trigger from the M-AWG provides fast switching of the EOM.

The geometric phase gate, that is employed to entangle the spins of two ions, is either realized with the axial mode of vibration, by employing the beam pair R2 and CC or with one of the radial modes by using the beam pair R4 and CC. In either case, two beams in a linear $\perp$ linear polarization are focused on the ion, which results in a polarization standing wave. This moving periodic potential couples to the ion motion, as explained in section 2.5. The optical power in each of the Raman beams on the ion position is typically around 5 mW. Initial cooling of the motional mode, that is used for the gate, close to its ground state is required to achieve a high fidelity.
All laser beams, except for photo-ionization and the 729 nm beam, are remotely controlled from the outside of the magnetic shielding enclosure and precisely focused on the ions via picomotor actuators[21].

4.3. Stabilization of the radio frequency potential

The segmented ion trap is supplied with an RF voltage of about 300 V peak-to-peak at a frequency of $\omega_{RF}/2\pi = 33$ MHz to confine the ions in the radial directions y and z. Axial confinement along the x-direction is achieved by a DC voltage of typically -6 V. This configuration gives rise to typical trap frequencies of $\omega_{x,y,z}/2\pi = \{1.5, 4.1, 4.9\}$ MHz. The radial motional modes are utilized for quantum logic operations, see section 2.5.2. Thus, the corresponding trap frequencies need to be as stable as possible for high operational performance and to reduce the calibration overhead. The RF voltage is actively stabilized based on a scheme, that was applied in a similar setup [Dil14]. A sketch of all components for the RF supply and stabilization is shown in figure 4.5. As an RF source, a DDS[22] with an 50 Ω output level of around -13 dBm at $2\pi\times33$ MHz is employed. The signal is fed to a water-cooled RF power amplifier[23] which features a high gain of around 46 dB. Subsequently, a custom-made helical resonator transforms the RF voltage to a higher amplitude and matches the 50 Ω output impedance of the amplifier to the high-impedance load, consisting of the ion trap and the vacuum feedthroughs. At the output of the helical resonator, a capacitive divider provides a high impedance output of about one-hundredth of the signal level at 300 V peak-to-peak. A 1:10 probe at the output of the capacitive divider measures the voltage and feeds it to an oscilloscope. The largest fraction of the signal is fed to a stabilization circuit, which is comprised of a

[21] e.g. 8353 Tiny Picomotor actuator, Newport Corporation
[22] R&S® SMB100A, ROHDE & SCHWARZ GmbH & Co. KG
[23] ZHL-5W-1, Mini-Circuits®

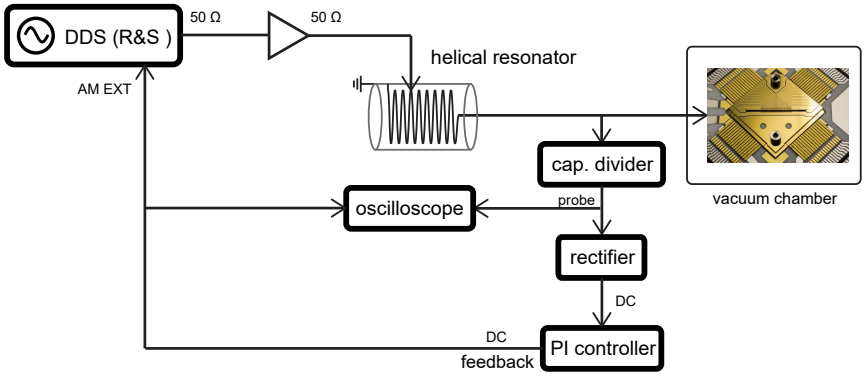

Figure 4.5.: Scheme for the ion trap RF supply and stabilization.

rectifier and a proportional-integral (PI) servo. In order to generate a suitable input signal for the PI controller, the RF voltage of around 3 V peak-to-peak is converted to DC by a half-wave rectifier with a time constant of about 10 µs. This DC voltage is supplied to a custom made PI control circuit, both circuits are sketched in appendix D. The error signal, for the PI controller, is generated from the difference of the rectified impedance matched input signal, to a stable reference voltage source[24], which can be adjusted by a voltage divider. The proportional gain for the controller is set by adjusting a trimpot resistor – increasing the resistance will raise the gain. Working parameters were found by observing the system behaviour over a few hours, the time constant of the PI circuit is around 2 µs.

The output of the controller serves as feedback to the amplitude modulation input of the DDS, which generates the radio frequency. A modulation bandwidth of $2\pi \times 50$ kHz sets a limit to the speed of the control loop. Typically, the modulation depth of this input is limited to 5% to prevent damage of the ion trap. The long-term stability of the control loop is assessed in section 6.2 and found to be excellent. All BNC wires, which carry the RF signal from the DDS to the amplifier and the helical resonator, are kept as short and rigid as possible. For this purpose, the DDS and the amplifier are placed on the optical table adjacently to the magnetic shielding around the vacuum chamber. This configuration significantly improved the passive stability of the system over a previous configuration where both components were placed below the optical table. For future experiments it is advisable to provide active temperature stabilization to the diode in the rectifier and the reference voltage source.

[24] REF01Z, +10 V output, typical temperature stability 3ppm/°C

5

Framework for Ion Crystal Separation

In this thesis a theoretical framework for the fast separation operation is developed and published in [Kau14]. The process of separating two-ion crystals in segmented Paul traps – i.e. the structural transition from two ions confined in a common well to ions confined in separate wells – is investigated theoretically. A successful experimental implementation of the results from this work is demonstrated in [Rus14].
The precise control of the separation process by application of suitable voltage ramps to the trap segments is non-trivial, as the harmonic confinement transiently vanishes during the process. This makes the ions strongly susceptible to background electric field noise, and to static offset fields in the direction of the trap axis. We analyze the reasons why large energy transfers can occur, which are impulsive acceleration, the presence of residual background fields and enhanced anomalous heating. For the impulsive acceleration, we identify the diabatic and adiabatic regimes, that are characterized by different scaling behavior of the energy transfer with respect to time. We propose a suitable control scheme based on experimentally accessible parameters. Simulations are used to verify both the high sensitivity of the separation result and the performance of our control scheme. Finally, we analyze the impact of trap geometry parameters on the crystal separation process.

Essential shuttling operations are separation and merging of linear ion crystals. It is important that they are fast on the typical timescale for quantum gates of 10-100μs, and in order to allow for gate operations or readout after the separation, a low energy transfer is required. Shuttling of trapped ions in segmented traps has been realized within a few oscillation cycles of the harmonic trap by time-dependent control of the trap voltages [Wal12; Bow12], at energy transfers below one motional quantum. Crystal separation in a segmented trap was first demonstrated in [Row02], at energy transfers of about 140 phonons within a separation time of 10 ms. With optimizations, separation

has been included to the set of methods for quantum computing, e.g. for quantum teleportation [Bar04] and entanglement purification [Rei06]. Currently, the best reported result is a gain of about two vibrational quanta per ion at a time duration of 55 μs [Bow12]. Our work is intended to explain why the separation process is challenging to control, and to provide a detailed methodology to overcome these challenges, also for traps with less beneficial properties as the one used in [Bow12]. The experimental challenge for the control of this process is given by the fact that the harmonic part of the electrostatic trap potential has to change its sign during this process and therefore has to cross zero. This situation of weak confinement reduces the attainable speed and potentially increases the final motional excitation. In order to make the process more robust and faster, it is desirable to achieve a large quartic component of the axial trapping potential.

Trap geometries tailored to improve separation performance were investigated in [Hom06a]. In [Niz12], geometry parameters for optimized separation in surface electrode traps were derived, and the role of enhanced anomalous heating due to transiently weak confinement was analyzed. In [Ebl10], robust separation operations on slow timescales were carried out by means of real-time observation of the ion positions and feedback on the segment voltages.

In this thesis, we analyze the separation process with the aim of achieving low energy transfers in segmented miniaturized Paul traps. We reduce our analysis to the process of separation ion crystals, as the process of merging ion crystals is merely the time reversed process. Furthermore, we restrict ourselves to the case of two ions. For separation and merging processes with several ions, the general procedures and conclusions are still valid.

In section 5.1, we introduce the formalism for describing the electrostatic potentials during the separation operations and the equilibrium positions of the ions, and we analyze the dependence of the equilibrium positions on the control parameters. In section 5.3, we give a detailed explanation of the possible reasons for high energy transfers. Based on these considerations, a procedure for the design of suitable voltage ramps is given in section 5.4. In section 5.5, we analyze the performance of these ramps by numerical simulations. Finally, in section 5.2, we compare typical examples for trap geometries and discuss the implication for ion separation.

5.1. Prerequisites for crystal separation

5.1.1. Electrostatic trap potentials

We desire to separate a two-ion crystal residing at center segment C along the trap axis x, to obtain two ions stored in separated potential wells at the position of the separation segments S neighboring C, see figure 5.1.

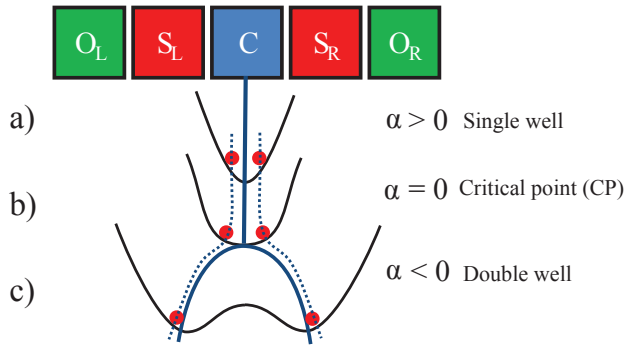

Figure 5.1.: The process of ion crystal separation. It is shown schematically how two ions are moved from the initial center segment C to different destination segments $S_{R,L}$ by changing a confining electrostatic potential from **a)** a strong harmonic confining potential ($\alpha > 0$) via **b)** a predominantly quartic potential ($\alpha \approx 0$) to **c)** a double-well potential ($\alpha < 0$). The external potential is determined by the voltages applied to the respective electrodes. The equilibrium positions are sketched as dashed lines. The outer electrodes O facilitate the separation process by increasing the transient quartic confinement and offer the possibility to cancel a possible axial background field by application of a differential voltage. The color coding of the segments and the corresponding voltages is used throughout the manuscript.

Note that we consider only the spatial dimension along the trap axis, as we assume that tight radial confinement persists throughout the process and the ions are always located on the rf node of the trap. Typical distances between segments range between 50 and 500 μm, while the initial ion distance is 2-4 μm. The total external electrostatic potential along the trap axis can be written as

$$\Phi(x) \approx \beta\, x^4 + \alpha\, x^2 + \gamma\, x \tag{5.1}$$

where the coefficients α, β, γ are given by the the trap geometry and the voltages applied to the trap segments. This Taylor approximation is valid as long as the the ions are located sufficiently close to $x = 0$, which is the center of the C segment. Throughout the separation process, the external potential is changing from a single well potential $\alpha_i > 0$ to a double well potential $\alpha_f < 0$, crossing the critical point (CP) at $\alpha = 0$. Note that $\beta > 0$ is required to guarantee confinement at $\alpha \leq 0$. The approximation of equation 5.1 holds for $\alpha \geq 0$ and for $\alpha \lesssim 0$ as long as the separation of the two potential wells is small compared to the width of segment C. When the distance of the ions from the center of the C segment becomes comparable to the width of the segment, anharmonic terms of order > 4 contribute significantly to the total potential. These are not taken into account here since the outcome of the separation process is determined around the CP, as will be pointed out in the following sections.

Beyond the CP, the equilibrium distance depends significantly on higher order terms of the potentials. However, the distance of the separated wells is still increasing monotonically for decreasing $\boldsymbol{\alpha}$ as long as the variation $\boldsymbol{\beta}$ is sufficiently small, and the corresponding trap frequencies in these wells are monotonically increasing. Thus, the motion beyond the CP corresponds to an ordinary shuttling process of a stiff harmonic trap. This suggests that the separation outcome should essentially not depend on higher order terms, a finding which is supported by numerical calculations in section 5.5.

For studies which require precision beyond the CP, the higher order terms can be taken into account numerically. A cubic term does not contribute to the potential if the trap is sufficiently symmetric along the trap axis.

Including Coulomb repulsion, the total electrostatic potential of a two-ion crystal at a center-of-mass position x_0 and distance d is given by

$$\Phi_{tot}(x_0, d) = \Phi(x_0 + d/2) + \Phi(x_0 - d/2) + \frac{\kappa}{d}, \tag{5.2}$$

with $\kappa = e/4\pi\epsilon_0$. At the CP, the harmonic confinement vanishes, and a weak residual confinement is maintained by the interplay between Coulomb repulsion and quartic part of the external potential. It is therefore desirable to maximize β at the CP. For a given trap geometry, the attainable β is limited by the voltage range which can be applied to the trap electrodes [1].

[1] The maximum voltage is ultimately limited by the electric breakdown threshold. In practice, as precisely controlled time-dependent voltage waveforms are to be applied to the trap segments, the voltage range will be determined by the electrical design, where one faces a trade-off between voltage range and output bandwidth [Bai13; Bow13].

The coefficients of the potential equation 5.1 are given by the segment bias voltages and the electrostatic properties of the trap:

$$\alpha = U_C\ \alpha_C + U_S\alpha_S + U_O\alpha_O \tag{5.3}$$

$$\beta = U_C\ \beta_C + U_S\beta_S + U_O\beta_O \tag{5.4}$$

$$\gamma = \Delta U_S\gamma_S + \Delta U_O\gamma_O + \gamma' \tag{5.5}$$

An offset parameter γ' is introduced for taking trap non-idealities – leading to a symmetry breaking force along the trap axis – into account, see section 5.3.2. In contrast to the symmetric quadratic and quartic contributions, the asymmetric tilt potential is controlled by the differential voltages $\Delta U_{S,O}$ between the corresponding left and right electrodes of the respective pair. The segment coefficients are given by Taylor expansions of the standard potentials $\phi_n(x)$, which are the dimensionless electrostatic potentials along the trap axis if a +1V bias is applied to segment n and all other segments are grounded [Bla11; Sin10]:

$$\phi_{n,m}(x) = \phi_n|_{x_0^{(m)}} + \phi_n'|_{x_0^{(m)}}\delta x + \frac{1}{2}\phi_n''|_{x_0^{(m)}}\delta x^2 + \frac{1}{24}\phi_n^{(4)}|_{x_0^{(m)}}\delta x^4 + \mathcal{O}\left(\delta x^6\right). \tag{5.6}$$

with $\delta x = x - x_0^{(m)}$, i.e. the Taylor expansions are carried out at center of segment m, $x_0^{(m)}$. The coefficients for Eqs. 5.3, 5.4, 5.5 are obtained for $m = C, n = C, S, O$:

$$\alpha_n = \frac{1}{2}f_n\phi_{n,C}''(0), \qquad \beta_n = \frac{1}{24}f_n\phi_{n,C}^{(4)}(0), \qquad \gamma_n = f_n\phi_{n,C}'(0), \tag{5.7}$$

with $f_C = 1$ and $f_{S,O} = 2$ accounting for two S, O segments acting symmetrically at $x = 0$. Note that $\gamma_C = 0$ by definition.
In the following, for numerical calculations, we use the specific geometry parameters of a three dimensional micro-structured segmented ion trap A as detailed in section 5.2. There, other traps and their geometry parameters are listed and analyzed as well.

5.1.2. Equilibrium positions

We consider two ions of mass m and charge e, with their equilibrium positions given by the center-of-mass x_0 and the equilibrium distance d:

$$x_{L,R} = x_0 \pm d/2, \tag{5.8}$$

determined by minimizing of the total electrostatic potential, given by equation 5.2.

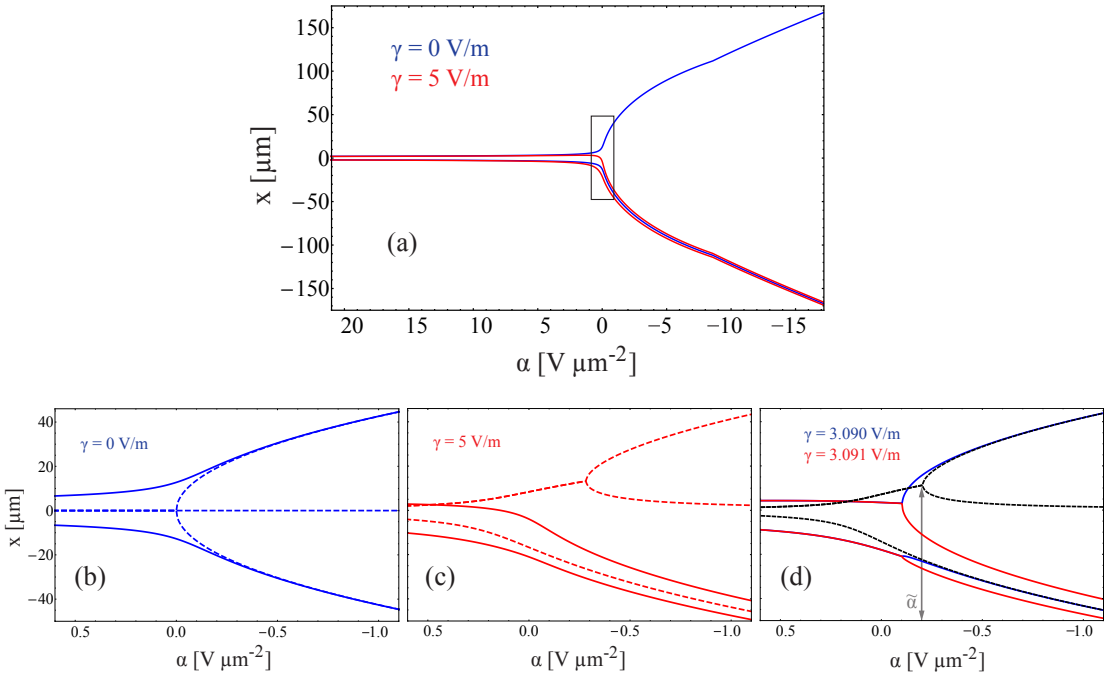

Figure 5.2.: Ion equilibrium positions near the critical point. **(a)** shows the equilibrium positions versus the harmonic parameter α. In the case of a perfectly compensated tilt (blue), the ions separate symmetrically, in the case of a large tilt (red), both ions move towards one side. Panels **(b)** and **(c)** show close-ups around the critical point for a perfectly compensated tilt and a large tilt respectively. Additionally, the extrema of the external potential are shown (dashed). In panel **(d)**, we display equilibrium positions and potential minima for tilt parameters slightly below (blue) and above (red) the critical tilt parameter. In contrast to the corresponding curves in b), the equilibrium positions exhibit cusps which lead to strongly enhanced acceleration.

The confinement is characterized by the local trap frequency, which is given by the curvature of the external potential at the ion positions:

$$\omega = \sqrt{\frac{e}{m}\Phi''(x_{L,R})}. \tag{5.9}$$

The extremal points of the external potential equation 5.1 are given by

$$x_0^{(0)} = \frac{\alpha}{3^{1/3}\zeta} - \frac{\zeta}{2\cdot 3^{2/3}\beta} \tag{5.10}$$

$$x_0^{(\pm)} = \frac{(i\sqrt{3}\pm 1)\alpha}{2\cdot 3^{1/3}\zeta} + \frac{(1\mp i\sqrt{3})\zeta}{4\cdot 3^{2/3}\beta} \tag{5.11}$$

$$\tag{5.12}$$

where

$$\zeta(\alpha,\beta,\gamma) = \left(9\beta^2\gamma + \sqrt{3}\sqrt{8\alpha^3\beta^3 + 27\beta^4\gamma^2}\right)^{1/3}. \tag{5.13}$$

Initially, at $\alpha = \alpha_i$, the confining harmonic part of the external potential and the Coulomb repulsion are dominant, thus we can neglect the quartic potential. The trap frequency is then given by $\omega^2 = 2\alpha e/m$ at an ion distance of $d = (\kappa/\alpha)^{1/3}$. At the CP, $\alpha = 0$, and without tilt, $\gamma = 0$, the ion distance is determined by quartic confinement and Coulomb repulsion:

$$d_{CP} = (2\kappa/\beta)^{1/5}. \tag{5.14}$$

The Coulomb repulsion pushes the ions away from the trap center (where the curvature of the external potential vanishes), such that a residual harmonic confinement persists because of the quartic term. The minimum trap frequency during the separation process is thus given by [Hom06a]

$$\omega_{CP} = \beta^{3/10}\,(3e/m)^{1/2}\,(2\kappa)^{1/5}. \tag{5.15}$$

Near the CP, the equilibrium distance can be computed from a perturbative expression up to second order:

$$d(\alpha) \approx d_{CP} - \frac{1}{5}\left(\frac{16}{\beta^4\kappa}\right)^{1/5}\alpha + \frac{2}{25}\left(\frac{4}{\beta^7\kappa^3}\right)^{1/5}\alpha^2, \tag{5.16}$$

for $|\alpha| \ll \beta d_{CP}^2$ and $|\alpha| \ll \kappa d_{CP}^{-3}$.
The center-of-mass position of the ion crystal near the critical point to first order in the tilt parameter γ is:

$$x_0(\alpha,\gamma) \approx \gamma\left(-\frac{1}{3\cdot 2^{2/5}\beta^{3/5}\kappa^{2/5}} - \frac{2^{1/5}}{45\cdot\beta^{6/5}\kappa^{4/5}}\alpha + \frac{26\cdot 2^{4/5}}{675\beta^{9/5}\kappa^{6/5}}\alpha^2\right) \tag{5.17}$$

If the ions are sufficiently separated, $\alpha \ll 0$, the Coulomb repulsion can be neglected and the equilibrium positions approximately coincide with the extrema of the external potential:

$$d_f = \sqrt{-2\alpha_f/\beta} \tag{5.18}$$

and the final trap frequency is given by $\omega_f^2 = -4\alpha_f e/m$.

5.1.3. Critical tilt value

A static background force along the trap axis can tilt the external potential and thus keep the ions confined in one common potential well throughout the separation process. We make use of the external potential minima Eqs. 5.12 to obtain an estimate for the tilt parameter $\tilde{\gamma}$, beyond which the separation ceases to work. In the following, we assume $\gamma > 0$.

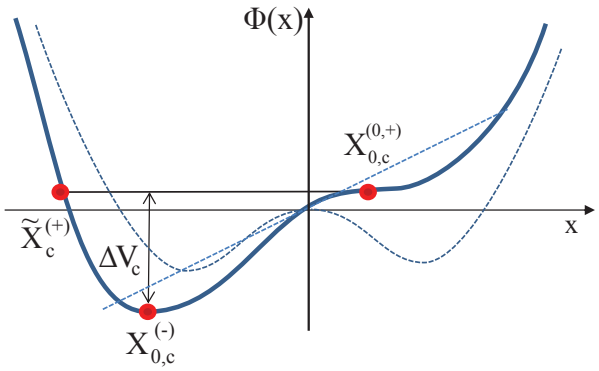

Figure 5.3.: Critically tilted potential, see text such that the Coulomb repulsion fails to push the right ion across the saddle point.

In the presence of a nonzero potential tilt, an imperfect bifurcation occurs, i.e. the second potential well opens up at $\tilde{\alpha} < 0$, see figure 5.2 c). We obtain a scaling law for $\tilde{\gamma}$ by calculating at which tilt parameter the original potential well is deep enough to keep both mutually repelling ions confined, see figure 5.3. The saddle point where the second potential well opens can be found by solving $x_{0,c}^{(0)} = x_{0,c}^{(+)}$ for $\tilde{\alpha}$, yielding $\tilde{\alpha} = -\frac{3}{2}\beta^{1/3}|\gamma|^{2/3}$. From this we obtain its position [2] to be $x_{0,c}^{(+,0)} = \frac{1}{2}(\gamma/\beta)^{1/3}$. At $\tilde{\alpha}$, the left potential minimum is located at twice the distance from the origin $x_{0,c}^{(-)} = -(\gamma/\beta)^{1/3}$.

[2] For $\gamma \geq 0$, $x_0^{(0)}$ corresponds to the left potential minimum which always exists, and for $\alpha < \tilde{\alpha} < 0$, $x_0^{(+)}$ corresponds to the right potential minimum and $x_0^{(-)}$ corresponds to the maximum of the separation

The potential attains the same value as on the saddle point $V(x_{0,c}^{(+,0)})$ at the position $\tilde{x}_c^{(+)} = -\frac{3}{2}(\gamma/\beta)^{1/3}$. The depth of the potential well defined by the saddle point when the right well opens is therefore

$$\Delta V_c = V(x_{0,c}^{(-)}) - V(x_{0,c}^{(+,0)}) = \frac{27}{16}\left(\frac{\gamma^4}{\beta}\right)^{1/3}. \tag{5.19}$$

We can now define a criterion which determines whether the ions are actually separated by comparing the Coulomb potential to the depth of the initial well at the CP, equation 5.19: If the Coulomb repulsion pushes the right ion beyond the saddle point $x_{0,c}^{(+,0)}$, it will end up in the right potential well, otherwise the two ions will stay in the left well. Thus, the Coulomb energy at an ion distance of $x_{0,c}^{(+,0)} - \tilde{x}_c^{(+)}$ has to be larger than the well depth ΔV_c. These considerations lead to a critical tilt value of

$$\tilde{\gamma} < \pm\, C_\gamma \left(\kappa^3 \beta^2\right)^{1/5}. \tag{5.20}$$

Despite the fact that the situation depicted figure 5.3 does not actually occur, as the external force at the saddle point vanishes and therefore cannot balance the Coulomb force, the obtained scaling behavior is confirmed by numerical calculations, revealing a prefactor of C_γ =1.06.
The result equation 5.20 enables us to determine the required degree of precision by which the background axial field has to be corrected. For this calculation, only the geometry parameters $\beta_{C,S,O}$ are needed. Furthermore, the sensitivity decreases as $\beta^{2/5}$, which directly characterizes the gain in robustness when the accessible voltage range is enhanced. For trap A (section 5.2), we derive a value of $\tilde{\gamma} \approx 3V/m$, corresponding to the requirement to set ΔU_O more accurately than about 9 mV.

5.2. Ion trap geometry optimization

We will show in section 5.3 that the outcome of a crystal separation operation is strongly determined by magnitude of the quartic confinement coefficient at the CP β_{CP} from equation 5.34. We thus investigate the effect of the trap geometry on the coefficients

barrier. By contrast, for $\gamma < 0$, $x_0^{(0)}$ corresponds to the right potential minimum, and for $\alpha < 0 < \tilde{\alpha}$, $x_0^{(+)}$ corresponds to the left minimum.

$\alpha_n, \beta_n, \gamma_n$ from Eqs. 5.7. We calculate the realistic potentials from electrostatic simulations [Sin10] to infer the geometry parameters according to equation 5.7. In particular, six different traps designs were studied, four of which are three-dimensional and two are surface-electrode traps. The results are shown in Tab. 5.1. The calculations are carried out for a generic simplified geometry shown in figure 5.4 d), which is essentially determined by the segment width w, the slit height h and the spacer thickness d for the three-dimensional traps. Trap A, B [Sch08] and C [Bla11] are similar segmented micro-structured ion traps . Trap B is subdivided into a loading region of larger geometry, B (wide), and a narrow processing region, B (narrow). The data for trap C pertains to a wedge segment of $w = 100\mu$m surrounded by larger segments. Trap D is a segmented planar ion trap [Nar11], the calculations are performed at a distance of 100 μm between the ion and the surface. Trap D2 is a planar ion trap featuring a segmented ground plane, otherwise identical to trap D. Trap A was used for all simulations in section 5.5.

Parameter	Unit	A	B (wide)	B (narrow)	C	D	D2
w	μm	200	250	125	100	200	200
h	μm	400	500	250	200	-	-
d	μm	250	125	125	250	-	-
α_C	μm^{-2}	-3.0	-2.5	-9.1	-6.4	-1.4	-12.0
β_C	10 μm^{-4}	2.7	1.7	19.9	14.4	1.5	-6.5
α_S	μm^{-2}	1.7	1.7	6.2	4.7	0.9	10.7
β_S	10 μm^{-4}	-3.0	-1.9	-22.1	-14.7	-1.7	5.6
γ_S	10^{-1} μm^{-1}	11.0	9.3	19.2	21.6	4.1	17.8
α_O	μm^{-2}	1.0	0.6	2.3	1.6	0.4	0.9
β_O	10 μm^{-4}	0.2	0.2	2.0	1.2	0.1	0.8
γ_O	10^{-1} μm^{-1}	3.2	2.2	4.3	3.2	1.2	2.2
$\omega_{CP}/2\pi$	MHz	0.18	0.14	0.29	0.26	0.14	0.11

Table 5.1.: Comparison of trap geometry parameters for different linear segmented Paul traps. Letters A to D denote different traps which are operated at various institutes, see text. Note that $\gamma_C = 0$ by definition. The trap frequency at the critical point is specified for U_{lim}=10V and $^{40}\text{Ca}^+$ ions.

For trap A and B (wide) we calculate similar parameters, however the minimum trap frequency during the separation is larger for trap A. Trap B (narrow) exhibits the highest minimum trap frequency of the six geometries as the total dimensions of this section of the trap are rather small. The wedge segment in trap C helps to increase the minimum trap frequency but choosing an overall smaller size seems to be a more favorable solution.

The planar trap D has a similar minimum trap frequency as trap B (wide) and is also suitable for separating ion crystals. The segmentation of the ground plane of this trap (D2) offers an enhanced α_C, i.e. a large trap frequency. The calculations show however that for a segmentation of the center electrode, the potentials become more anharmonic and the Taylor approximation equation 5.1 breaks down. Thus, the sign and magnitude ordering of the coefficients might be different from the other geometries, therefore the geometry parameters and the ion height above the surface should be carefully chosen to allow for successful separation operations.

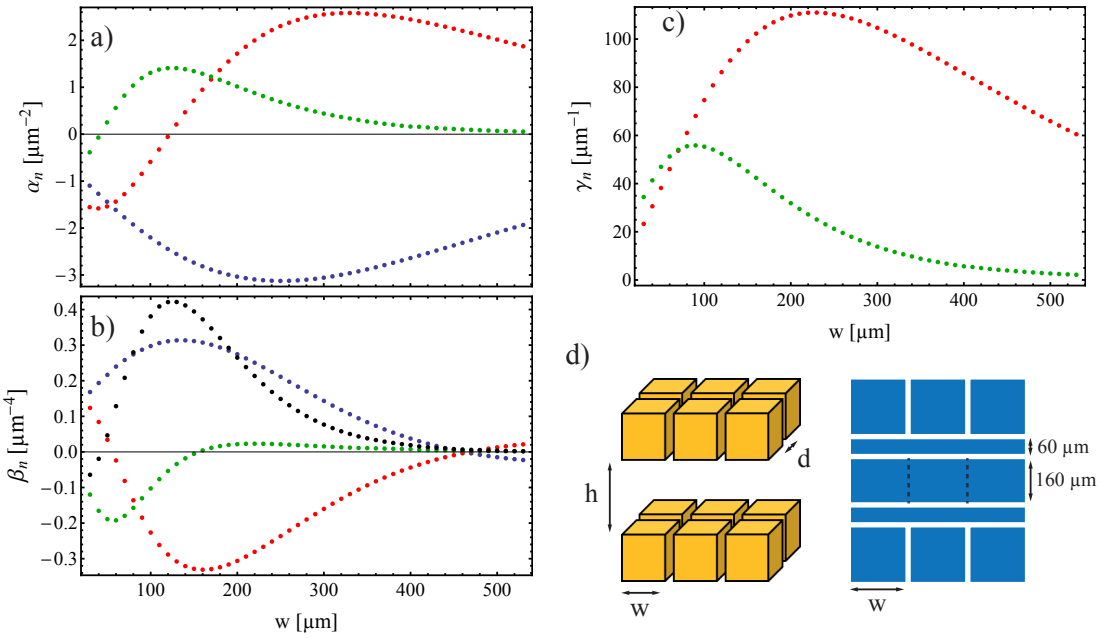

Figure 5.4.: Calculated geometry parameters $\alpha_n, \beta_n, \gamma_n$ and the maximum β_{CP} at the critical point for a linear segmented Paul trap with dimensions $h = 400$ μm, $d = 250$ μm as a function of the segment width w. The color code is as above: blue - C, red - S, green - O. The limiting voltage for the electrodes is $U_{lim} = 10V$.

For trap A we calculated the geometry parameters for varying segment width w, the result is shown in figure 5.4. We analyze the dependance of all potential coefficients on w with parameters h and d held constant. For separation operations the optimum segment width would be at about $w = 125\mu$m, while the actual segment width of the trap is $w = 200\mu$m. We could therefore obtain a roughly twofold increase of β_{CP} bought at the expense of a reduced trap frequency for ion storage due to the reduced α_C coefficient.

Finally, we investigate the dependence of β_{CP} on the overall trap geometry size. We therefore pick trap parameters h and d from the range of typical values and determine the optimum segment width w for these. Defining the effective trap size $d_{eff} = \left(w^2 + h^2 + d^2\right)^{1/2}$, we find a scaling behavior of $\beta_{CP} \approx 2.2 \cdot 10^{24} V \cdot d_{eff}^{-4}$, i.e. the best attainable value for the quartic confinement coefficient scales as the inverse fourth power with the effective trap size, which is the similar to the presumed distance scaling law for anomalous heating [Bro15]. We conclude that for a trap architecture aiming at shuttling-based scalable quantum information, the considerations presented here should be incorporated into the design process to facilitate crystal separation operations.

5.3. Intricacies of ion crystal separation

5.3.1. Impulsive acceleration at the critical point

In this section, we show that the energy transfer can be quantitatively described by a simple model, which interpolates between impulsive acceleration for short times and adiabatic behavior for long times. We first derive the impulsive approximation, and then refine the model to include the onset of adiabaticity. We also confirm the validity of our model by simulations.

A naïve approach towards crystal separation is the linear interpolation between two voltage sets pertaining to a single well and a double well, leading to a constant variation rate of the harmonic coefficient α. As this does not involve a dedicated control of the ion distance, it is equivalent to a rapid sweep across a structural transition of the ion crystal. This leads to an unfavorable power-law scaling of the energy transfer with respect to the sweep time [Ulm13], which prevents attaining adiabaticity.

In the following, we derive an approximation for the energy transfer, assuming the variation of α around the CP to be uniform. We consider the energy transfer to be caused by impulsive displacement: At the CP, the equilibrium distance changes most rapidly, while the confinement - and therefore the restoring forces - are reduced. Figure 5.5 a) shows that the situation corresponds to a harmonic oscillator which is suddenly dragged at uniform speed, causing displacement and therefore a gain in potential energy.

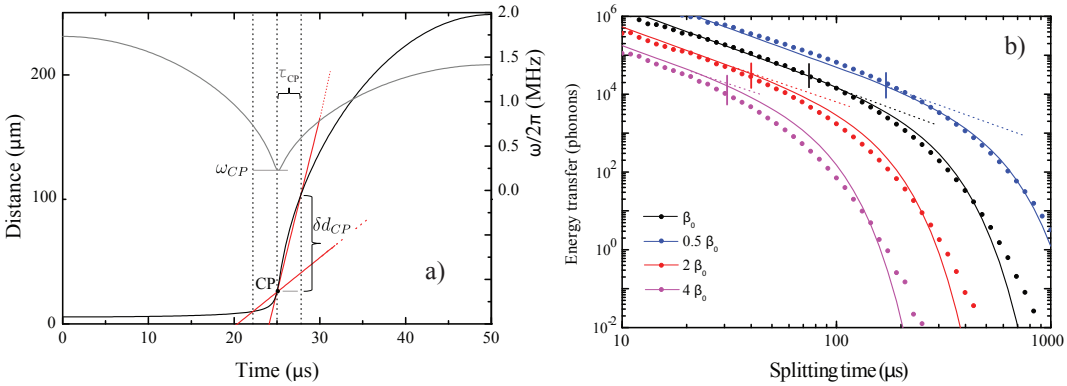

Figure 5.5.: Impulsive acceleration at the critical point. **a)** shows the equilibrium distance (black) versus time. The red lines depict the approximate slopes $\dot{d}_{CP}$ within time τ_{CP} before and beyond the CP. They illustrate how the impulsive displacement δd_{CP} equation 5.23 is obtained from slope beyond the CP, and why the difference of the slopes, i.e. the second derivative $\ddot{d}_{CP}$, determines the onset of adiabaticity (see text). It is also shown how the trap frequency (gray) varies strongly during the CP trap period. **b)** compares the final excitation obtained from the simple approximation Eqs. 5.25 (dashed), 5.30 (solid) to simulation results (dots). The onset of adiabaticity $\chi = 1$, is marked with vertical bars. The calculations are carried out for a harmonic coefficients $\alpha(t)$ linearly varying around the CP, and different constant values for the quartic coefficient β.

Within the characteristic timescale set by half a the trap oscillation cycle $\tau_{CP}/2 = \pi/\omega_{CP}$, this yields the displacement:

$$\begin{aligned} \delta d_{CP} &\approx \dot{d}_{CP}\, \xi\, \tau_{CP}/2 && (5.21)\\ &\approx \left.\frac{\partial d}{\partial \alpha}\right|_{CP} \dot{\alpha}_{CP}\, \xi\, \tau_{CP}/2 && (5.22)\\ &\approx \left(\beta_{CP}^4\, \kappa\right)^{-1/5} \dot{\alpha}_{CP}\, \xi\, \tau_{CP}/2, && (5.23) \end{aligned}$$

where equation 5.16 was used in the last line. The factor $\xi < 1$ accounts for a reduction of the displacement, which is due to the fact that the trap frequency rapidly increases beyond the CP. Thus, the restoring forces set in before $\tau_{CP}/2$ and the resulting displacement is reduced with respect to the dragged oscillator at constant frequency. This sudden

displacement mechanism is sketched in figure 5.5 a). The potential energy of an ion is consequently increased by

$$\delta E = \frac{1}{2} m\omega_{CP}^2 \left(\delta d_{CP}/2\right)^2 \tag{5.24}$$

$$= \frac{\pi^2}{8}\, \xi^2\, m \left(\beta_{CP}^4\, \kappa\right)^{-2/5} \dot{\alpha}_{CP}^2, \tag{5.25}$$

which serves as an approximation of the final energy transfer.
For a sufficiently small $|\dot{\alpha}|_{CP}$, adiabaticity sets in and the energy transfer scales exponentially with the separation time. The reason for this is that the Coulomb repulsion serves to push the ions outwards, providing smooth variation of the equilibrium distance as compared to discontinuous behavior of the minima of the external potential, see figure 5.2 b). It therefore leads to rapid, but continuous variation of the equilibrium positions with α. The onset of the adiabatic regime is identified by comparing displacement δd_{CP} to the change of the equilibrium distance within τ_{CP} *below* the CP (see figure 5.5 a)), which means that the ion acceleration around the CP is sufficiently slow to prevent sudden displacement. We therefore compare the acceleration $\ddot{d}_{CP}$ to the reference acceleration $d_{CP}\omega_{CP}^2$. Note that

$$\ddot{d}_{CP} = \left.\frac{\partial^2 d}{\partial \alpha^2}\right|_{CP} \dot{\alpha}_{CP}^2 + \left.\frac{\partial d}{\partial \alpha}\right|_{CP} \ddot{\alpha}_{CP}. \tag{5.26}$$

For sufficiently uniform variation of α, the second term can generally be neglected, such that by using equation 5.16, we obtain

$$\ddot{d}_{CP} = \frac{2}{25} \left(\frac{4}{\beta_{CP}^7 \kappa^3}\right)^{1/5} \dot{\alpha}_{CP}^2. \tag{5.27}$$

This yields the adiabaticity parameter

$$\chi = \frac{\ddot{d}_{CP}}{d_{CP}\omega_{CP}^2} \tag{5.28}$$

$$= \frac{4}{25}\frac{m}{3e} 2^{-1/5} \beta_{CP}^{-9/5} \kappa^{-6/5} \dot{\alpha}_{CP}^2 \tag{5.29}$$

We empirically find the following model, which describes the exponential decrease of the energy transfer in the adiabatic regime $\chi < 1$:

$$\delta E' \approx \delta E \exp\left[c\, \frac{\chi - 1}{\chi}\right], \tag{5.30}$$

where c is a scaling constant. Numerical simulations are carried out for different constant values for β and a linear variation of α around the CP. The results are shown in figure 5.5 b). It can be seen that the approximations Eqs. 5.25,5.30 hold over a wide range of separation times and quartic coefficients, and that large energy transfers in the regime of 10^4-10^6 phonons are readily obtained. The simulations yield values of the model parameters of $\xi^2 \approx 0.1$ and $c^2 \approx 0.1$. We conclude that in this regime, the energy transfer depends only on the ion mass, the variation rate of α and the quartic confinement at the CP. As can be seen from the simulation results, still large energy transfers are obtained at the onset of adiabaticity, such that separation at energy transfers on the single phonon level would require separation times on the order of several hundreds of μs.
As we will show in further sections, this problem can be overcome using ramps that ensure a small ion acceleration $\ddot{d}_{CP}$ at the CP.
Thus, the energy transfer can be reduced by ensuring a small variation rate of α at the CP.

5.3.2. Uncompensated potential tilt

A residual static force along the trap axis, expressed by the coefficient γ' in equation 5.5, can originate from stray charges, laser induced charging of the trap [Har10], trap geometry imperfections or residual ponderomotive forces along the trap axis. The behavior of the equilibrium positions in the presence of an imperfectly compensated tilt, shown in figure 5.2, reveals a discontinuity for the critical $\tilde{\gamma}$, leading to diverging acceleration. The divergence of the acceleration impedes us to perform the separation process adiabatically for $|\gamma| \lesssim \tilde{\gamma}$, i.e. the voltages can not be changed sufficiently slow to suppress motional excitation. Thus, one might encounter the situation that the tilt is sufficiently well compensated to allow for separation, but sufficiently low excitations cannot be obtained irrespectively of the separation time and other control parameters. For small tilt parameters, $|\gamma| \ll \tilde{\gamma}$, we can employ the perturbative expressions Eqs. 5.16, 5.17 of the equilibrium positions to obtain

$$\frac{\partial^2 x_{R,L}}{\partial \alpha^2} = \frac{\partial^2 x_0}{\partial \alpha^2} \pm \frac{1}{2}\frac{\partial^2 d}{\partial \alpha^2} = \gamma \frac{52 \cdot 2^{4/5}}{675 \beta^{9/5} \kappa^{6/5}} \pm \frac{2}{25}\left(\frac{4}{\beta^7 \kappa^3}\right)^{1/5} \tag{5.31}$$

We can estimate the tilt parameter at which the acceleration of one of the ions is twice as large as the tilt-free case determined by equation 5.27 to be about 67% of the critical tilt $\tilde{\gamma}$. Due to the divergence of the acceleration at $\tilde{\gamma}$, we can expect the actual

acceleration at this tilt value to be substantially larger, we thus conclude that a residual tilt $|\gamma| \ll \tilde{\gamma}$ is required to realize crystal separation at low motional excitation. A possible experimental scheme for this has been demonstrated in [Ebl10]: The separation process is performed on a slow (second) timescale under continuous Doppler cooling and detection. The ion positions are extracted from the camera image, and a deviation of the center-of-mass from the initial value is restored by automatic adjustment of the outer electrode differential voltage ΔU_O.

5.3.3. Anomalous heating at the critical point

Micro-structured ion traps exhibit *anomalous heating*, i.e. the mean phonon number increases due to thermalization with the electrodes at a timescale much faster than predicted by the assumption that only Johnson-Nyquist noise is present [Bro15]. This process can be modeled as $\dot{\bar{n}} = \Gamma_h$, with the heating rate $\Gamma_h(\omega) = S_E(\omega)e^2/4m\hbar\omega$ where the spectral electric-field-noise density S_E depends on the trap frequency ω. A polynomial decrease $S_E \propto \omega^{-a}$ is often assumed, where experimentally determined values for the exponent a range from 0.5 to 2.5. Additionally, peaked features might arise in the noise spectrum which are caused by technical sources. Moreover, the absolute values of the heating rates strongly depend on the properties of the electrode surfaces. Typical values at trap frequencies in the 1 MHz regime range from 0.1 to tens of phonons per millisecond. As the trap frequency is strongly decreased around the CP, we can expect a significant amount of excess energy after the separation caused by anomalous heating, increasing for longer separation durations [Niz12]. We model this contribution by integrating over a time dependent heating rate:

$$\Delta\bar{n}_{th} = \int_0^T \Gamma_h\left(\omega(t)\right) dt. \tag{5.32}$$

For the simulations that follow we will employ an experimentally determined relation for trap A (section 5.2) which is $\Gamma_h(\omega) \approx 6.3 \cdot (\omega/2\pi\mathrm{MHz})^{-1.81}\, ms^{-1}$. This does not depend on the geometry of trap A but on the properties of our trap apparatus.
In the case of imperfect control of the ion distance around the CP, section 5.3.1, or in the presence of an uncompensated tilt, section 5.3.2, one will attempt to reduce the motional excitation by separating very slowly. This might however be unsuccessful as anomalous heating will strongly contribute to the energy gain at large separation

times. Experimental procedures for ensuring a sufficient degree of control are therefore ultimately required.

5.4. Voltage ramp design

In this section we explain our scheme for designing voltage ramps for the separation process. Our intention is to provide a scheme which can be applied to any given trap geometry. We do explicitly not rely on the precise knowledge of the electrostatic trap potentials, but rather on quantities which can be measured with reasonable effort. Furthermore, we describe how a single voltage level can be used as a tuning parameter to achieve the optimum result. Our scheme assumes that the tilt potential is perfectly compensated, $\gamma = 0$. We proceed as follows: We first describe how the segment voltages are supposed to vary with the harmonicity parameter α, where we simply fix voltage levels on a small set of mesh points. We then show how this is used in conjunction with a chosen distance-versus-time and available distance-versus-α information to obtain time-domain voltage ramps which can be employed in the experiment.

5.4.1. Static voltage sets

The calculation of suitable voltage ramps relies on the signs and on the magnitude ordering of the geometry parameters. In Table 5.1 we list values for several different micro-structured traps. We assume that any reasonable segmented trap geometry will exhibit similar characteristics. From the results of section 5.3, it is clear that we desire a large positive value of β_{CP}. We assume that the voltages which can be applied to the segments are limited by hardware constraints to the symmetric maximum/minimum values $\pm U_{lim}$. To achieve the largest possible β at the CP, we begin the separation protocol by ramping the O segments to $+U_{lim}$, keep them at constant bias during around the CP, and ramp them back to zero bias after the separation.
The CP is defined by the condition $\alpha = 0$, which is accomplished by suitable voltages $U_{C,S}$. This leaves one degree of freedom, which can be eliminated by maximizing β_{CP}. We solve equation 5.3 for U_C :

$$U_C = \frac{1}{\alpha_C} \left(\alpha - \alpha_O U_O - \alpha_S U_S \right) . \tag{5.33}$$

The largest possible β_{CP} is then given by inserting this result into equation 5.4 and setting $U_O^{(CP)} = +U_{lim}, U_S^{(CP)} = -U_{lim}$:

$$\max_{U_C,U_S} \beta_{CP} = \left(\beta_O + \frac{\beta_C}{\alpha_C}\alpha_S - \beta_S - \frac{\beta_C}{\alpha_C}\alpha_O\right) U_{lim} \tag{5.34}$$

Static separation voltage sets are obtained by fixing the initial, CP and final voltage configurations and interpolating between these. The procedure consists of the following steps:

1. Determine the initial $\alpha_i > 0$ from equation 5.3 using the initial voltages $U_C^{(i)} < 0$ V, $U_S^{(i)} = U_O^{(i)} = 0$ V.

2. Choose the voltages at the CP such that the maximum β_{CP} is attained, by setting $U_O^{(CP)} = +U_{lim}, U_S^{(CP)} = -U_{lim}$ and $U_C^{(CP)}$ from equation 5.33 for $\alpha = 0$. If the geometry parameters are such that $U_C^{(CP)}$ exceeds $\pm U_{lim}$, set $U_C^{(CP)} = -U_{lim}$ and obtain $U_S^{(CP)}$ solving equation 5.3 for U_S rather than U_C. A variable offset $\Delta U_C^{(CP)}$ is added to $U_C^{(CP)}$, which serves to guarantee that the CP voltage set actually corresponds to $\alpha = 0$. It is therefore a tuning parameter which allows for compensation of imperfections. A similar technique has been employed experimentally in [Bow12]. [3].

3. Determine the desired final voltages. We choose $U_C^{(f)} = 0$ V, $U_S^{(f)} = U_S^{(CP)} = -U_{lim}$ and $U_O^{(f)} = 0$ V. This choice is convenient when $U_C^{(i)} \approx -U_{lim}$ and ensures that the ions are finally kept close to the respective centers of the S segments with a trap frequency similar to the initial one. Obtain α_f from equation 5.3.

4. For approaching the CP, $\alpha_i \geq \alpha > 0$, set

$$U_S(\alpha) = \left(1 - \frac{\alpha}{\alpha_i}\right) U_S^{(CP)} \tag{5.35}$$

and

$$U_O(\alpha) = \begin{cases} 2\left(1 - \frac{\alpha}{\alpha_i}\right) U_{lim} & \alpha > \frac{\alpha_i}{2} \\ U_{lim} & \alpha \leq \frac{\alpha_i}{2} \end{cases} \tag{5.36}$$

and obtain $U_C(\alpha)$ from equation 5.33.

[3] If the magnitude of $U_S^{(CP)}$ is chosen smaller than U_{lim}, this leads to smaller values of β_{CP} and a larger ion separation at the CP. This offers the possibility for well-controlled studies of the dependence of the separation process on the quartic confinement at the CP.

5. Beyond the CP, $0 \geq \alpha \geq \alpha_f$, set

$$U_S(\alpha) = -U_{lim} \tag{5.37}$$

and

$$U_O(\alpha) = \begin{cases} U_{lim} & \alpha > \frac{\alpha_f}{2} \\ 2\left(1 - \frac{\alpha}{\alpha_f}\right) U_{lim} & \alpha \leq \frac{\alpha_f}{2} \end{cases} \tag{5.38}$$

and obtain $U_C(\alpha)$ from equation 5.33.

5.4.2. Time domain ramps

We now show how to design suitable time-domain voltage ramps $U_n(t)$ that will assure well-controlled separation. It has been shown in section 5.3.1 that a small value of the acceleration at the CP, $\ddot{d}_{CP}$, is required for achieving a low energy transfer. This in turn is guaranteed by well-controlled variation of the distance $d(t)$ throughout the separation process. As $d(\alpha)$ is monotonically decreasing with α, it can be inverted to obtain $\alpha(d)$ which is used to compute the final voltage ramp as $U_n(\alpha(d(t)))$ (see figure 5.6.).
Possible choices for $d(t)$ are a sine-squared ramp

$$d(t) = d_i + (d_f - d_i) \sin^2\left(\frac{\pi t}{2T}\right) \tag{5.39}$$

or a polynomial ramp

$$d(t) = d_i + (d_i - d_f)\left(-10\frac{t^3}{T^3} + 15\frac{t^4}{T^4} - 6\frac{t^5}{T^5}\right) \tag{5.40}$$

Both ramps fulfill $d(0) = d_i, d(T) = d_f, \dot{d}(0) = \dot{d}(T) = 0$. The polynomial ramp, used in the following, additionally fulfills $\ddot{d}(0) = \ddot{d}(T) = 0$, while the second derivative of the sine-squared ramp displays discontinuities. However, these features presumably play no role in experiments, as the voltage ramps are generally subject to discretization and filtering. Different methods can be employed for the determination of $d(\alpha)$:

- The equilibrium distance can be computed by employing realistic trap potentials from simulation data, using the voltage configuration pertaining to a given α as determined by the static voltage sets $U_n(\alpha)$. This method requires the simulated potentials to match the actual trap potential with great precision.

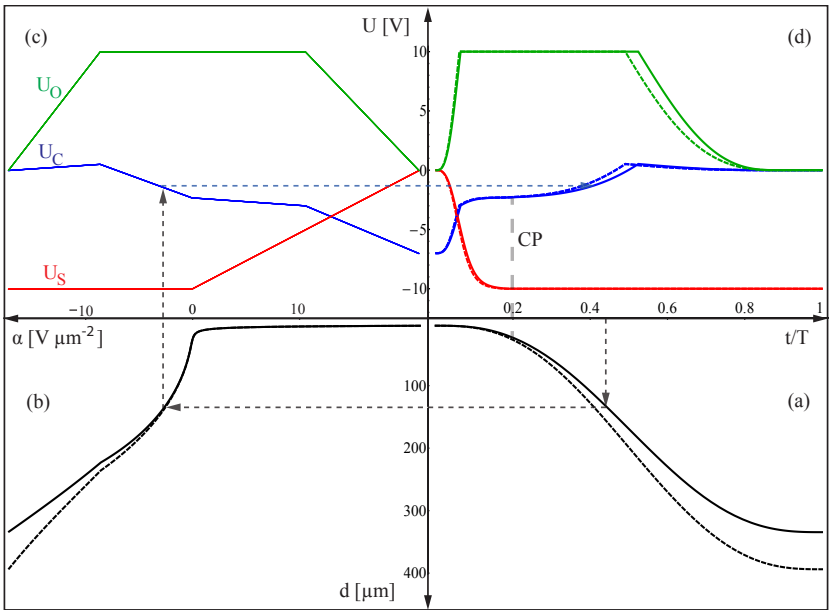

Figure 5.6.: Voltage ramp transfer to the time domain. Note that all four axes pertain to different quantities, and that the axis pointing downwards goes to increasing distances. The reading direction is clockwise, starting in the bottom right corner: A predefined time-to-distance function $d(t)$ shown in panel **a)** is used in conjunction with α-to-distance information $\alpha(d)$ shown in **b)** to determine the time-dependent electrode voltages $U_n(t)$ using the static voltage sets $U_n(\alpha)$ from panel **c)**. The resulting ramps $U_n(t)$ are shown in **d)**. The dashed curves are corresponding to the case when the voltage ramps are calculated according to the presented method, but realistic trap potentials from simulations are used to determine d_f and $d(\alpha)$. The dashed arrows exemplify how a specific value U_C is obtained.

- The equilibrium distance can be computed using values from calibration measurements for the coefficients α_n, β_n. This circumvents the need for simulations and accounts for parameter drifts. It only yields valid values for distances which are small compared to the electrode width, however we will show in section 5.5 that this procedure yields useful voltage ramps.

- Ion distances can be measured by imaging the ion crystal on a camera, while voltages configurations for decreasing α values are applied. This is the most direct method, as the ion distance in image pixels can be gauged by measuring the trap frequency from resolved sideband spectroscopy [Jec11]. The imaging magnification is determined from the trap frequency by using $d = \left(\frac{2e\kappa}{m\omega^2}\right)^{1/3}$. This method benefits from the accuracy of resolved sideband spectroscopy, which is typically between 10 kHz and 100 Hz.

5.5. Simulation results

In order to analyze the sensitivity of the separation process and the performance of our ramp design protocol, we numerically solve the classical equations of motion. For the time- and energy-scales and potential shapes under consideration, we expect quantum effects to play no significant role. For the case of single-ion shuttling, the occurrence of quantum effects is thoroughly discussed in [Für14].
We perform the simulations using either the Taylor approximation of the potentials or the realistic potentials from electrostatic simulations [Sin10] for trap A, which is similar to that described in [Sch08]. The voltage ramps $U_i(t)$ are used in conjunction with the potentials to yield the equations of motion for the ion positions $x_1 < x_2$. Employing the Taylor approximation potential equation 5.1, these read

$$-m\ddot{x}_{1,2} = 4\beta(t)x_{1,2}^3 + 2\alpha(t)x_{1,2} + \gamma \pm \frac{\kappa}{(x_2 - x_1)^2}, \tag{5.41}$$

where the coefficients are given by using the voltage ramps in Eqs. 5.3, 5.4, 5.5. For realistic trap potentials, we obtain

$$-m\ddot{x}_{1,2} = \sum_{n=C,S,O} U_n(t) \left.\frac{d\phi_n}{dx}\right|_{x_{1,2}} \pm \frac{\kappa}{(x_2 - x_1)^2} \tag{5.42}$$

The possibility to perform the simulations with approximate and realistic potentials serves the purpose of verifying the performance of the voltage ramps. These are determined purely by trap properties around the CP, which are conveniently accessible by measurements. More precisely, the time-domain voltage ramps are based on a $d(\alpha)$ dependency given by the Taylor approximation potential according to figure 5.6, while the resulting energy transfer pertaining to these ramps can be obtained from simulations using realistic potentials.
Note that a nonzero tilt can be present in the simulations based on the realistic potentials by summing separately over electrodes O_L and O_R and adding the differential voltage $\pm\Delta U_O$ given by γ/γ_O accordingly. The calculations presented here employ the mass of $^{40}Ca^+$ ions which we use in our experiments, and all simulations were performed for a limiting voltage range $U_{lim} = 10$ V.
Eqs. 5.41 or 5.42 are solved numerically using the *NDSolve* package from *Mathematica*, with the ions starting at rest. The final oscillation of each ion around its equilibrium position is analyzed and yields the energy transfer expressed as the mean phonon number

$\bar{n} = \Delta E/\hbar\omega_f$. We distinguish several regimes of laser-ion interaction: i) If the vibrational excitation becomes so large that the average Doppler shift per oscillation cycle exceeds the natural linewidth of a cycling transition, ion detection by counting resonance fluorescence photons will be impaired. ii) Measurement of the energy transfer i.e. by probing on a stimulated Raman transition [Wal12] typically requires mean phonon numbers below about 300. iii) The Lamb-Dicke regime of laser-ion interaction, where coherent dynamics on resolved sidebands can be driven [Lei03a] is typically attained below about 10 phonons. The borders between these regimes depend on the trap frequency, ion mass and the specific atomic transitions to be driven, thus the regimes are indicated as broad gray bands in figure 5.7. Note that if final excitations in the measurable regime are obtained, an electrical counter kick can be applied for bringing the oscillation to rest [Wal12].

5.5.1. Dependence on separation time

We first analyze the dependence of the energy transfer on the duration of the separation process T, the result is shown in figure 5.7. The calculation is carried out for the ideal case of perfectly compensated potential tilt. We see that the final excitation becomes sufficiently low to remain in the Lamb-Dicke regime for typical laser-ion interaction settings at times larger than about 40 μs, which clearly outperforms the naïve approach of voltage interpolation from section 5.3.1.
We also take into account increased anomalous heating around the CP by employing the averaged heating rate according to equation 5.32. We see that for our specific heating rates, the limit of about one phonon per ion can not be overcome, but as the anomalous heating contribution is scaling as T, the separation result becomes rather insensitive with respect to the precise choice of the T for $T \gtrsim 50\ \mu s$.
The simulation results verify our approach of calculating the voltage ramps using the Taylor approximated potentials. One recognizes that the resulting energy transfer in this case is larger by a factor of about two throughout the entire range of separation durations. This is due to the fact that the Taylor expansion leads to deviating voltages pertaining to the CP, which are sufficiently strong to increase the acceleration as explained in section 5.3.1. The discrepancy becomes irrelevant for separation times larger than $T = 60\ \mu$s. At around 60 to 70 μs the oscillatory excitation becomes smaller than $\bar{n} = 0.1$, corresponding to the limit we can currently resolve in our experiment. The slight inaccuracy for low phonon numbers is due to numerical artifacts. Even lower

energy transfers at shorter T could possibly be achieved by ramp engineering, i.e. by the application of shortcut-to-adiabaticity approaches [Für14; Pal13].

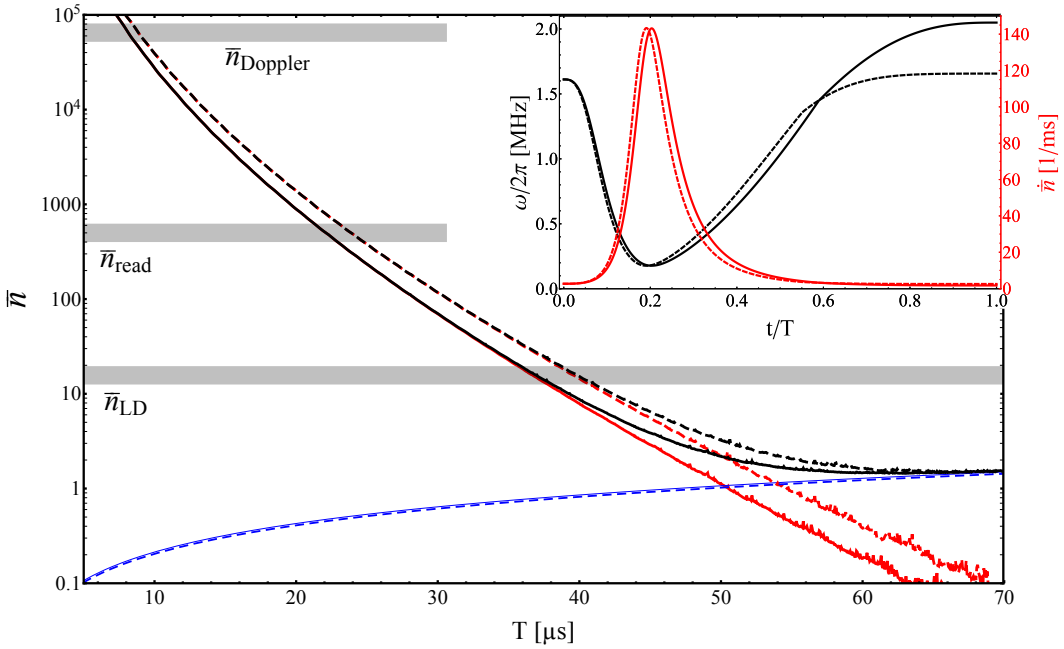

Figure 5.7.: Energy transfer versus separation time: Oscillatory (red) and thermal excitation (blue), and the sum of both (black) versus the separation duration T. The solid lines correspond to the calculation using the Taylor approximation, the dashed lines correspond to the full potential calculation, see text. Grey bands seperate different regimes of laser-ion interaction, see text. The thermal excitation was deduced from experimental heating rate data according to section 5.3.3. The inset shows the trap frequency (black) and the corresponding heating rate (red) as a function of normalized time during the separation process.

5.5.2. Sensitivity analysis

Two crucial parameters for the separation operation are the offset voltage at the CP $\Delta U_C^{(CP)}$ and the potential tilt γ. Small variations of these parameters lead to strong coherent excitations as shown in figure 5.8.

The CP voltage offset $\Delta U_C^{(CP)}$ serves both for modeling and compensation of inaccuracies of the trap potentials, leading to a wrongly determined CP voltage configuration and therefore to increased acceleration. It is implemented into the simulations by just adding it to $U_C^{(CP)}$ as determined by equation 5.33 in the calculation of the static voltage sets.

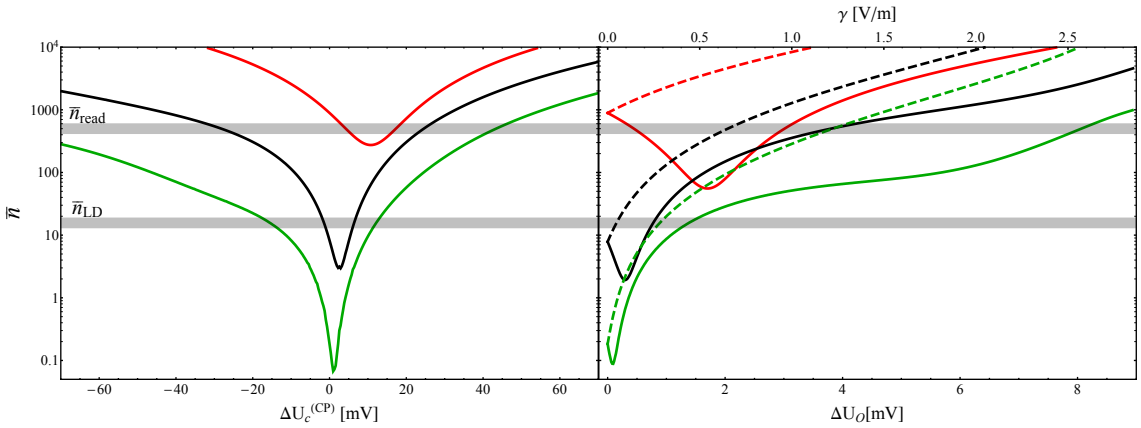

Figure 5.8.: Mean coherent excitation as a function of the offset voltage at the center segment at the CP (a) and the tilt force γ (b). The tilt voltage $+\Delta U_O$ is applied to the right outer segment and $-\Delta U_O$ is applied to the left outer segment. The mean phonon number for the right ion is depicted by dashed lines and by solid lines for the left ion. The curves correspond to different separation times: $T = 60\mu s$ (green), $T = 40\mu s$ (black), $T = 20\mu s$ (red). The critical tilt is at $\tilde{\gamma} = 3$ V/m.

We see that even for sufficiently slow separation, the Lamb-Dicke regime can only be attained if this voltage offset, and therefore the CP voltages in general, are correct within a window of about 20 mV, on the other hand it becomes clear that this voltage serves as convenient fine tuning parameter. The minimum excitation does not occur at $\Delta U_C^{(CP)} = 0$, but is slightly shifted to positive values.

This can be understood by considering that $|\dot{\alpha}|_{CP}$ is increased for any $\Delta U_C^{(CP)} \neq 0$, but $\ddot{\alpha}_{CP}$ is decreased for $\Delta U_C^{(CP)} > 0$. With $\partial d/\partial\alpha$, the second term in equation 5.26 leads to a reduced total acceleration for small positive $\Delta U_C^{(CP)}$. Larger values again lead to increased acceleration because of a smaller β_{CP} value. All other calculations in this work are done using $\Delta U_C^{(CP)} = 0$.

For the case of an uncompensated tilt γ', we observe an even stronger dependence of the energy transfer. Fine tuning of the voltage difference on the outer segments ΔU_O on the sub-mV level is required to reach the single phonon regime. Moreover, we observe that moderate uncompensated potential tilts reduce the energy transfer to one of the ions, as its CP acceleration is reduced by a more smooth $x(\alpha)$ dependence. This might be of interest for specific applications where only the energy transfer to one of the ions is of importance.

5.5.3. Dependence on the limiting voltage

Finally, we study the dependence of the energy transfer on the limiting voltage U_{lim}. We find that by increasing the voltage limit, beyond $U_{lim} = 10$ V used so far, we can obtain lower coherent excitations as shown in figure 5.9.

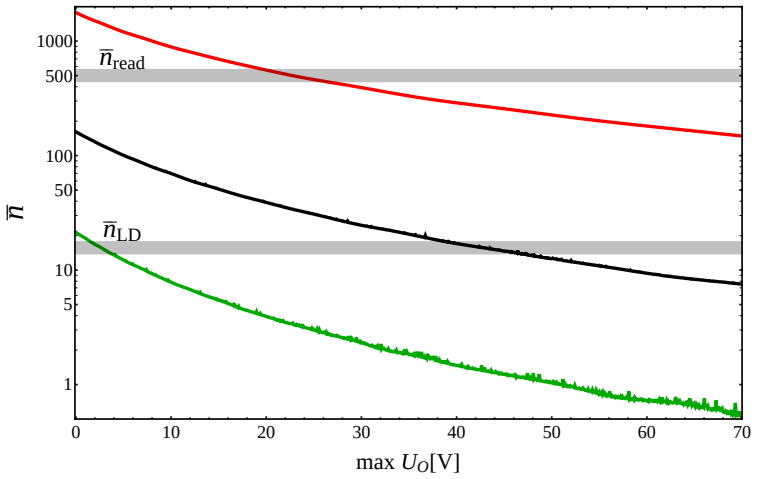

Figure 5.9.: Dependence on the voltage limit: Oscillatory excitation as a function of the maximum voltage on the outer segments with all other limiting voltages remaining unchanged. The curves correspond to different separation times: $T = 40\mu s$ (green), $T = 30\mu s$ (black), $T = 20\mu s$ (red).

For this simulation, only the maximum voltage on the outer segments (max U_O) is increased and all other limits remain unchanged. We infer that by increasing the voltage limit on these electrodes up to about 50 V, one can reduce the mean phonon number by a factor of ≈ 8 for $T = 60\mu$s. For lower separation durations the enhancing factor becomes slightly smaller.

Conclusion

We have pointed out the pitfalls for ion crystal separation: Uncontrolled separation and uncompensated background fields lead to enhanced acceleration of the ions when the single well potential is transformed into a double well, which would require separation times in the millisecond range to keep the motional excitation near the single phonon level. This in turn leads to strong anomalous heating due to the reduced confinement

during the separation process. We presented a framework to design voltage ramps which allow for coping with these problems. The scheme does only rely on measured calibration data which is obtained for the initial situation, where the ions are tightly confined in a single potential well. We carried out simulations, which elucidate the energy transfer mechanisms, and verify the performance of our scheme for the voltage ramp calculation. We showed that excitations near the single phonon level can be obtained for the specific trap apparatus we use. Furthermore, we analyzed the suitability of different trap geometries for ion crystal separation by means of electrostatic simulations. We concluded that crystal separation becomes easier for smaller trap structures, and that dedicated optimization of the geometry can be helpful. In future work, we envisage to analyze how crystal separation can be performed on faster timescales by using shortcut-to-adiabaticity approaches, with an emphasis on robustness against experimental imperfections.

6

Experiment Characterization

High fidelity quantum logic operations impose stringent requirements on noise suppression and accurate control. As the entangling quantum gate for two ions is carried out on a shuttling-insensitive radial mode of motion, the requirements on this particular mode are high. In this chapter, the stability and control of the motional modes are investigated. Specifically the ground state cooling, the heating rate, the long- and short-term stability of the modes are characterized. Additionally the performance of the optical setup is assessed.

6.1. Ground state cooling and motional heating

A trapped ion resembles a single elementary charge, which is typically located some tens or hundreds of micrometers from the trap surface. Electric field fluctuations, generated on the surface, can excite the motional modes of an ion – this effect is commonly referred to as anomalous heating. Contrary to technical noise on the electrodes, which originates from the electrical circuitry around the trap, the origin of anomalous heating is not clear [Bro15; Hit13]. Contaminants on the surface are likely to be responsible for the effect, as two research groups have demonstrated reduction of heating by in-situ cleaning of the trap surface via ion bombardment [Hit12; Dan14]. Cooling the ion trap to cryogenic temperatures can also substantially reduce the heating rate [Des06; Lab08]. Both approaches involve significant additional experimental effort. We aim at achieving sufficiently low heating rates at decent technological overhead. In particular, our trap is coated with a 8 µm layer of gold. This is empirically known to yield heating rates in the few phonons per second regime for comparable traps [Bla10; Kie15].
A single ion is used as a probe for the anomalous heating on the three motional modes $\omega_{x,y,z}$ at frequencies $2\pi \times \{1.5, .3.7, 4.6\}$ MHz. Initially, the ion is cooled close to the

ground state of motion by initial Doppler cooling and subsequent resolved sideband cooling. Analysis of the mean phonon number $\bar{n}$ is provided by a resolved-sideband method, which is based on phonon-number-dependent coupling strengths of three transitions, see section 2.3: carrier (car), blue sideband (bsb) and red sideband (rsb). Probing these transitions with variable pulse time yields Rabi oscillations, which are employed to deduce the mean phonon number from a fit, see appendix B.1. An example for an axial motional mode, which is cooled close to the ground state by the laser beams R1 and R2, is given in figure 6.1.

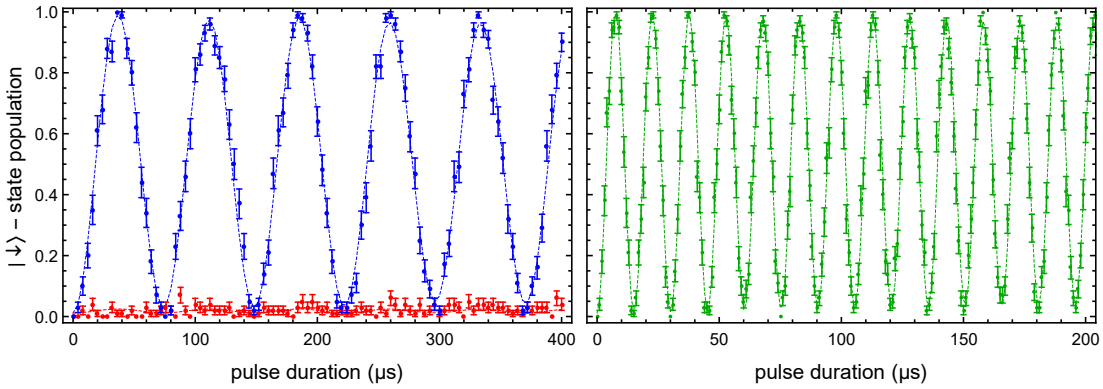

Figure 6.1.: Rabi oscillation data for the axial mode of vibration and the corresponding carrier transition of a single ground-state-cooled ion. Probing the bsb (blue), rsb (red) and carrier (green) transition yields a mean phonon occupation number of only $\bar{n} = 0.014(2)$ from a fit (dashed line). The base Rabi frequency is determined to be $\Omega_R/2\pi = 67.8\,\mathrm{kHz}$ and the Lamb-Dicke parameter is $\eta = 0.203$. The axial trap frequency is $\omega_x/2\pi = 1.487\,\mathrm{MHz}$. Each data point corresponds to 100 measurements, error bars correspond to the standard error from binomial readout statistics.

Sideband cooling in this experiment is performed on the axial mode only, the radial modes are Doppler cooled. The cooling sequence in this example is comprised of 110 cooling pulses, where the first 15 pulses are applied to the second red sideband right after Doppler cooling to remove two phonons with a single pulse. The subsequent pulses are applied on the first red sideband, and the pulse duration is increased for the last cooling pulses as the mean Rabi frequency decreases with decreasing temperature. A single cooling pulse takes on average 19 µs, after each pulse a 2 µs optical σ^+ pumping pulse is applied. Including short switching delays, the total time for the resolved sideband cooling sequence in this case is 2.4 ms. The cooling sequence in this example is optimized for a low mean phonon number, the duration is not optimized. However, we achieve

comparable results with mean phonon numbers $\bar{n} \ll 1$, with less pulses. Thus, in future experiments, the thermal occupation after initial Doppler cooling should be analyzed and, if necessary, optimized. Furthermore, sideband cooling efficiency could be increased by increasing the duration of concatenated cooling pulses continuously. Currently, the pulse duration is increased in only three to four steps. A viable alternative to resolved sideband cooling would be sympathetic electromagnetically-induced-transparency laser cooling [Lin13].

For the shuttling-insensitive quantum gate, which is conducted on the radial modes of motion, it is necessary to cool the radial modes close to the ground state, see figure 6.2.

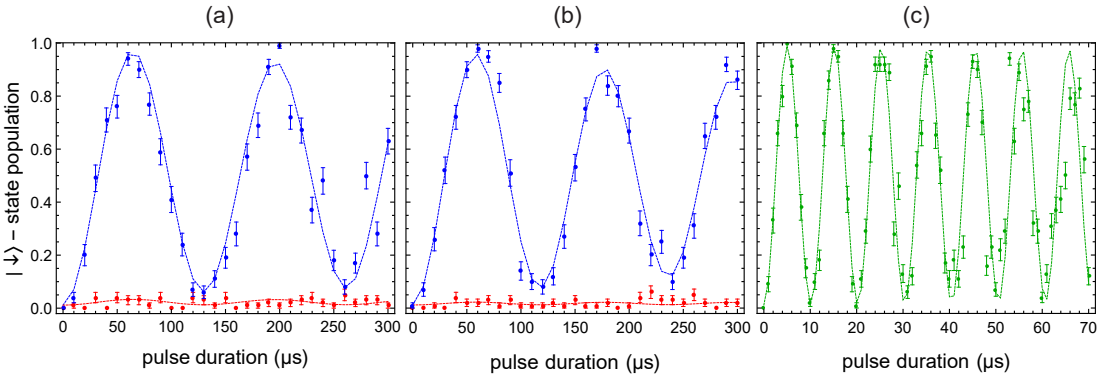

Figure 6.2.: Rabi oscillation data for the radial vibrational modes in the ground state of motion – (a): ω_y and (b): ω_z. The carrier transition data (c) correspond to the ω_y measurement and is virtually identical for the ω_z measurement where slightly different cooling pulses are used. The frequency of the ω_y-mode is $2\pi\times3.739\,\mathrm{MHz}$ – a fit yields a mean phonon number of $\bar{n} = 0.023(6)$, a Lamb-Dicke parameter of $\eta = 0.077$ and a base Rabi frequency of $\Omega_R/2\pi = 99.1\,\mathrm{kHz}$. For the ω_z-mode at $2\pi\times4.591\,\mathrm{MHz}$, the estimated mean phonon number $\bar{n} = 0.012(4)$ is lower and the parameters $\eta = 0.087$ and $\Omega_R/2\pi = 97.9\,\mathrm{kHz}$ are similar. Each data point corresponds to 100 measurements, error bars correspond to the standard error from binomial readout statistics.

The laser beams R1 and R4 are employed to create an effective k-vector in the radial direction, which couples to both radial modes ω_y and ω_z. Thus, the Rabi oscillations on each mode are affected by the temperature of the other *spectator* mode, see appendix B.1 for a theoretical description. To precisely determine the mean phonon number, both radial modes are cooled with resolved sideband cooling. In the ω_y-mode measurement, cooling is performed with 70 cooling pulses on the probed mode and 20 pulses on the spectator ω_z-mode. The total duration of the cooling sequence is 2.5 ms. In the ω_z-mode

measurement, cooling is performed with 120 cooling pulses on the probed mode and 20 pulses on the spectator ω_y-mode. The total duration of the cooling sequence is around 3.7 ms. As in the axial cooling sequence, the cooling duration is not optimized and can be improved by the aforementioned measures. Compared to the axial mode, the radial mode frequencies are substantially higher and the mean phonon number after initial Doppler cooling is lower, see section 2.1.1. For the $\omega_{x,y,z}$-modes a theoretical Doppler limit of $\bar{n} = \{7.3, 2.6, 2.0\}$ is calculated. However, due to the smaller Lamb-Dicke factor η, an increased laser intensity is required, compared to the axial modes of motion, to achieve a similar base Rabi frequency.

To measure the heating rate, all lasers are switched off for a variable idle time once a motional mode is prepared in the ground state. Subsequently, the increased mean phonon number is determined with the described method. The result for the heating rate measurement of the three center of mass modes is shown in figure 6.3.

In contrast to the axial mode, the radial modes are additionally excited by electric field noise between the RF and DC electrodes, which originates from fluctuating voltages. Therefore, the radial modes are more sensitive to technical noise, and careful wiring of the experimental apparatus yields heating rates of the radial modes, which are comparable to the low heating rate on the axial mode. Considerable effort was devoted to ensure this, since the radial quantum gate is carried out on one of the radial modes of vibration. The spectral density of electric field noise S_E is computed from the heating rate $\dot{\bar{n}}$ by the following relation [Bro15]

$$S_E(\omega_i) = \dot{\bar{n}} \frac{4 m_I \hbar \omega_i}{e^2} \tag{6.1}$$

where m_I is the mass of a $^{40}Ca^+$ ion of 6.636×10^{-26} kg, ω_i is the angular frequency of a motional mode and e is the elementary charge. By computing this quantity for our results, we find, that the spectral density of electric field noise on the two modes ω_x and ω_z is comparable. The spectral noise density on the ω_y-mode is about five times higher than on the other two modes, which is attributed to pronounced technical noise in the y-direction (DC electrode direction).

We employ the spectral noise density, to compare our results to other experiments, where different ion species and trap frequencies are used. An extensive review and analysis of experimental data of anomalous heating in ion traps is provided in [Bro15]. The heating rate of a trapped ion typically decreases with the temperature of the trap surface, increases with a lower ion distance from the trap electrodes and decreases for higher

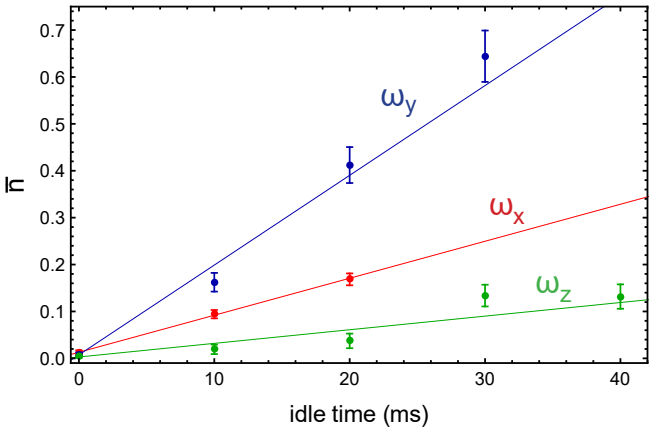

Figure 6.3.: Measured heating rate of the motional modes $\omega_{x,y,z}$ in the laser interaction zone (LIZ), which corresponds to electrode 20. The axial mode ω_x corresponds to red red data points, blue data points are measured on the radial ω_y-mode and green data points belong to the radial ω_z-mode. Error bars correspond to the standard error of the parameter estimate. A linear weighted least square fit yields the heating rate of each mode, the results are summarized in table 6.1.

mode	$\omega/2\pi$ (MHz)	η	$\bar{n}_{min}$	$\dot{\bar{n}}$ (1/sec)	S_E (V^2/m^{2}Hz)
ω_x	1.487	0.203	0.014(2)	7.9(2)	$8.1(2) \times 10^{-14}$
ω_y	3.739	0.077	0.023(6)	19(2)	$4.9(5) \times 10^{-13}$
ω_z	4.591	0.087	0.012(4)	2.9(7)	$9(2) \times 10^{-14}$

Table 6.1.: Characteristic data for the center of mass modes in the axial directions ω_x and the radial direction $\omega_{y,z}$. The measurements for the Lamb-Dicke parameter η and the smallest obtained mean phonon number $\bar{n}_{min}$ are shown in figure 6.1 and 6.2. A spectroscopic measurement is utilized to determine the trap frequencies with precision below 1 kHz. The heating rates $\dot{\bar{n}}$ and the spectral density of the electric field noise S_E are determined from a linear fit to the experimental data, see figure 6.3.

trapping frequencies. Different scaling laws for these parameters have been calculated and observed in experiments, which support or rebut various proposed origins of the noise. The topic is complex and multifaceted and thus requires further experimental and theoretical investigation, to better understand the origin of the anomalous heating in ion traps.

We compare our results to other ion traps operated at room temperature and comparable trapping frequencies. The distance of a single ion in our trap from the trap electrodes is 230 µm. Compared to similarly sized traps the spectral noise density i.e. the heating rate of the trap is very low. In fact, lower spectral noise densities at room temperature were

only achieved in ion traps which are more than 3.4 times larger than our trap [Ben08; Hom06b; Pou12]. In traps with small electrode-ion distances, low heating rates are achieved by cryogenic setups [Nie14; Chi14] or in situ cleaning of the trap surface [Dan14; McC15b].
The low heating rate of the ion trap allows for a long series of excitation-sensitive quantum operations without additional experimental overhead.

6.2. Stability of the radial potential

The stability of the radial motional modes is crucial to our approach for a scalable quantum computation architecture since one of these modes is used for the entangling gate operation. Thus, the radio frequency supply voltage of the ion trap is actively stabilized as described in section 4.3. The active regulation needs to provide decent stability on a short timescale, for sufficient motional coherence – to allow for high fidelity entangling gates, as investigated in section 6.3 – and on a long timescale to significantly reduce the calibration overhead during the experiments. In this section, the long term stability of a radial mode is characterized. To determine the frequency of the motional transition more precisely than a conventional spectroscopic measurement, a Ramsey spectroscopy experiment is carried out [Let04; Rus12].

Initially, the ion is cooled to the ground state of motion of both radial modes. A $\pi/2$-pulse on the blue sideband, followed by a Ramsey delay time and a final $\pi/2$-pulse ($+90°$ phase shift) on the blue sideband comprise the experimental sequence. A second, almost identical, experiment is conducted, where the phase shift of the final $\pi/2$-pulse is $-90°$. The two experiments are executed alternately – the difference of the two signals is proportional to a phase ϕ, when the detuning from resonance is small. The phase is employed to determine the deviation from the resonance frequency $\Delta\omega_{bsb} = \phi/T$, where T is the Ramsey delay time. Repeating this experiment over several minutes allows us to analyze the stability of the mode. However, the measured quantity $\Delta\omega_{bsb}$ is also affected by drifts of the carrier transition which are caused by drifts of the quantizing magnetic field. To isolate this effect, a measurement of the carrier transition detuning $\Delta\omega_{car}$ is carried out after each measurement of the blue sideband detuning. Calculating the difference of the two measurements serves to determine the stability of the radial secular mode $\Delta\omega_z(t) = \Delta\omega_{car}(t) - \Delta\omega_{bsb}(t)$.
The achievable measurement precision is limited by binomial shot-noise of the Ramsey

measurements. Thus, it is desirable to use long Ramsey delay times, as the accumulated phase is proportional to T and the measurement sensitivity is improved. However, motional decoherence reduces the Ramsey contrast on the blue sideband for large delay times, see section 6.3. To account for this, the phase is calculated by $\phi \approx \arcsin(b/c)$, where b is the difference of the two measured signals ($+90°$ and $-90°$-trace) and c is the Ramsey contrast. Measurement errors are derived with Gaussian error propagation from this relation. Consequently, a reduced contrast impairs the measurement sensitivity and we use a delay time of 1 ms in this measurement.
The corresponding data for the entangling gate mode ω_z with active stabilization is shown in figure 6.4.

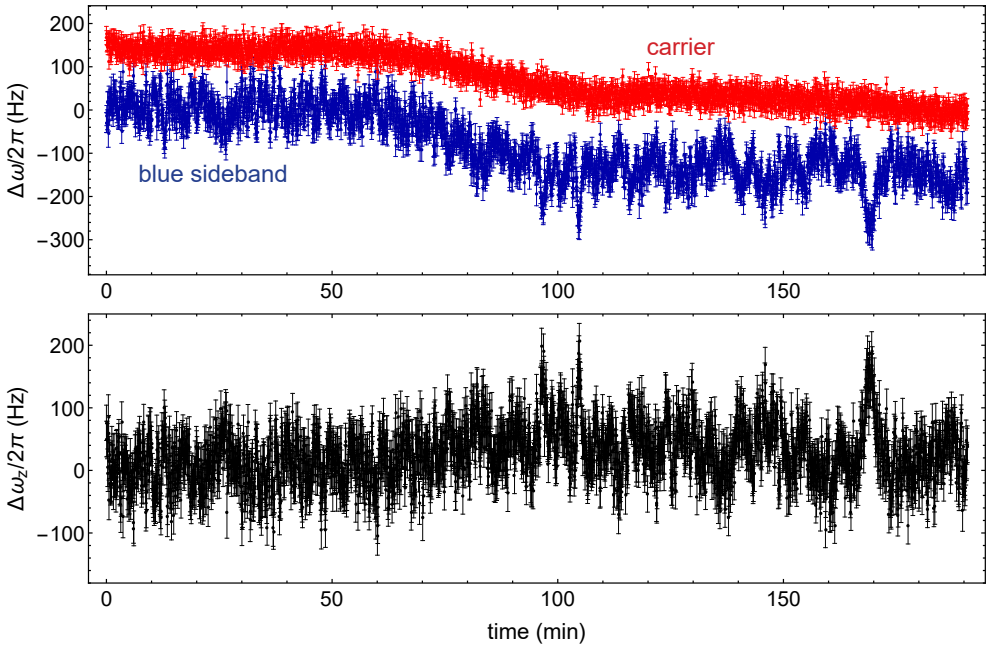

Figure 6.4.: Measurement of the frequency stability of the radial secular mode ω_z, at an absolute frequency of $\omega_z/2\pi = 4.434\,\mathrm{MHz}$, with active RF voltage stabilization. The data in the top panel shows red data points for $\Delta\omega_{car}$ and blue data points for $\Delta\omega_{bsb}$. Black data points in the lower panel show the secular frequency deviation $\Delta\omega_z$, which is calculated from the difference of the data in the top panel, to correct for the drift of the magnetic field that affects $\Delta\omega_{car}$. The Ramsey delay time for this measurement is 1 ms. Each data point corresponds to 2×50 single measurements, where each of the two Ramsey sequences is executed 50 times.

For a measurement time over three hours with active stabilization, the secular frequency exhibits excellent stability. The measurement is not shot-noise limited and minor frequency fluctuations are observed. The drift of the carrier transition frequency is around $2\pi\times40\,\mathrm{Hz}$ per hour, which is small, compared to the absolute Zeeman splitting of about $2\pi\times10.5\,\mathrm{MHz}$. It is suspected to be caused by thermal fluctuations near the permanent magnets, which generate the magnetic field. During all experiments, the magnetic shielding is closed, to ensure thermal stability of the RF electronics, which are close to the vacuum chamber.
To investigate the quality of the active RF stabilization further, a measurement without stabilization is carried out – the results are illustrated in figure 6.5. The instabilities are

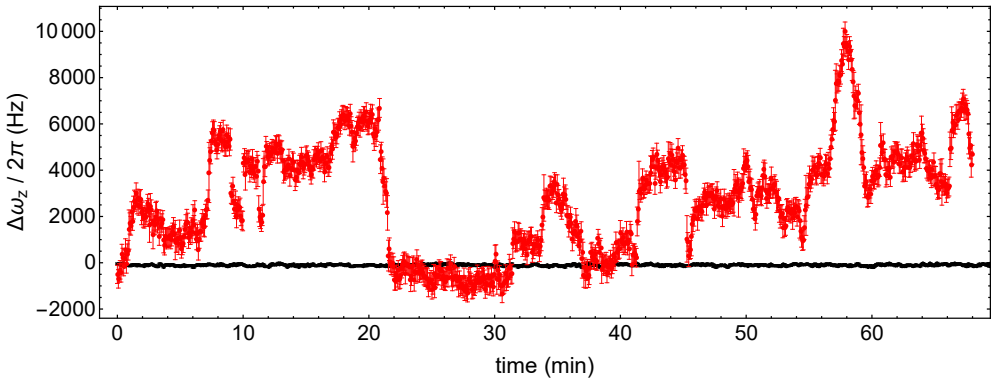

Figure 6.5.: Measured frequency stability of the radial secular mode $\Delta\omega_z$ without active stabilization (red data points). The trap frequency is $\omega_z/2\pi = 4.878\,\mathrm{MHz}$. Black data points correspond to the data for $\Delta\omega_z$ with stabilization, as shown in figure 6.4, where $\omega_z/2\pi = 4.434\,\mathrm{MHz}$. The measurement is performed in the same fashion, as with active stabilization. The carrier frequency is drift free for the short time interval, thus only the $\Delta\omega_z$ trace is shown. The Ramsey delay time in this measurement is 100 µs. Each measurement corresponds to 2×50 single measurements, where each of the two Ramsey sequences is executed 50 times.

significantly larger, sudden drifts of around 6000 Hz within 2 minutes are observed.
To analyze the frequency stability of the ion oscillation, the overlapping Allan variance is calculated [How81; Ril08]. From a set of M frequency measurements f_i, which are individually sampled from a time interval τ_0, it is given by

$$\sigma_y^2(\tau) = \frac{1}{2m^2(M-2m+1)} \sum_{j=1}^{M-2m+1} \left(\sum_{i=j}^{j+m-1} f_{i+m} - f_i \right)^2 \tag{6.2}$$

with $\tau = \tau_0 \cdot m$, where m is an integer and is denoted as averaging factor. Specifically, a frequency measurement f_i corresponds to a single measurement of $\Delta\omega(t)/2\pi$, which is the mean of 100 single measurements – each with a Ramsey delay time of 1 ms. Thus, a single measurement f_i corresponds to a sample time interval of $\tau_0 = 1\ \text{ms} \cdot \sqrt{100} = 10$ ms. However, it takes around 2.1 s in practice to carry out the 100 single measurements due to state preparation, laser cooling and fluorescence readout. The corresponding data for the Allan deviation $\sqrt{\sigma_y^2(\tau)}$ is shown in figure 6.6.

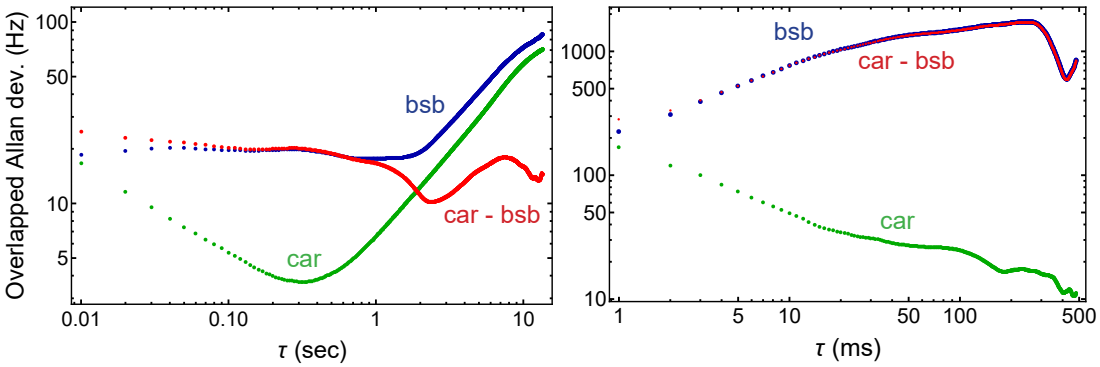

Figure 6.6.: Overlapping Allan deviation of the radial secular frequency measurement with (left) and without (right) active RF level stabilization. Green data points correspond to $\Delta\omega_{car}/2\pi$, blue data points to $\Delta\omega_{bsb}/2\pi$ and red data points to the difference of both $\Delta\omega_z/2\pi$. The data with stabilization is taken from a three hour measurement with 1 ms Ramsey delay time, see figure 6.4. Data without stabilization is taken from a one hour measurement with 0.1 ms Ramsey delay time, see figure 6.5.

As the carrier frequency measurement is shot-noise limited, it becomes more precise for longer averaging, which corresponds to larger τ. After a minimum is reached around $2\pi\times4$ Hz, the drift is clearly observable in the Allan deviation. The sideband measurement is not shot-noise limited, thus the Allan deviation does not decrease for increased averaging. For longer averaging times, the frequency drifts along with the carrier frequency. For the difference signal, which corresponds to the radial secular trap frequency ω_z, no drift is observed. Thus, the drift of the blue sideband for $\tau > 1$ s is entirely caused by the carrier drift.

The radial frequency ω_z is stable below $2\pi\times20$ Hz for long averaging times τ which corresponds to a relative frequency stability of about 5 ppm over three hours. A similar value is achieved when only evaluating one hour of the data to make it comparable to the non-stabilized measurement. We consider the frequency stability of the RF electronics,

which drive the AOMs, to be better than the measured mode frequency stability. Without stabilization, we estimate the motional frequency stability to be around $2\pi\times1000\,\mathrm{Hz}$. Since the radial secular frequency is proportional to the RF voltage, we estimate the voltage amplitude fluctuations to be reduced by a factor of 50, which corresponds to a 34 dB reduction in the level of trap frequency voltage noise and drift. Comparable results are achieved in [Joh16]. In conclusion, the radio frequency potential is sufficiently stabilized on long timescales, to allow for high fidelity entangling gates with virtually no need for recalibration of the trap frequencies.

6.3. Motional coherence

For a high fidelity geometric phase gate, it is necessary to prevent motional dephasing of the gate mode during the gate duration, when spin and motion are entangled. In order to characterize the motional coherence time a Fock state Ramsey experiment is conducted [Tur00], which produces a superposition state of the type $|\downarrow\rangle\,(|n=0\rangle + |n=1\rangle)$. The motional coherence time of this state is limited by the inverse heating rate. Additionally, fluctuations of secular trap frequencies lead to a faster decay.
The experiment is conducted as follows: Initially, a single ion is prepared in the ground state of motion $|\uparrow\rangle\,|n=0\rangle$ and transferred by a $\pi/2$-pulse on the carrier transition (R1,CC laser beams) to the spin superposition state $|\uparrow\rangle\,|n=0\rangle + |\downarrow\rangle\,|n=0\rangle$, normalization factors are omitted. A π-pulse on the red motional sideband produces the desired Fock state superposition $|\downarrow\rangle\,(|n=0\rangle + |n=1\rangle)$. The state evolves freely during a given wait time and then, the sequence is carried out in reversed order with a π-pulse on the red sideband, followed by a $\pi/2$-pulse on the carrier transition. The phase of the final $\pi/2$-pulse is scanned to produce a sinusoidal signal, which determines the Ramsey contrast and thus the motional coherence between the states ($|n=0\rangle$ and $|n=1\rangle$). A reduced measurement scheme allows us to obtain the contrast, by only measuring the phases 0 and $\pi/2$ which corresponds to the operators σ_x and σ_y on the Hilbert space, spanned by $|n=0\rangle$ and $|n=1\rangle$. The Ramsey contrast is then given by $2\cdot\sqrt{(\sigma_x^P-\frac{1}{2})^2+(\sigma_y^P-\frac{1}{2})^2}$, where σ_i^P is the measured probability for the σ_i operator. Measurement errors are calculated via Gaussian error propagation from this formula, where errors $\Delta\sigma_x^P$ correspond to the standard error from binomial readout statistics. The measurement results for all three motional modes are shown in figure 6.7. For uncorrelated Gaussian phase noise, the contrast exhibits an exponential decay [Tur00]. When correlated noise is introduced and

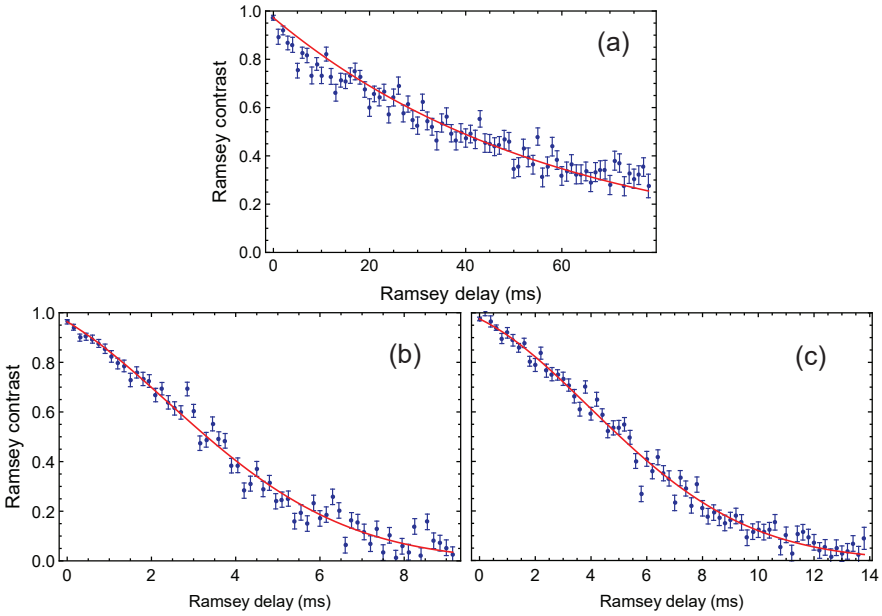

Figure 6.7.: Measurement of the motional coherence of the axial mode ω_x (a), the lower radial mode ω_y (b) and the higher radial mode ω_z (c). The experiment is triggered to the AC line for the measurements, data without triggering is shown in appendix A. The red line corresponds to a weighted least square fit of the form $f(t) = A\,\exp(-\gamma t - \gamma_2^2 t^2)$, the obtained parameters and coherence times are summarized in table 6.2. Each data point corresponds to more than 2×600 measurements.

the noise is not pure Gaussian noise, the decay function becomes more complex [Cyw08]. To account for correlated phase noise, the fit function is not a pure exponential decay but is of the type $e^{-\gamma t - \gamma_2^2 t^2}$. The coherence time $\tau_{1/e}$ is determined from the crossing of the weighted least square fit with the $1/e$ threshold and the uncertainty is determined from the crossing of the 68% confidence bands of the fit function with that threshold. The axial vibrational mode ω_x features a long coherence time of around 60 ms, which corresponds to about 60% of the theoretical limit given by the heating rate. Carrying out the sequence without triggering to the AC line yields a comparable coherence time, which leads to the conclusion that the axial mode is only marginally affected by 50 Hz noise. We conclude, that the DC voltage supply is stable and features low noise.
In contrast, the radial modes ω_y and ω_z are affected by 50 Hz noise, since the coherence time is increased by a factor of 20, when the experiment is triggered to the AC line. With triggering, the coherence time of the ω_y-mode is extended to 4.4 ms and the ω_z-mode to 6.5 ms. These values correspond to about 15% respectively 5% of the heating-rate-

induced limit.
The decay curves are more similar to a Gaussian decay which is an indicator for correlations in the noise present in the system, rather than pure Gaussian uncorrelated phase noise. Furthermore, the ratio between the Gaussian and exponential fit parameters γ_2/γ is 0 for the axial modes and around 2 for the radial modes. Thus, the pronounced motional decoherence on the radial modes seems to be caused by correlated noise.

mode	ω_x	ω_x	ω_y	ω_y	ω_z	ω_z
$\omega/2\pi$ (MHz)	1.487	1.487	3.592	3.592	4.473	4.473
AC trigger	-	enabled	-	enabled	-	enabled
$\tau_{1/e}^{meas}$ (ms)	58.7(9)	58(1)	0.248(4)	4.39(6)	0.323(7)	6.47(7)
$\tau_{1/e}^{theo}$ (ms)	102	102	30	30	121	121
$\gamma/10^3$ (Hz)	0.017(1)	0.017(1)	1.5(2)	0.10(1)	1.0(2)	0.054(5)
$\gamma_2/10^3$ (Hz)	0	0	3.2(1)	0.168(7)	2.5(1)	0.124(4)
γ_2/γ	0	0	2.1	1.7	2.5	2.3

Table 6.2.: Coherence times $\tau_{1/e}^{meas}$ obtained from a fit to the experimental data. A theoretically obtainable coherence time $\tau_{1/e}^{theo}$ is determined from the inverse heating rate measured on that day. Fit parameters γ and γ_2 belong to the nonlinear fit for the Ramsey contrast $f(t) = A\ \exp(-\gamma t - \gamma_2^2 t^2)$.

Radial trap frequencies in our ion trap are less sensitive to relative RF voltage amplitude fluctuations, than axial trap frequencies are sensitive to relative DC voltage amplitude fluctuations. The RF amplitude is actively stabilized during the measurements. However, generating a stable RF voltage with an amplifier and a helical resonator is challenging. Stability on short timescales should be improved in the future, whereas the long-term stability of the RF potential is excellent, as measured in section 6.2. The achieved coherence time for the radial gate mode ω_z is sufficient to perform a high fidelity quantum gate on this mode, as demonstrated in section 8.4. However, a longer coherence time will allow for higher gate fidelities, as calculated in appendix B.3.

6.4. Magnetic field gradient

For scalable quantum logic operations in our architecture, the ions are moved along the trap axis. During these operations the qubits are often in spin superposition states

of the type $|\uparrow\rangle + e^{i\phi}|\downarrow\rangle$ – precise knowledge and control of the phase ϕ is crucial for a high quality of concatenated quantum operations. Due to space limitations from the magnetic shielding enclosure, the permanent magnet coils, which generate the magnetic field, are not set up in a Helmholtz configuration. Thus, the absolute B-field is not homogeneous along the trap axis. Qubits in a superposition state traveling through this magnetic field will accumulate a phase, which needs to be characterized and corrected in the experimental sequence. To measure the magnetic field along the trap axis, a Ramsey experiment is carried out [Bla09]. A single ion is initialized in the laser interaction zone (LIZ: electrode 20) by a $\pi/2$ pulse on the R1-CC carrier transition to a spin superposition state and then moved along the trap axis to position x. A variable hold time leads to a phase accumulation, which is proportional to the difference of the Zeeman splitting in the LIZ and the local Zeeman splitting at the axial location x. Subsequent shuttling to the LIZ followed by a $\pi/2$ with phase 0° for the σ_x operator or 90° for the σ_y operator allows the determination of the accumulated phase. Details on this method and applications for

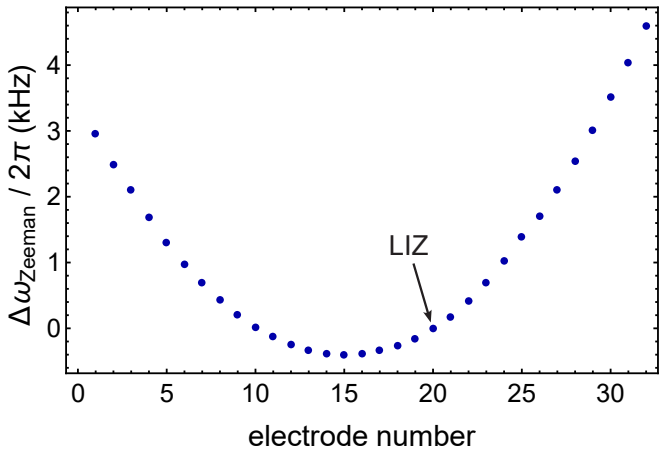

Figure 6.8.: Measurement of the difference in Zeeman splitting $\Delta\omega_{Zeeman}$ with respect to the LIZ along the 32 DC trap electrodes. The magnetic field inhomogeneity is caused by magnetic coils, which are not set up in a Helmholtz configuration. Error bars are too small to be indicated in this image. Scalable quantum logic experiments presented in this thesis are conducted by shuttling ions between electrodes 11 and 29.

precision magnetometry measurements, which are conducted in our setup, are published in [Rus17]. The results for the measured magnetic field along the trap axis are shown in figure 6.8. Frequency deviations of several kilohertz are observed within the relevant position range for the quantum information experiments. Thus, even short storage times in the quantum logic sections lead to a considerable phase accumulation, which needs to

be corrected, to maintain the quality of the concatenated quantum logic operations. A detailed explanation on how this is applied in practice is provided in section 8.5.

6.5. Optical performance

Driving high fidelity single-qubit rotations requires a stable optical Raman laser beam setup. Specifically, laser beam intensity, beam pointing, beam polarization and the relative optical phase between individual beams need to be precisely controlled. The optical components are installed in a compact configuration in an enclosure – see section 4.2 – and the laser beams are sent via optical single mode fibers to the vacuum chamber, which improves beam pointing stability with respect to a free space configuration. To drive single-qubit rotations between the states $|\uparrow\rangle$ and $|\downarrow\rangle$ the co-propagating laser beams R1 and CC are employed, which do not couple to the ion motion and thus do not require ground state cooling. The results for driving many of these transitions are shown in figure 6.9.

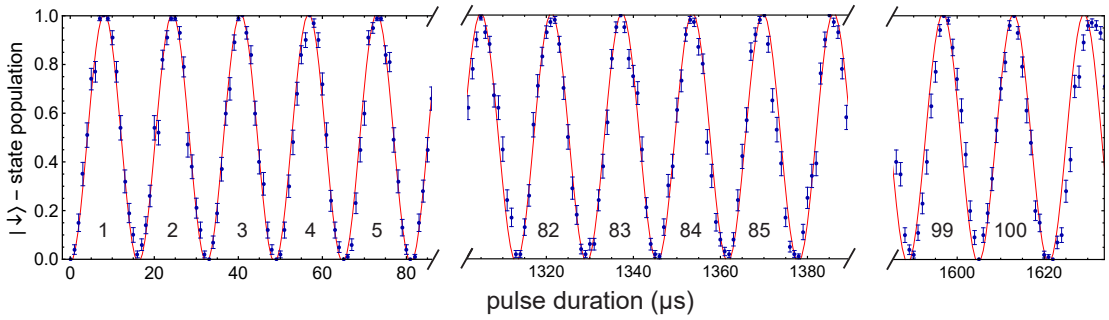

Figure 6.9.: Single-qubit rotations driven by the co-propagating Raman laser beams R1 and CC. Integer numbers indicate full 2π rotations from 1 to 100. Each data point is the mean of 100 single measurements, error bars correspond to the standard error from binomial readout statistics. A weighted least square fit of the type $\frac{A}{2} \cdot \cos(\omega t - \pi) + c$ is applied and yields the fit parameters amplitude $A = 1.0$, center $c = 0.5$ and Rabi frequency $\omega = 387.598(7)$ kHz which corresponds to a time of 8.1 µs for a single π-rotation. The Raman detuning for the measurement is $\Delta = 2\pi \times 3$ THz and the optical power of each laser beam is around 6 mW. Both beams are guided to the experiment through the same optical fiber and are focused to a FWHM diameter of about 30 µm on the ion.

Due to the active laser intensity stabilization via an EOM, up to around 200 full π rotations at a pulse time of 1.6 ms can be driven without loss of contrast with the optical

setup. For longer pulse times, the contrast is maintained but deviations in the Rabi frequency emerge, which correspond to intensity fluctuations of the laser light. The measurement takes around one hour. Therefore, random fluctuations on the minute time scale cannot be excluded. For long pulse times, we suspect thermal drifts from continuous AOM operation to be responsible. Nevertheless, the quality of the optical system is considered to be excellent and sufficient for our experiments.
The entangling gate sequence is a concatenation of single-qubit rotations and two-qubit displacement pulses, see section 8.4. Single-qubit rotations are driven simultaneously on two ions in the laser interaction zone. Thus, a high quality of these operations is crucial to the entangling gate fidelity. As the typical distance of two ions is only around 4 µm and the laser beam waist is about ten times larger, the ions are equally illuminated if the laser beam is aligned on the center of the two-ion crystal. The results of this simultaneous driving are shown in figure 6.10.

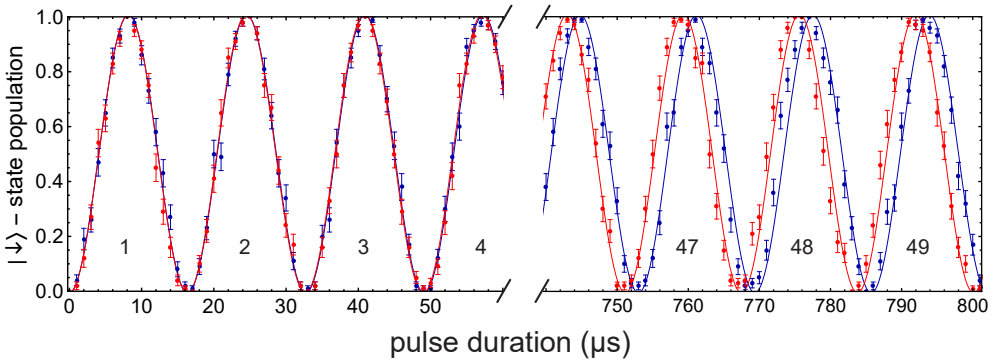

Figure 6.10.: Simultaneous single-qubit rotations on two ions driven by the co-propagating Raman laser beams R1 and CC. Red data points belong to the first ion and blue data points belong to the second ion. Integer numbers indicate full 2π rotations from 1 to 49. The measurement and fit procedure is identical to the single ion measurement – the data for each ion is analyzed individually. The amplitude and center parameters are identical for each ion but the Rabi frequency of the second ion is larger. For the first ion a Rabi frequency of $\omega_1 = 383.83(2)$ kHz is determined from the fit and for the second ion $\omega_2 = 384.78(2)$ kHz respectively.

For long pulse times a slightly asymmetric illumination of the two ions is observed. The second ion features a Rabi frequency which is 0.24% higher compared to the Rabi frequency of the first ion. In practice, the pulse time τ_π for a single π rotation is calibrated. The difference in the Rabi frequency directly translates to a difference in τ_π for the two ions. If the pulse time is considered to be set perfectly for ion one and 0.24%

off for ion two, the single π-rotation on ion two will still achieve a population transfer that corresponds to 99.9985% of the population transfer that is driven on ion one due to the robustness of the sinusoidal shape. Thus, we conclude that single π-rotations can be performed with a negligible asymmetry of only $1.5 \cdot 10^{-5}$ simultaneously on two ions in our setup. It needs to be emphasized that this value does not correspond to the absolute quality of the single-qubit operation but only to the symmetry of the operation. The absolute population transfer quality of single-qubit gates is investigated via randomized benchmarking on a single ion in section 8.2.

7

Fast Ion Crystal Rotation

We demonstrate a SWAP gate between laser-cooled ions in a segmented microtrap via fast physical swapping of the ion positions. This operation is used in conjunction with qubit initialization, manipulation and readout, and with other types of shuttling operations such as linear transport and crystal separation and merging. Combining these operations, we perform quantum process tomography of the SWAP gate. The swap operation is demonstrated with motional excitations below 0.05(1) quanta for all six collective modes of a two-ion crystal, for a process duration of 42 μs. Extending these techniques to three ions, we reverse the order of a three-ion crystal and reconstruct the truth table for this operation.
The results, which are presented in this chapter, are published in [Kau17a].

For universal quantum computation, two-qubit gates need to be performed between arbitrary pairs of ions, such that reordering ion strings becomes necessary. Furthermore, if multiple ion species [Hom13] are employed for sympathetic cooling [Kie00] or ancilla-based syndrome readout via inter-species gates [Bal15; Tan15], deterministic ion reconfiguration is ultimately required.
To that end, ion traps bearing junctions with T [Hen06], X [Bla09; Wri13] or Y [Shu14] geometry have been developed and tested. Junctions increase the trap design complexity and allow only for sequential ion transport. Shuttling through junctions may yield large motional excitations, precluding the execution of two-qubit gates. Within this thesis, we demonstrate deterministic ion reordering via on-site swapping of ions through application of suitable electric potentials. The advantages of this operation are that it does not require sophisticated electrode structures, and that parallel multi-site swap operations may be performed. In contrast to reordering via laser-driven SWAP gates, physical ion swapping does not require laser beams and can therefore be performed at any trap site. Furthermore, the physical SWAP operation does not affect the internal

(qubit) states, such that virtually perfect operation fidelities are readily obtained. While it was shown [Spl09] that segmented traps allow for ion swapping, we demonstrate this process on fast timescales, comparable to qubit operation times. Motional excitation is avoided, such that the ions stay within the Lamb-Dicke regime for all collective modes of vibration of a two-ion crystal. To highlight that this operation is deterministic and that it can be used in conjunction with other qubit operations, we integrate it within a sequence of shuttling, separation [Bow12; Rus14; Kau14] and merging operations and qubit manipulations to realize quantum process tomography of the SWAP gate. By performing the swap operation on ground-state cooled ions and combining it with qubit manipulations, we demonstrate its potential use for scalable quantum logic.

7.1. Fast SWAP operation

The on-site swapping process of a two-ion crystal is depicted in figure 7.1. We start with the crystal axially confined by applying a voltage U_c to the trapping electrodes (blue segments in figure 7.1). Control over the ion crystal rotation is achieved via a diagonal, symmetry-breaking dc quadrupole potential, generated by ramping up a voltage $+(-)U_d$ to the electrodes neighboring the trap site, shown in green (red) in figure 7.1. The polarity on the electrode pair left of the trapping site is inverted as compared to the electrode pair to the right. With the diagonal potential applied, the trapping voltage U_c is decreased, and a positive offset voltage U_o is ramped up at all neighboring segments. The corresponding increase of the axial confinement drives the ion crystal through a structural transition from horizontal to vertical alignment. Simultaneously, the diagonal potential generated by U_d is ramped down to 0 V. With the ions vertically aligned, the process is conducted in reverse order, with inverted polarity of the diagonal voltage U_d. We optimize the voltage ramps by probing the final motional excitation on the vibrational modes which are most affected, i.e. the axial *stretch* and the lower frequency radial *rocking* mode. The motional excitation is measured by driving Rabi oscillations on the red and blue motional sidebands pertaining to the respective modes of vibration, see appendix B.1. Each mode is cooled close to the ground state via sideband cooling before the swapping operation, reaching mean phonon numbers between 0.016(4) (axial stretch mode) and 0.37(1) (lower frequency radial COM mode). Rabi oscillations are recorded over pulse areas of up to 8π pertaining to the blue sideband ground-state Rabi frequency. Fits assuming oscillatory excitation, i.e. a coherent state of the corresponding mode,

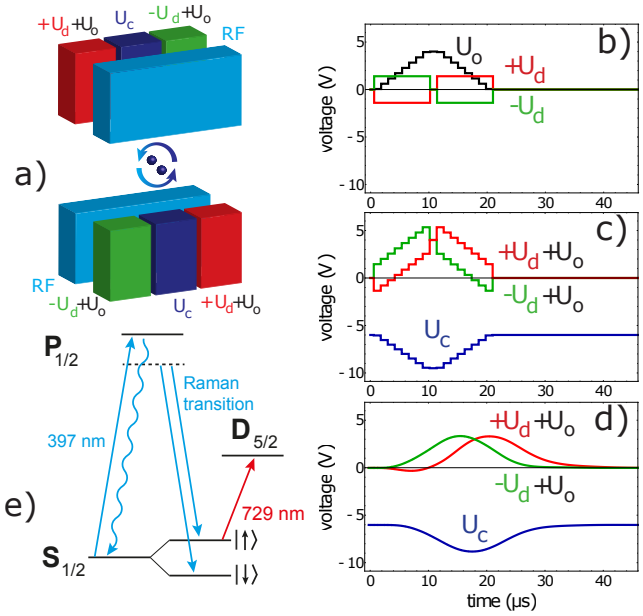

Figure 7.1.: Ion swapping in a segmented trap. **a)** shows the relevant trap electrodes, indicating how the trapping voltage U_c, diagonal voltage U_d and offset voltage U_o controlling the process are applied. Panels **b)** and **c)** show the voltage ramps in the form of discrete samples, as they are programmed to the arbitrary waveform generator. Here, b) shows U_d and U_o, while c) shows the actual electrode voltages. Panel **d)** shows the voltage ramps, measured after the low-pass filter, which leads to smoothing and delay of the ramps. **e)** shows the relevant part of the level scheme of $^{40}Ca^{+}$.

reveal the mean phonon number [Lei03b; Wal12; Rus14].

Initially, a trapping voltage U_c =-6 V yields horizontal crystal alignment at an axial center-of-mass (COM) vibrational frequency of $2\pi\times$ 1.488 MHz. The radial COM frequencies are $2\pi\times$ 1.927 MHz and $2\pi\times$ 3.248 MHz. We define the dimensionless time $\tau = t/T$ for the total swapping time T. The least motional excitation is found for the following ramp parameters: The diagonal voltage U_d is ramped up rapidly within τ =0.05, to an optimum value of 1.4 V. For driving the ion crystal into vertical alignment, the axial COM frequency has to exceed the lower radial COM frequency. To that end, U_c is ramped down to -9.5 V, while at the same time an additional offset voltage $U_o = +4$ V is ramped up at all neighboring electrodes. Both U_c and U_o are ramped within τ =0.05 to τ =0.45. The polarity change of the diagonal voltage U_d happens during τ =0.45 to τ =0.55. The resulting voltage ramps are depicted in figure 7.1.

The swapping operation was tested for increasing times T, until we found the shortest time with negligible motional excitation of T =22 μs, which – including the 50 kHz

low-pass filters – corresponds to an actual duration of 42 μs. We measure the mean phonon number increase for all modes, and compare to reference measurements directly after sideband cooling, see table 7.1.

motional mode	**$\omega/2\pi$ (MHz)**	**η**	**$\bar{n}$**	**$\bar{n}$ increase**
axial ω_x c.o.m.	1.488	0.127	0.082(6)	-
axial ω_x c.o.m. with SWAP		0.129	0.131(7)	0.049(9)
axial ω_x stretch	2.578	0.100	0.016(4)	-
axial ω_x stretch with SWAP		0.099	0.029(5)	0.013(6)
radial ω_y c.o.m.	1.927	0.069	0.365(13)	-
radial ω_y c.o.m. with SWAP		0.070	0.394(13)	0.029(18)
radial ω_y rocking	1.195	0.090	0.14(10)	-
radial ω_y rocking with SWAP		0.090	0.18(11)	0.041(15)
radial ω_z c.o.m.	3.248	0.066	0.099(9)	-
radial ω_z c.o.m. with SWAP		0.066	0.115(10)	0.015(14)
radial ω_z rocking	2.875	0.072	0.069(8)	-
radial ω_z rocking with SWAP		0.072	0.081(7)	0.012(10)

Table 7.1.: Measured phonon numbers on the six collective motional modes of a two ion crystal with and without the swapping operation. The column **$\bar{n}$ increase** is the difference between a measurement with and without swapping and corresponds to the motional excitation from the swapping. The Rabi oscillation data corresponding to these measurements is shown in appendix A.

For the axial modes, we find mean phonon number increases of 0.05(1) on the COM mode and 0.013(6) on the stretch mode. For the lower-frequency radial modes, corresponding to the plane in which the crystal rotates, we obtain 0.03(2) on the COM mode and 0.04(2) on the rocking mode. The higher-frequency radial mode, which is least affected from from the swapping, features 0.02(1) on the COM and 0.01(1) on the rocking mode. Rabi oscillation data probed after swapping is shown in figure 7.2.

Linear transport of ions along the trap axis is performed by gradually reducing the negative dc trapping voltage of U_c = -6 V at the initial segment to 0 V, while applying

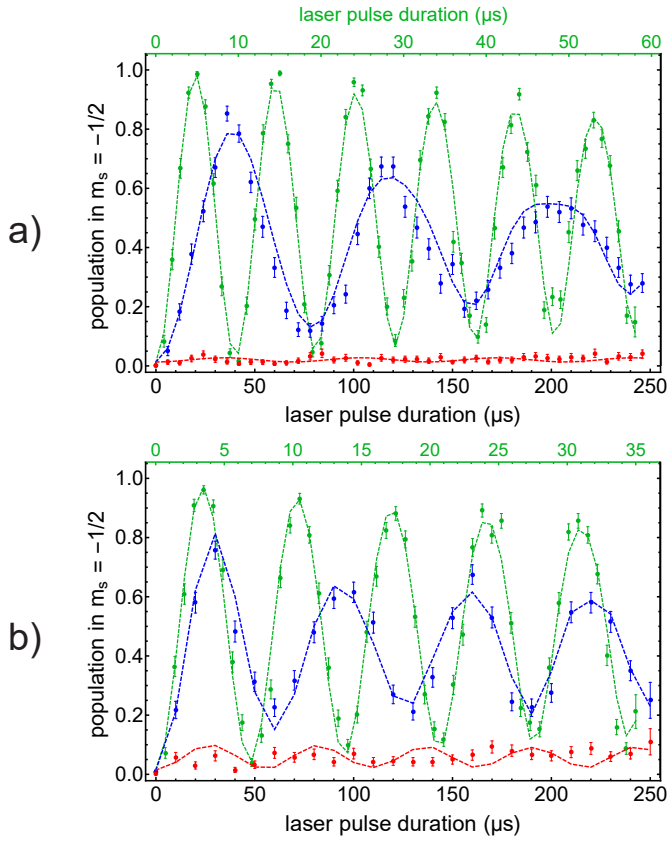

Figure 7.2.: Rabi oscillation data probed after swapping for verification of low excitation: **a)** shows data for the axial stretch mode, while **b)** shows data for the lower-frequency radial rocking mode. In both panels, the blue (red) points correspond to the blue (red) motional sideband, while the green points correspond to the carrier transition. The dashed lines are fits using a model assuming oscillatory excitation. All curves indicate the probability for having at least one of the ions' state flipped to $|\downarrow\rangle$. Note that the time axis for the carrier data is scaled differently (upper axis ticks). Each data point corresponds to 200 state interrogations, error bars correspond to the standard error from binomial readout statistics.

a trapping voltage at the neighboring destination segment. We perform adiabatic transport at a duration of 28 μs per trap segment pair, spaced by 200 μm. Transport over more than one segment pair is performed by concatenation of these operations. Separation and merging operations require switching between single- and double-well potentials, where the transient low axial confinement causes excitation [Kau14]. We employ tailored voltage waveforms and accurate cancellation of residual forces along the

trap axis, enabling separation/merging of two-ion crystals within 100 μs at excitations of 5(2) phonons per ion [Rus14].

7.2. Process tomography of a two-ion SWAP operation

The sequence for process tomography is depicted in figure 7.3. First, the two-ion crystal is prepared by Doppler cooling and pumping in the laser interaction zone (LIZ: electrode 20).

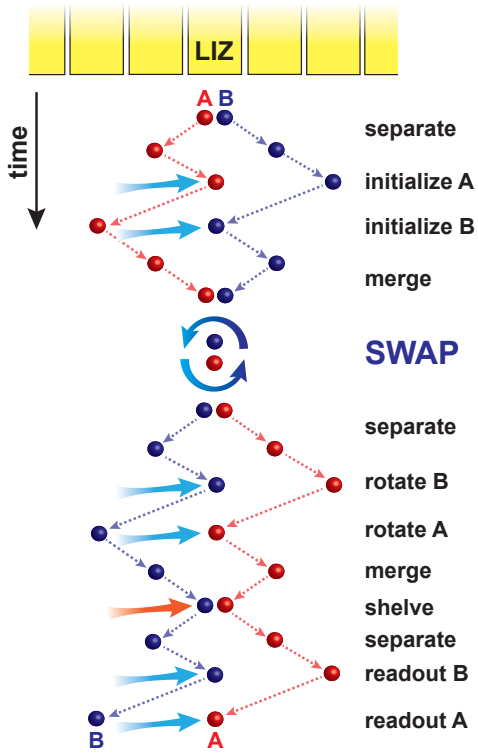

Figure 7.3.: Experimental quantum process tomography sequence for characterizing the SWAP operation. Each of the qubits A and B is shuttled to the laser interaction zone for initialization laser pulses, followed by a fast SWAP operation and subsequent individual qubit rotations. The SWAP operation is realized in 42 μs. Finally, the state is read out via electron shelving and fluorescence detection.

After separation, each qubit is individually shuttled into the LIZ, where one of the qubit rotation operations $\{\mathbb{1}, R_X(\pi/2), R_Y(\pi/2), R_X(\pi)\}$ is applied to bring the respective

qubit to the state $\{|\uparrow\rangle, |\uparrow\rangle - i|\downarrow\rangle, |\uparrow\rangle - |\downarrow\rangle, |\downarrow\rangle\}$. The ions are merged in the LIZ, where the swapping takes place. The crystal is again separated, and the ions are individually exposed to the analysis pulses $\{\mathbb{1}, R_X(\pi/2), R_Y(\pi/2)\}$ for measuring the operators $\{\sigma_z, \sigma_y, \sigma_x\}$. After another merging operation in the LIZ, the population transfer $|\uparrow\rangle \leftrightarrow |D_{5/2}\rangle$ takes place. The ions are again separated and individually shuttled to the LIZ, where state-dependent fluorescence is observed. Both qubits are shelved *before* fluorescence detection, to avoid depolarization of a remotely stored qubit from scattered light near 397 nm during the readout of the other qubit.
The analysis laser pulses have to be corrected for phases arising from axial ion movement in the inhomogeneous magnetic field. Qubit i located at axial position $x_i(t)$ at time t accumulates a phase which is determined by the deviation of the magnetic field from its value at the LIZ, $\Delta B(x)$:

$$\phi_i = \frac{\mu_B g_J}{\hbar} \int_{t_i^{(i)}}^{t_i^{(a)}} \Delta B(x_i(t))dt. \tag{7.1}$$

Here, $t_i^{(i)}$ denotes the instant of the state preparation for qubit i and $t_i^{(a)}$ denotes the instant of its analysis pulse. The magnetic field inhomogeneity along the trap axis is mapped out by using a single ion as a probe: Initialized in a superposition state, it is shuttled to the destination site x and kept on hold for a variable time t. After shuttling back to the LIZ, a refocusing π-pulse is applied, followed by another wait time of duration t with the ion placed at the LIZ. Finally, state tomography reveals the accumulated phase $\phi(x,t) = \frac{\mu_B g_J}{\hbar}\Delta B(x) \cdot t + \phi_0$, where ϕ_0 is a constant phase accumulated during the shuttling. By performing such measurements for different phase accumulation times t at different locations x, we map out the qubit frequency shift across segments 18-22 with a mean accuracy of about $2\pi\times1$ Hz. With the positions $x_i(t)$ computed from the sequence data and simulated electrostatic trap potentials [Sin10], the phases ϕ_i can be also computed and used for correcting the phases of the analysis pulses. For each of the 16 prepared states, 9 measurements are performed, each independently repeated 1000 times. A density matrix is obtained via linear inversion for each input state. From these density matrices, the process χ-matrix is reconstructed via a second linear inversion. Computing the trace norm $Tr\left(\chi^{\dagger}_{meas}\chi_{ideal}\right)$, we find a mean process fidelity of 98.1(5)%. Performing process tomography without SWAP operation, we obtain a mean process fidelity of 98.7(4)%. Thus, on the given level of accuracy, we conclude that the SWAP operation does not significantly affect the measured process fidelity, which is limited mainly by readout errors and systematic errors of the correction

phases. Readout errors have been independently measured using a sequence without the SWAP operation, for details see appendix B.2. The errors are dominated by the limited lifetime of the metastable $D_{5/2}$ state, imperfect electron shelving and state initialization. Applying correction for readout errors to the SWAP data, we obtain a mean process fidelity of 99.5(5)%. The resulting χ-matrix is displayed in figure 7.4 and the numerical data is shown in appendix A.

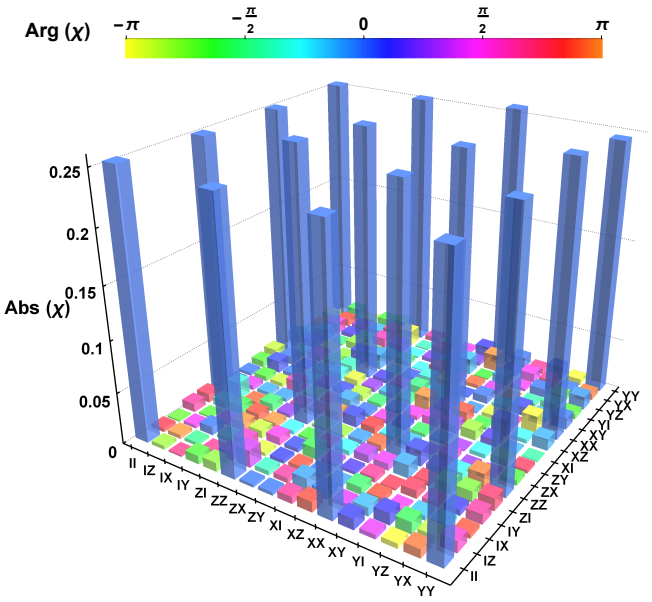

Figure 7.4.: Reconstructed process χ-matrix for the SWAP operation. The absolute value of each matrix element is represented by the bar height, the phase is indicated by the color. The 16 elements which match the ideal absolute value of 0.25 have a controlled phase of $\arg(\chi_{ij}) \approx 0$. All other elements are close to the ideal value of zero and have random phases. Each of the 144 preparation/measurement settings is probed on average 1260 times.

7.3. Reordering of a three-ion crystal

The techniques described above are extended to three qubits, where we demonstrate reordering from configuration ABC to configuration CBA. The experimental sequence is sketched in figure 7.5, the full detailed sequence can be found in appendix C.1.

Rather than performing quantum process tomography, we restrict the measurements to the logical (Z) basis, thus we reconstruct the truth table of the reordering operation.

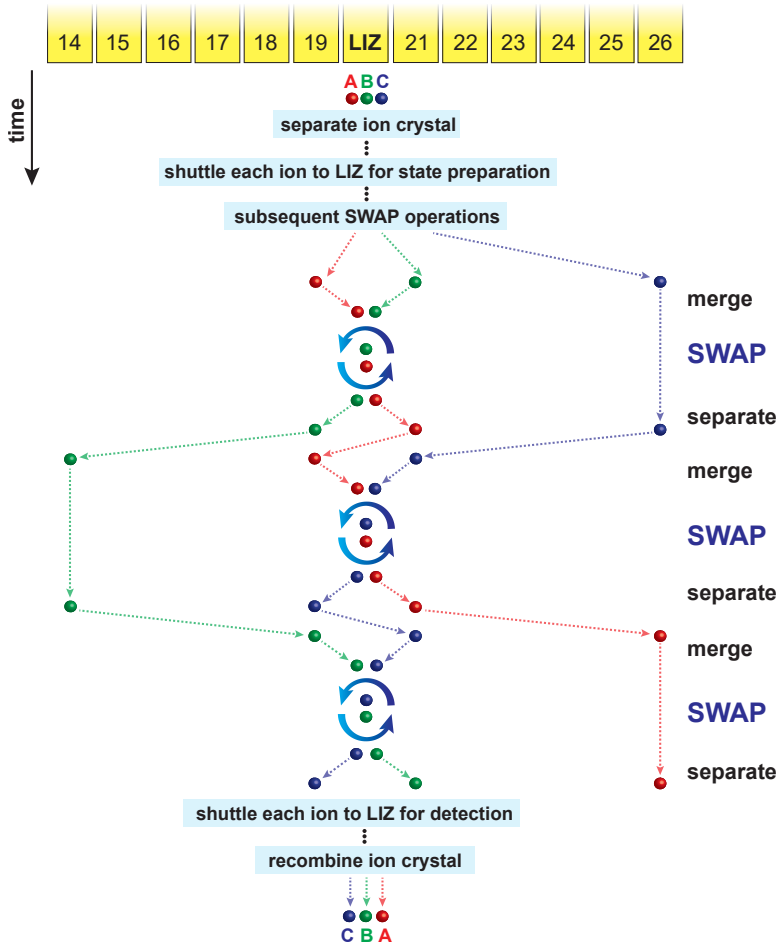

Figure 7.5.: Experimental sequence for the reordering of a three-ion crystal from configuration ABC to configuration CBA by employing three consecutive SWAP operations. The separation, merging, state preparation and state detection operations at the beginning and the end of the sequence are omitted in this sketch, see full text for details.

Starting from a three-ion crystal ABC in the LIZ, we separate into AB and C by performing the separation with a properly adjusted axial bias field [Bow12]. Ion C is moved to segment 26, then ions AB are moved back into the LIZ, where separation into A and B takes place. Then, A, B and C are subsequently moved into the LIZ and initialized to either $|\uparrow\rangle$ or $|\downarrow\rangle$. Now, the ions are merged pairwise at the LIZ, where swapping and subsequent separation take place. The respective third ion is stored six segments away to the left or right, such that its trapping potential does not affect the separation/merging and swapping operations. The three subsequent swaps

$AB \rightarrow BA$, $AC \rightarrow CA$ and $BC \rightarrow CB$ establish the desired order CBA. Then, the ions are individually moved to the LIZ for shelving, and then individually moved to the LIZ for fluorescence readout. We measure the final spin configuration for 8 different input states. The resulting truth table is shown in figure 7.6 and the numerical data is shown in appendix A. We obtain a mean fidelity of 98.47(9)% in the logical basis. The mean fidelity with readout error correction is 99.96(13)%. The sequence consists of three separation, three merging, three swapping and 30 linear transport operations. The execution time of this process is 5.7 ms, where 93% of which is devoted to shuttling operations.

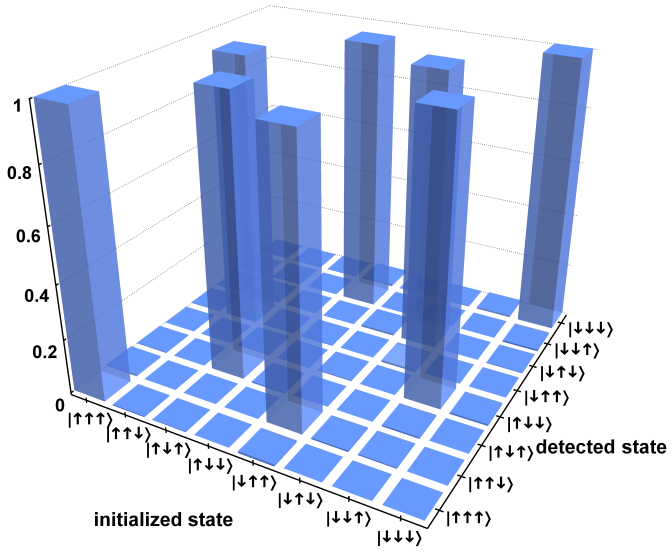

Figure 7.6.: Measured truth table for three-ion reconfiguration from ABC to CBA, using three consecutive two-ion SWAP operations. Each ion was prepared in either $|\uparrow\rangle$ or $|\downarrow\rangle$. Each input state is probed on average 2500 times. The measured probability to detect a particular state is represented by the height of the bars.

8

Scalable Entanglement Generation

Our approach for a scalable quantum computer is based on ion shuttling operations in conjunction with quantum logic gates [Kie02] – we have demonstrated the required fast ion shuttling operations in micro-structured ion traps [Wal12; Rus14; Kau17a]. High fidelity entangling gates can only be performed with low motional excitation of the gate bus mode, thus it is necessary to execute fast ion shuttling operations with low motional excitation. We use radial secular modes, which are less excited than axial modes from shuttling operations, as bus modes for the two-qubit entangling gate. In this chapter, it is demonstrated how fast ion shuttling operations are used in conjunction with concatenated single- and two-qubit gates, to operate a programmable four qubit quantum processor.

8.1. Cold shuttling operations

We desire to perform shuttling operations with low motional excitation in our quantum processor, which allow for subsequent high fidelity entangling gates. Fast transport operations have been realized with low axial motional excitation in a similar trap [Wal12; Bow12]. The separation operation requires careful calibration [Kau14] and has been realized in a similar ion trap [Rus14]. Since the entangling gate is performed on the radial ω_z mode, we focus on analyzing the motional excitation of the radial modes from the shuttling operations in this section. The trap frequencies are $\omega_{x,y,z}/2\pi = \{1.49, 4.08, 4.87\}$ MHz in the experiments, which are presented in this section.

8.1.1. Cold ion transports

To investigate the motional excitation from ion transports, a single ion is cooled close to the ground state with resolved sideband cooling in the LIZ. It is then shuttled to the adjacent segment 19 within 30 µs. After an idle time of 30 µs on the electrode, the ion is shuttled back to the LIZ and spends an additional 30 µs idle time in the LIZ. Idle times are employed to account for distortions of the DC waveforms, caused by the low-pass filters. The entire procedure is repeated 20 times, which results in a total amount of 40 transport operations and idle times of identical duration. Subsequently, the motional excitation is determined by probing the red and blue sideband and the carrier transition. A reference measurement – with a static single ion – is carried out to determine the mean ground state population, which is around $\bar{n} = 0.34(2)$ and $\bar{n} = 0.08(1)$ for the radial ω_y mode and ω_z mode respectively. The difference to this measurement yields the motional excitation from the transport operations. We find a motional excitation per transport of $\bar{n} = 0.028(2)$ and $\bar{n} = 0.025(1)$ for the radial ω_y mode and ω_z mode respectively. A second reference measurement is carried out, where the ion spends half the duration of the entire sequence in the LIZ, and the other half on segment 19. From this measurement, it is found that the motional excitation is solely caused by motional heating and no coherent excitation is observed. The anomalous heating during this measurement day was at least by a factor of ten higher than in the results reported in section 6.1. This is attributed to technical noise from changed electrical connections at the apparatus. Thus, we estimate to reach significantly lower motional excitation per transport, when the heating rates are reduced to the former values.

8.1.2. Cold ion crystal separation

We investigate the motional excitation from the separation operation of a two-ion crystal, which is one of the fundamental shuttling operations in our quantum processor. To investigate the motional excitation from the separation and recombination operation, initially two ions are cooled in the LIZ close to the ground state of all four common radial motional modes. Subsequently, the two-ion crystal is separated within 80 µs or 160 µs and the individual ions are kept on the electrodes 19 and 21 for an idle time of 50 µs. The ions are then recombined in the LIZ and a second identical idle time is applied before the motional state is read out for all four radial motional modes. A reference measurement,

which is carried out without the shuttling operations and idle times, allows to determine the initial motional excitation. The difference to this measurement corresponds to the excitation from the separation and recombination operation. The excitation from both operations is assumed to be identical, since the ion movement is identical but in reversed order. Thus, we divide the total excitation by two and derive the motional excitation per separation or recombination operation – the results are listed in table 8.1.

secular mode	separation duration (µs)	motional excitation ($\bar{n}$)	estimated heating ($\bar{n}$)
$\omega_y^{\text{c.o.m.}}$	80	0.00(1)	0.06
$\omega_y^{\text{rocking}}$	80	0.12(1)	-
$\omega_z^{\text{c.o.m.}}$	80	0.03(1)	0.05
$\omega_z^{\text{rocking}}$	80	0.03(1)	-
$\omega_y^{\text{c.o.m.}}$	160	0.06(1)	0.1
$\omega_y^{\text{rocking}}$	160	0.10(1)	-
$\omega_z^{\text{c.o.m.}}$	160	0.12(1)	0.09
$\omega_z^{\text{rocking}}$	160	0.02(1)	-

Table 8.1.: Measured motional excitation on the radial secular modes of a two-ion crystal, from a single separation operation and a subsequent 50 µs idle time. The estimation for the heating per separation duration is based on the results from the cold shuttling operations, see above. The secular mode frequencies are: $\omega_y^{\text{c.o.m.}} = 2\pi\times4.08\,\text{MHz}$, $\omega_y^{\text{rocking}} = 2\pi\times3.77\,\text{MHz}$, $\omega_z^{\text{c.o.m.}} = 2\pi\times4.87\,\text{MHz}$, $\omega_z^{\text{rocking}} = 2\pi\times4.61\,\text{MHz}$.

We find, that for the radial c.o.m. modes the excitation is dominated by motional heating. The excitation of around $\bar{n} = 0.1$ for the ω_y rocking mode is probably a coherent excitation, since motional heating of the rocking modes is assumed to be negligible. However, for a conclusive understanding of the motional excitation from the separation operation, more advanced measurement and analysis schemes need to be developed in future experiments.

In conclusion, we have demonstrated transport and separation operations, which add small motional excitation to the radial vibrational modes. These shuttling operations allow for concatenated entangling gate operations on the radial modes in our trapped-ion quantum processor.

8.2. Single-qubit gates

High fidelity single-qubit gates are a requirement for large scale fault tolerant quantum computing. An error per gate below 10^{-4} is desirable [Lad10; Kni10]. To characterize the performance of single qubit gates in our quantum processor a randomized benchmarking technique is employed [Bro11]. Initially, a single ion is cooled with Doppler cooling and initialized to the state $|\uparrow\rangle$ via optical pumping. A sequence of single-qubit gates is then performed on the ion with the co-propagating Raman laser beams R1 and CC. Specifically, the sequence is comprised of a randomized concatenation of N_g computational gates. Each computational gate is constituted of a Pauli gate, which corresponds to a π-pulse, and a Clifford gate, which corresponds to a $\pi/2$-pulse. A Pauli gate is described by the operator $e^{-i\pi\sigma_p/2}$ where the matrix σ_p is randomly chosen from $\{\pm\sigma_x, \pm\sigma_y, \pm\sigma_z, \pm I\}$. Clifford gates are described by $e^{-i\pi\sigma_c/4}$ with a randomly chosen $\sigma_c \in \{\pm\sigma_x, \pm\sigma_y\}$. Pauli gates are implemented by carefully calibrated laser pulses with a duration of 15.64 µs and Clifford gates with individually calibrated pulses of duration 7.84 µs. In order to calibrate the pulse duration of a π-pulse precisely, around 20 concatenated π-pulses with variable duration are applied on the ion. The duration of a single π-pulse is then determined by dividing the total pulse time on the 20th maximum or minimum of the Rabi oscillations by 20. The identity operator $\pm I$ for the Pauli gate is implemented by applying no laser pulse – the same holds for the $\pm\sigma_z$ operator, which is implemented by shifting the qubit phase by imprinting a phase on subsequent gates. Thus, each computational gate contains on average a pulse area of two $\pi/2$-pulses. The randomized sequences are designed, so that at the end of every sequence the final qubit state is either $|\uparrow\rangle$ or $|\downarrow\rangle$, which guarantees a higher detection accuracy than superposition states. In the experiment, each sequence is repeated 500 times, the overlap of the detected ion state either $|\uparrow\rangle$ or $|\downarrow\rangle$ with the expected outcome of the sequence is denoted gate fidelity. Subsequently, a new entirely random sequence of equal length N_g is generated and executed 500 times. At least 40 different sequences are measured for each N_g, which amounts to more than 20000 single measurements per sequence length. Fluorescence detection is performed after electron shelving within 1.2 ms with a PMT – the detection time can readily be chosen in the 0.7 ms regime. However, for this experiment we aim for excellent readout. The results of this measurement are shown in figure 8.1.

The state preparation and measurement quality derived from this measurement yields an excellent value of 99.923(3)%. Our achieved fidelity of a single computational gate

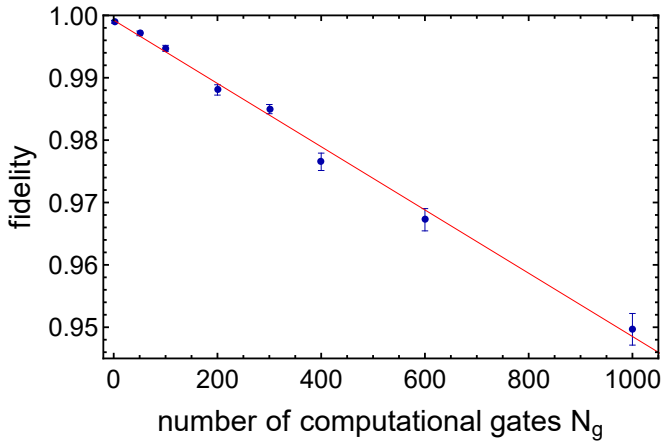

Figure 8.1.: Randomized benchmarking data for single-qubit gates – the mean fidelity is shown as a function of the number of computational gates N_g, performed on a single static ion. A weighted least squares fit gives a negative slope of $5.1(2) \cdot 10^{-5}$ which corresponds to the error per computational gate. The state preparation and measurement error is determined from the y-axis intercept to be as low as $7.7(3) \cdot 10^{-4}$. Error bars correspond to the standard error of the mean fidelity for each number of computational gates. Each data point corresponds to more than 20000 individual measurements.

of 99.9949(2)% is significantly above the threshold for fault-tolerant quantum computation and en par with state of the art laser driven gates performed by other research groups [Gae16; Bal16].

The total probability to scatter a photon during a Raman π-pulse transition following [Oze07] is given by:

$$P_{total} = \left(\frac{\gamma\pi}{\omega_f}\right)\frac{2\Delta^2 + (\Delta - \omega_f)}{\Delta(\Delta - \omega_f)} \tag{8.1}$$

where γ is the natural decay rate of the $P \leftrightarrow S$ transition of $2\pi\times23.05\,\mathrm{MHz}$ [Het15], ω_f is the fine structure splitting of $2\pi\times6.69\,\mathrm{THz}$ and Δ is the Raman detuning of $+2\pi\times3.1\,\mathrm{THz}$, which is used for this experiment – each laser beam is operated at a power of around 1 mW on the ion. The result is an error from photon scattering of $3.1 \cdot 10^{-5}$, which constitutes the largest fraction of the measured gate error. The remaining error is attributed to imperfect pulse time calibration – on the order of $1 \cdot 10^{-5}$ error per gate, see section 6.5 – as well as fluctuations of the stabilized laser intensity.

8.3. Four-qubit register operation

A scalable quantum computer needs to perform high fidelity operations on a large number of qubits. We thus extend the randomized benchmarking of single-qubit gates, which is presented in the previous section, to four ions. The experimental sequence is sketched in figure 8.2.

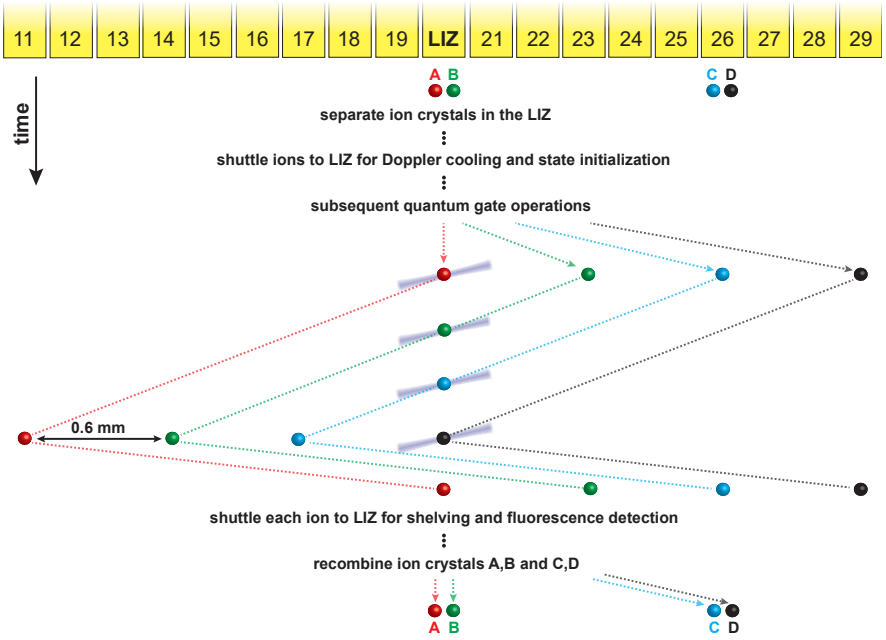

Figure 8.2.: Simultaneous randomized benchmarking procedure for single-qubit gates on four ions. The numbers from 11 to 29 indicate DC electrodes of the segmented ion trap, which features in total 32 DC electrodes. Each ion is moved to the laser interaction zone N_t-times where a number of N_g computational single-qubit gates is performed on the ion. The full experimental sequence is shown in appendix C.2.

Initially, two ion pairs A,B and C,D are trapped at electrode 20 (LIZ) and 26. A series of shuttling operations separates the pairs and transports each ion individually to the LIZ where Doppler cooling is applied to each ion. Afterwards each ion is again shuttled to the LIZ for state initialization to the state $|\uparrow\rangle$ by optical pumping at 729 nm – this step cannot be carried out immediately after Doppler cooling since the cooling light at 397 nm would depolarize the spins of the other ions. Once all four ion spins are initialized, each ion is shuttled to the LIZ repeatedly for single-qubit randomized

benchmarking laser pulses, which are carried out as in the previous section. The ions are moved in parallel, via concatenated segment-to-segment shuttling operations, where each transport is executed within 60 µs. For state detection, we apply state selective electron shelving, followed by fluorescence detection on each ion individually in the LIZ. Finally, the ions are merged into pairs and the entire sequence is repeated. The Raman laser parameters are the same as in section 8.2.
To characterize the performance of single-qubit gates in a four-ion register, we carry out an experiment for $N_t = 1$. The results are shown in figure 8.3.

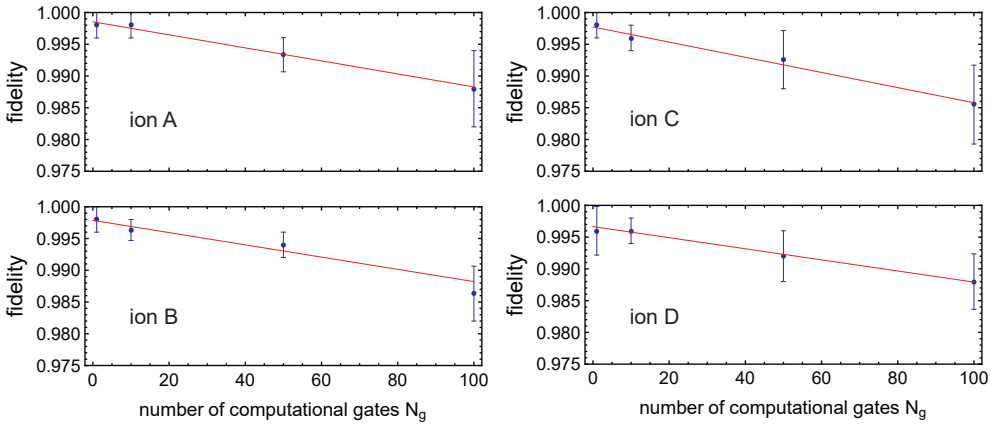

Figure 8.3.: Simultaneous four-ion randomized benchmarking of single-qubit gates for $N_t = 1$ (each ion is transported to the LIZ N_t-times) and a variable number of single-qubit gates N_g on each ion. A linear weighted least squares fit gives the error per computational gate for each ion and the state preparation and measurement error, see table 8.2. The fidelity is calculated from the median, which is more robust than the mean value with respect to outliers. Error bars correspond to the median absolute deviation. Each data point is comprised of more than 20000 single measurements, except for $N_g = 10$, where 12500 measurements are taken.

In contrast to the static single ion measurement, more outliers for larger N_g are observed. These are attributed to pulse area instabilities on the timescale of several minutes, which are more pronounced from the longer overall experiment duration due to the four-ion shuttling operations. In table 8.2 the errors per computational gate and the state preparation and measurement errors are listed.

The low error per computational gate is similar for each ion, we thus conclude that we can perform high fidelity single-qubit operations in the four qubit register without crosstalk between the qubits. Overall, the error per computational gate is about a factor of two higher, compared to the static single-qubit experiment. However, in

ion	error per gate (10^{-5})	SPAM error (10^{-3})
A	10(1)	1.4(4)
B	10(2)	2.1(7)
C	12(2)	2.2(4)
D	9(1)	3.3(3)

Table 8.2.: Fit results from the simultaneous four-ion randomized benchmarking for $N_t = 1$ and a variable number of single-qubit computational gates N_g on each ion. The error per computational single-qubit gate is determined from the slope of the linear fit. The SPAM error denotes the state preparation and measurement error, which is determined from the y-axis intercept of the fit.

this former experiment the calibration routines for the π and $\pi/2$-pulse times were carried out extensively and reached a higher precision. Furthermore, during the four-ion measurement, the measured fidelities fluctuate more than in the single-ion measurement. This is attributed to pulse area fluctuations, due to the increased overall sequence duration. We estimate that, with a comparable calibration of the pulse times and better pulse area stability, a similar performance can be realized for the four-qubit register.
The state preparation and measurement error is also by a factor of two higher, compared to the static single-qubit experiment, which is caused by the limited lifetime of the metastable $D_{5/2}$-state of around 1.2 s. After the shelving procedure is executed on ion A for instance, all other ions are shuttled to the LIZ for shelving. Afterwards, ion A is shuttled to the LIZ again for state detection with resonant 397 nm light. The time between shelving and state detection for this ion is around 2.7 ms. Since the metastable state decays exponentially an error of $2.2 \cdot 10^{-3}$ arises from this idle time. This error needs to be divided by two, since on average only half of the randomized benchmarking experiments result in the state $|\uparrow\rangle$, which is shelved to the metastable state. Thus, a calculated error of $1.1 \cdot 10^{-3}$ arises from the limited metastable state decay for ion A, which is close to the experimentally determined SPAM error. For ions B, C and D the error rises in this order since the time between shelving and detection is longer. Before fluorescence detection of ion B is performed for instance, the detection of ion A is executed within 1.2 ms and thus contributes significantly to the metastable state decay of ion B. This effect can be reduced by shorter state detection times and faster shuttling and shelving operations in future experiments.
In the four-ion experiment, which is presented above, each ion is moved to the LIZ only once for the execution of computational gates, i.e. $N_t = 1$. As a consequence, each ion is

either in the spin state $|\uparrow\rangle$ or $|\downarrow\rangle$ after application of the randomized gate sequence. Both states are not sensitive to magnetic field fluctuations and a high fidelity is demonstrated. In complex quantum information algorithms however, it can be necessary to increase the number of shuttling operations, i.e. $N_t > 1$. This means that ions are shuttled in spin superposition states along the trap axis. Thus, the states accumulate a phase and are prone to magnetic field noise [Rus17]. The accumulated phase is calibrated in a separate measurement and fed forward to subsequent computational gates – this technique is already successfully demonstrated in section 7.2. It is desirable to perform the gate pulses on a resonant carrier transition, to prevent further phase accumulation from a detuned driving field. We thus stabilize the carrier frequency in the experiment. After readout of all four ions, a single ion is used to measure the deviation of the carrier frequency from the Zeeman splitting in a Ramsey experiment, i.e. the absolute magnetic field. The deviation frequency is updated for subsequent measurement cycles, thus compensating for small absolute magnetic field drifts. To investigate the performance of the four-qubit register further, we choose $N_t = N_g$ and execute only one computational gate on each ion, when it is moved to the LIZ. The results of the measurement are shown in figure 8.4.

The performance is worse than for $N_t = 1$ and we refrain from fitting the data. In this measurement, the time between each computational gate on each ion is about 1.57 ms, because the ions are shuttled alternately to the LIZ in between the gates. Within this duration, the spin superposition states are prone to decoherence. For a sequence length of six computational gates an idle time of $5 \times 1.57\,\text{ms} = 7.85\,\text{ms}$ arises for each ion. Compared to the coherence time of around 300 ms, this effect is non-negligible and contributes to the gate error. If the gate pulses are applied with a detuned frequency, spin superposition states accumulate a phase during the idle time, which is proportional to the detuning from the resonance. Subsequent gate pulses are not corrected for this phase and thus lead to impaired results. We actively stabilize the carrier frequency better than $2\pi \times 10\,\text{Hz}$. However, a detuning of $2\pi \times 5\,\text{Hz}$ already leads to an accumulated phase of 0.05 rad in each idle time. To investigate if the gate errors are related to the shuttling of the four ions we perform a reference measurement with a single static trapped ion in the LIZ. The computational randomized gate sequence is identical to the four-ion experiment. After each computational gate, an artificial idle time of 1.57 ms is installed, to emulate the situation for a single ion in the four-ion measurement. The results of the measurement are shown in figure 8.5.

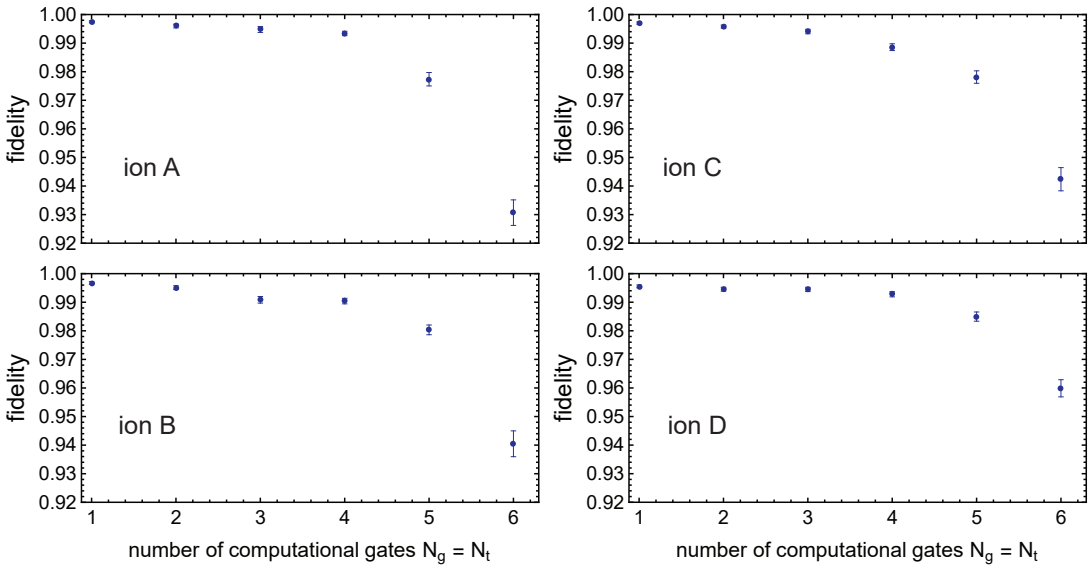

Figure 8.4.: Simultaneous four-ion randomized benchmarking of single-qubit gates for $N_g = N_t$. When each ion is shuttled to the LIZ, only one computational gate is executed on the ion. The fidelity is a mean fidelity, calculated from individual randomized benchmarking experiments. Error bars correspond to the standard error of the mean fidelity and each measurement is comprised of more than 11000 single measurements.

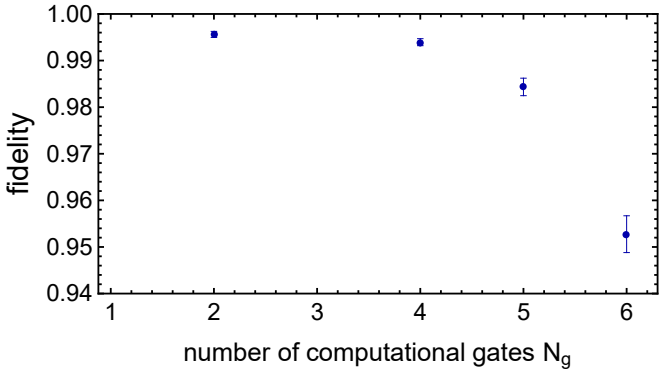

Figure 8.5.: Randomized benchmarking of single-qubit gates on a single static ion with an artificial idle time of 1.57 ms after each computational gate. This measurement serves as a reference measurement to investigate the gate error in the four-ion experiment, shown in figure 8.4. The fidelity is a mean fidelity, calculated from individual randomized benchmarking experiments. Error bars correspond to the standard error of the mean fidelity and each measurement is comprised of more than 11000 single measurements.

The result is almost identical to the four-qubit register operation. We thus conclude, that the gate error in the four-ion experiment is dominated by the idle time between the computational gates on each ion. We find that the phase correction for the inhomogeneous magnetic field – which is necessary as the ions travel in an inhomogenous magnetic field, see section 7.2 – is performed with high accuracy and does not impede the gate operations significantly.
In summary, we have demonstrated high fidelity single-qubit operations in a four-qubit register, without crosstalk between the qubits. However, the results are impaired when the number of shuttling operations between the operations is increased, due to significant idle times. Decreasing these idle times, by performing faster shuttling operations, will significantly reduce the gate errors in future experiments.

8.4. Shuttling-insensitive entangling gate

Creating entanglement between two qubits is a fundamental requirement for a universal quantum computer [DiV00] and laser-driven geometric phase gates have been realized with high fidelity on trapped ions [Gae16; Bal16]. We use this two-qubit gate type in our setup to create entanglement between two trapped $^{40}Ca^{+}$ ions. The gate requires the vibrational mode of the ions, which is used as a bus mode, to be close to the ground state of motion. Since we employ ion shuttling operations along the trap axis in our architecture for a scalable quantum processor, small excitations of the axial mode of motion are inevitable. We thus use one of the shuttling-insensitive radial vibrational modes, the higher frequency $\omega_z^{\text{c.o.m.}}$-mode, as a gate bus mode. The negligible motional excitation of this mode from the shuttling operations is demonstrated in section 8.1 and chapter 7. In this section, the shuttling-insensitive two-qubit gate operation is demonstrated and the limiting factors are characterized.
Initially, two ions are cooled to the motional ground state of all four radial modes ($\omega_y^{\text{c.o.m.}}, \omega_y^{\text{rocking}}, \omega_z^{\text{c.o.m.}}$ and $\omega_z^{\text{rocking}}$) with resolved sideband cooling by the Raman laser beams R4 and R1. Then, both ions are initialized by optical pumping to the separable quantum state $|\psi\rangle = |\uparrow\uparrow\rangle$. A combination of single-qubit rotations and a geometric phase gate is then used to entangle the spins of two ions – the maximally entangled Bell state $|\psi\rangle = 1/\sqrt{2}(|\uparrow\uparrow\rangle + i\,|\downarrow\downarrow\rangle)$ is created. The experimental sequence is shown in figure 8.6.

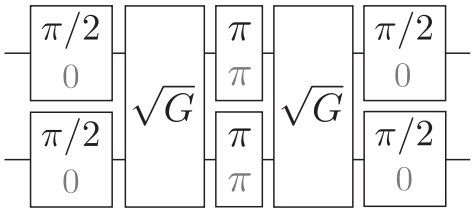

Figure 8.6.: Quantum circuit of a two-loop geometric phase gate for the creation of a Bell state. Solid numbers indicate the pulse area of single-qubit rotations whereas gray numbers denote the phase of the respective pulses.

The combination of a two-ion entangling operation $\hat{G} = diag(1, i, i, 1)$ and the single-qubit rotations constitutes the unitary operator

$$\hat{U}_1 = \frac{e^{i\pi/4}}{\sqrt{2}} \begin{pmatrix} 1 & 0 & 0 & i \\ 0 & 1 & -i & 0 \\ 0 & -i & 1 & 0 \\ i & 0 & 0 & 1 \end{pmatrix}. \tag{8.2}$$

Single-qubit rotations are performed simultaneously on two ions by the laser beams R1 and CC with high fidelity, as characterized in section 8.2. In order to perform the geometric phase gate $\hat{G}$, the laser beams R4 and CC create an optical traveling standing wave in the radial direction which gives rise to an a.c. Stark shift. This wave couples to the center of mass mode of the two ions ω_z and establishes a spin-dependent optical dipole force, which drives the two ions in phase space. The spin states are driven along a closed loop in phase space, at the end of a loop the states are entangled. We drive two closed loops in phase space – interrupted by a spin-echo π-pulse – to decrease the sensitivity of the gate for qubit frequency errors and to reduce off-resonant excitation [Lei03a]. A detailed explanation of the gate is provided in section 2.5. The laser beams R4 and CC are detuned by $\Delta_{R4-CC} = (\omega_z + \delta)/2\pi$ where δ denotes the gate detuning, which is much smaller than the secular trap frequency ω_z. The path duration of the spin states in phase space – i.e. half of the gate duration $(t_g/2)$ – is determined by the inverse gate detuning, which corresponds to the oscillation frequency of the a.c. Stark shift in the reference frame of the ions.
Once the Bell state is created, the two-ion crystal is separated and the ions are shuttled

individually to the LIZ, in order to analyze the quantum state via full state tomography, as described in section 7.2. The ions accumulate a phase between the Bell state creation and analysis pulses due to the shuttling operations in the inhomogeneous magnetic field along the trap axis. We demonstrated how this phase can be accounted for and corrected in the phase of the analysis pulses. However, in this experiment, we only desire to assess the fidelity of the produced Bell state, which is not affected by a global phase of the state. Thus, we do not correct for the accumulated phase in this experiment. A density matrix is reconstructed from the state tomography measurement – the result is shown in figure 8.7.

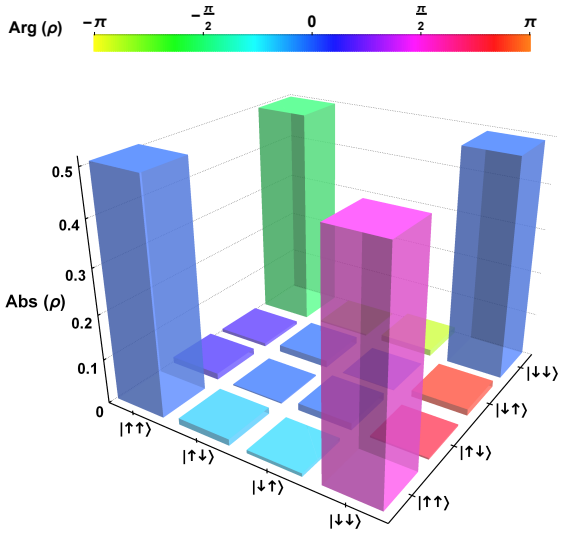

Figure 8.7.: Density matrix ρ of a two-ion Bell state – reconstructed from full state tomography including correction for readout errors. Each of the nine measurement operators $\{\sigma_x\sigma_x, \sigma_x\sigma_y, ...\}$ is measured more than 4200 times, in total 2×38000 single measurements are performed to determine a Bell state fidelity of $\mathcal{F} = 99.5(1)\%$. A numerical representation of the data is available in appendix A.

A standardized measure for the overlap of two quantum states $\rho = |\psi_1\rangle\langle\psi_1|$ and $\sigma = |\psi_2\rangle\langle\psi_2|$ is the fidelity

$$\mathcal{F}(\rho,\sigma) = \left(Tr\left[\sqrt{\sqrt{\rho}\,\sigma\sqrt{\rho}}\right]\right)^2. \tag{8.3}$$

To compute the fidelity of the experimentally created Bell state, we calculate the quantity $\mathcal{F}(\rho_{exp}, \rho_{ideal})$ with the ideal Bell state $|\psi_{ideal}\rangle = 1/\sqrt{2}(|\uparrow\uparrow\rangle + e^{i\phi}|\downarrow\downarrow\rangle)$, where the global

phase ϕ is adjusted to generate the maximum overlap. In the same manner as in the two-ion process tomography in section 7.2, a correction for readout errors is applied and the confidence intervals for the mean fidelity are determined via parametric bootstrapping, see appendix B.2. From more than 76000 single measurements, we achieve a fidelity for the produced Bell state of $\mathcal{F} = 99.5(1)\%$ with correction for readout errors and $\mathcal{F} = 99.1(1)\%$ without correction. The total gate duration is around 110 µs, where each of the two loops in phase space takes around 50 µs, set by the gate detuning $\delta = 2\pi\times 20\,\mathrm{kHz}$. The duration of the gate laser pulses is thus $t_g = 100\,\mu\mathrm{s}$. The detuning of the Raman laser beams from the cycling transition is $\Delta = -2\pi\times 750\,\mathrm{GHz}$. Each of the Raman laser beams is focused on the ions with an optical power of about 3 mW. A combination of the RF level of 300 V peak-to-peak and the DC voltage of −6 V on the LIZ trapping electrode generate the secular trap frequencies $\omega_{x,y,z}/2\pi = \{1.49, 3.83, 4.65\}$ MHz. The Lamb-Dicke parameter for the radial two-ion ω_z gate mode is 0.062.
A detailed analysis of the error sources for the two-qubit gate in our experimental setup is provided in the appendix B.3. The calculated sources of gate infidelity are listed in table 8.3.

Error source	Calculated fidelity error (%)
motional dephasing ($\tau_{1/e}$ =6.5 ms)	0.46
Raman and Rayleigh photon scattering	0.13
gate parameter calibration	< 0.1
motional heating ($\dot{\bar{n}} = 2.9/\mathrm{s}$)	0.007
motional temperature ($\bar{n} \lesssim 0.1$)	0.001
total	0.7

Table 8.3.: Error budget for the two-qubit gate with gate time $t_g = 100\,\mu\mathrm{s}$ and Raman detuning $\Delta = -2\pi\times 750\,\mathrm{GHz}$.

The total calculated gate fidelity error of 0.7% is consistent with the measured gate fidelity of 99.5(1)% since the gate parameter calibration error of 0.1% is only an upper bound. The gate fidelity is mainly limited by motional dephasing and photon scattering. Reducing the motional dephasing of the gate mode ω_z is a technical challenge, which requires a thorough electrical configuration of the entire setup. A new laser source will provide more optical power and thus reduce the scattering error significantly. Reducing the gate parameter calibration error is feasible by employing fit routines to the calibration measurements. Other error sources such as off-resonant excitation, unequal illumination of the ions, spin dephasing from magnetic field noise, motional Kerr cross-coupling, amplitude and phase noise in the Raman laser beams are either strongly suppressed by

the spin-echo gate scheme and the shaping of the gate pulses, or completely negligible and thus do not contribute significantly to the error budget.
In conclusion, we have demonstrated a shuttling insensitive two-qubit entangling gate, that operates below the error threshold of $\approx 1\%$ for fault tolerant quantum computation [Kni05; Rau07] and compatible with our architecture for a scalable quantum processor. We have identified the dominant error sources, which can be reduced with moderate experimental effort to achieve higher entangling gate fidelities.

8.5. Scalable creation of long-lived multipartite entanglement

In the previous chapters, ion shuttling operations and laser-driven quantum logic gates in a micro-structured ion trap are presented. We employ these experimental building blocks to demonstrate the deterministic generation of multipartite entanglement. Four qubits are sequentially entangled by laser-driven pairwise gate operations. Between these, the qubit register is dynamically reconfigured via ion shuttling operations, where ion crystals are separated and merged, and ions are moved in and out of a fixed laser interaction zone. A sequence consisting of three pairwise entangling gates yields a four-ion GHZ state $|\psi\rangle = \frac{1}{\sqrt{2}}(|0000\rangle + |1111\rangle)$, and full quantum state tomography reveals a Bell state fidelity of 94.4(3)%. We analyze the decoherence of this state and employ dynamic decoupling on the spatially distributed constituents to maintain 69(5)% coherence at a storage time of 1.1 seconds.
The results, which are presented in this section, are published in [Kau17b].

As a benchmark for QC capabilities, the generation and properties of multipartite entangled states have been studied intensively. On the one hand, generating and maintaining such states lies at the heart of QC, on the other hand large multipartite entangled states represent a resource for the measurement-based QC approach [Rau01; Lan13]. The first generation of a four-particle Greenberger-Horne-Zeilinger (GHZ) state has been accomplished at a state fidelity of 57% by the NIST group [Sac00], while eight-qubit W-states at 76% fidelity have been created later by the Innsbruck group [Häf05b]. Furthermore, GHZ states of up to 14 trapped ions have been created [Mon11b], and it has been shown that these states are rather fragile in the presence of correlated noise. While large-scale entanglement of thousands of optical modes [Yok13] or atoms [McC15a]

has also been demonstrated, QC requires *deterministic* entanglement generation with capabilities for storage and *individual* manipulation and readout of the qubits.
In this work, we demonstrate the scalable generation of GHZ states of up to four trapped ions. Our method is based on single-qubit rotations, pairwise two-qubit entangling gates and shuttling operations. Gate operations are driven by laser beams which are directed to one fixed trap site, the laser interaction zone (LIZ). By shuttling only the required ions to this trap site, crosstalk is strongly suppressed as compared to static ion-crystal registers, as memory ions, which are not to be affected by gate operations, are stored several hundreds of microns away from the LIZ. We also demonstrate that GHZ coherence can be maintained over long storage times by dynamical decoupling on the distributed components. Here, the constituent ions are kept in pairs and shuttled repeatedly into the LIZ, where the decoupling rotations take place.

8.5.1. Experimental parameters and techniques

In the following, we summarize the experimental parameters and techniques, which are used to perform a scalable quantum logic circuit in our setup:

- The trap is placed in a μ-metal enclosure for shielding of fluctuating ambient magnetic fields, the quantizing magnetic field is generated by permanent magnets and all experiments are synchronized to the ac power line frequency. This yields a Ramsey coherence time of around 300 ms [Rus16] for a single qubit.

- The heating rates of the ion trap are on the order of a few Hz, as investigated in section 6.1. The combination of low heating rates and long spin coherence times allows for concatenated quantum gate operations.

- The secular trap frequencies in this experiment are $\omega_{x,y,z}= 2\pi \times \{1.5, 4.1, 4.9\}$ and the voltage of the RF trap drive is about 320 V peak-to-peak at a frequency of $2\pi\times33$ MHz. We find the long-term relative secular trap frequency stability to be about 5 ppm, see section 6.2

- The Zeeman sublevels $|0\rangle \equiv |\downarrow\rangle \equiv |S_{1/2}, m_J = -\frac{1}{2}\rangle$ and $|1\rangle \equiv |\uparrow\rangle \equiv |S_{1/2}, m_J = +\frac{1}{2}\rangle$ are separated by $2\pi\times10.5$ MHz.

- The detuning for the stimulated Raman transitions in this experiment is $\Delta = -2\pi \times 290\,\mathrm{GHz}$.
- A single π-rotation is realized by a 10 µs pulse, see section 8.2 for the characterization of single-qubit logic gates.
- A geometric phase gate is used for two-ion entanglement. At a detuning of $\delta = 2\pi \times 25\,\mathrm{kHz}$ from the higher frequency radial center-of-mass mode, the gate operation (including single-qubit rotations) takes about 100 µs. We achieve a Bell-state fidelity of 99.0(4)%, mainly limited by off-resonant photon scattering[1].
- Since the entangling gate requires the ions to be close to the ground state of motion, we apply resolved sideband cooling to all ions. A single cooling pulse takes on average 15 µs. We either cool single ions or pairs of two ions and cool all radial modes with about 40 pulses per mode.
- Each laser beam is directed at the LIZ, and all operations are robust with respect to excitation of the axial ion motion: the entangling gate (driven on a radial secular mode), single-qubit rotations (driven by co-propagating laser beams) and electron shelving by 729 nm light (laser beam directed perpendicular to trap axis).
- Ion shuttling along the trap axis is performed by concatenated segment-to-segment transports of 200 µm, where each operation takes 30 µs. In section 8.1, we measure the motional excitation on the radial gate mode to be below 0.03 phonons per transport.
- Separation of a two-ion crystal is realized by increasing the voltage on the trapping segment and lowering the voltage on the adjacent segments [Kau14; Rus14] within 160 µs. The operation and its reversed counterpart – the recombination of two individual ions – are only carried out in the LIZ as it requires careful calibration of the electrode voltages. Separation and recombination operations lead to a motional excitation of about 0.1 phonons on the gate mode, see section 8.1.

[1] In section 8.4, a higher two-qubit gate fidelity is presented. An increased Raman detuning is employed to reduce the photon scattering error.

The geometric phase gate $\hat{G} = \mathrm{diag}(1, i, i, 1)$ is used, in conjunction with single-qubit rotations, to generate the unitary $\hat{U}_1$ for entanglement seeding and the C-NOT equivalent unitary $\hat{U}_2$, see figure 8.8:

$$\hat{U}_1 = \frac{e^{i\pi/4}}{\sqrt{2}} \begin{pmatrix} 1 & 0 & 0 & i \\ 0 & 1 & -i & 0 \\ 0 & -i & 1 & 0 \\ i & 0 & 0 & 1 \end{pmatrix}, \quad \hat{U}_2 = \begin{pmatrix} 0 & 1 & 0 & 0 \\ -i & 0 & 0 & 0 \\ 0 & 0 & i & 0 \\ 0 & 0 & 0 & 1 \end{pmatrix}. \tag{8.4}$$

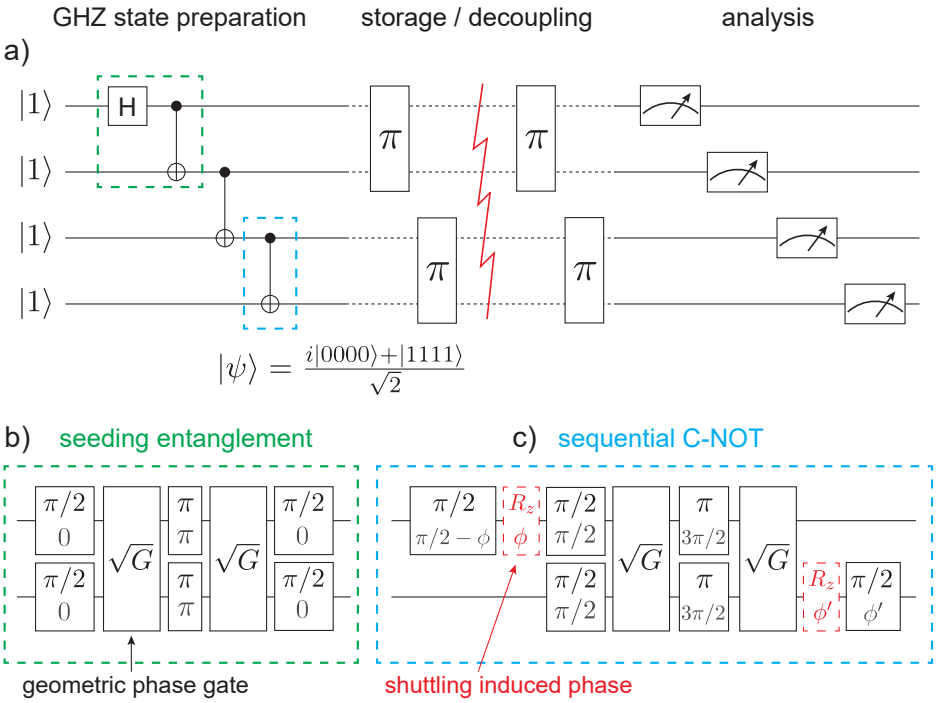

Figure 8.8.: (a) Quantum circuit for the creation, storage and analysis of a four-ion GHZ state. The state is generated by three subsequent entangling gates. Evenly spaced dynamical decoupling π-pulses are employed to achieve long coherence times, followed by state tomography on the individual ions. The green (b) and blue (c) dashed boxes show how the respective entangling gates are realized in the experiment – they correspond to the unitary operators $\hat{U}_1$ and $\hat{U}_2$, from equation 8.4 . The black numbers for the single-qubit operations represent the laser pulse areas, whereas gray numbers indicate the phase of the respective pulse. Red boxes represent an additional phase, which arises from the shuttling operations, see text.

The sequential C-NOT $\hat{U}_2$ requires shuttling of a single ion to the LIZ for a single-qubit rotation, a subsequent recombination of two ions in the LIZ for an entangling gate, followed by a separation operation and a final transport of a single ion to the LIZ for a single-qubit rotation.

8.5.2. Four-ion entanglement

In order to generate multipartite entanglement, we employ a sequence of two-ion entangling gates and single-qubit operations to create a GHZ state $|\Psi\rangle = 1/\sqrt{2}\,(i\,|0000\rangle + |1111\rangle)$. The experimental sequence, including the shuttling operations, is sketched in figure 8.9 and in appendix C.3 the full experimental sequence is shown.

The sequence is comprised of five blocks: An initial *cooling block* prepares the ions close to the ground state of motion of the radial secular modes, which is crucial for high-fidelity gate operations in the subsequent *quantum logic block*. After state preparation, the coherence can be maintained through an optional *rephasing block*. To analyze the final state, quantum state tomography is performed in the *analysis block*. A *final block* contains a magnetic field tracking measurement and an ion repositioning sequence, which enables the next repetition of the entire sequence. In the following, we describe these operational blocks.

Initially, ion pair A, B is stored at electrode 20 in the LIZ and ion pair C, D is stored at electrode 26. Ion pair A, B is then shuttled to electrode 14 and pair C, D is shuttled to the LIZ for a separation operation, which transfers ion C to electrode 19 and ion D to electrode 21. Ion pair A, B and the single ions C and D are consecutively transported to the LIZ for ground state cooling and spin initialization to $|\psi\rangle = |1111\rangle$. Subsequently, we perform quantum logic operations to generate the maximally entangled GHZ state via the quantum circuit shown in figure 8.8, which is comprised of one- and two-qubit quantum logic operations. Application of the unitary $\hat{U}_1$ on the ion pair A, B in the LIZ generates the state $|\psi\rangle = (i\,|0011\rangle + |1111\rangle)/\sqrt{2}$, where ions A and B are entangled. The entanglement is extended to all qubits by subsequent application of the C-NOT unitary $\hat{U}_2$ on qubits B,C and C,D. This leads to the final state $|\psi\rangle = (i\,|0000\rangle + |1111\rangle)/\sqrt{2}$, with the constituent qubits distributed over a macroscopic distance of 1.8 mm.

Since qubits in superposition states are shuttled along the trap axis, they accumulate a phase ϕ due to the inhomogeneous magnetic field [Rus17]. In total, four of these phases need to be considered in the quantum gate sequence.

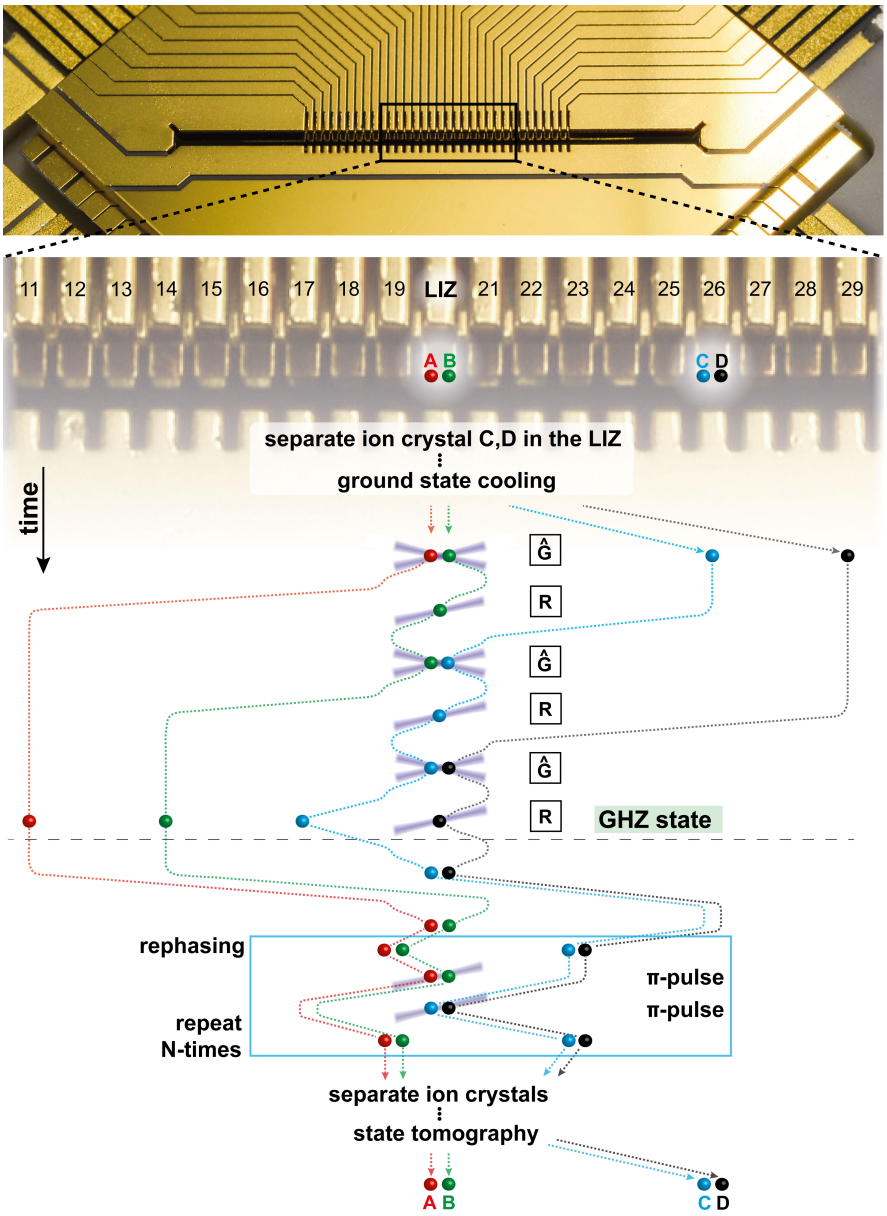

Figure 8.9.: Experimental shuttling sequence for the creation, storage and analysis of a four-ion GHZ state. The state creation takes place above the dashed line. Laser driven quantum operations, i.e. entangling gates $\hat{G}$ or single-qubit rotations R are carried out in the laser interaction zone (LIZ). After the GHZ state is created, it can be stored for hundreds of ms by dynamical decoupling. The ions are not stored in the LIZ to prevent depolarization from residual light near the cycling transition. The full experimental sequence is shown in appendix C.3.

We find each of them to be constant over time and to be $\phi < \pm 0.6$ rad. The phase is compensated for by adjusting the phase of an adjacent single-qubit rotation, see figure 8.8 c).
We perform quantum state tomography by subsequent shuttling of each of the ions to the LIZ. For each ion, one of the analysis rotations $\{I, R_X(\pi/2), R_Y(\pi/2)\}$ is carried out in order to measure the operators $\{\sigma_z, \sigma_y, \sigma_x\}$. As we are only interested in the GHZ state fidelity irrespective of the relative phase (see below), the analysis pulses are not corrected for additional phase accumulation.
After the application of tomography rotations, each ion is shuttled to the LIZ for population transfer $|\uparrow\rangle \leftrightarrow |D_{5/2}\rangle$ via electron shelving. The ions are again individually shuttled to the LIZ, where state-dependent fluorescence is observed. All qubits are shelved *before* fluorescence detection, to avoid depolarization of a remotely stored qubit from scattered light near 397 nm.
After measurement, we carry out the magnetic field tracking block. Ion A, placed at the LIZ, is used to measure the drift of the qubit frequency in two Ramsey experiments with 5 ms interrogation time, and 0° and 90° analysis phase, respectively. From these two measurements, we infer the deviation from the actual qubit frequency, and correct it for subsequent measurement cycles. Finally, the ions are merged into pairs and the entire sequence is repeated. In order to obtain the fidelity of the prepared state, we reconstruct density matrices $\hat{\rho}$ from the measurement data and compute the state fidelity

$$\mathcal{F}(\hat{\rho}) = \max_{\theta} \langle \Psi(\theta) | \hat{\rho} | \Psi(\theta) \rangle \tag{8.5}$$

with respect to a GHZ state of arbitrary relative phase θ:

$$|\Psi(\theta)\rangle = \tfrac{1}{\sqrt{2}} \left(|0000\rangle + e^{i\theta} |1111\rangle \right). \tag{8.6}$$

We first perform linear inversion of the measurement data, which consists of 4×50900 measurements in total. This yields a density matrix, from which a fidelity of $\mathcal{F} = 92.60\%$ is extracted. As a density matrix obtained from linear inversion can feature negative eigenvalues due to statistical errors, the density matrix obtained from linear inversion is not suitable for estimation of a confidence interval via parametric bootstrapping. We additionally perform a maximum-likelihood (ML) state reconstruction [Řeh07]. Using the physical density matrix from the ML reconstruction for parametric bootstrapping, we estimate a fidelity of $\mathcal{F}_{ML} = 92.50(37)\%$, such that linear inversion and ML estimation yield consistent results.

By running the sequence without quantum logic operations, we determine the readout errors [Kau17a]. State preparation and measurement (SPAM) errors are dominated by the limited lifetime of the $D_{5/2}$ state of 1.2 s. For instance, for ion A, the time between shelving and fluorescence detection is 2.7 ms, leading to an estimated decay-induced SPAM error of 0.2%. An actual error of 0.4% is measured for ion A, the remaining error is attributed to shuttling-induced motional excitation, which affects the shelving efficiency. This is either due to residual coupling of 729 nm shelving laser to axial motion, or due to residual radial excitation from shuttling. Including correction for SPAM errors, the fidelity obtained from linear inversion is $\mathcal{F}$ =94.38%. The obtained density matrix is displayed in figure 8.10.

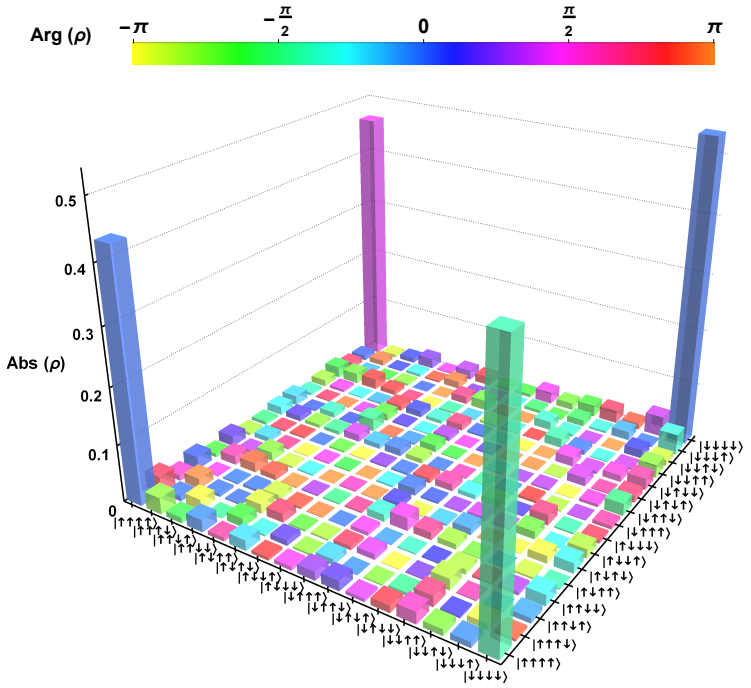

Figure 8.10.: Reconstructed density matrix of a maximally entangled four-ion GHZ state with correction for readout errors. Linear reconstruction with correction for SPAM errors yields a state fidelity of $\mathcal{F} = 94.38\%$. The numerical data is shown in appendix A.

Here, ML estimation with parametric bootstrapping yields $\mathcal{F}_{ML}$ =94.28(30)%. Additionally, we perform statistical tests based on Hoeffding's tail inequality [Mor13], confirming that the measurement data is statistically consistent with the state described by the reconstructed density matrices.

The theoretical fidelity limit for our setting is 97%, since the two-qubit entangling gate is performed three times at a fidelity of 99.0(4)%. We attribute the discrepancy from this result to imperfect calibration of the individually calibrated entangling gates and the correction phases ϕ, as well as the finite accuracy of the magnetic field tracking measurements. The entangling gates require individual calibration due to small motional excitation – mainly from heating – which results in a reduced coupling to the driving field and thus requires a slightly increased power for the entangling gate pulse.
The execution time for the creation of the GHZ state after sideband cooling is 3.1 ms, where 11% is used for quantum gates and the remainder is dedicated to shuttling operations, see appendix C.3 for details. This illustrates that currently, the shuttling overhead dominates the time budget of the quantum CCD operation. However, a significant leeway for optimization of these operations via technological and methodological improvements exists.

8.5.3. Dynamical decoupling

Magnetically sensitive multi-qubit GHZ states are prone to *super-decoherence*, which is caused by correlated local magnetic field noise [Mon11b]. We measure the coherence time of a four-ion GHZ state and employ dynamical decoupling to achieve extended lifetimes. Here, repeated π-flips of the qubits serve to effectively cancel the coupling of the qubits to a drifting offset magnetic field [Van05]. Once the GHZ state is created, the four individually trapped ions are merged to ion pairs A, B and C, D to reduce the amount of shuttling operations in the rephasing block. After storing the ion pairs at segments 19 and 23, they are alternately shuttled to the LIZ and subjected to π-pulses. The pulses are evenly spaced within the storage time, thus only an odd number of pulses is suitable for decoupling. After the rephasing block, the ion pairs are separated into individually trapped ions for state analysis. We utilize a reduced measurement scheme, by measuring the operators $\{\sigma_x^{(A)}\sigma_x^{(B)}\sigma_x^{(C)}\sigma_x^{(D)}\}$ and $\{\sigma_x^{(A)}\sigma_x^{(B)}\sigma_x^{(C)}\sigma_y^{(D)}\}$. To infer the GHZ coherence of the state, each of the two operators is measured at least 200 times. The parity contrast and its statistical measurement error are determined from the measurement results via ML parameter estimation [Rus17]. The results of these measurements are shown in figure 8.11. The coherence time of the GHZ state without rephasing pulses is about 20 ms. By applying $N_\pi = 15$ rephasing pulses on each ion pair, we achieve coherence times exceeding one second. As can be seen from figure 8.11, the coherence decay is not described by a simple model. We attribute this to noise

at frequencies that match the inverse time difference between subsequent decoupling pulses [Kot11].

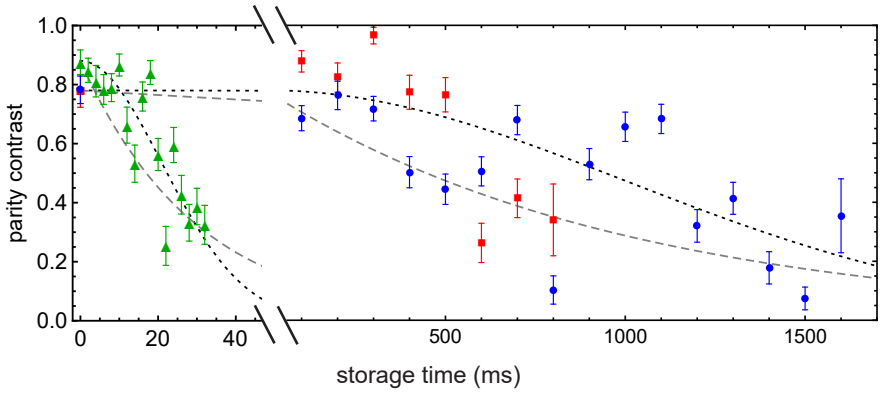

Figure 8.11.: Preservation of the parity contrast of a four-ion GHZ state by dynamical decoupling. Green triangles for short times correspond to a measurement without the execution of the rephasing block. Blue circles represent a measurement with $N_\pi = 15$ rephasing pulses on each qubit, while red squares correspond to $N_\pi = 3$. The dotted black line represents a Gaussian decay, whereas the gray dashed line represents an exponential decay. The data shown is not corrected for SPAM errors.

8.6. Lifetime of entangled states

We have demonstrated the scalable generation of long-lived entangled states of up to four ions in the previous section. Maintaining the coherence of such states is important to the measurement based approach to quantum computing [Rau01; Lan13] and quantum error correction [Nig14; Lin16]. For GHZ states, consisting up to $N = 14$ qubits, a $1/N^2$ scaling law was found for the coherence time [Mon11a]. The magnetically sensitive states are prone to superdecoherence, which is caused by correlated Gaussian phase noise of the magnetic field. The influence of decoherence on the entanglement dynamics of a four-ion GHZ state has been investigated experimentally [Bar10].

Here, we measure the coherence of up to four entangled ions in our setup and compare the results to the findings of other research groups. Specifically, we create the entangled quantum states $|\Psi_2\rangle = 1/\sqrt{2}(|00\rangle + e^{i\phi}|11\rangle)$, $|\Psi_3\rangle = 1/\sqrt{2}(|000\rangle + e^{i\phi}|111\rangle)$ and $|\Psi_4\rangle = 1/\sqrt{2}(|0000\rangle + e^{i\phi}|1111\rangle)$. The three-ion entangled state $|\Psi_3\rangle$ was created in the same fashion as the four-ion state $|\Psi_4\rangle$.

Results for the single ion superposition state $|\Psi_1\rangle = 1/\sqrt{2}(|0\rangle + e^{i\phi}|1\rangle)$ are published in [Rus16] and are measured in the same setup. We plot the obtained $1/\sqrt{e}$ coherence times of the states versus the number of the qubits in figure 8.12.

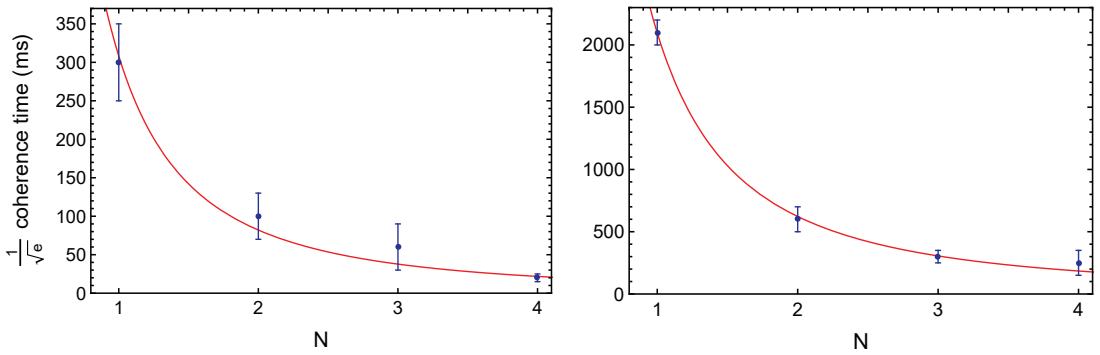

Figure 8.12.: Measured coherence times of N entangled qubits. **Left:** Data with a variable storage time after state generation. **Right:** A single spin-echo π-pulse, in the center of the variable storage time, extends the coherence times. For $N = 3, 4$ the state is a GHZ state, for $N = 2$ a Bell state and for $N = 1$ a spin superposition state. The red line is an exponential weighted least square fit of the form Ce^{-kN}. The decay factor according to the fit is $k = 1.9(1)$ for the data without rephasing and $k = 1.75(6)$ for the data with a spin-echo pulse.

The data needs to be interpreted with care, as the quantity of data sets is rather low and the measurements were taken over the course of several months, as explained in the following. Nevertheless, the coherence of the entangled states seems to be affected by correlated Gaussian phase noise, which results in a $\propto 1/N^2$ scaling of the GHZ state lifetime [Mon11a]. The authors use magnetic coils to generate the magnetic field – in our setup, the field is generated by permanent magnets [Rus16]. We emphasize that the coherence times and the error bars are estimates, as the data is affected by non-stationary magnetic field fluctuations. The corresponding data for $|\Psi_1\rangle$ is shown in [Rus16] and for $|\Psi_2\rangle, |\Psi_3\rangle, |\Psi_4\rangle$ in appendix A and section 8.5. The measurements for $|\Psi_1\rangle$ were taken in April 2016, whereas $|\Psi_2\rangle$ and $|\Psi_3\rangle$ were measured in August 2016 and $|\Psi_4\rangle$ was measured in September 2016. Since no changes were made to the setup during this time span, we consider the data sets to be consistent. The measurement for $|\Psi_2\rangle$ was executed with both ions stored in the LIZ, all other measurements were carried out with ions stored on individual electrodes, separated by 600 µm.
For future investigations of the decoherence mechanisms in our system, it would be desirable to perform the measurements within a few days, in order to increase comparability

between the data sets. Furthermore, the quantity of data sets should be increased, to obtain the coherence times with a higher precision. Our apparatus also enables us to observe the spatial dependence of the coherence of entangled states, by storing the ions in distant locations, similarly to [Rus17].

9

Towards Quantum Simulation

Multiple cold trapped ions form crystals, when confined in a common harmonic potential due to the Coulomb repulsion, as described in section 2.2. Two-dimensional zigzag crystals offer the possibility of exploring quantum many-body physics, for instance frustrated quantum Ising models [Kim10; Ber12]. Essentially, an analogue quantum simulator [Fey82] can be constructed from such a physical system. In figure 9.1, an exemplary fluorescence image of a planar seven-ion crystal is shown.

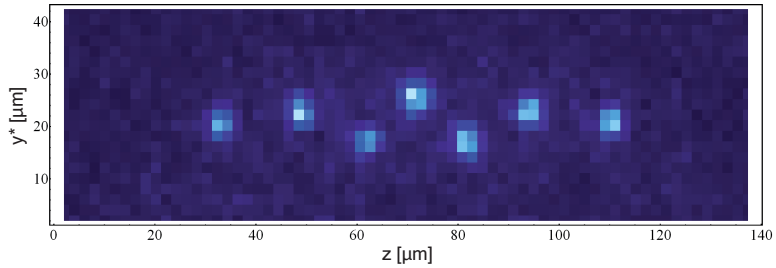

Figure 9.1.: Exemplary fluorescence image of a planar seven-ion crystal. In this image, the trap axis is aligned in the z-direction. Image taken from [Kau12a].

The key ingredient for the proposed experiments are state-dependent optical dipole forces [Mon96; Lei03a] on planar ion crystals. A spin-dependent force – created by two superposed Raman laser beams – is used two entangle the spins of two ions in our experiments, see section 8.4. The force is applied on a common motional mode of the ion crystal, which needs to be cooled close to the motional ground state before the force is applied. A planar ion crystal, which consists of N ions, features in total $3N$ motional modes. Out of these, $2N$ modes are aligned in the plane of the crystal. Coupling to the modes with laser beams is more challenging than in a one-dimensional ion crystal,

since the Lamb-Dicke factors are reduced [Ber12]. Furthermore, in a one-dimensional crystal, it is possible to overlap the effective wave vector precisely with the motional mode vectors. Thus, the laser beams couple only to N modes of the ion crystal and overlapping motional mode frequencies do not play a role. However, in a planar ion crystal, the $2N$ motional mode frequencies need to be well separated to allow for individual addressing of the mode.

9.1. Three-ion planar crystal

Motional mode vectors of *zigzag modes* in two-dimensional ion crystals point in various directions [Kau12b; Kau12a]. In the experiment, we couple to two of these modes of a three-ion zigzag crystal, which are shown in figure 9.2.

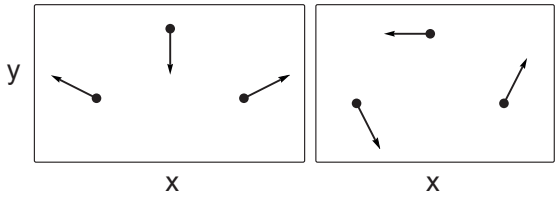

Figure 9.2.: Motional mode vectors of two zigzag modes of a three-ion planar crystal, which is confined in the x-y plane. The mode in the left panel is henceforth denoted as the *squish mode* and the mode in the right panel is denoted as the *vortex mode*. Along the trap axis x, the distance between the ions is 3 µm – along the radial y-direction, it is 1.8 µm. The effective wave vector of the coupling Raman laser beams is aligned in the x-direction.

The three-ion crystal is trapped in a harmonic potential, which is generated by a single electrode DC voltage of $-7.4\,\mathrm{V}$ and an RF voltage of about $280\,\mathrm{V}$ peak-to-peak. These voltages give rise to the secular trap frequencies $\omega_{x,y,z} = 2\pi \times \{1.652, 2.424, 3.795\}$ MHz – the resulting anisotropy parameter is $\alpha = \omega_x^2/\omega_y^2 = 0.464$. For the squish mode, a frequency of $2\pi\times1.15\,\mathrm{MHz}$ is determined from a spectroscopic measurement – for the vortex mode we measure $2\pi\times1.39\,\mathrm{MHz}$. There are two additional zigzag modes in the crystal plane at higher frequencies [Kau12b]. We restrict our measurements to the lower frequency modes, because linear combinations of motional modes can overlap near the zigzag mode frequencies.

9.2. Ground state cooling of zigzag modes

We apply laser pulses to cool the modes to the motional ground state. The beam waist of all laser beams is sufficiently large to couple equally well to all three ions. Initially, the three ions are cooled via Doppler cooling. Afterwards, a sequence of resolved sideband cooling laser pulses is executed on one of the zigzag modes – we use the laser beams R1 and R2 to generate an effective wave vector in the axial x-direction. Specifically, we use 60 red sideband cooling pulses of 6 µs duration, followed by 60 pulses of 12 µs duration, concluded by 60 pulses of 18 µs duration. Subsequently, the spins of the three ions are initialized to the $|\uparrow\uparrow\uparrow\rangle$ state via optical pumping. The motional excitation is then probed with a laser pulse of variable duration on the red and blue sideband of the zigzag mode. Electron shelving and fluorescence readout are used, to read out the spin state. We detect the fluorescence of all three ions simultaneously with a PMT. A detection time of 10 ms is used to distinguish between the four possible outcomes of the total amount of fluorescence – zero, one, two or three ions in the spin state $|\downarrow\rangle$. We observe the population of the initialized state $|\uparrow\uparrow\uparrow\rangle$ as a function of the probe pulse duration to estimate the motional excitation of the probed motional mode. The resulting Rabi oscillation data on the squish mode is shown in figure 9.3 and the result for the vortex mode is shown in appendix A.

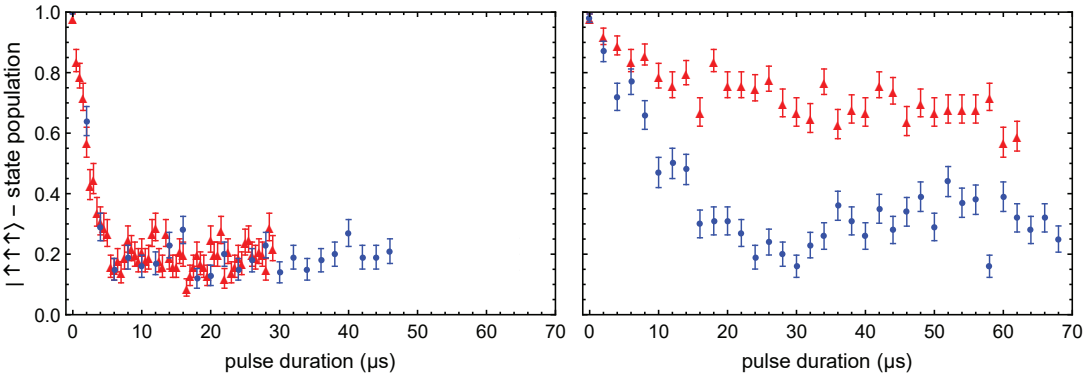

Figure 9.3.: Ground state cooling of the zigzag squish mode of a three-ion zigzag crystal. **Left:** Rabi oscillation data on the red sideband (red triangles) and the blue sideband (blue circles) of the squish mode, after Doppler cooling. **Right:** Rabi oscillation data after resolved sideband cooling of the squish mode. Each data point corresponds to 100 measurements, error bars correspond to the standard error from binomial readout statistics.

After Doppler cooling, the red and blue sideband are indistinguishable, which indicates a mean phonon occupation number of $\bar{n} \gtrsim 7$. After resolved sideband cooling however, the red and blue sidebands are distinguishable and we estimate, that both zigzag modes are cooled to $\bar{n} < 1$.

9.3. Spin-dependent force on a zigzag mode

From the low motional excitation, we infer that the two zigzag modes are in the Lamb-Dicke regime, which allows for coherent displacements in phase space via spin-dependent forces [Mon96; Lei03a]. During the displacement operations, spin and motion of the ions are entangled – the phase space trajectory of a single ion has been observed experimentally [Pos10b].
We perform Doppler cooling and resolved sideband cooling on the squish mode, followed by spin state initialization to $|\uparrow\uparrow\uparrow\rangle\,|n \approx 000\rangle$. Subsequently, we execute the light shift gate pulse sequence on the three ions simultaneously, which is sketched in figure 8.6 – it corresponds to a spin-echo sequence with initial and final single-qubit $\pi/2$-rotations and two spin-dependent light-shift force pulses, which are separated by a rephasing π-pulse. We vary the duration of the spin-dependent force pulses to observe the population dynamics. State readout is performed in the same fashion, as in the sideband cooling experiment. The single-qubit rotations are carried out with the laser beams R1 and CC and the spin-dependent light force pulses are driven by the beams R2 and CC, which create an effective wave vector along the axial x-direction. The frequencies of the laser beams R2 and CC generate a moving standing wave, see section 2.5 – they are detuned by $\delta_f = \omega_L - \omega_{squish}$, where $\omega_L \equiv \omega_{R2} - \omega_{CC}$ and ω_{squish} is the motional frequency of the squish mode of $2\pi\times 1.15\,\mathrm{MHz}$. We choose a force detuning of $\delta_f = 2\pi\times 100\,\mathrm{kHz}$ and the detuning of the Raman laser beams from the cycling transition is $\Delta = -2\pi\times 130\,\mathrm{GHz}$. The light force pulse of variable duration t corresponds to a displacement $\alpha(t)$ in phase space (see equation 2.20). After a duration of $t = 2\pi K/\delta_f$, where $K \in \mathbb{N}$, a loop in phase space is closed and we expect the coherent state to return to its initial position $|\uparrow\uparrow\uparrow\rangle\,|n \approx 000\rangle$. The result of the experiment is shown in figure 9.4.

We observe spin population dynamics, which are similar to the results for a transverse modes in a linear three-ion crystal [Kim09]. The fringe decay is more pronounced, compared to these experiments, since only one zigzag mode is cooled to the motional

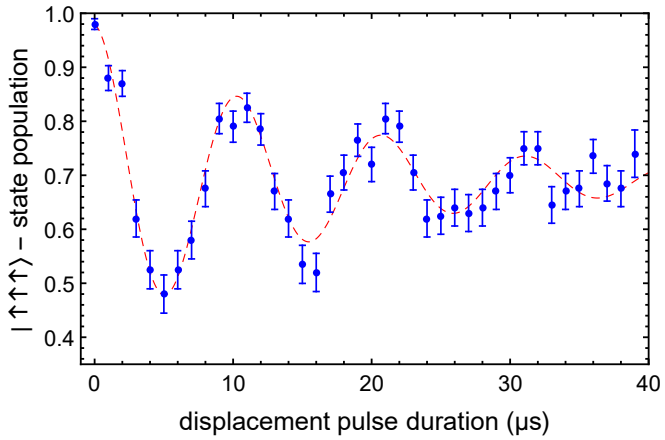

Figure 9.4.: Optical dipole force on the zigzag squish mode. The spin state population of a three-ion zigzag crystal is shown as a function of the displacement laser pulse duration on the zigzag squish mode. The dashed red line corresponds to a weighted least squares fit of the form $P_{|\uparrow\uparrow\uparrow\rangle}(t) = A\,\cos(2\pi\nu t)e^{-\gamma t} + C$, where t is the displacement pulse duration, γ is an empirical decay factor and A, C are constants. The fit yields the parameters: ν =96 kHz, γ =60 kHz, $A = 0.3$ and $C = 0.69$. The result for the oscillation frequency ν is in good agreement with the experimentally set laser detuning from the squish mode $\delta_f = 2\pi\times100$ kHz. Each measurement is repeated 100 times, error bars correspond to the standard error from binomial readout statistics.

ground state. The other five common motional modes in the crystal plane, which couple to the driving laser field, are cooled via Doppler cooling and thus outside the Lamb-Dicke regime. The fringe contrast can also be impaired by additional decoherence effects, such as motional heating [Tur00], photon scattering [Oze07] or quantum jumps [DF00]. We consider these effects to be negligible for the observed decay in our experiment, and attribute the fringe decay to the motional excitation of the spectator modes.

In the proposal for a trapped-ion quantum simulator [Ber12], which is based on planar crystals, the effective wave vector of the coupling laser field is aligned almost parallel to the z-direction. This allows for the coupling to the N transverse modes of the planar crystal, rather than to the $2N$ planar modes, as conducted in our experiment. In our setup, a similar configuration can be achieved by employing the laser beams R4 and CC, rather than the beams R2 and CC. Additionally, the radial trap axes y and z should be rotated by around 40°, to align the crystal plane almost vertically to the coupling wave vector. A rotation of the radial trap axes can be achieved by applying an offset voltage to all DC electrodes. Furthermore, the laser beams could be tilted with respect to the radial trap axes to require a smaller offset voltage. The timescale of the proposed

quantum simulator [Ber12] for the spin-spin interactions is in the millisecond regime. Given the characterization of the experiment (chapter 6), we are optimistic that relevant decoherence mechanisms would be small enough to allow for operations in this regime. Ions in planar crystals experience pronounced micromotion. Our results show, that sideband cooling and quantum gates are not inhibited by this effect.
To our knowledge, this is the first realization of ground state cooling and a spin-dependent dipole force on a zigzag mode of a planar ion crystal. We are confident, that our experimental system will allow for the investigation of frustrated quantum Ising models, via spin-spin interactions, in small two-dimensional ion crystals – the demonstrated spin-dependent optical dipole force on a zigzag mode is an important step towards a trapped-ion quantum simulator.

10

Outlook

In this work, the fabrication and operation of a scalable trapped-ion quantum processor is presented. The device is a reconfigurable quantum register, which is also known as quantum charge-coupled device [Kie02]. Ion qubits are moved between linear Paul traps to a laser interaction zone, where few-qubit quantum logic gates are executed. Our device performs single- and two-qubit logic operations above the threshold for fault tolerant quantum computing. A scalable quantum logic circuit, which is comprised of such operations, is performed on four qubits, to generate a maximally entangled Greenberger-Horne-Zeilinger state $|\psi\rangle = \frac{1}{\sqrt{2}}(|0000\rangle + |1111\rangle)$ with a state fidelity of 94.4(3)%. The four constituent entangled ions are spatially separated over a distance of 1.8 mm. A dynamical decoupling technique is employed, to maintain 69(5)% coherence at a storage time of 1.1 seconds. We therefore demonstrate the *deterministic* generation of a multipartite entangled state, with its constituents distributed over a *macroscopic range*, which persists for an unprecedented *long storage time*.

In this chapter, we propose experimental advancement, to improve the performance of complex quantum logic circuits in our device. We desire to scale our system to an $N > 10$ qubit processor, as sketched in figure 10.1.

To realize such multi-qubit algorithms in our setup, it is also necessary to implement advanced control schemes for the conjunction of shuttling operations and quantum logic gates. This is equivalent to a quantum compiler and an operating system for the quantum processor. Conclusively, we give an outlook on future experiments in our device and assess the current status, with respect to the realization of a *logical qubit* [Ber17], which is comprised of several entangled physical qubits [Sho95; Ste96].

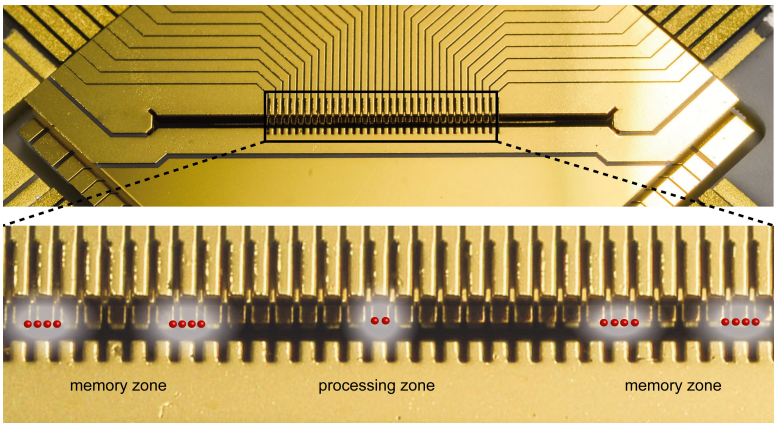

Figure 10.1.: Envisioned quantum register size for future experiments.

10.1. Experimental advancement

We drive single and two-qubit quantum logic gates with stimulated Raman transitions near 397 nm. The performance of both gates is beyond the threshold for fault tolerant quantum computation, but can still be improved by reducing the photon scattering rate during the gate operation. This requires a larger detuning from the atomic resonance, and thus increased optical power. A new frequency-doubled titanium sapphire laser source will be operational soon and deliver a twentyfold increased optical intensity, which will reduce the photon scattering error significantly. This will enable us to reduce the two-qubit gate duration by one order of magnitude to below 10 µs, while maintaining a high gate fidelity.

We perform the two-ion entangling gate on a radial secular mode and the gate fidelity is currently limited by electrical noise between the RF and DC electrodes. Eliminating this noise requires a thoroughly designed electrical configuration of the apparatus, which provides sufficient shielding and simultaneously avoids multiple ground connections. Due to a higher gate speed in the future, this noise will contribute significantly less to the gate error. However, reducing the gate speed by orders of magnitude will require advanced experimental schemes [GR03; Cam10; Rom12].

To increase the operational speed of our quantum processor, it is imperative to speed up the shuttling operations. This can be realized by changing the low-pass filter between trap electrodes and voltage supply, which currently limits electrode-to-electrode transports to around 30 µs. However, a new filter should still provide decent noise suppression at

the low transient axial trap frequencies during the separation operation.
For long-distance transports between multiple electrodes, we currently use concatenated electrode-to-electrode transports, where ions are accelerated and decelerated multiple times. This method should be altered to a scheme, that updates all involved electrodes simultaneously and enables a faster transport over multiple electrodes with only one acceleration and one deceleration phase, that is capable of creating coherent excitation.
The stability of the quantizing magnetic field, which is generated by permanent magnets, is important to single-qubit rotations in the quantum logic circuits. We observed, that small field drifts correlate with the temperature of the magnets. Therefore, the qubit frequency stability would benefit from temperature-stabilized magnets. Alternatively, the magnets could be combined with other magnets with a different temperature dependence, to make them more robust with respect to temperature changes.
The capabilities of our quantum processor could be increased by a second laser interaction zone in the future, which would allow for a higher degree of parallelization. Furthermore, a second ion species for sympathetic recooling would be desirable, to remove residual motional excitation of the ions without disturbing the qubit state. Ground state cooling could be performed with sympathetic electromagnetically-induced-transparency laser cooling [Lin13]. A second ion species would also increase the versatility of our device, as information can be stored and measured in such a qubit, without disturbing the qubits of another species.
In quantum circuits, such as the quantum teleportation circuit, conditional measurement operations are used. The result of a projective measurement on one qubit, determines the parameters for operations on another qubit. In our setup, this would require a tight focusing of the cycling transition laser beam near 397 nm, such that distant qubits are not depolarized. Additionally, the result of the photo-multiplier measurement would need to be processed in real time and fed forward to subsequent quantum logic operations.

10.2. Control advancement

Our quantum processor is capable of performing more complex quantum logic circuits, than the four-qubit entanglement circuit, which is presented in this thesis. We aim to scale the operations up to more than ten qubits in the future. Our universal set of gate operations is comprised of only two gates – single-qubit rotations and an entangling geometric phase gate. The four-qubit GHZ state circuit is comprised of these operations

and was developed and optimized by hand. Optimizing the circuit followed the paradigm, to use as few shuttling operations and logic gates as possible. More complex algorithms however, will require an automated optimization as in [Neb09; Mar16], because the parameter space is too large for manual optimization. Such an optimization routine is also referred to as *quantum compiler*.
The quantum processor also requires an *operating system*, which is currently under development. The system will reduce the programming time for quantum algorithms significantly. Programming of experimental sequences currently requires careful attention, as ion trajectories need to be tracked manually in the code. The new operating system will offer preprogrammed blocks of shuttling and logic operations. It will also optimize the electric DC potential along the trap axis to allow for fast shuttling operations with a large qubit register.
Low-pass filters between DC supply and trap electrodes distort the waveforms, which are designed in the control computer. By measuring the transfer function of the filters, it is possible to account for this distortion in the voltage ramp design, and thus un-distort the waveforms. This procedure will result in a higher degree of control over the ion motion. We estimate, that shuttling operations can be realized significantly faster with this technique, featuring less motional excitation.

10.3. Quantum error correction

A fault-tolerant quantum computer requires quantum error correction (QEC), to correct for detrimental coupling to the outside world. Error correction is not as simple, as in a classical computer, due to a number of reasons. A single qubit is often in a superposition state, consequently a continuum of errors can occur on it. If we measure a qubit, we destroy the quantum information, which it contains and due to the no-cloning theorem [Woo82], it is not possible to create redundant copies of the qubit information. However, there exist QEC schemes, which encode the information of a single logical qubit, in an entangled state of multiple physical qubits [Sho95; Ste96]. If, for instance, a bit flip error occurs, the QEC code can detect this error and correct for it without a projective measurement of the logical qubit. An experimental realization of a QEC algorithm is demonstrated in [Nig14] with a linear ion string. The authors encode one logical qubit in seven physical ion qubits and are able to "...detect one bit flip error, one phase flip error, or a combined error of both, regardless on which of the qubits they occur."

Their encoding scheme is the topological seven-qubit color code [Bom06], which features an important property, called *transversality* – if one desires to perform a single-qubit rotation on the logical qubit, it suffices to perform this operation simultaneously on the seven physical qubits.
A comprehensive analysis of QEC schemes for trapped ion systems is provided in [Ber17]. The authors develop concrete QEC schemes and assess their performance with numerical simulations.
In the following, we introduce one scheme that could be realized in our setup in future experiments, see figure 10.2. The basic idea is, to map an *error syndrome* to an ancillary qubit and read out its state. The result of the measurement determines, whether an error occurred to the logical qubit and needs to be corrected. Subsequently, the ancillary qubit is reinitialized and used for additional error syndrome readout.
A variety of experimental building blocks is required to successfully implement this sequence. Reordering of a three-ion crystal, with three sequential two-ion rotation operations, was successfully demonstrated in our setup and could be straightforwardly extended to a four-ion crystal [Kau17a]. We estimate, that the operation could also be performed simultaneously on a string of more than two ions. The remaining required shuttling operations have been demonstrated in our setups in [Wal12; Rus14] and in this thesis. Some experimental development will be necessary to separate a four-ion crystal into a two-ion pair and two single ions, within a short time and without significant motional excitation. In the current situation, we do not have a second ion species available for sympathetic recooling. An execution of the sequence at a reduced performance should still be feasible, before the experimental hardware for a second ion species is installed. The sequence requires measurement and real time feedback operations, which are currently not available in our setup. However, we plan to implement this functionality soon. The sequence also requires single-qubit and two-qubit quantum logic gates, which have been demonstrated in a scalable scheme at high fidelity in this thesis.
Extensive numerical simulations are carried out, by the authors of [Ber17]. They find, that repeated runs of the presented scheme can extend the coherence time of a logical qubit by a factor of two, compared to an unprotected physical qubit. However, the experimental parameters, which are used in their simulation, are anticipated future values. For instance, the infidelity of a two-qubit gate is anticipated to be $2 \cdot 10^{-4}$. This is one order of magnitude better, than the best gate infidelity of $5 \cdot 10^{-3}$ in our setup, and a factor of four better than the best reported infidelity for a two-qubit gate [Gae16].

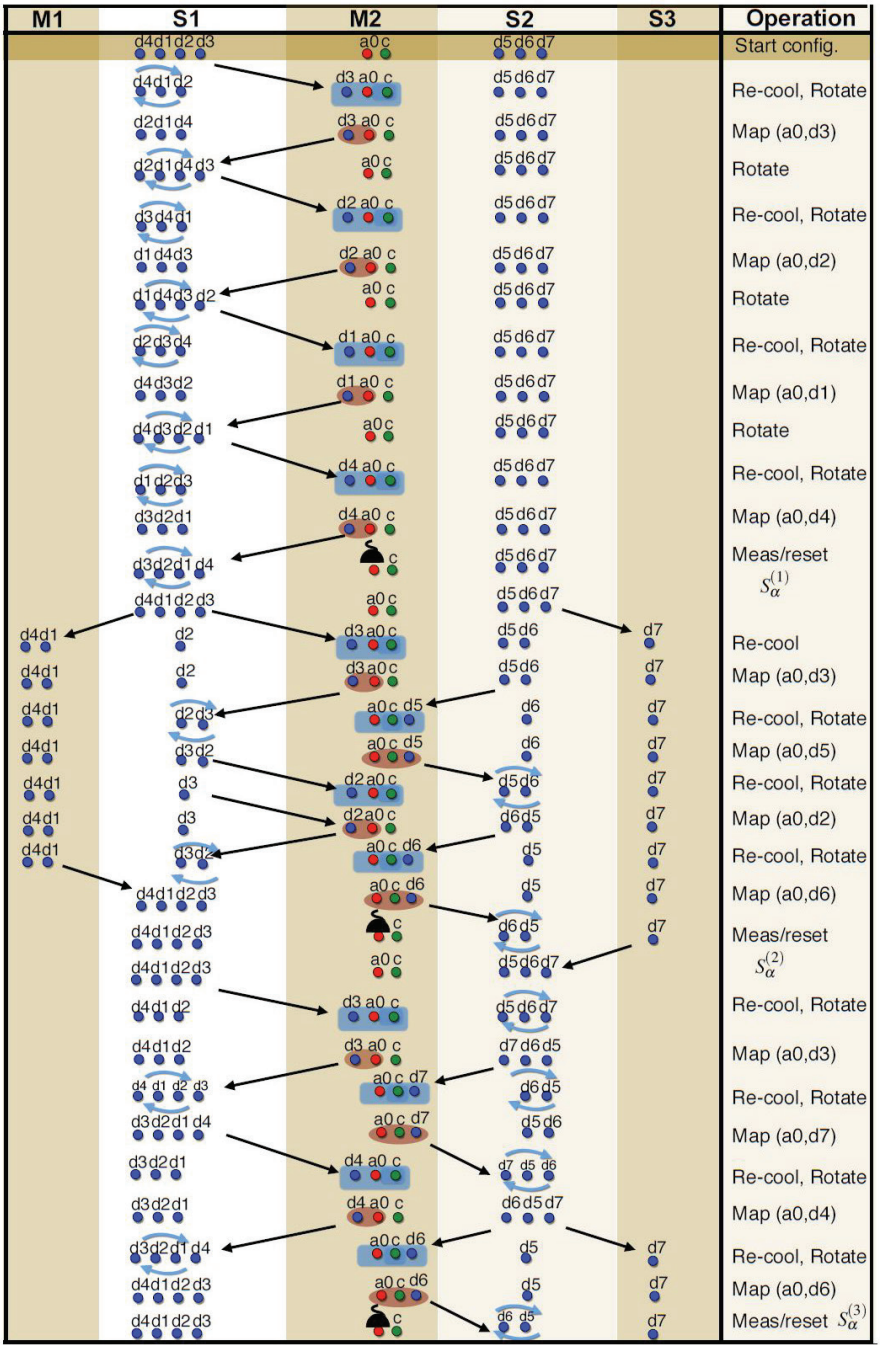

Figure 10.2.: Envisioned quantum error correction scheme for a segmented ion trap. Image taken from [Ber17]. Ions are shuttled along the horizontal direction between five different ion trap zones M1,S1,M2,S2 and S3. The time axis for the operations is top down. Blue ions are data ions and a red ion represents an ancillary ion of the same species, such as $^{40}Ca^{+}$. A green ion, which could be $^{88}Sr^{+}$, is used for sympathetic recooling. Red ellipses indicate two-ion entangling gates and blue rectangles show sympathetic recooling operations.

The performance of single-qubit gates in our setup would need to improve by a factor of five to meet the anticipated parameters. We expect to approach the required parameter regime for quantum logic gates by implementing the planned experimental improvements, which are described in section 10.1. For shuttling operations, an improvement of duration and motional excitation by a factor of about 2-3 is required. We estimate that such improvement can be realized, by employing a filter-un-distortion technique, as described in section 10.2. State discrimination via fluorescence detection is anticipated to be performed within 30 µs, which is an order of magnitude faster, than in our current setup. Improving the photon collection efficiency will probably require an optical setup with increased numerical aperture to observe the ions.
To conclude, we estimate that the envisioned scheme could be realized in our apparatus, when a second ion species and conditional measurement operations are added to our experiment. With the current experimental performance of quantum logic gates, shuttling operations and state discrimination, the regime of beneficial QEC would not be reached, according to numerical simulations. Therefore, the performance of the experimental building blocks requires continuous development to reach the goal of keeping an encoded qubit alive.

10.4. Large-scale quantum computing

A large-scale trapped-ion quantum computer will probably require photonic interconnects between individual ion trap computation modules [Mon14; Inl17], see figure 10.3. The idea is, to guarantee a high degree of control for few-qubit quantum registers. Probabilistic photonic interfaces between separate registers could be used to create entanglement between distant ion traps [Moe07; Olm09].
We have demonstrated scalable quantum logic operations in our apparatus and our research group is currently working on the realization of a quantum CCD with a photonic interface, see figure 10.3.
The goal is, to use the device for the realization of a quantum repeater node, which allows for the transmission of quantum information over large distances [Pfi16]. The envisioned protocol is based on creating entanglement between ions in different quantum repeater nodes, by coupling them to photons in a cavity.

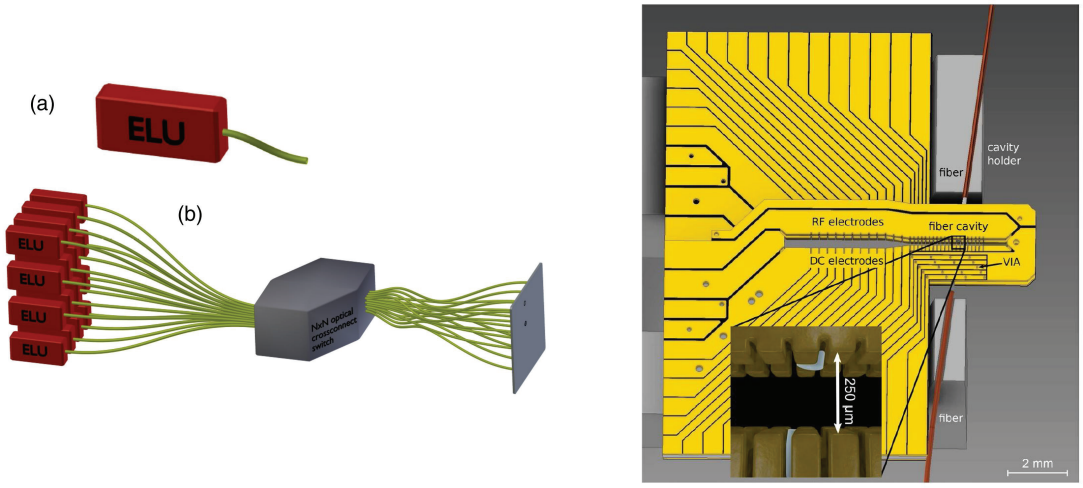

Figure 10.3.: Photonic interconnects for quantum information processing. **Left:** Proposed large-scale modular quantum computer with individual computation modules (ELU), connected by optical fibers. Each of the modules should contain 10-100 atomic ion qubits. Image taken from [Mon14]. **Right:** Micro-structured ion trap with an integrated optical fiber cavity. The dimensions of the ion trap are similar to the trap, which is presented in this thesis. Image taken from [Pfi16].

Aside from the ion-light coupling, shuttling and quantum logic operations are required to realize the protocol. With further technical development, similar devices could be used for a large-scale modular quantum computer.

A

Appendix – Measurement Data

Motional coherence data without AC trigger (section 6.3)

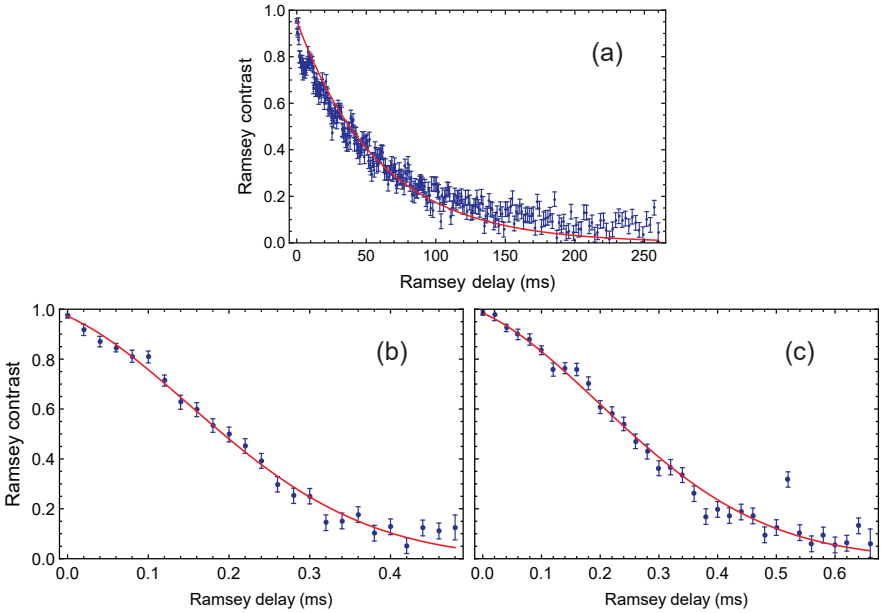

Figure A.1.: Measurement of the motional coherence of the axial mode ω_x (a), the lower radial mode ω_y (b) and the higher radial mode ω_z (c) without triggering to the AC line. The red line corresponds to a weighted least square fit of the form $f(t) = A\exp(-\gamma t - \gamma_2^2 t^2)$, the obtained parameters and coherence times are summarized in table 6.2. Each data point corresponds to 2×600 measurements.

Motional excitation from the swapping operation (section 7.1)

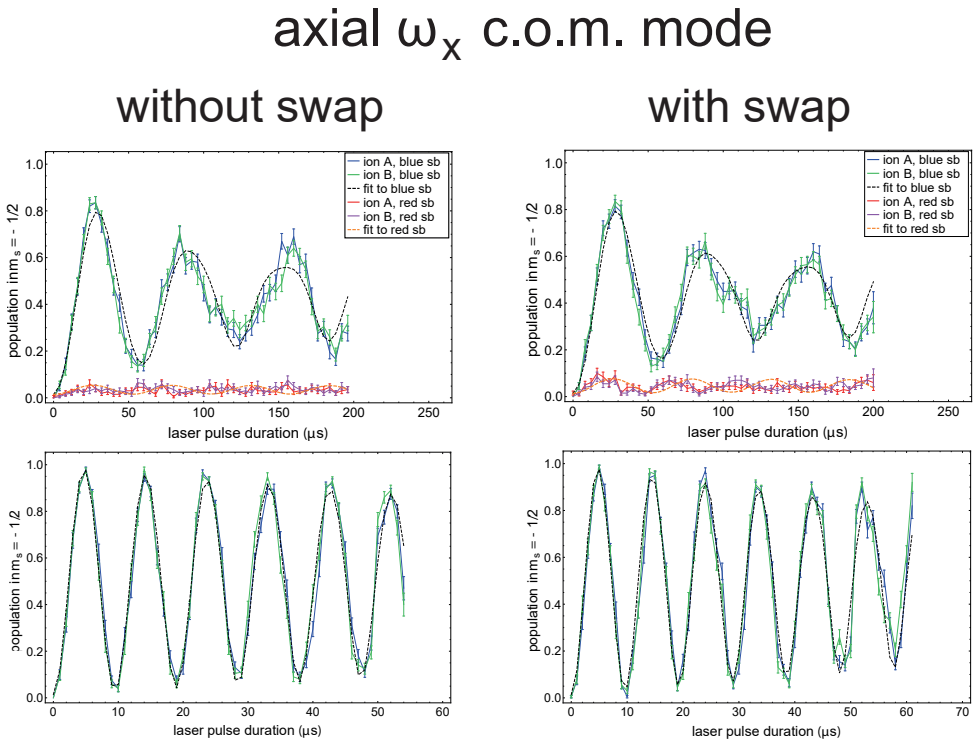

Figure A.2.: Rabi oscillation data from two ground state cooled ions A and B to investigate the motional excitation from the swapping operation – results are listed in table 7.1. The data without the swap operation features a wait time, that is equal to the swapping duration, to make the measurements comparable. For each mode the carrier transition is measured additionally to the red and blue sideband. The dashed line corresponds to a fit, see section 7.1. Each data point corresponds to 200 state interrogations, error bars correspond to the standard error from binomial readout statistics.

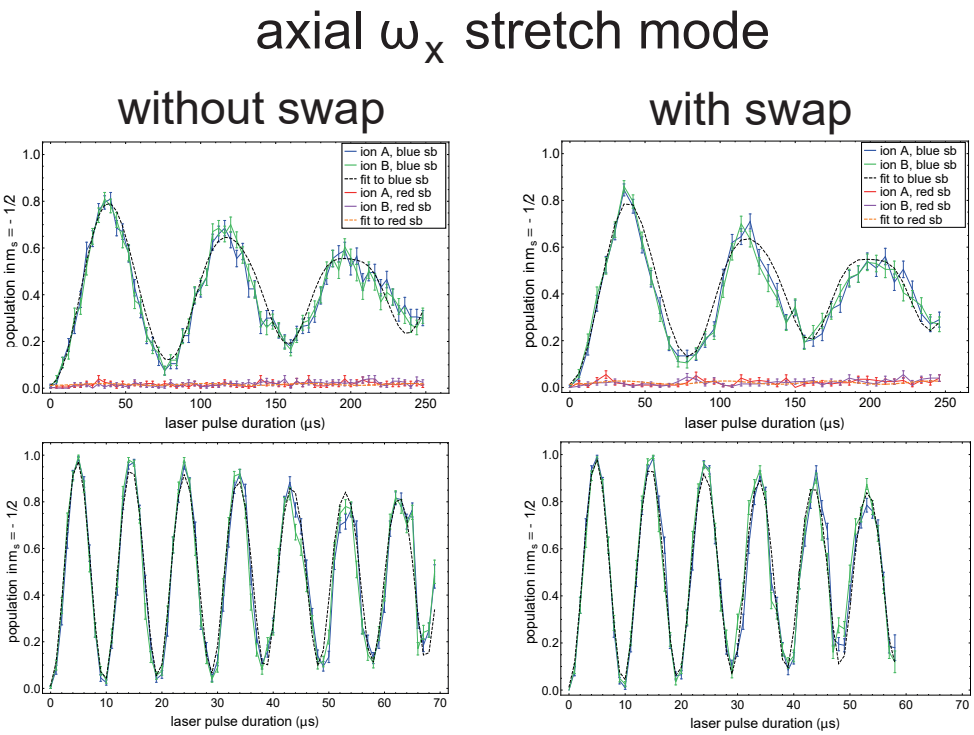

Figure A.3.: Rabi oscillation data from two ground state cooled ions A and B to investigate the motional excitation from the swapping operation – results are listed in table 7.1.

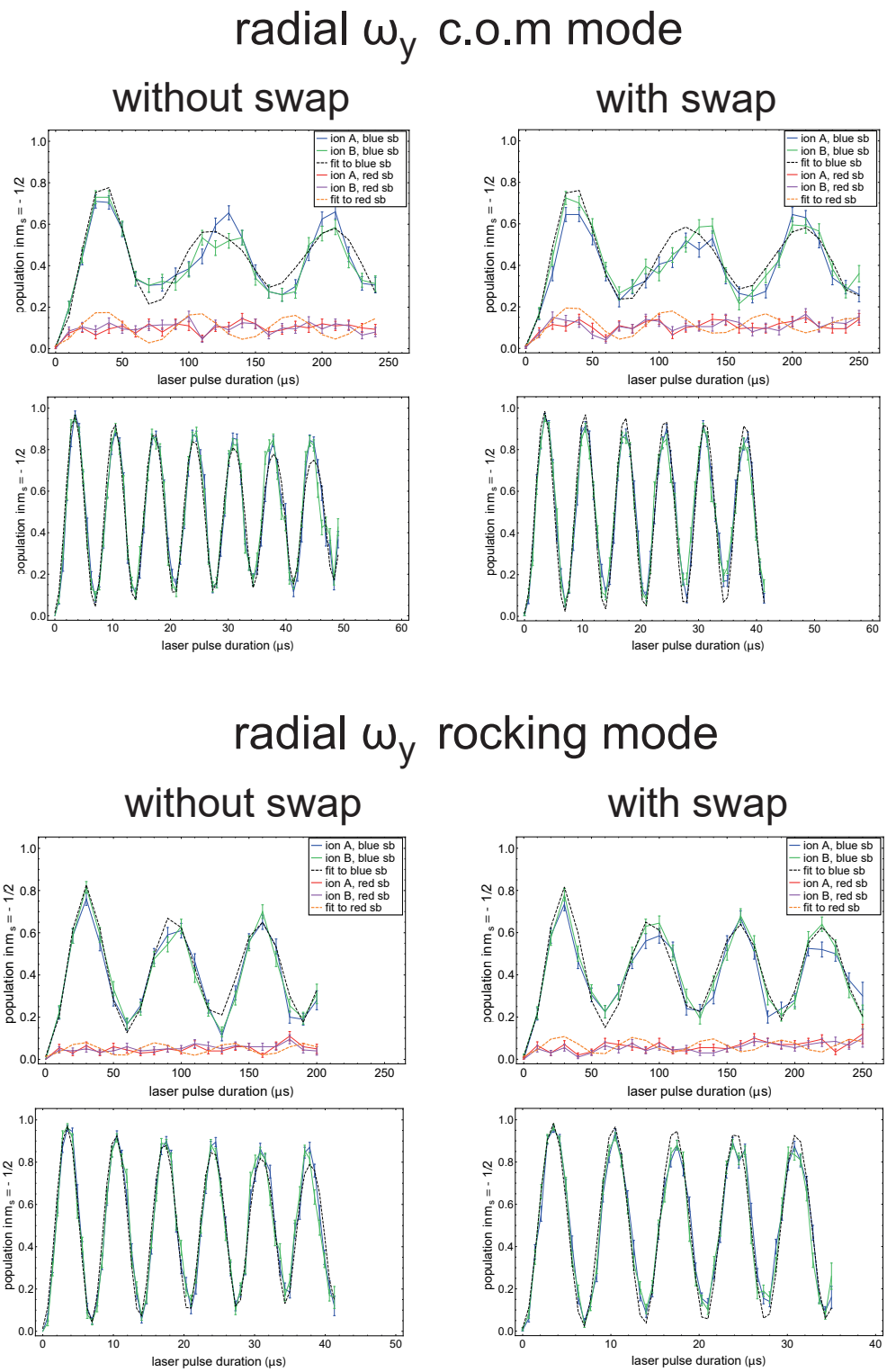

Figure A.4.: Rabi oscillation data from two ground state cooled ions A and B to investigate the motional excitation from the swapping operation – results are listed in table 7.1.

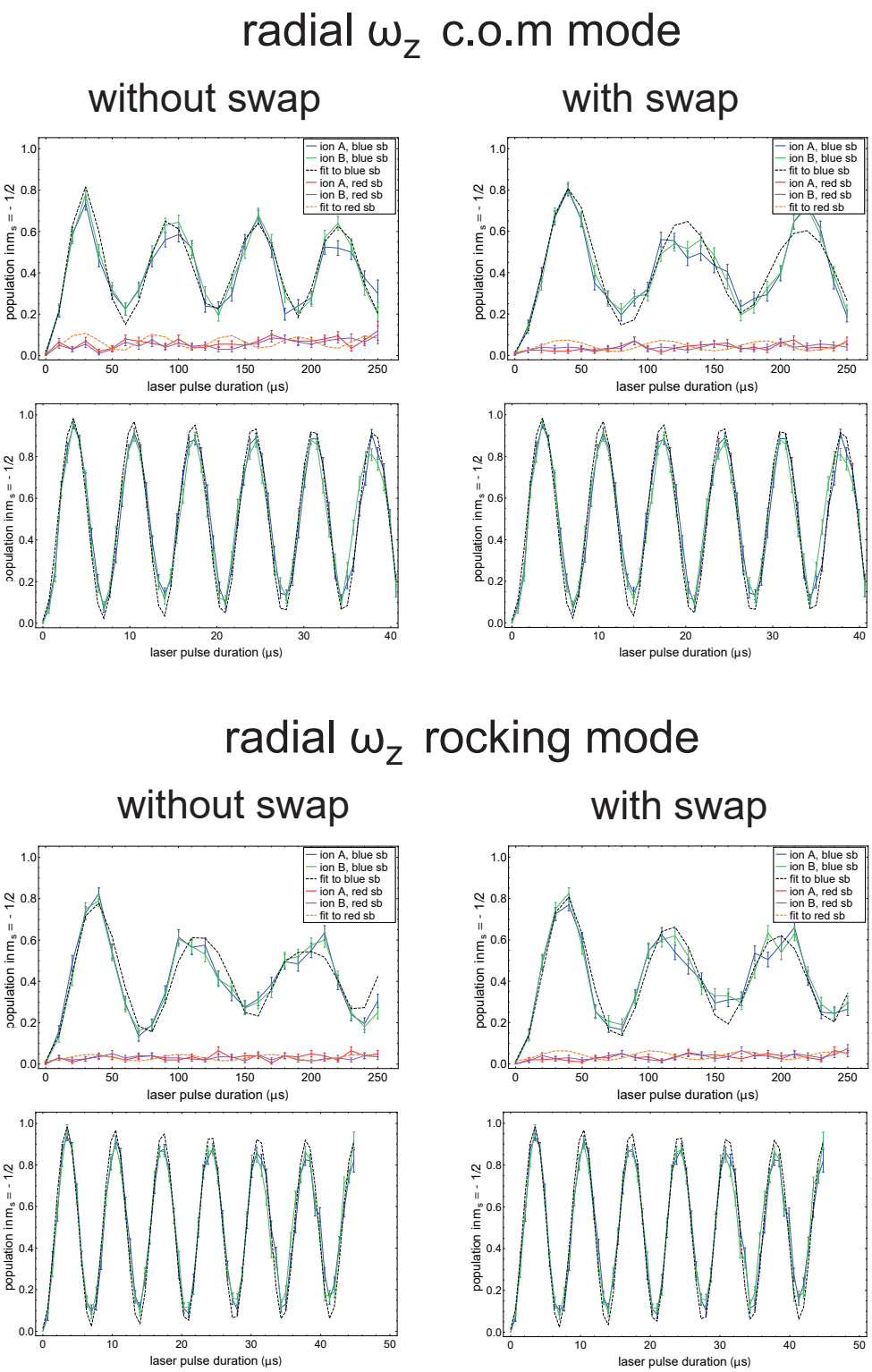

Figure A.5.: Rabi oscillation data from two ground state cooled ions A and B to investigate the motional excitation from the swapping operation – results are listed in table 7.1.

χ-matrix determined from quantum process tomography (section 7.2)

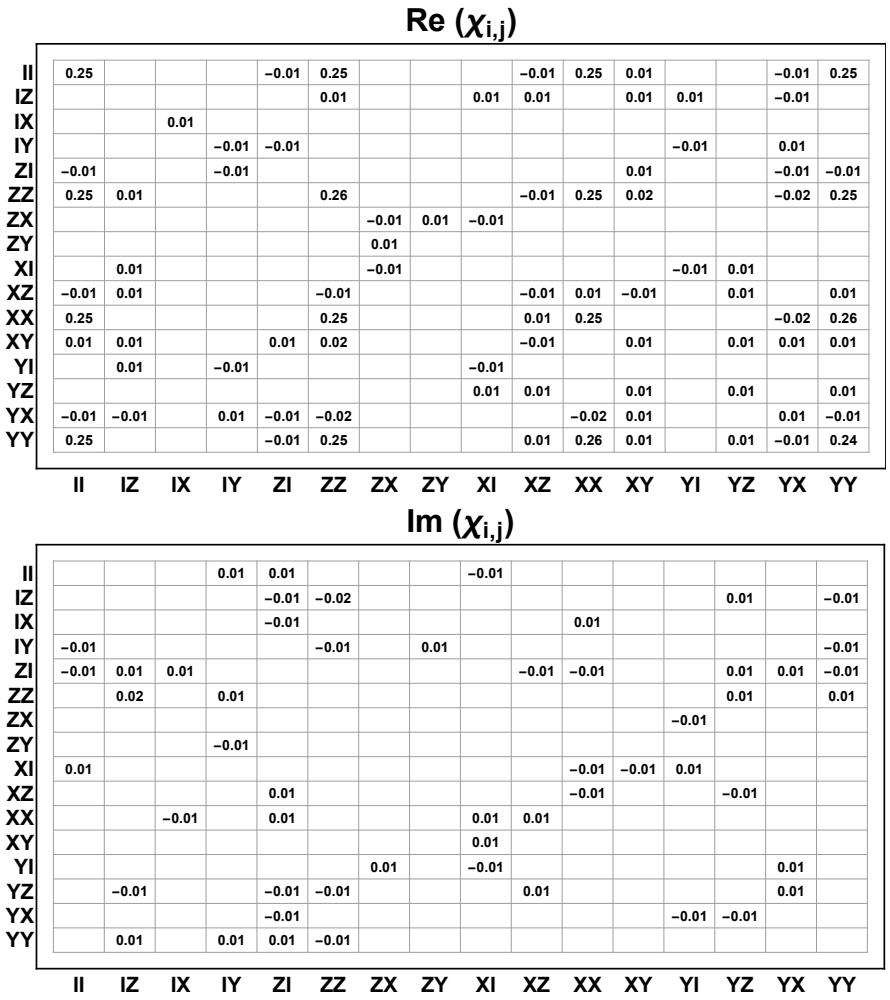

Figure A.6.: Real and imaginary part of the χ-matrix, which was obtained in the quantum process tomography shown in figure 7.4 of the main text. The absolute value of empty fields is smaller than 0.01.

Three-ion truth table (section 7.3)

	$\|\uparrow\uparrow\uparrow\rangle$	$\|\uparrow\uparrow\downarrow\rangle$	$\|\uparrow\downarrow\uparrow\rangle$	$\|\uparrow\downarrow\downarrow\rangle$	$\|\downarrow\uparrow\uparrow\rangle$	$\|\downarrow\uparrow\downarrow\rangle$	$\|\downarrow\downarrow\uparrow\rangle$	$\|\downarrow\downarrow\downarrow\rangle$
$\|\uparrow\uparrow\uparrow\rangle$	1.001	0.007	0.003	0	0.002	0	0	0
$\|\uparrow\uparrow\downarrow\rangle$	−0.004	0	0	0	0.998	0.006	0.003	0
$\|\uparrow\downarrow\uparrow\rangle$	−0.002	0	1.002	0.007	0	0	0	0.001
$\|\uparrow\downarrow\downarrow\rangle$	0	0	−0.004	0	−0.002	0	0.998	0.009
$\|\downarrow\uparrow\uparrow\rangle$	−0.007	0.995	0	0.003	0	0.007	0	0
$\|\downarrow\uparrow\downarrow\rangle$	0	−0.005	0	0	−0.007	1.001	0	0.003
$\|\downarrow\downarrow\uparrow\rangle$	0	−0.004	−0.006	0.999	0	0	0	0.006
$\|\downarrow\downarrow\downarrow\rangle$	0	0	0	−0.006	0	−0.002	−0.007	1.002

Figure A.7.: Measured three-ion truth table corresponding to the reconfiguration of a three-ion crystal. Small negative values arise due to the readout error correction.

Bell state density matrix (section 8.4)

Re (ρ)

	$\|\uparrow\uparrow\rangle$	$\|\uparrow\downarrow\rangle$	$\|\downarrow\uparrow\rangle$	$\|\downarrow\downarrow\rangle$
$\|\uparrow\uparrow\rangle$	0.506	0.013	0.006	−0.039
$\|\uparrow\downarrow\rangle$	0.013	0.003	0.016	−0.003
$\|\downarrow\uparrow\rangle$	0.006	0.016	0.001	−0.013
$\|\downarrow\downarrow\rangle$	−0.039	−0.003	−0.013	0.49

Im (ρ)

	$\|\uparrow\uparrow\rangle$	$\|\uparrow\downarrow\rangle$	$\|\downarrow\uparrow\rangle$	$\|\downarrow\downarrow\rangle$
$\|\uparrow\uparrow\rangle$	0	0.006	0.004	−0.495
$\|\uparrow\downarrow\rangle$	−0.006	0	0	−0.002
$\|\downarrow\uparrow\rangle$	−0.004	0	0	−0.006
$\|\downarrow\downarrow\rangle$	0.495	0.002	0.006	0

Figure A.8.: Real and imaginary part of the experimentally reconstructed density matrix ρ of a two-qubit Bell state, as shown in figure 8.7. The data is corrected for readout errors.

Four-ion GHZ state density matrix (section 8.5.2)

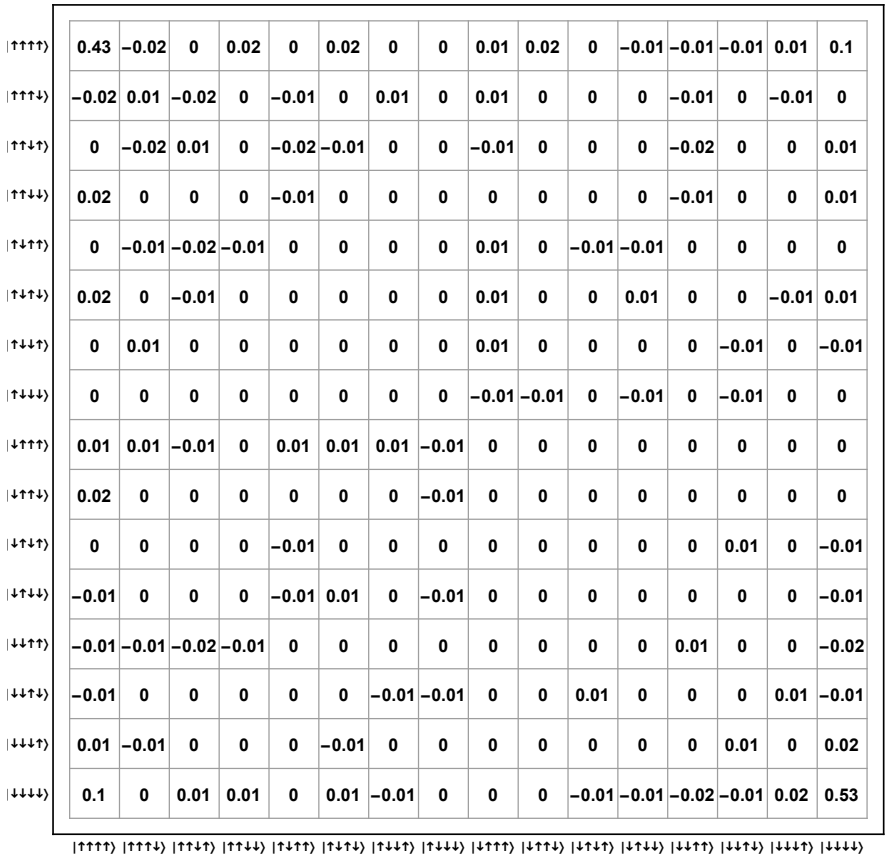

Figure A.9.: Real part of the experimentally reconstructed density matrix ρ of a four-qubit GHZ state, including correction for readout errors.

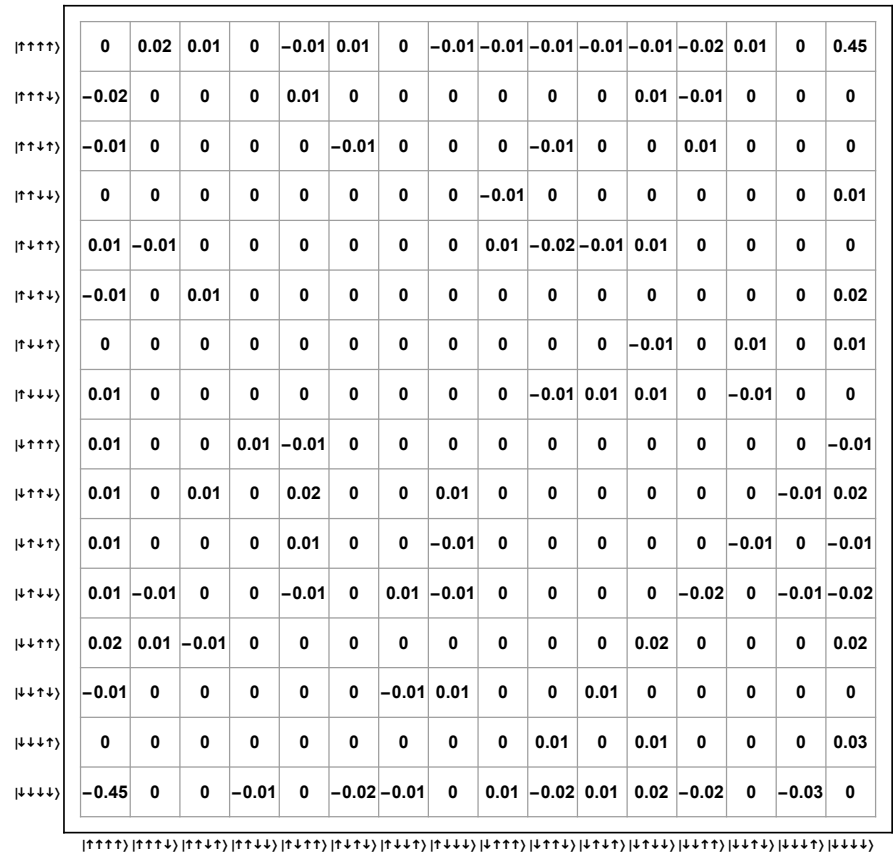

Figure A.10.: Imaginary part of the experimentally reconstructed density matrix ρ of a four-qubit GHZ state, including correction for readout errors.

Lifetime of entangled states (section 8.6)

Here, the lifetime measurement data from section 8.6 is shown. The parity contrast is determined from a reduced measurement scheme and corresponds to the coherence of the entangled state, see section 8.5. A maximum likelihood method is used to compute the contrast and the error bars [Rus16].

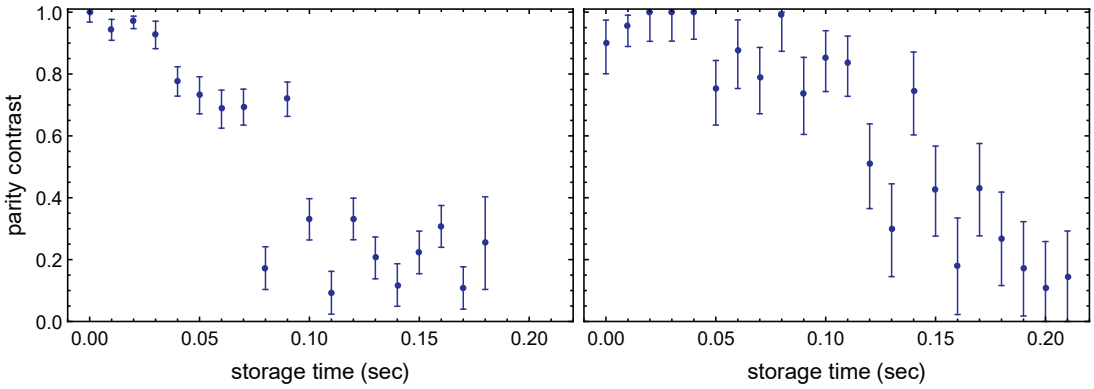

Figure A.11.: Lifetime measurement of a two-ion Bell state $|\Psi_2\rangle = 1/\sqrt{2}(|00\rangle + e^{i\phi}|11\rangle)$. In this measurement, both ions are stored in the LIZ during the storage time. Both measurements are identical – in the left panel, each data point corresponds to 2×200 measurements and in the right panel, each data point corresponds to 2×40 measurements to increase robustness with respect to magnetic field drifts. We estimate a $1/\sqrt{e}$ coherence time of 100(30) ms from this data.

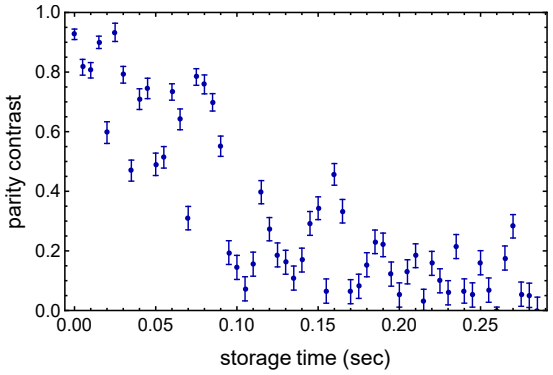

Figure A.12.: Lifetime measurement of a three-ion GHZ state $|\Psi_3\rangle = 1/\sqrt{2}(|000\rangle + e^{i\phi}|111\rangle)$. Each data point corresponds to 2×600 measurements, we estimate a $1/\sqrt{e}$ coherence time of 60(30) ms from this data.

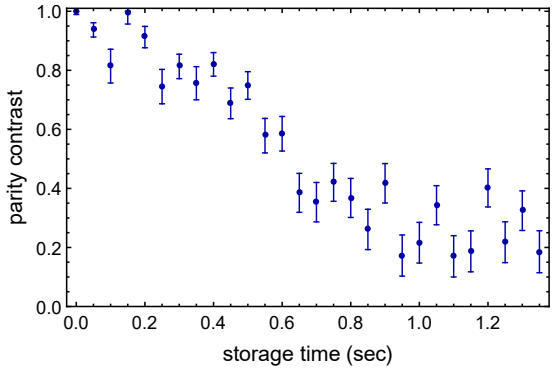

Figure A.13.: Lifetime measurement of a two-ion Bell state $|\Psi_2\rangle = 1/\sqrt{2}(|00\rangle + e^{i\phi}|11\rangle)$ **with a rephasing spin-echo π-pulse**. In this measurement, both ions are stored in the LIZ during the storage time. Each data point corresponds to 2×200 measurements, we estimate a $1/\sqrt{e}$ coherence time of 600(100) ms from this data.

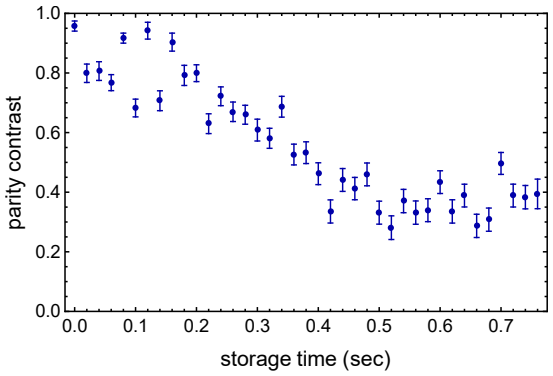

Figure A.14.: Lifetime measurement of a three-ion GHZ state $|\Psi_3\rangle = 1/\sqrt{2}(|000\rangle + e^{i\phi}|111\rangle)$ **with a rephasing spin-echo π-pulse**. Each data point corresponds to 2×600 measurements, we estimate a $1/\sqrt{e}$ coherence time of 300(50) ms from this data.

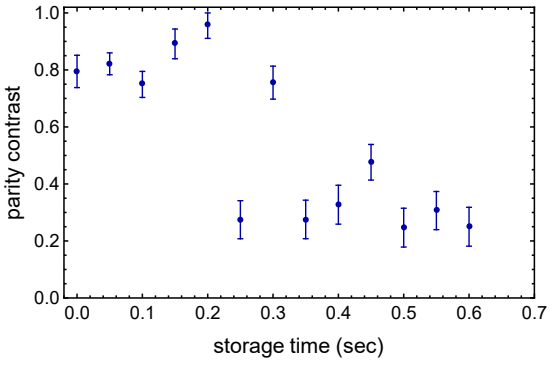

Figure A.15.: Lifetime measurement of a four-ion GHZ state $|\Psi_4\rangle = 1/\sqrt{2}(|0000\rangle + e^{i\phi}|1111\rangle)$ **with a rephasing spin-echo π-pulse**. Each data point corresponds to 2×200 measurements, we estimate a $1/\sqrt{e}$ coherence time of 250(100) ms from this data.

Ground state cooling of the zigzag vortex mode (section 9.2)

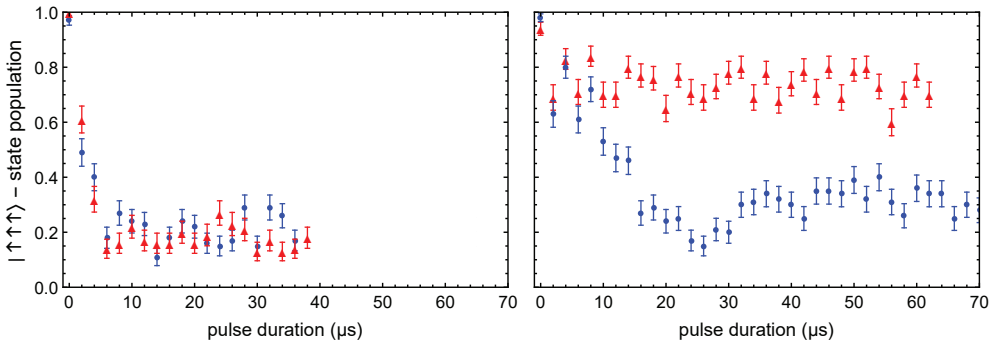

Figure A.16.: Ground state cooling of the zigzag vortex mode of a three-ion zigzag crystal. **Left:** Rabi oscillation data on the red sideband (red triangles) and the blue sideband (blue circles) of the vortex mode after Doppler cooling. **Right:** Rabi oscillation data after resolved sideband cooling of the vortex mode. Results of ground state cooling on the squish mode are shown in chapter 9. Each data point corresponds to 100 single measurements, error bars correspond to the standard error from binomial readout statistics.

B

Appendix – Methods And Data Analysis

B.1. Motional state readout

Here, we provide details on the motional state readout, see section 7.1 of the main text. To investigate the motional excitation from the swapping operation, we cool each of the six secular modes of the two ion crystal close to the motional ground state via resolved sideband cooling on the stimulated Raman transition. We either perform the swapping operation or wait for the respective duration to obtain reference data. Subsequently, we drive Rabi oscillations on the stimulated Raman transition, either the carrier (phonon number change $\Delta n = 0$), red ($\Delta n = -1$) or blue ($\Delta n = +1$) sideband transition of the particular secular mode to be measured on both ions for a variable time t. The ions are jointly shelved to the metastable state for spin readout, then the ion crystal is separated, and state-dependent fluorescence is observed individually for each ion. We thus obtain single ion data for sideband Rabi oscillations of the secular modes of the two ion crystal. The data for all secular modes is shown in figures A.2 through A.5.
We jointly fit the measurement data for carrier and sidebands to a model describing Rabi oscillations of two homogeneously driven ions on arbitrary sideband transitions, valid also outside the Lamb-Dicke regime. We consider an initial number state characterized by the phonon number n on mode i, and a phonon number difference per spin flip Δn, where $\Delta n = +(-)1$ for the first blue (red) sideband. The light-motion coupling for a given secular mode i is described by the carrier Rabi frequency Ω, the Lamb-Dicke factor η_i, and the matrix elements

$$\begin{aligned} m_1 &= M_{n,n+\Delta n} \\ m_2 &= M_{n+\Delta n,n+2\Delta n}, \end{aligned} \tag{A-1}$$

where $M_{n,n+\Delta n}$ is given by equation 2.15. By analytically solving the time-dependent Schrödinger equation, we obtain the following expressions for the probabilities to find both ions in $|\downarrow\rangle$, $P_{\downarrow\downarrow}$, both ions in $|\uparrow\rangle$, $P_{\uparrow\uparrow}$, and both ions in different spin states, $P_{\uparrow\downarrow} = P_{\downarrow\uparrow}$:

$$\begin{aligned}
P_{\uparrow\uparrow,\Delta n,\eta_i}(t) &= \left(\frac{1}{m_1^2+m_2^2}\right)^2 \times \left[m_2^4 + 2m_1^2 m_2^2 e^{-\gamma t}\cos\left(\sqrt{\frac{m_1^2+m_2^2}{2}}\Omega t\right)\right. \\
&\quad \left. + \frac{m_1^4}{2}\left(1 + e^{-\gamma t}\cos\left(\sqrt{2(m_1^2+m_2^2)}\ \Omega t\right)\right)\right] \\
P_{\downarrow\downarrow,\Delta n,\eta_i}(t) &= \left(\frac{m_1 m_2}{m_1^2+m_2^2}\right)^2 \times \left[\frac{3}{2} + \frac{1}{2}e^{-\gamma t}\cos\left(\sqrt{2(m_1^2+m_2^2)}\ \Omega t\right)\right. \\
&\quad \left. - 2e^{-\gamma t} cos\left(\sqrt{\frac{m_1^2+m_2^2}{2}}\Omega t\right)\right] \\
P_{\uparrow\downarrow,n,\Delta n,\eta_i}(t) &= P_{\downarrow\uparrow,n,\Delta n,\eta_i}(t) = \frac{m_1^2}{4(m_1^2+m_2^2)}\left(1 - e^{-\gamma t}\cos\left(\sqrt{2(m_1^2+m_2^2)}\ \Omega t\right)\right)
\end{aligned} \tag{A-2}$$

where n is the initial quantum number, Δn is the phonon number change per single spin flip, and t is the time of exposure to the driving field. We assume all secular modes of the ion crystal to be in a coherent (Glauber) state after the swapping operation. This assumption is justified, as the duration of the swapping is small compared to the inverse heating rates (typically 0.3 s per phonon on the axial COM mode), and the initial state is rather close to the ground state. Thermal and coherent excitation on spectator modes leads to dephasing of the Rabi oscillations, which is described empirically by the additional decay factors $e^{-\gamma t}$. For each spin configuration $s_1 s_2$, we describe the measured signals by averaging over $P_{s_1 s_2,n,\Delta n,\eta_i}(t)$ and weighting with the phonon number distribution for a coherent state with mean phonon number $\bar{n}_i$:

$$P_{s_1 s_2,\bar{n}_i,\Delta n,\eta_i}(t) = \sum_{n=0}^{N} e^{-\bar{n}_i}\frac{\bar{n}_i^n}{n!}P_{s_1 s_2,n,\Delta n,\eta_i}(t), \tag{A-3}$$

where N is a cutoff phonon number. We use a fit to the first red and blue sidebands as well as the carrier transition to determine the average phonon number of each motional mode. For each fit, the floating parameters are Ω, η_i and $\bar{n}_i$. The obtained phonon numbers are listed in table 7.1.

As the fluorescence readout is performed separately for the two ions, the recorded signals

correspond to the probability of finding ion 1 in $|\downarrow\rangle$ ($P_{\downarrow\downarrow,\bar{n}_i,\Delta n,\eta_i}(t) + P_{\downarrow\uparrow,\bar{n}_i,\Delta n,\eta_i}(t)$) and of finding ion 2 in $|\downarrow\rangle$ ($P_{\downarrow\downarrow,\bar{n}_i,\Delta n,\eta_i}(t) + P_{\uparrow\downarrow,\bar{n}_i,\Delta n,\eta_i}(t)$). In the main part of this work, the average of these probabilities, $\frac{1}{2}\left(P_{\downarrow\uparrow,\bar{n}_i,\Delta n,\eta_i}(t) + P_{\uparrow\downarrow,\bar{n}_i,\Delta n,\eta_i}(t) + 2P_{\downarrow\downarrow,\bar{n}_i,\Delta n,\eta_i}(t)\right)$ is shown in figure 7.2.

B.2. Readout error correction for quantum process tomography

Here, we provide details on readout error correction, see section 7.2 of the main text. For the measurements on full process tomography for two ions, 16 different settings for preparation $s = \{s_1, s_2\}$ with $s_i \in \{|\uparrow\rangle, |\uparrow\rangle - i\,|\downarrow\rangle, |\uparrow\rangle - |\downarrow\rangle, |\downarrow\rangle\}$ and 9 different setting for detection $d = \{d_1, d_2\}$ with $d_i \in \{Z, Y, X\}$ are probed. Each setting (s, d) is probed on average N times. Small fluctuations of the measurement numbers between different settings arise from postselection removal of events where ions are lost or crystal melting occurs, these fluctuations are ignored in the following. For each setting, $N_f^{(s,d)}$ events out of N detections yield the fluorescence result $f = \{f_1, f_2\}$, where $f_i = \{\text{dark,bright}\}$. From this data, event frequencies $P_f^{(s,d)} = N_f^{(s,d)}/N$ are calculated. For a given preparation setting s , these frequencies are used for linear inversion to obtain the resulting density matrix $\rho^{(s)}$. The set of 16 resulting density matrices is used for a second linear inversion to obtain the resulting process matrix χ_{meas}. The process fidelity F with respect to the ideal process χ_{ideal} is then given by the trace norm $F = Tr(\chi_{ideal}^{\dagger}\chi_{meas})$.

We estimate confidence intervals for the mean process fidelity via parametric bootstrapping. For this, we generate 500 instances of random measurement data. For each instance, we use the event frequencies $P_f^{(s,d)}$ to generate multivariate random integers $\tilde{N}_f^{(s,d)}$, drawn from a multinomial distribution $f(\{\tilde{N}_f^{(s,d)}\}, \{P_f^{(s,d)}\})$, where $\sum_f \tilde{N}_f^{(s,d)} = N$ and $\sum_f P_f^{(s,d)} = 1$. These random event numbers serve to calculate random event frequencies $\tilde{P}_f^{(s,d)}$, which are used in turn to generate random process matrices $\tilde{\chi}_{meas}$. Averaging over the 500 instances, we obtain the mean process fidelity along with a confidence interval.
In order to correct for readout errors, we perform the same procedure *without* SWAP operation, obtaining the event frequencies $\bar{P}_f^{(s,d)}$, the density matrices $\bar{\rho}^{(s)}$ and the process matrix $\bar{\chi}_{meas}$. We restrict ourselves to the prepared spin configurations which are eigenstates of the Z_i operators, $s' \in \{|\uparrow\uparrow\rangle, |\uparrow\downarrow\rangle, |\downarrow\uparrow\rangle, |\downarrow\downarrow\rangle\}$. The diagonal elements

of the reconstructed density matrices $\bar{\rho}_{kk}^{(s')}$ indicate the conditional probabilities to detect fluorescence result f_k for preparation setting s' and detection setting $d = Z_1 Z_2$. Under the assumption of uncorrelated readout errors, these probabilities $\bar{\rho}_{kk}^{(s')}$ are products of the probabilities to detect dark/bright events for the ion in $|\uparrow\rangle/|\downarrow\rangle$ for each ion i:

$$\begin{aligned} \bar{\rho}_{kk}^{(s')} &= P_{f_k}^{(s',Z_1Z_2)} \\ &= p_1(f_{k,1}|s'_1) \cdot p_2(f_{k,2}|s'_2), \end{aligned} \tag{A-4}$$

This holds under the assumption of perfect state preparation. It further holds that

$$\begin{aligned} p_i(\mathrm{dark}_i|\uparrow_i) &\lesssim 1 \\ p_i(\mathrm{bright}_i|\uparrow_i) &\gtrsim 0 \\ p_i(\mathrm{dark}_i|\downarrow_i) &\gtrsim 0 \\ p_i(\mathrm{bright}_i|\downarrow_i) &\lesssim 1 \\ p_i(\mathrm{dark}_i|\uparrow_i) + p_i(\mathrm{bright}_i|\uparrow_i) &= 1 \\ p_i(\mathrm{dark}_i|\downarrow_i) + p_i(\mathrm{bright}_i|\downarrow_i) &= 1 \end{aligned} \tag{A-5}$$

We calculate the readout probabilities $p_i(f_{k,i}|s_i)$ by using the former normalization, e.g.

$$\begin{aligned} p_1(\mathrm{dark}_1|\uparrow_1) &= \tfrac{1}{2} P_{\mathrm{dark}_1\mathrm{dark}_2}^{(\uparrow_1\uparrow_2,Z_1Z_2)} \\ &+ \tfrac{1}{2} P_{\mathrm{dark}_1\mathrm{bright}_2}^{(\uparrow_1\uparrow_2,Z_1Z_2)} \\ &+ \tfrac{1}{2} P_{\mathrm{dark}_1\mathrm{dark}_2}^{(\uparrow_1\downarrow_2,Z_1Z_2)} \\ &+ \tfrac{1}{2} P_{\mathrm{dark}_1\mathrm{bright}_2}^{(\uparrow_1\downarrow_2,Z_1Z_2)} \end{aligned} \tag{A-6}$$

These readout probabilities are used to form the readout probability matrix M,

$$M_{jk} = p_1(f_{j,1}|s'_{k,1}) \cdot p_2(f_{j,2}|s'_{k,2}). \tag{A-7}$$

This matrix determines the observed event frequencies *including* readout errors $\bar{P}_f^{(s,d)}$ from the event frequencies $\hat{\bar{P}}_f^{(s,d)}$ determined by the density matrix describing the state *before* readout:

$$\bar{P}_f^{(s,d)} = M \cdot \hat{\bar{P}}_f^{(s,d)}, \tag{A-8}$$

where the index f is running over the different observable fluorescence results. Thus, we can obtain the corrected event frequencies from

$$\hat{\bar{P}}_f^{(s,d)} = M^{-1} \cdot \bar{P}_f^{(s,d)}. \tag{A-9}$$

The corrected event frequencies can then be used for obtaining the process matrix as above, and parametric bootstrapping can be applied. From the fidelities obtained from parametric bootstrapping with the identity operation, we indeed obtain unit fidelity within the statistical error. This confirms the validity of the assumptions that the errors of preparation and single-qubit rotations are insignificant as compared to readout errors, and that the readout errors are uncorrelated.
We can thus apply the readout error correction to the tomography data for the SWAP gate:

$$\hat{P}_f^{(s,d)} = M^{-1} \cdot P_f^{(s,d)}. \tag{A-10}$$

Performing parametric bootstrapping for this case, we also generate a random instance of the identity data along with the random instance of the SWAP data, such that both M^{-1} and $\tilde{P}_f^{(s,d)}$ are random quantities. This way, we take the statistical errors of the readout correction into account.
From the identity measurement, we infer the following readout probabilities:

$$\begin{aligned} p_1(\text{dark}_1|\uparrow_1) &= 0.9941(7) \\ p_2(\text{dark}_2|\uparrow_2) &= 0.9924(9) \\ p_1(\text{bright}_1|\downarrow_1) &= 0.9888(10) \\ p_2(\text{bright}_2|\downarrow_2) &= 0.9945(7) \end{aligned} \tag{A-11}$$

The resulting corrected process χ-matrix is visualized in figure 7.4 of the main text. We additionally present the numerical data in figure A.6.
For the three-ion measurements, we proceed in a similar way. There are however only 8 preparation settings, only one detection setting (Z) and 8 fluorescence combinations. The observed event frequencies can be directly interpreted as elements of the process matrix in the truncated basis, such that no linear inversions are carried out and the readout correction can be directly applied. For the process fidelity in the truncated basis, we report the fidelities with significantly reduced statistical error, despite the fact that roughly the same number of measurements are used for each preparation setting.

The reason for this is that we prepare *and* detect only in the logical basis in this case, which leads to detection event probabilities always close to either 0 or 1. This leads to reduced shot noise.

B.3. Two-qubit gate error estimation

In the following, the experimental error sources and limitations of the two-qubit gate fidelity (section 8.4 of the main text) are analyzed analogously to [Bal14; Bal16], where good agreement between error model and experimentally realized high fidelity quantum gates is found.

Photon scattering error

During the entangling gate operation, the ions travel along a closed loop in phase space driven by strong Raman laser beams. Photons can be scattered inelastically in this process due to Raman scattering, which changes the internal state of the ions. Elastic scattering events – Rayleigh scattering – also occur and disturb the phase space trajectory with photon recoil events. To quantify this negative effect on the entangling gate fidelity, we employ the total probability P_{total} to scatter a photon during a Raman π-pulse as given by equation 8.1. In contrast to the single ion experiments, the Raman detuning Δ is about ten times smaller due to limited laser power. The duration for a single π-pulse is around 8 µs whereas the gate time t_g is 100 µs. We thus calculate the error from scattering to be $(100\,\mu s/8\,\mu s) \cdot P_{total} = 1.3 \cdot 10^{-3}$. We emphasize, that this estimation is based on the assumption that the single-qubit rotation, which is driven by the R1 and CC laser beams, operates at a similar optical power as the beams that drive the gate R4 and CC.

Motional dephasing error

While the ion spin and motion are entangled, the trap frequency ω_z must remain stable, otherwise the entangling gate fidelity is affected by the motional dephasing as characterized in section 6.3. Following [Bal16], the gate error caused by motional dephasing is determined by $0.297 \cdot \frac{t_g}{\tau_{1/e}}$, which results from integrating a master equation

with a suitable Lindblad operator. The motional coherence time with triggering to the AC line of the ω_z gate mode is $\tau_{1/e} = 6.5\,\mathrm{ms}$. The error from motional dephasing is thus estimated to be $4.6 \cdot 10^{-3}$.

Systematic errors

The duration t_g and the intensity of the gate laser pulses for the standing wave are calibrated individually in the experiment. For the calibration of the gate duration, the gate detuning is set to a fixed value. The entangling gate is then executed with variable gate time and the spin populations $P_{\uparrow\uparrow}(t_g), P_{\downarrow\uparrow}(t_g), P_{\uparrow\downarrow}(t_g), P_{\downarrow\downarrow}(t_g)$ are measured. To set the gate duration correctly, we choose a duration where the sum of the population of the odd spin states is close to zero, i.e. $P_{\downarrow\uparrow}(t_g) + P_{\uparrow\downarrow}(t_g) \approx 0$. We estimate to achieve $< 1\%$ inaccuracy in this calibration, which results in a gate fidelity error of $< 1.4 \cdot 10^{-3}$ given by $(\Delta\delta \cdot t_g)^2[1 + 2K(1 + 2\bar{n})]/16K^2$ following [Bal14], where $\Delta\delta < 2\pi \cdot 200\,\mathrm{Hz}$ is the absolute error in the gate detuning, $t_g = 100\,\mu\mathrm{s}$ is the gate duration, $K = 2$ is the number of loops in phase space and $\bar{n} \approx 0.1$ is the temperature of the gate mode.
Once the gate time is set, a calibration measurement for the intensity of the laser pulses – denoted as gate power P_g – is executed. The gate is driven by the laser beams R4 and CC. However, we only vary the intensity of the CC laser light. The calibration procedure corresponds to the execution of an entangling gate with fixed gate time and variable gate power P_g. Each of the spin populations $P_{\uparrow\uparrow}(P_g), P_{\downarrow\downarrow}(P_g)$ is then balanced as well as possible to 1/2 on an accuracy level of around 1% which results in a systematic error $\approx 1 \cdot 10^{-4}$, analogously to [Bal14].
Since the error from an incorrectly set gate time can be corrected to a certain degree by a correctly chosen gate power, we estimate the systematic errors from calibration of the gate parameters to be $< 1 \cdot 10^{-3}$.

Other sources of error

The entangling gate can be affected by other sources of error, which contribute an error below 10^{-4} in our setup and thus only contribute marginally to the error budget. In this section, we quantify and discuss the error sources following [Bal16].
During the gate operation where spin and motion are entangled, any undesired motional transitions due to motional heating will affect the gate fidelity. Since the motional

heating of the ions in our setup is small, this error is negligible. For a heating rate of the gate mode of $\dot{\bar{n}} = 2.9/\mathrm{s}$ a fidelity error of $\dot{\bar{n}} \cdot t_g/(2K) = 7 \cdot 10^{-5}$ is calculated [Bal14], where $K = 2$ is the number of loops in phase space and $t_g = 100\,\mu\mathrm{s}$ the gate duration.

Thermal occupation of motional modes results in a larger ion wave-packet size. Consequently, the coupling strength of the ions to the driving laser field is reduced, which ultimately reduces the gate fidelity. Contrary to quantum gates on the axial mode of vibration, where the lasers couple only to two motional modes, the effective Raman k-vector couples to four vibrational radial modes. Thus, one needs to consider three spectator modes when the gate is executed on the radial $\omega_z^{\mathrm{c.o.m.}}$-mode. All modes are cooled with resolved sideband cooling to a mean phonon occupation number $\bar{n} \lesssim 0.1$. An analytical model is developed in [Bal16], which describes the fidelity error from thermally occupied motional modes by $\pi^4\eta^4\bar{n}(2\bar{n}+1)/4$, where η is the Lamb-Dicke parameter of a motional mode and $\bar{n}$ is the mean phonon occupation number of the mode. The authors use a numerical simulation to verify that this model describes the error contribution for both spectator modes and the gate mode accurately for low phonon numbers $\bar{n} < 1$. In our experiment, the Lamb-Dicke parameters for the radial modes are for the ω_y c.o.m. and rocking mode $\eta_y = 0.05$ and for the ω_z c.o.m. and rocking mode $\eta_z = 0.06$. The combined error from motional excitation on the vibrational modes is thus estimated to be around $1 \cdot 10^{-5}$.

Since the gate is executed with a spin-echo pulse, the ions spend an equal amount of time in the spin states $|\uparrow\rangle$ and $|\downarrow\rangle$. Therefore, an unequal illumination of the two ions by the Raman beams does not contribute to the gate error budget.

Errors from off-resonant excitation of the carrier transition and the spectator modes are strongly suppressed due to smoothing of the turn-on and turn-off transients of the gate pulses.

Errors from spin dephasing from magnetic field noise are negligible, since our apparatus features long spin coherence times as demonstrated in [Rus16]. The error is further reduced since the gate is executed in a spin-echo scheme.

Motional modes that involve relative motion of the ions such as the axial breathing mode or the two radial rocking modes experience anharmonic effects due to the Coulomb repulsion. Thus, motional Kerr cross-coupling between these modes can lead to a reduction of the gate fidelity if one of them is used as a gate mode. Since we execute the gate on the radial $\omega_z^{\mathrm{c.o.m.}}$-mode, the gate fidelity is not impaired by this effect.

An estimation of the gate error from amplitude and phase noise in the Raman laser

beams requires thorough characterization measurements and is expected to be negligible. Since our gate fidelity is dominated by other effects we neglect this error contribution.

C

Appendix – Experimental Sequences

C.1. Three-ion crystal reconfiguration

Here, we describe in detail how the reordering of the three-ion crystal ABC to CBA is accomplished, which is presented in section 7.3 of the main text. The experimental sequence is sketched in figure C.1. The sequence starts with a three-ion crystal, trapped in a harmonic potential at electrode 20, which is called laser interaction zone (LIZ) since all lasers are targeted at this electrode. The sequence is partitioned in three sequences: *pre-sequence, main-sequence* and *post-sequence*. First, the pre-sequence is executed. Then, the main-sequence is executed and repeated 90 times. After the final repetition of the main sequence, the post-sequence is executed.

Pre-sequence: At the beginning of the pre-sequence, the three-ion crystal is Doppler cooled with a 397 nm laser. The crystal is then separated by applying the separation voltage ramps with an additional calibrated axial bias field, such that the two ions A and B deterministically move to the left and ion C moves to the far right. The two-ion crystal AB is then shuttled to the LIZ, where Doppler cooling is applied. A potential well at electrode 14 is generated, which is of the same depth as on electrode 26, such that the potential well at the LIZ is properly centered and symmetric. The two-ion crystal AB is then separated, and each of the three ions A, B and C is shuttled individually to the LIZ for Doppler cooling and detection of ion loss events. In this part of the sequence, only **sequential transports** are used, where one transport corresponds to the movement of one ion from one electrode to a neighboring electrode, while the other ions remain at their position.

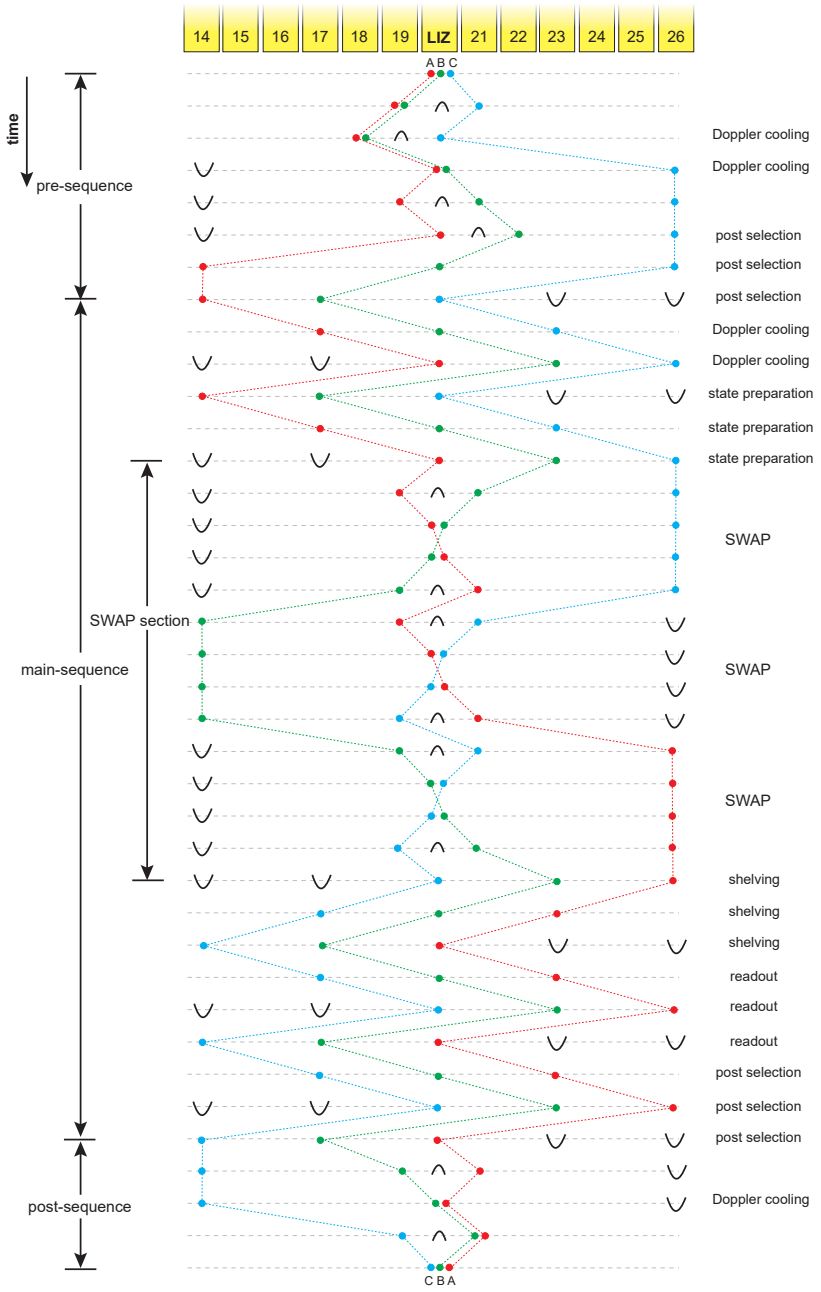

Figure C.1.: Full experimental sequence for the reconfiguration of a three-ion crystal from ABC to CBA by using three consecutive two-ion SWAP operations. Black potential wells or barriers are applied to achieve a symmetric potential along the trap axis, thus placing the ions in the center of the laser beams.

Main sequence: In the main sequence, each ion is shuttled individually to the LIZ for Doppler cooling. Afterwards, each ion is optically pumped at the LIZ for state initialization to either $|\uparrow\rangle$ or $|\downarrow\rangle$. The total state of the three ions is then initialized to one of eight possible configurations. Thus, the entire sequence is performed for each of the eight possible input states.
Subsequently, the reordering of the three ions via two-ion swap operations is carried out. At first, the ions A and B are merged in the LIZ and the crystal swapping operation is executed. Thus, the order of the ions along the trap axis is changed to BAC. The two-ion crystal is then separated and the ions A and C are shuttled to the LIZ and merged together. Another swap operation is conducted, such that the order of the ions is changed to BCA. After that, the ions B and C are merged at the LIZ for a final swap operation to yield the desired order of CBA.
Afterwards, each ion is shuttled to the LIZ for electron shelving and subsequent detection of the spin state. It is important to perform the shelving operation on the ions *before* the detection operation takes place. The latter is done by illumination with 397 nm laser light, as residual stray light on an un-shelved ion can depolarize the internal state, even if the ion is located several electrodes away.
In the main sequence, **parallel transports** are used, where all three separately trapped ions move simultaneously from one site to another. One parallel transport operation corresponds to the simultaneous movement of each of the ions from their initial electrode to one neighboring electrode.

Post-sequence: In the post-sequence, the individually trapped ions C, B and A are shuttled to the LIZ for post-selection of ion loss events. Afterwards, the ions A and B are merged, followed by a recombination of the ion C to the two-ion crystal BA, thus yielding the three-ion crystal CBA.
The duration of the entire sequence amounts to 109.8 ms, while the most relevant part - the main sequence - takes 38.6 ms. The tables B - E show more details on the shuttling operations which are employed. The shuttling operations require 23 % of the total duration of the main-sequence. In the following, we explain the reason for this overhead and how to reduce it.

shuttling operation	**duration (μs)**	**quantity**
separation	260	5
recombination	260	5
sequential transport	120	70
parallel transport (3 ions)	100	48
SWAP	42	3
total shuttling operation time	15.9 ms	
total sequence duration	109.8 ms	
percentage of shuttling operations	14.5 %	

Table A.: Shuttling operations and timings used in the **entire sequence**.

shuttling operation	**duration (μs)**	**quantity**
separation	260	2
sequential transport	120	31
total shuttling operation time	4.2 ms	
total sequence duration	39.7 ms	
percentage of shuttling operations	10.6 %	

Table B.: Operations used in the **pre-sequence**.

operation	**duration (μs)**	**quantity**
separation	260	3
recombination	260	3
sequential transport	120	30
parallel transport (3 ions)	100	48
SWAP	42	3
Doppler cooling	2500	17
fluorescence detection	1200	6
shelving	600	3
other operations (spin init., dwell times, compensation pot. ramps)	1700	-
total shuttling operation time	10.1 ms	
total sequence duration	63.5 ms	
percentage of shuttling operations	15.9 %	

Table C.: Shuttling operations used in the **main-sequence**.

The swapping operations require trap operation at a rather low RF level to make the swapping operation feasible, as the DC supply is limited to ±10 V, and the axial confinement has to exceed the radial confinement in one direction during the swap operation. The low-frequency radial mode is only at $\omega/2\pi = 1.93$ MHz. While we have verified that the excitation from the swapping operation is negligible, the linear transport operations add a slight amount of excitation if executed at low RF trap-drive amplitude. In the two-ion process tomography, this effect is negligible since only a few shuttling operations are used. By contrast, for the three-ion crystal reconfiguration, the amount of transport operations is much larger, such that we need to execute some of the shuttling operations more slowly for optimum readout fidelity.
In contrast to the two-ion measurements, the separation and recombination operations are executed slower: 260μs as compared to 100μs. Also, the sequential transports are slower: 120μs as compared to 28μs. This will be improved in future experiments, such that swapping can be executed at higher RF levels.

shuttling operation	**duration (μs)**	**quantity**
recombination	260	2
sequential transport	120	9
total shuttling operation time	1.6 ms	
total sequence duration	6.6 ms	
percentage of shuttling operations	24.3 %	

Table D.: Shuttling operations used in the **post-sequence**.

operation	**duration (μs)**	**quantity**
separation	260	3
recombination	260	3
sequential transport	120	30
SWAP	42	3
other operations (dwell times, compensation pot. ramps)	400	-
total shuttling operation time	5.3 ms	
total section duration	5.7 ms	

Table E.: Shuttling operations used in the **SWAP-section**.

C.2. Four-qubit randomized benchmarking

In the following, a sketch of the full experimental sequence of the four-qubit randomized benchmarking experiment is provided, which is presented in section 8.3 of the main text.

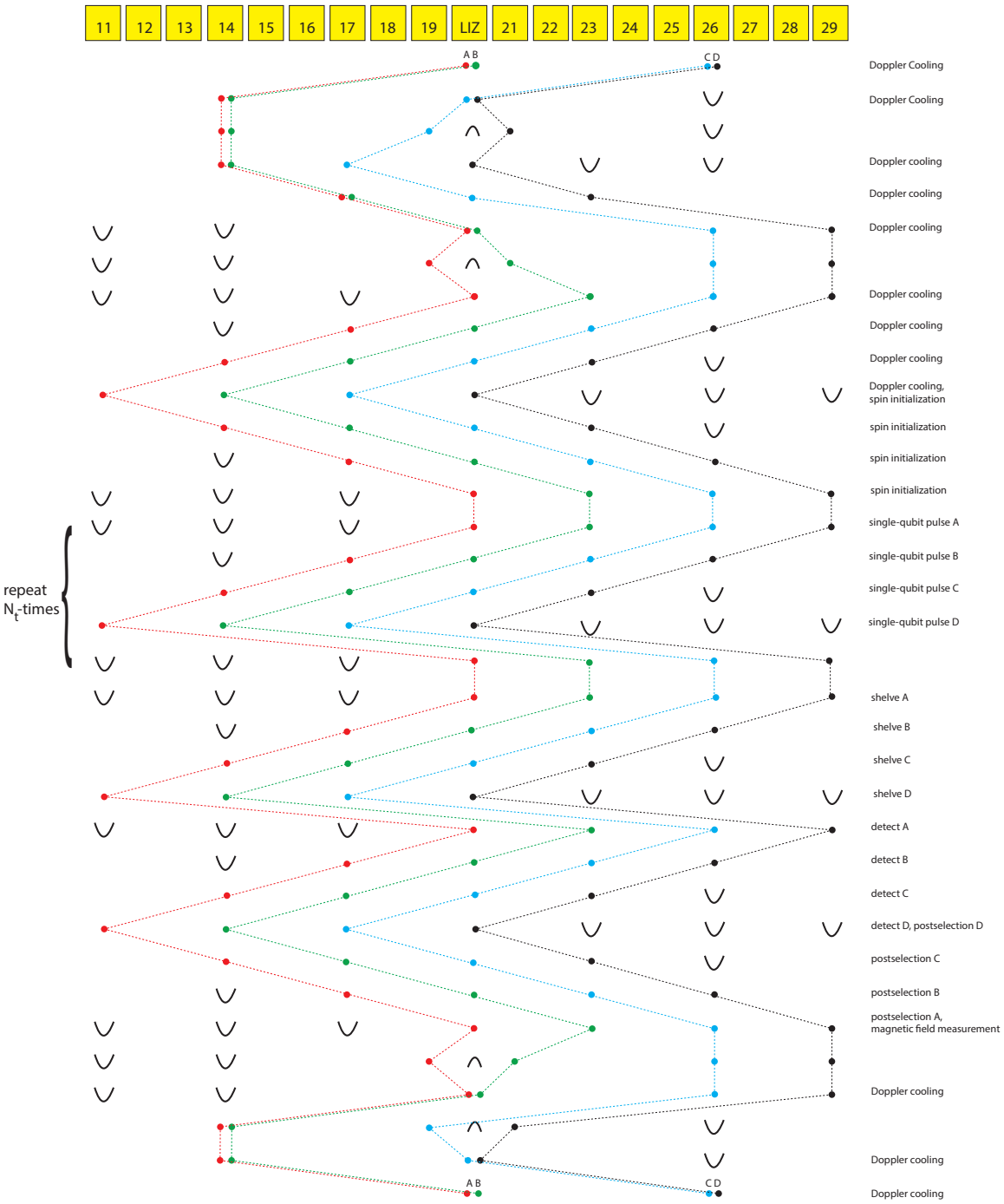

Figure C.2.: Full experimental sequence for the simultaneous single-qubit randomized benchmarking on four ions. Black potential wells or barriers are applied to achieve a symmetric potential along the trap axis, thus placing the ions in the center of the laser beams.

C.3. Four-qubit entanglement

In the following, details on the four-ion entanglement sequence are provided, which is presented in section 8.5 of the main text. In figure C.3 a sketch of the full experimental sequence is shown.
The sequence comprised of five blocks: cooling block, quantum logic block, rephasing block, analysis block, final block. The timing tables for all five blocks are presented separately.
The *swing-off time* is an artificially introduced idle time after shuttling operations. It is employed to account for DC waveform distortions by external low-pass filters. Symmetry potentials are used to establish a symmetric potential along the trap axis, thus placing the ions in the center of the laser beams. The duration, which is needed to ramp the voltage for that potential up or down is specified by *apply symmetry potential*.

operation	**duration** (µs)	N_{op}	**total duration** (µs)
Doppler cooling	1201	11	13206
fluorescence detection	1501	8	12004
magnetic field measurement	8224	1	8224
sideband cooling	7773	1	7773
parallel transport	60	69	4140
sequential transport	30	81	2430
electron shelving	401	4	1605
apply symmetry potential	24	62	1488
swing-off time	50	28	1400
separation/recombination	160	8	1280
LIZ potential change	48	24	1152
geometric phase gate	102	3	306
spin initialization	53	5	266
$\pi/2$-pulse	4	8	32
switch intensity stabilization	10	2	20
analysis pulse	4	4	16

Table F.: Timing table for the entire four-ion entanglement sequence **without** rephasing. The integer number N_{op} denotes how often an operation of a particular duration is performed. The entire sequence is performed within 55.3 ms. The duration for the magnetic field measurement and for sideband cooling are aggregated from their constituent single operation durations.

operation	**duration** (µs)	N_{op}	**total duration** (µs)
sequential transport	30	24	720
parallel transport	60	18	1080
apply symmetry potential	24	17	408
LIZ potential change	48	14	672
swing off time	50	7	350
separation/recombination	160	1	160
Doppler cooling	1201	7	8404
sideband cooling	7773	1	7773
spin initialization	53	5	266
switch intensity stabilization	10	1	10

Table G.: Timing table for the **cooling block** in the four-ion entanglement sequence. The block is performed within 19.8 ms, which corresponds to 35.9% of the entire sequence duration.

operation	**duration** (µs)	N_{op}	**total duration** (µs)
sequential transport	30	33	990
apply symmetry potential	24	9	216
LIZ potential change	48	5	240
swing-off time	50	11	550
separation/recombination	160	5	800
$\pi/2$-pulse	4	8	32
geometric phase gate	102	3	306

Table H.: Timing table for the **quantum logic block** in the four-ion entanglement sequence. The block is performed within 3.1 ms, which corresponds to 5.7% of the entire sequence duration.

operation	**duration** (µs)	N_{op}	**total duration** (µs)
sequential transport	30	21	630
parallel transport	60	18	1080
apply symmetry potential	24	14	336
LIZ potential change	48	12	576
swing-off time	50	10	500
separation/recombination	160	4	640
π-pulse	10	2	20
switch intensity stabilization	10	6	60

Table I.: Timing table for the **rephasing block** in the four-ion entanglement sequence. The block is performed within 3.8 ms.

operation	**duration** (µs)	N_{op}	**total duration** (µs)
parallel transport	60	36	2160
apply symmetry potential	24	24	576
swing-off time	50	6	300
electron shelving	401	4	1605
fluorescence detection	1501	4	6002
analysis pulse	4	4	16

Table J.: Timing table for the **analysis block** in the four-ion entanglement sequence. The block is performed within 10.7 ms, which corresponds to 19.3% of the entire sequence duration.

operation	**duration** (µs)	N_{op}	**total duration** (µs)
sequential transport	30	24	720
parallel transport	60	15	900
apply symmetry potential	24	12	288
LIZ potential change	48	5	240
swing-off time	50	4	200
separation/recombination	160	2	320
Doppler cooling	1200,5	4	4802
fluorescence detection	1501	4	6002
magnetic field measurement	8224	1	8224
switch intensity stabilization	10	1	10

Table K.: Timing table for the **final block** in the four-ion entanglement sequence. The block is performed within 21.7 ms, which corresponds to 39.2% of the entire sequence duration.

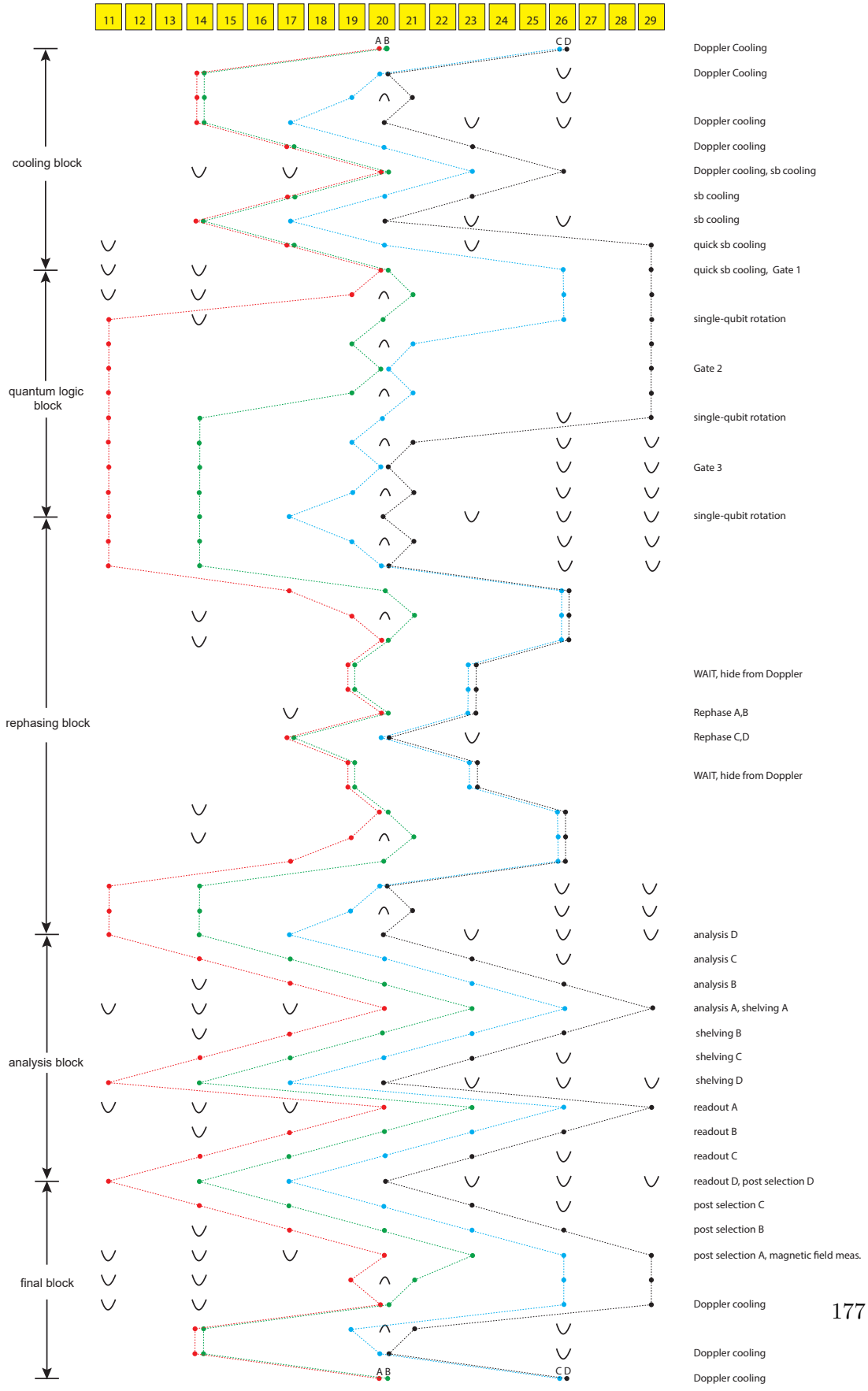

Figure C.3.: Full experimental sequence for the creation of a four-ion GHZ state.

D

Appendix – Blueprints

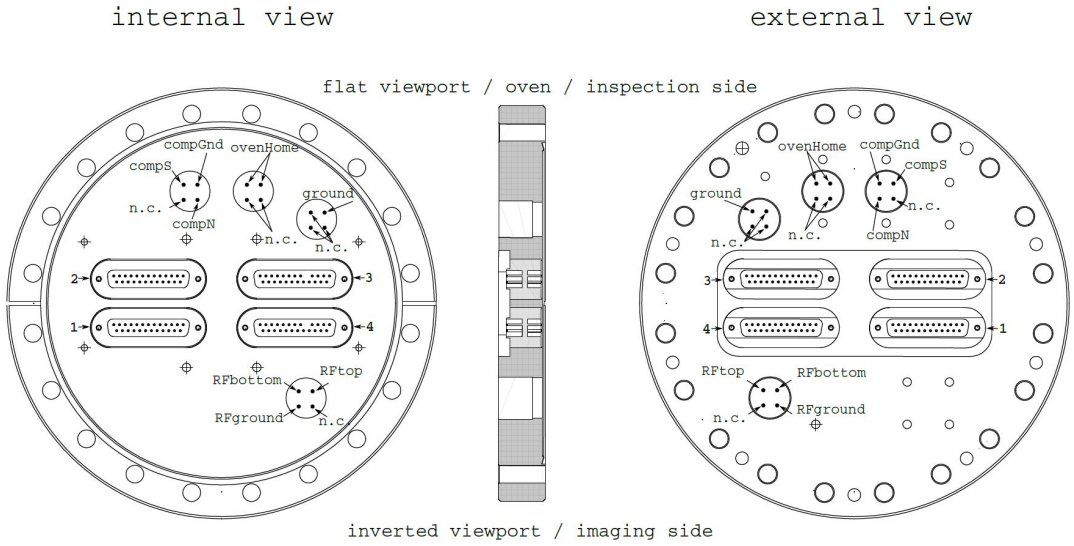

Figure D.1.: Electrical connections on the vacuum flange.

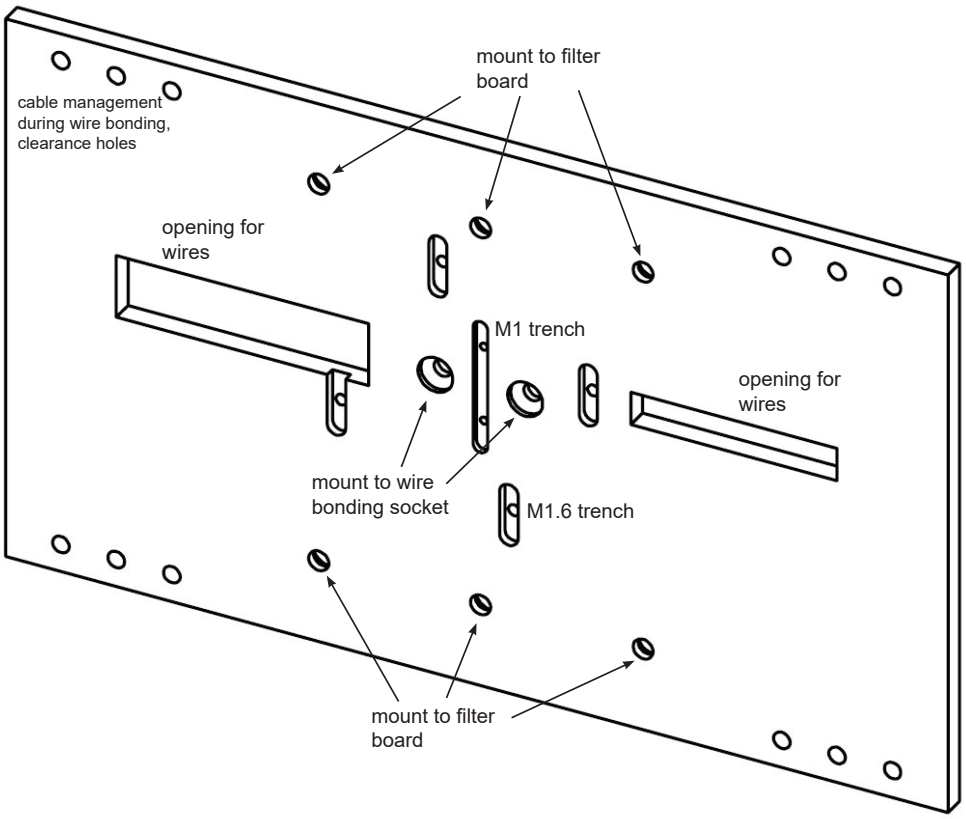

Figure D.2.: Custom-made trap assembly tool, which is used to assemble the alumina layers and during wire bonding. The tool is a solid aluminum plate with outside dimensions 100 mm x 170 mm x 4 mm. For the trap assembly, M1 and M1.6 nuts are placed in the corresponding trenches to prevent movement of the nuts. After trap alignment the filter board is mounted to the support layer, which is placed below the trap. Subsequently, wire bonding is executed and the assembly tool is fixed by corresponding screw holes to the heated wire bonding socket. The filter board is then fixed to the assembly tool by screws which are countered with nuts from the back side. Several openings and clearance holes allow for proper cable management of the numerous DC and RF supply wires.

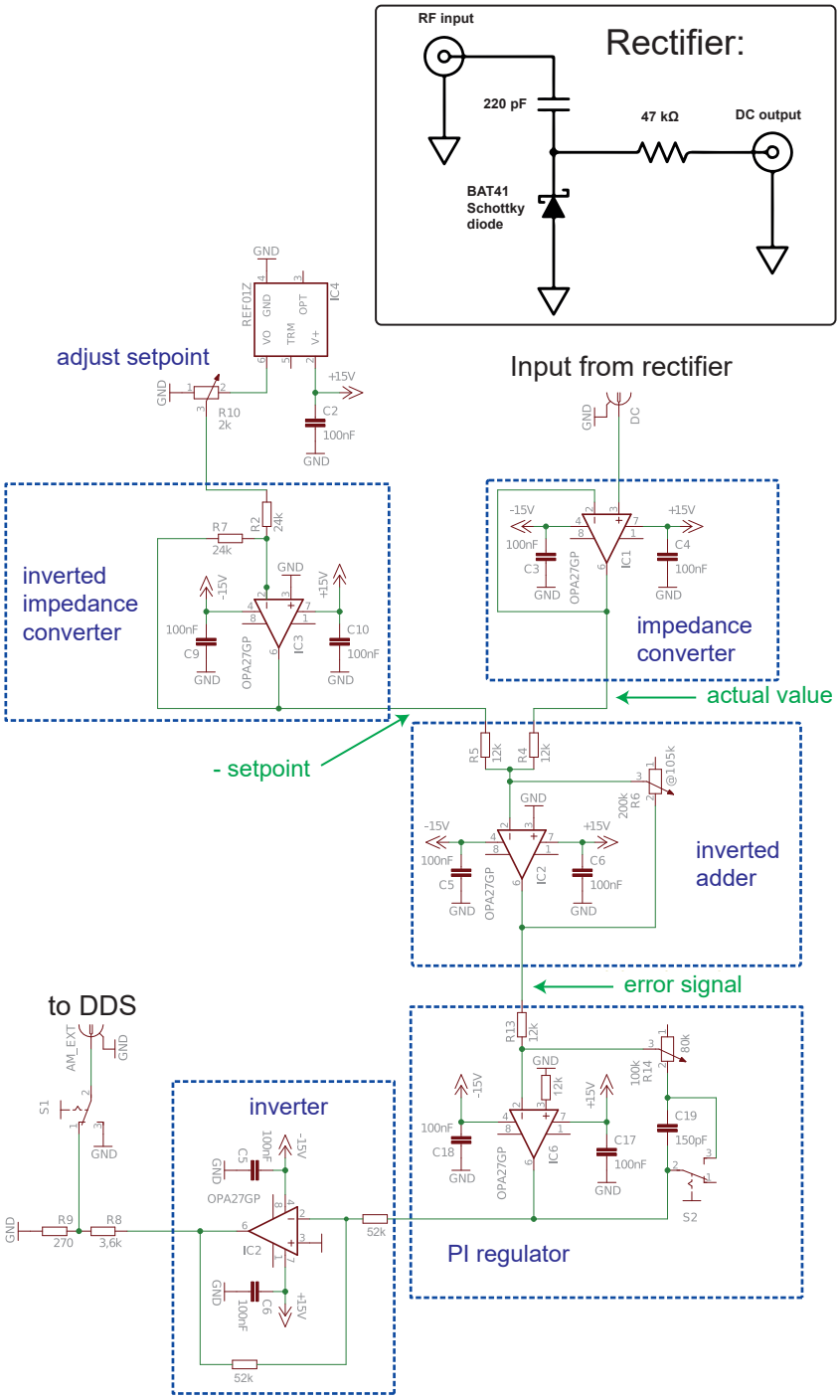

Figure D.3.: Circuit diagram of the rectifier and the PI regulator, that is used to stabilize the RF voltage supply for the ion trap. The circuit was developed according to [Dil14] and slightly modified in this thesis: a 12 kΩ resistor was added to the non-inverting input of the PI regulator operational amplifier to compensate current offsets, an inverter was added before the output to the DDS.

List of Figures

List of Scientific Publications

Publications – presented in this thesis

- H. Kaufmann, T. Ruster, C. T. Schmiegelow, M. A. Luda, V. Kaushal, J. Schulz, D. von Lindenfels, F. Schmidt-Kaler, and U. G. Poschinger. *Scalable creation of long-lived multipartite entanglement.* In: arXiv:1707.03695 (2017), submitted to Phys. Rev. Lett.

- H. Kaufmann, T. Ruster, C. T. Schmiegelow, M. A. Luda, V. Kaushal, J. Schulz, D. von Lindenfels, F. Schmidt-Kaler, and U. G. Poschinger. *Fast ion swapping for quantum-information processing.* In: Phys. Rev. A **95**, 052319 (2017)

- H. Kaufmann, T. Ruster, C. T. Schmiegelow, F. Schmidt-Kaler, and U. G. Poschinger. *Dynamics and control of fast ion crystal splitting in segmented Paul traps.* In: New Journal of Physics **16**, 073012 (2014)

Further publications

- T. Ruster, H. Kaufmann, M. A. Luda, V. Kaushal, C. T. Schmiegelow, F. Schmidt-Kaler, and U. G. Poschinger. *Entanglement-based dc magnetometry with separated ions.* In: arXiv:1704.01793 (2017), accepted for publication in Phys. Rev. X

- T. Ruster, C. T. Schmiegelow, H. Kaufmann, C. Warschburger, F. Schmidt-Kaler, and U. G. Poschinger. *A long-lived Zeeman trapped-ion qubit.* In: Applied Physics B **122**, 254 (2016)

- C. T. Schmiegelow, H. Kaufmann, T. Ruster, J. Schulz, V. Kaushal, M. Hettrich, F. Schmidt-Kaler, and U. G. Poschinger. *Phase-Stable Free-Space Optical Lattices for Trapped Ions.* In: Phys. Rev. Lett. **116**, 033002 (2016)

- I. Talukdar, D. J. Gorman, N. Daniilidis, P. Schindler, S. Ebadi, H. Kaufmann, T. Zhang, and H. Häffner. *Implications of surface noise for the motional coherence of trapped ions.* In: Phys. Rev. A **93**, 043415 (2016)

- C. T. Schmiegelow, J. Schulz, H. Kaufmann, T. Ruster, U. G. Poschinger, and F. Schmidt-Kaler. *Transfer of optical orbital angular momentum to a bound electron.* In: Nat. Commun. **7**, 12998 (2016)
- M. F. Brandl, M. W. van Mourik, L. Postler, A. Nolf, K. Lakhmanskiy, R. R. Paiva, S. Möller, N. Daniilidis, H. Häffner, V. Kaushal, T. Ruster, C. Warschburger, H. Kaufmann, U. G. Poschinger, F. Schmidt-Kaler, P. Schindler, T. Monz, and R. Blatt. *Cryogenic setup for trapped ion quantum computing.* In: Rev. Sci. Instrum. **87**, 113103 (2016)
- M. Hettrich, T. Ruster, H. Kaufmann, C. F. Roos, C. T. Schmiegelow, F. Schmidt-Kaler, and U. G. Poschinger. *Measurement of Dipole Matrix Elements with a Single Trapped Ion.* In: Phys. Rev. Lett. **115**, 143003 (2015)
- T. Ruster, C. Warschburger, H. Kaufmann, C. T. Schmiegelow, A. Walther, M. Hettrich, A. Pfister, V. Kaushal, F. Schmidt-Kaler, and U. G. Poschinger. *Experimental realization of fast ion separation in segmented Paul traps.* In: Phys. Rev. A **90**, 033410 (2014)
- F. Ziesel, T. Ruster, A. Walther, H. Kaufmann, K. Singer, F. Schmidt-Kaler, and U. G. Poschinger. *Experimental creation and analysis of displaced number states.* In: Journal of Physics B **46**, 104008 (2013)
- H. Kaufmann, S. Ulm, G. Jacob, U. Poschinger, H. Landa, A. Retzker, M. B. Plenio, and F. Schmidt-Kaler. *Precise Experimental Investigation of Eigenmodes in a Planar Ion Crystal.* In: Phys. Rev. Lett. **109**, 263003 (2012)
- A. Bermudez, J. Almeida, K. Ott, H. Kaufmann, S. Ulm, U. Poschinger, F. Schmidt-Kaler, A. Retzker, and M. B. Plenio. *Quantum magnetism of spin-ladder compounds with trapped-ion crystals.* In: New Journal of Physics **14**, 093042 (2012)

Bibliography

[All11] D. T. C. Allcock, L. Guidoni, T. P. Harty, C. J. Ballance, M. G. Blain, A. M. Steane, and D. M. Lucas. *Reduction of heating rate in a microfabricated ion trap by pulsed-laser cleaning*. In: New Journal of Physics **13**, 123023 (2011) (cit. on p. 5).

[Asp82] A. Aspect, J. Dalibard, and G. Roger. *Experimental Test of Bell's Inequalities Using Time-Varying Analyzers*. In: Phys. Rev. Lett. **49**, 1804–1807 (1982) (cit. on p. 2).

[Bai13] M. T. Baig, M. Johanning, A. Wiese, S. Heidbrink, M. Ziolkowski, and C. Wunderlich. *A scalable, fast, and multichannel arbitrary waveform generator*. In: Review of Scientific Instruments **84**, 124701 (2013) (cit. on p. 56).

[Bal14] C. J. Ballance. *High-Fidelity Quantum Logic in Ca^+*. In: Ph.D. thesis, University of Oxford, Department of Physics (2014) (cit. on pp. 23, 162–164).

[Bal15] C. J. Ballance, V. M. Schäfer, J. P. Home, D. J. Szwer, S. C. Webster, D. T. C. Allcock, N. M. Linke, T. P. Harty, D. P. L. Aude Craik, D. N. Stacey, A. M. Steane, and D. M. Lucas. *Hybrid quantum logic and a test of Bell's inequality using two different atomic isotopes*. In: Nature **528**, 384–386 (2015) (cit. on p. 95).

[Bal16] C. J. Ballance, T. P. Harty, N. M. Linke, M. A. Sepiol, and D. M. Lucas. *High-Fidelity Quantum Logic Gates Using Trapped-Ion Hyperfine Qubits*. In: Phys. Rev. Lett. **117**, 060504 (2016) (cit. on pp. 5, 109, 115, 162–164).

[Bar04] M. D. Barrett, J. Chiaverini, T. Schaetz, J. Britton, W. M. Itano, J. D. Jost, E. Knill, C. Langer, R. Ozeri, and D. J. Wineland. *Deterministic quantum teleportation of atomic qubits*. In: Nature **429**, 737–739 (2004) (cit. on pp. 4, 54).

[Bar10] J. T. Barreiro, P. Schindler, O. Gühne, T. Monz, M. Chwalla, C. F. Roos, M. Hennrich, and R. Blatt. *Experimental multiparticle entanglement dynamics induced by decoherence*. In: Nature Physics **6**, 943–946 (2010) (cit. on p. 128).

[Bar13] R. Barends, J. Kelly, A. Megrant, D. Sank, E. Jeffrey, Y. Chen, Y. Yin, B. Chiaro, J. Mutus, C. Neill, P. O'Malley, P. Roushan, J. Wenner, T. C. White, A. N. Cleland, and J. M. Martinis. *Coherent Josephson Qubit Suitable for Scalable Quantum Integrated Circuits*. In: Phys. Rev. Lett. **111**, 080502 (2013) (cit. on p. 6).

[Bar14] R. Barends, J. Kelly, A. Megrant, A. Veitia, D. Sank, E. Jeffrey, T. C. White, J. Mutus, A. G. Fowler, B. Campbell, Y. Chen, Z. Chen, B. Chiaro, A. Dunsworth, C. Neill, P. O'Malley, P. Roushan, A. Vainsencher, J. Wenner, A. N. Korotkov, A. N. Cleland, and J. M. Martinis. *Superconducting quantum circuits at the surface code threshold for fault tolerance*. In: Nature **508**, 500–503 (2014) (cit. on p. 6).

[Bar16] R. Barends, A. Shabani, L. Lamata, J. Kelly, A. Mezzacapo, U. L. Heras, R. Babbush, A. G. Fowler, B. Campbell, Y. Chen, Z. Chen, B. Chiaro, A. Dunsworth, E. Jeffrey, E. Lucero, A. Megrant, J. Y. Mutus, M. Neeley, C. Neill, P. J. J. O'Malley, C. Quintana, P. Roushan, D. Sank, A. Vainsencher, J. Wenner, T. C. White, E. Solano, H. Neven, and J. M. Martinis. *Digitized adiabatic quantum computing with a superconducting circuit.* In: Nature **534**, 222–226 (2016) (cit. on p. 6).

[Bar57] J. Bardeen, L. N. Cooper, and J. R. Schrieffer. *Theory of superconductivity.* In: Physical Review **108**, 1175 (1957) (cit. on p. 5).

[Bel64] J. S. Bell. *On the Einstein-Podolsky-Rosen paradox.* In: Physics **1**, 195–200 (1964) (cit. on p. 2).

[Ben08] J. Benhelm, G. Kirchmair, C. F. Roos, and R. Blatt. *Experimental quantum-information processing with $^{43}Ca^{+}$ ions.* In: Phys. Rev. A **77**, 062306 (2008) (cit. on p. 84).

[Ben80] P. Benioff. *The computer as a physical system: A microscopic quantum mechanical Hamiltonian model of computers as represented by Turing machines.* In: Journal of Statistical Physics **22**, 563–591 (1980) (cit. on p. 2).

[Ber12] A. Bermudez, J. Almeida, K. Ott, H. Kaufmann, S. Ulm, U. Poschinger, F. Schmidt-Kaler, A. Retzker, and M. B. Plenio. *Quantum magnetism of spin-ladder compounds with trapped-ion crystals.* In: New Journal of Physics **14**, 093042 (2012) (cit. on pp. 8, 131, 132, 135, 136).

[Ber17] A. Bermudez, X. Xu, R. Nigmatullin, J. O'Gorman, V. Negnevitsky, P. Schindler, T. Monz, U. G. Poschinger, C. Hempel, J. Home, F. Schmidt-Kaler, M. Biercuk, R. Blatt, S. Benjamin, and M. Müller. *Assessing the progress of trapped-ion processors towards fault-tolerant quantum computation.* In: arXiv:1705.02771 (2017) (cit. on pp. 5, 137, 141, 142).

[Ber97] E. Bernstein and U. Vazirani. *Quantum Complexity Theory.* In: SIAM Journal on Computing **26**, 1411–1473 (1997) (cit. on p. 2).

[Bla09] R. B. Blakestad, C. Ospelkaus, A. P. VanDevender, J. M. Amini, J. Britton, D. Leibfried, and D. J. Wineland. *High-Fidelity Transport of Trapped-Ion Qubits through an* **X***-Junction Trap Array.* In: Phys. Rev. Lett. **102**, 153002 (2009) (cit. on pp. 10, 91, 95).

[Bla10] R. B. Blakestad. *Transport of Trapped-Ion Qubits within a Scalable Quantum Processor.* In: Ph.D. thesis, University of Colorado, Department of Physics (2010) (cit. on pp. 27, 30, 79).

[Bla11] R. B. Blakestad, C. Ospelkaus, J. H. VanDevender, M. J. Wesenberg, J. Biercuk, D. Leibfried, and D. Wineland. *Near-ground-state transport of trapped-ion qubits through a multidimensional array*. In: Phys. Rev. A **84**, 032314 (2011) (cit. on pp. 57, 62).

[Bol85] J. J. Bollinger, J. D. Prestage, W. M. Itano, and D. J. Wineland. *Laser-Cooled-Atomic Frequency Standard*. In: Phys. Rev. Lett. **54**, 1000–1003 (1985) (cit. on p. 5).

[Bom06] H. Bombin and M. A. Martin-Delgado. *Topological Quantum Distillation*. In: Phys. Rev. Lett. **97**, 180501 (2006) (cit. on p. 141).

[Bow12] R. Bowler, J. Gaebler, Y. Lin, T. R. Tan, D. Hanneke, J. D. Jost, J. P. Home, D. Leibfried, and D. J. Wineland. *Coherent Diabatic Ion Transport and Separation in a Multizone Trap Array*. In: Phys. Rev. Lett. **109**, 080502 (2012) (cit. on pp. 9, 10, 53, 54, 70, 96, 103, 105).

[Bow13] R. Bowler, U. Warring, J. W. Britton, B. C. Sawyer, and J. Amini. *Arbitrary waveform generator for quantum information processing with trapped ions*. In: Review of Scientific Instruments **84**, 033108 (2013) (cit. on p. 56).

[Bro11] K. R. Brown, A. C. Wilson, Y. Colombe, C. Ospelkaus, A. M. Meier, E. Knill, D. Leibfried, and D. J. Wineland. *Single-qubit-gate error below 10^{-4} in a trapped ion*. In: Phys. Rev. A **84**, 030303 (2011) (cit. on p. 108).

[Bro15] M. Brownnutt, M. Kumph, P. Rabl, and R. Blatt. *Ion-trap measurements of electric-field noise near surfaces*. In: Rev. Mod. Phys. **87**, 1419–1482 (2015) (cit. on pp. 64, 68, 79, 82).

[Bro17] J. Brox, P. Kiefer, M. Bujak, H. Landa, and T. Schaetz. *Spectroscopy and Directed Transport of Topological Solitons in Crystals of Trapped Ions*. In: arXiv:1704.03786 (2017) (cit. on p. 8).

[Cam10] W. C. Campbell, J. Mizrahi, Q. Quraishi, C. Senko, D. Hayes, D. Hucul, D. N. Matsukevich, P. Maunz, and C. Monroe. *Ultrafast Gates for Single Atomic Qubits*. In: Phys. Rev. Lett. **105**, 090502 (2010) (cit. on pp. 5, 138).

[Cas17] D. Castelvecchi. *Quantum computers ready to leap out of the lab in 2017*. In: Nature **541**, 9–10 (2017) (cit. on p. 1).

[Chi03] I. Chiorescu, Y. Nakamura, C. J. P. M. Harmans, and J. E. Mooij. *Coherent quantum dynamics of a superconducting flux qubit*. In: Science **299**, 1869–1871 (2003) (cit. on p. 6).

[Chi14] J. Chiaverini and J. M. Sage. *Insensitivity of the rate of ion motional heating to trap-electrode material over a large temperature range*. In: Phys. Rev. A **89**, 012318 (2014) (cit. on p. 84).

[Cho14] J. M. Chow, J. M. Gambetta, E. Magesan, D. W. Abraham, A. W. Cross, B. R. Johnson, N. A. Masluk, C. A. Ryan, J. A. Smolin, S. J. Srinivasan, and M. Steffen. *Implementing a strand of a scalable fault-tolerant quantum computing fabric*. In: Nat. Commun. **5**, 4015 (2014) (cit. on p. 6).

[Chu98] I. L. Chuang, N. Gershenfeld, and M. Kubinec. *Experimental Implementation of Fast Quantum Searching*. In: Phys. Rev. Lett. **80**, 3408–3411 (1998) (cit. on pp. 3, 7).

[Cir95] J. I. Cirac and P. Zoller. *Quantum Computations with Cold Trapped Ions*. In: Phys. Rev. Lett. **74**, 4091–4094 (1995) (cit. on pp. 4, 7).

[Coo56] L. N. Cooper. *Bound Electron Pairs in a Degenerate Fermi Gas*. In: Phys. Rev. **104**, 1189–1190 (1956) (cit. on p. 5).

[Cou92] J.-Y. Courtois and G. Grynberg. *Probe transmission in one-dimensional optical molasses: Theory for linearly cross-polarized cooling beams*. In: Phys. Rev. A **46**, 7060–7078 (1992) (cit. on p. 23).

[Cyw08] Ł. Cywiński, R. M. Lutchyn, C. P. Nave, and S. Das Sarma. *How to enhance dephasing time in superconducting qubits*. In: Phys. Rev. B **77**, 174509 (2008) (cit. on p. 89).

[Cór15] A. D. Córcoles, E. Magesan, S. J. Srinivasan, A. W. Cross, M. Steffen, J. M. Gambetta, and J. M. Chow. *Demonstration of a quantum error detection code using a square lattice of four superconducting qubits*. In: Nat. Commun. **6**, 6979 (2015) (cit. on p. 6).

[DF00] C. Di Fidio and W. Vogel. *Damped Rabi oscillations of a cold trapped ion*. In: Phys. Rev. A **62**, 031802 (2000) (cit. on p. 135).

[Dan14] N. Daniilidis, S. Gerber, G. Bolloten, M. Ramm, A. Ransford, E. Ulin-Avila, I. Talukdar, and H. Häffner. *Surface noise analysis using a single-ion sensor*. In: Phys. Rev. B **89**, 245435 (2014) (cit. on pp. 79, 84).

[Das17] S. Das, V. E. Elfving, S. Faez, and A. S. Sørensen. *Interfacing Superconducting Qubits and Single Optical Photons Using Molecules in Waveguides*. In: Phys. Rev. Lett. **118**, 140501 (2017) (cit. on p. 7).

[Deb16] S. Debnath, N. M. Linke, C. Figgatt, K. A. Landsman, K. Wright, and C. Monroe. *Demonstration of a small programmable quantum computer with atomic qubits*. In: Nature **536**, 63–66 (2016) (cit. on pp. 3, 4, 8).

[Des06] L. Deslauriers, S. Olmschenk, D. Stick, W. K. Hensinger, J. Sterk, and C. Monroe. *Scaling and Suppression of Anomalous Heating in Ion Traps*. In: Phys. Rev. Lett. **97**, 103007 (2006) (cit. on pp. 5, 79).

[Deu85] D. Deutsch. *Quantum Theory, the Church-Turing Principle and the Universal Quantum Computer*. In: Proceedings of the Royal Society of London A: Mathematical, Physical and Engineering Sciences **400**, 97–117 (1985) (cit. on pp. 2, 3).

[Deu89] D. Deutsch. *Quantum computational networks*. In: Proceedings of the Royal Society of London A: Mathematical, Physical and Engineering Sciences **425**, 73–90 (1989) (cit. on p. 3).

[DiV00] D. P. DiVincenzo. *The Physical Implementation of Quantum Computation*. In: Fortschritte der Physik **48**, 771–783 (2000) (cit. on pp. 3, 115).

[DiV95] D. P. DiVincenzo. *Two-bit gates are universal for quantum computation*. In: Phys. Rev. A **51**, 1015–1022 (1995) (cit. on p. 2).

[Dil14] M. Dillmann. *Stabilisierung der radialen Säkularfrequenzen gefangener Ionen in einer segmentierten Paul-Falle*. In: Master's thesis, Johannes Gutenberg-Universität Mainz (2014) (cit. on pp. 50, 181).

[Dre83] R. W. P. Drever, J. L. Hall, F. V. Kowalski, J. Hough, G. M. Ford, A. J. Munley, and H. Ward. *Laser phase and frequency stabilization using an optical resonator*. In: Applied Physics B **31**, 97–105 (1983) (cit. on p. 47).

[Dür99] W. Dür, H.-J. Briegel, J. I. Cirac, and P. Zoller. *Quantum repeaters based on entanglement purification*. In: Phys. Rev. A **59**, 169–181 (1999) (cit. on p. 5).

[Ebl10] J. Eble, S. Ulm, P. Zahariev, F. Schmidt-Kaler, and K. Singer. *Feedback-optimized operations with linear ion crystals*. In: Journal of the Optical Society of America B **27**, A99–A104 (2010) (cit. on pp. 54, 68).

[Ein35] A. Einstein, B. Podolsky, and N. Rosen. *Can Quantum-Mechanical Description of Physical Reality Be Considered Complete?* In: Phys. Rev. **47**, 777–780 (1935) (cit. on p. 2).

[Enz00] D. G. Enzer, M. M. Schauer, J. J. Gomez, M. S. Gulley, M. H. Holzscheiter, P. G. Kwiat, S. K. Lamoreaux, C. G. Peterson, V. D. Sandberg, D. Tupa, A. G. White, R. J. Hughes, and D. F. V. James. *Observation of Power-Law Scaling for Phase Transitions in Linear Trapped Ion Crystals*. In: Phys. Rev. Lett. **85**, 2466–2469 (2000) (cit. on p. 16).

[Far01] E. Farhi, J. Goldstone, S. Gutmann, J. Lapan, A. Lundgren, and D. Preda. *A Quantum Adiabatic Evolution Algorithm Applied to Random Instances of an NP-Complete Problem*. In: Science **292**, 472–475 (2001) (cit. on p. 3).

[Fey82] R. P. Feynman. *Simulating physics with computers*. In: International Journal of Theoretical Physics **21**, 467–488 (1982) (cit. on pp. 1, 2, 131).

[Fey86] R. P. Feynman. *Quantum mechanical computers*. In: Foundations of Physics **16**, 507–531 (1986) (cit. on p. 2).

[Fow12] A. G. Fowler, M. Mariantoni, J. M. Martinis, and A. N. Cleland. *Surface codes: Towards practical large-scale quantum computation.* In: Phys. Rev. A **86**, 032324 (2012) (cit. on p. 6).

[Für14] H. A. Fürst, M. H. Goerz, U. G. Poschinger, M. Murphy, S. Montangero, T. Calarco, F. Schmidt-Kaler, K. Singer, and C. P. Koch. *Controlling the transport of an ion: classical and quantum mechanical solutions.* In: New Journal of Physics **16**, 075007 (2014) (cit. on pp. 73, 75).

[GR03] J. J. García-Ripoll, P. Zoller, and J. I. Cirac. *Speed Optimized Two-Qubit Gates with Laser Coherent Control Techniques for Ion Trap Quantum Computing.* In: Phys. Rev. Lett. **91**, 157901 (2003) (cit. on p. 138).

[Gae16] J. P. Gaebler, T. R. Tan, Y. Lin, Y. Wan, R. Bowler, A. C. Keith, S. Glancy, K. Coakley, E. Knill, D. Leibfried, and D. J. Wineland. *High-Fidelity Universal Gate Set for $^9Be^+$ Ion Qubits.* In: Phys. Rev. Lett. **117**, 060505 (2016) (cit. on pp. 5, 109, 115, 141).

[Gro97] L. K. Grover. *Quantum Mechanics Helps in Searching for a Needle in a Haystack.* In: Phys. Rev. Lett. **79**, 325–328 (1997) (cit. on p. 3).

[Han10] D. Hanneke, J. P. Home, J. D. Jost, J. M. Amini, D. Leibfried, and D. J. Wineland. *Realization of a programmable two-qubit quantum processor.* In: Nature Physics **6**, 13–16 (2010) (cit. on p. 9).

[Har10] M. Harlander, M. Brownnutt, W. Hänsel, and R. Blatt. *Trapped-ion probing of light-induced charging effects on dielectrics.* In: New Journal of Physics **12**, 093035 (2010) (cit. on p. 67).

[Har14] T. P. Harty, D. T. C. Allcock, C. J. Ballance, L. Guidoni, H. A. Janacek, N. M. Linke, D. N. Stacey, and D. M. Lucas. *High-Fidelity Preparation, Gates, Memory, and Readout of a Trapped-Ion Quantum Bit.* In: Phys. Rev. Lett. **113**, 220501 (2014) (cit. on pp. 5, 6).

[Har16] T. P. Harty, M. A. Sepiol, D. T. C. Allcock, C. J. Ballance, J. E. Tarlton, and D. M. Lucas. *High-Fidelity Trapped-Ion Quantum Logic Using Near-Field Microwaves.* In: Phys. Rev. Lett. **117**, 140501 (2016) (cit. on p. 5).

[Hen06] W. K. Hensinger, S. Olmschenk, D. Stick, D. Hucul, M. Yeo, M. Acton, L. Deslauriers, C. Monroe, and J. Rabchuk. *T-junction ion trap array for two-dimensional ion shuttling, storage, and manipulation.* In: Applied Physics Letters **88**, 034101 (2006) (cit. on pp. 10, 95).

[Het15] M. Hettrich, T. Ruster, H. Kaufmann, C. F. Roos, C. T. Schmiegelow, F. Schmidt-Kaler, and U. G. Poschinger. *Measurement of Dipole Matrix Elements with a Single Trapped Ion.* In: Phys. Rev. Lett. **115**, 143003 (2015) (cit. on pp. 12, 109).

[Hit12] D. A. Hite, Y. Colombe, A. C. Wilson, K. R. Brown, U. Warring, R. Jördens, J. D. Jost, K. S. McKay, D. P. Pappas, D. Leibfried, and D. J. Wineland. *100-Fold Reduction of Electric-Field Noise in an Ion Trap Cleaned with In Situ Argon-Ion-Beam Bombardment*. In: Phys. Rev. Lett. **109**, 103001 (2012) (cit. on pp. 5, 79).

[Hit13] D. Hite, Y. Colombe, A. Wilson, D. Allcock, D. Leibfried, D. Wineland, and D. Pappas. *Surface science for improved ion traps*. In: MRS Bulletin **38**, 826–833 (2013) (cit. on pp. 4, 79).

[Hom06a] J. P. Home and A. M. Steane. *Electrode Configurations for Fast Separation of Trapped Ions*. In: Quantum Inf. and Comput. **6**, 289–325 (2006) (cit. on pp. 54, 59).

[Hom06b] J. Home. *Entanglement of Two Trapped-Ion Spin Qubits*. In: Ph.D. thesis, Oxford University (2006) (cit. on p. 84).

[Hom09] J. P. Home, D. Hanneke, J. D. Jost, J. M. Amini, D. Leibfried, and D. J. Wineland. *Complete Methods Set for Scalable Ion Trap Quantum Information Processing*. In: Science **325**, 1227–1230 (2009) (cit. on p. 9).

[Hom13] J. P. Home. *Quantum Science and Metrology with Mixed-Species Ion Chains*. In: Advances in Atomic, Molecular, and Optical Physics **62**, 231 –277 (2013) (cit. on p. 95).

[How81] D. A. Howe, D. W. Allan, and J. A. Barnes. *Properties of Signal Sources and Measurement Methods*. In: Proceedings of the 35th Annual Symposium on Frequency Control (1981) (cit. on p. 86).

[Häf05a] H. Häffner, W. Hänsel, C. F. Roos, J. Benhelm, D. Chek-al-kar, M. Chwalla, T. Körber, U. D. Rapol, M. Riebe, P. O. Schmidt, C. Becher, O. Gühne, W. Dür, and R. Blatt. *Scalable multiparticle entanglement of trapped ions*. In: Nature **438**, 643–646 (2005) (cit. on p. 4).

[Häf05b] H. Häffner, W. Hänsel, C. Roos, J. Benhelm, D. Chek-al-kar, M. Chwalla, T. Körber, U. Rapol, M. Riebe, P. Schmidt, C. Becher, O. Gühne, W. Dür, and R. Blatt. *Scalable multiparticle entanglement of trapped ions*. In: Nature **438**, 643 (2005) (cit. on p. 119).

[Inl17] I. V. Inlek, C. Crocker, M. Lichtman, K. Sosnova, and C. Monroe. *Multispecies Trapped-Ion Node for Quantum Networking*. In: Phys. Rev. Lett. **118**, 250502 (2017) (cit. on p. 143).

[Jam98] D. F. V. James. *Quantum dynamics of cold trapped ions with application to quantum computation*. In: Applied Physics B **66**, 181–190 (1998) (cit. on pp. 16, 17).

[Jec11] A. Jechow, E. Streed, B. G. Norton, M. Petrasiunas, and D. Kielpinski. *Wavelength-scale imaging of trapped ions using a phase Fresnel lens*. In: Optics letters **36**, 1371–1373 (2011) (cit. on p. 72).

[Joh16] K. G. Johnson, J. D. Wong-Campos, A. Restelli, K. A. Landsman, B. Neyenhuis, J. Mizrahi, and C. Monroe. *Active stabilization of ion trap radiofrequency potentials.* In: Review of Scientific Instruments **87**, 053110 (2016) (cit. on p. 88).

[Jos74] B. D. Josephson. *The discovery of tunnelling supercurrents.* In: Rev. Mod. Phys. **46**, 251–254 (1974) (cit. on p. 6).

[Kau12a] H. Kaufmann. *Experimentelle und theoretische Untersuchung von Zickzack-Ionenkristallen.* In: Master's thesis, Johannes Gutenberg-Universität Mainz (2012) (cit. on pp. 17, 131, 132).

[Kau12b] H. Kaufmann, S. Ulm, G. Jacob, U. Poschinger, H. Landa, A. Retzker, M. B. Plenio, and F. Schmidt-Kaler. *Precise Experimental Investigation of Eigenmodes in a Planar Ion Crystal.* In: Phys. Rev. Lett. **109**, 263003 (2012) (cit. on pp. 8, 17, 132).

[Kau14] H. Kaufmann, T. Ruster, C. T. Schmiegelow, F. Schmidt-Kaler, and U. G. Poschinger. *Dynamics and control of fast ion crystal splitting in segmented Paul traps.* In: New Journal of Physics **16**, 073012 (2014) (cit. on pp. 10, 27, 53, 96, 99, 105, 121).

[Kau17a] H. Kaufmann, T. Ruster, C. T. Schmiegelow, M. A. Luda, V. Kaushal, J. Schulz, D. von Lindenfels, F. Schmidt-Kaler, and U. G. Poschinger. *Fast ion swapping for quantum-information processing.* In: Phys. Rev. A **95**, 052319 (2017) (cit. on pp. 10, 95, 105, 126, 141).

[Kau17b] H. Kaufmann, T. Ruster, C. T. Schmiegelow, M. A. Luda, V. Kaushal, J. Schulz, D. von Lindenfels, F. Schmidt-Kaler, and U. G. Poschinger. *Scalable creation of long-lived multipartite entanglement.* In: arXiv:1707.03695 (2017) (cit. on p. 119).

[Kel15] J. Kelly, R. Barends, A. G. Fowler, A. Megrant, E. Jeffrey, T. C. White, D. Sank, J. Y. Mutus, B. Campbell, Y. Chen, Z. Chen, B. Chiaro, A. Dunsworth, I.-C. Hoi, C. Neill, P. J. J. O'Malley, C. Quintana, P. Roushan, A. Vainsencher, J. Wenner, A. N. Cleland, and J. M. Martinis. *State preservation by repetitive error detection in a superconducting quantum circuit.* In: Nature **519**, 66–69 (2015) (cit. on pp. 3, 6).

[Kie00] D. Kielpinski, B. E. King, C. J. Myatt, C. A. Sackett, Q. A. Turchette, W. M. Itano, C. Monroe, D. J. Wineland, and W. H. Zurek. *Sympathetic cooling of trapped ions for quantum logic.* In: Phys. Rev. A **61**, 032310 (2000) (cit. on pp. 5, 95).

[Kie01] D. Kielpinski, V. Meyer, M. A. Rowe, C. A. Sackett, W. M. Itano, C. Monroe, and D. J. Wineland. *A Decoherence-Free Quantum Memory Using Trapped Ions.* In: Science **291**, 1013–1015 (2001) (cit. on p. 5).

[Kie02] D. Kielpinski, C. Monroe, and D. J. Wineland. *Architecture for a large-scale ion-trap quantum computer.* In: Nature **417**, 709–711 (2002) (cit. on pp. 8, 9, 105, 137).

[Kie15] D. Kienzler. *Quantum Harmonic Oscillator State Synthesis by Reservoir Engineering*. In: Ph.D. thesis, Eidgenössische Technische Hochschule Zürich (2015) (cit. on pp. 27, 79).

[Kim09] K. Kim, M.-S. Chang, R. Islam, S. Korenblit, L.-M. Duan, and C. Monroe. *Entanglement and Tunable Spin-Spin Couplings between Trapped Ions Using Multiple Transverse Modes*. In: Phys. Rev. Lett. **103**, 120502 (2009) (cit. on p. 134).

[Kim10] K. Kim, M.-S. Chang, S. Korenblit, R. Islam, E. E. Edwards, J. K. Freericks, G.-D. Lin, L.-M. Duan, and C. Monroe. *Quantum simulation of frustrated Ising spins with trapped ions*. In: Nature **465**, 590–593 (2010) (cit. on p. 131).

[Kni05] E. Knill. *Quantum computing with realistically noisy devices*. In: Nature **434**, 39–44 (2005) (cit. on p. 119).

[Kni10] E. Knill. *Physics: Quantum computing*. In: Nature **463**, 441–443 (2010) (cit. on p. 108).

[Koc07] J. Koch, T. M. Yu, J. Gambetta, A. A. Houck, D. I. Schuster, J. Majer, A. Blais, M. H. Devoret, S. M. Girvin, and R. J. Schoelkopf. *Charge-insensitive qubit design derived from the Cooper pair box*. In: Phys. Rev. A **76**, 042319 (2007) (cit. on p. 6).

[Kot11] S. Kotler, N. Akerman, Y. Glickman, A. Keselman, and R. Ozeri. *Single-ion quantum lock-in amplifier*. In: Nature **473**, 61–65 (2011) (cit. on p. 128).

[Lab08] J. Labaziewicz, Y. Ge, P. Antohi, D. Leibrandt, K. R. Brown, and I. L. Chuang. *Suppression of Heating Rates in Cryogenic Surface-Electrode Ion Traps*. In: Phys. Rev. Lett. **100**, 013001 (2008) (cit. on p. 79).

[Lad10] T. D. Ladd, F. Jelezko, R. Laflamme, Y. Nakamura, C. Monroe, and J. L. O'Brien. *Quantum computers*. In: Nature **464**, 45–53 (2010) (cit. on pp. 1, 6, 7, 108).

[Lan13] B. P. Lanyon, P. Jurcevic, M. Zwerger, C. Hempel, E. A. Martinez, W. Dür, H. J. Briegel, R. Blatt, and C. F. Roos. *Measurement-Based Quantum Computation with Trapped Ions*. In: Phys. Rev. Lett. **111**, 210501 (2013) (cit. on pp. 3, 119, 128).

[Lan14] H. Landa, A. Retzker, T. Schaetz, and B. Reznik. *Entanglement Generation Using Discrete Solitons in Coulomb Crystals*. In: Phys. Rev. Lett. **113**, 053001 (2014) (cit. on p. 8).

[Lee05] P. J. Lee, K.-A. Brickman, L. Deslauriers, P. C. Haljan, L.-M. Duan, and C. Monroe. *Phase control of trapped ion quantum gates*. In: Journal of Optics B: Quantum and Semiclassical Optics **7**, S371 (2005) (cit. on p. 21).

[Lei03a] D. Leibfried, B. DeMarco, V. Meyer, D. Lucas, M. Barrett, J. Britton, W. M. Itano, B. Jelenkovic, C. Langer, T. Rosenband, and D. J. Wineland. *Experimental demonstration of a robust, high-fidelity geometric two ion-qubit phase gate*. In: Nature **422**, 412–415 (2003) (cit. on pp. 4, 7, 21, 22, 74, 116, 131, 134).

[Lei03b] D. Leibfried, R. Blatt, C. Monroe, and D. Wineland. *Quantum dynamics of single trapped ions*. In: Rev. Mod. Phys. **75**, 281–324 (2003) (cit. on pp. 15, 18–20, 97).

[Lek17] B. Lekitsch, S. Weidt, A. G. Fowler, K. Mølmer, S. J. Devitt, C. Wunderlich, and W. K. Hensinger. *Blueprint for a microwave trapped ion quantum computer*. In: Science Advances **3**, 2 (2017) (cit. on p. 8).

[Let04] V. Letchumanan, P. Gill, E. Riis, and A. G. Sinclair. *Optical Ramsey spectroscopy of a single trapped $^{88}Sr^{+}$ ion*. In: Phys. Rev. A **70**, 033419 (2004) (cit. on p. 84).

[Lin13] Y. Lin, J. P. Gaebler, T. R. Tan, R. Bowler, J. D. Jost, D. Leibfried, and D. J. Wineland. *Sympathetic Electromagnetically-Induced-Transparency Laser Cooling of Motional Modes in an Ion Chain*. In: Phys. Rev. Lett. **110**, 153002 (2013) (cit. on pp. 81, 139).

[Lin16] N. M. Linke, M. Gutierrez, K. A. Landsman, C. Figgatt, S. Debnath, K. R. Brown, and C. Monroe. *Fault-tolerant quantum error detection*. In: arXiv:1611.06946 (2016) (cit. on p. 128).

[Lin17] N. M. Linke, D. Maslov, M. Roetteler, S. Debnath, C. Figgatt, K. A. Landsman, K. Wright, and C. Monroe. *Experimental comparison of two quantum computing architectures*. In: Proceedings of the National Academy of Sciences **114**, 3305–3310 (2017) (cit. on p. 7).

[Mac12] T. Macha. *Frequenzstabilisierung eines Titan-Saphir-Lasers und Verbesserung von Qubits mit Ca^{+}-Ionen*. In: Master's thesis, Johannes Gutenberg-Universität Mainz (2012) (cit. on p. 47).

[Man80] Y. I. Manin. *Computable and Uncomputable (in Russian)*. In: Sovetskoye Radio, Moscow (1980) (cit. on p. 2).

[Man99] Y. I. Manin. *Classical computing, quantum computing, and Shor's factoring algorithm*. In: arXiv:quant-ph/9903008 (1999) (cit. on p. 2).

[Mar02] J. M. Martinis, S. Nam, J. Aumentado, and C. Urbina. *Rabi Oscillations in a Large Josephson-Junction Qubit*. In: Phys. Rev. Lett. **89**, 117901 (2002) (cit. on p. 6).

[Mar03] C. Marquet, F. Schmidt-Kaler, and D. F. V. James. *Phonon–phonon interactions due to non-linear effects in a linear ion trap*. In: Applied Physics B **76**, 199–208 (2003) (cit. on pp. 16, 17).

[Mar16] E. A. Martinez, T. Monz, D. Nigg, P. Schindler, and R. Blatt. *Compiling quantum algorithms for architectures with multi-qubit gates*. In: New Journal of Physics **18**, 063029 (2016) (cit. on p. 140).

[McC15a] R. McConnell, H. Zhang, J. Hu, S. Ćuk, and V. Vuletić. *Entanglement with negative Wigner function of almost 3,000 atoms heralded by one photon*. In: Nature **519**, 439–442 (2015) (cit. on p. 119).

[McC15b] R. McConnell, C. Bruzewicz, J. Chiaverini, and J. Sage. *Reduction of trapped-ion anomalous heating by in situ surface plasma cleaning*. In: Phys. Rev. A **92**, 020302 (2015) (cit. on p. 84).

[Mie13] M. Mielenz, J. Brox, S. Kahra, G. Leschhorn, M. Albert, T. Schaetz, H. Landa, and B. Reznik. *Trapping of Topological-Structural Defects in Coulomb Crystals*. In: Phys. Rev. Lett. **110**, 133004 (2013) (cit. on p. 8).

[Miz07] A. Mizel, D. A. Lidar, and M. Mitchell. *Simple Proof of Equivalence between Adiabatic Quantum Computation and the Circuit Model*. In: Phys. Rev. Lett. **99**, 070502 (2007) (cit. on p. 3).

[Moe07] D. L. Moehring, P. Maunz, S. Olmschenk, K. C. Younge, D. N. Matsukevich, L.-M. Duan, and C. Monroe. *Entanglement of single-atom quantum bits at a distance*. In: Nature **449**, 68–71 (2007) (cit. on pp. 5, 143).

[Moe11] D. L. Moehring, C. Highstrete, D. Stick, K. M. Fortier, R. Haltli, C. Tigges, and M. G. Blain. *Design, fabrication and experimental demonstration of junction surface ion traps*. In: New Journal of Physics **13**, 075018 (2011) (cit. on p. 10).

[Moh17] M. Mohseni, P. Read, H. Neven, S. Boixo, V. Denchev, R. Babbush, A. Fowler, V. Smelyanskiy, and J. Martinis. *Commercialize early quantum technologies*. In: Nature **543**, 171–174 (2017) (cit. on p. 1).

[Mon11a] T. Monz, P. Schindler, J. T. Barreiro, M. Chwalla, D. Nigg, W. A. Coish, M. Harlander, W. Hänsel, M. Hennrich, and R. Blatt. *14-Qubit Entanglement: Creation and Coherence*. In: Phys. Rev. Lett. **106**, 130506 (2011) (cit. on pp. 4, 7, 128, 129).

[Mon11b] T. Monz, P. Schindler, J. T. Barreiro, M. Chwalla, D. Nigg, W. A. Coish, M. Harlander, W. Hänsel, M. Hennrich, and R. Blatt. *14-Qubit Entanglement: Creation and Coherence*. In: Phys. Rev. Lett. **106**, 130506 (2011) (cit. on pp. 119, 127).

[Mon14] C. Monroe, R. Raussendorf, A. Ruthven, K. R. Brown, P. Maunz, L.-M. Duan, and J. Kim. *Large-scale modular quantum-computer architecture with atomic memory and photonic interconnects*. In: Phys. Rev. A **89**, 022317 (2014) (cit. on pp. 4, 8, 143, 144).

[Mon16a] A. Montanaro. *Quantum algorithms: an overview*. In: Npj Quantum Information **2**, 15023 (2016) (cit. on p. 3).

[Mon16b] T. Monz, D. Nigg, E. A. Martinez, M. F. Brandl, P. Schindler, R. Rines, S. X. Wang, I. L. Chuang, and R. Blatt. *Realization of a scalable Shor algorithm*. In: Science **351**, 1068–1070 (2016) (cit. on p. 4).

[Mon95a] C. Monroe, D. M. Meekhof, B. E. King, W. M. Itano, and D. J. Wineland. *Demonstration of a Fundamental Quantum Logic Gate*. In: Phys. Rev. Lett. **75**, 4714–4717 (1995) (cit. on p. 4).

[Mon95b] C. Monroe, D. M. Meekhof, B. E. King, S. R. Jefferts, W. M. Itano, D. J. Wineland, and P. Gould. *Resolved-Sideband Raman Cooling of a Bound Atom to the 3D Zero-Point Energy*. In: Phys. Rev. Lett. **75**, 4011–4014 (1995) (cit. on p. 20).

[Mon96] C. Monroe, D. M. Meekhof, B. E. King, and D. J. Wineland. *A "Schrödinger Cat" Superposition State of an Atom*. In: Science **272**, 1131–1136 (1996) (cit. on pp. 22, 131, 134).

[Mor13] T. Moroder, M. Kleinmann, P. Schindler, T. Monz, O. Gühne, and R. Blatt. *Certifying Systematic Errors in Quantum Experiments*. In: Phys. Rev. Lett. **110**, 180401 (2013) (cit. on p. 126).

[Nak99] Y. Nakamura, Y. A. Pashkin, and J. Tsai. *Coherent control of macroscopic quantum states in a single-Cooper-pair box*. In: Nature **398**, 786–788 (1999) (cit. on p. 6).

[Nar11] S. Narayanan, N. Daniilidis, S. A. Möller, R. Clark, F. Ziesel, K. Singer, F. Schmidt-Kaler, and H. Häffner. *Electric field compensation and sensing with a single ion in a planar trap*. In: Journal of Applied Physics **110**, 114909 (2011) (cit. on p. 62).

[Neb09] V. Nebendahl, H. Häffner, and C. F. Roos. *Optimal control of entangling operations for trapped-ion quantum computing*. In: Phys. Rev. A **79**, 012312 (2009) (cit. on p. 140).

[Nie00] M. A. Nielsen and I. L. Chuang. *Quantum Computation and Quantum Information*. In: Cambridge University Press (2000) (cit. on pp. 1–3, 24).

[Nie14] M. Niedermayr, K. Lakhmanskiy, M. Kumph, S. Partel, J. Edlinger, M. Brownnutt, and R. Blatt. *Cryogenic surface ion trap based on intrinsic silicon*. In: New Journal of Physics **16**, 113068 (2014) (cit. on p. 84).

[Nig14] D. Nigg, M. Müller, E. A. Martinez, P. Schindler, M. Hennrich, T. Monz, M. A. Martin-Delgado, and R. Blatt. *Quantum computations on a topologically encoded qubit*. In: Science **345**, 302–305 (2014) (cit. on pp. 4, 8, 128, 140).

[Nis07] A. O. Niskanen, K. Harrabi, F. Yoshihara, Y. Nakamura, S. Lloyd, and J. S. Tsai. *Quantum Coherent Tunable Coupling of Superconducting Qubits*. In: Science **316**, 723–726 (2007) (cit. on p. 7).

[Niz12] A. H. Nizamani and W. K. Hensinger. *Optimum electrode configurations for fast ion separation in microfabricated surface ion traps*. In: Applied Physics B **106**, 337–338 (2012) (cit. on pp. 54, 68).

[Olm09] S. Olmschenk, D. N. Matsukevich, P. Maunz, D. Hayes, L.-M. Duan, and C. Monroe. *Quantum Teleportation Between Distant Matter Qubits*. In: Science **323**, 486–489 (2009) (cit. on pp. 5, 143).

[Oze07] R. Ozeri, W. M. Itano, R. B. Blakestad, J. Britton, J. Chiaverini, J. D. Jost, C. Langer, D. Leibfried, R. Reichle, S. Seidelin, J. H. Wesenberg, and D. J. Wineland. *Errors in trapped-ion quantum gates due to spontaneous photon scattering*. In: Phys. Rev. A **75**, 042329 (2007) (cit. on pp. 109, 135).

[Pai11] H. Paik, D. I. Schuster, L. S. Bishop, G. Kirchmair, G. Catelani, A. P. Sears, B. R. Johnson, M. J. Reagor, L. Frunzio, L. I. Glazman, S. M. Girvin, M. H. Devoret, and R. J. Schoelkopf. *Observation of High Coherence in Josephson Junction Qubits Measured in a Three-Dimensional Circuit QED Architecture*. In: Phys. Rev. Lett. **107**, 240501 (2011) (cit. on p. 6).

[Pal13] M. Palmero, E. Torrontegui, D. Guéry-Odelin, and J. G. Muga. *Fast transport of two ions in an anharmonic trap*. In: Phys. Rev. A **88**, 053423 (2013) (cit. on p. 75).

[Pau90] W. Paul. *Electromagnetic traps for charged and neutral particles*. In: Rev. Mod. Phys. **62**, 531–540 (1990) (cit. on pp. 4, 8, 13, 14).

[Pfi16] A. D. Pfister, M. Salz, M. Hettrich, U. G. Poschinger, and F. Schmidt-Kaler. *A quantum repeater node with trapped ions: a realistic case example*. In: Applied Physics B **122**, 89 (2016) (cit. on pp. 5, 143, 144).

[Pos09] U. G. Poschinger, G. Huber, F. Ziesel, M. Dei"s, M. Hettrich, S. A. Schulz, G. Poulsen, M. Drewsen, R. J. Hendricks, K. Singer, and F. Schmidt-Kaler. *Coherent Manipulation of a $^{40}Ca^{+}$ Spin Qubit in a Micro Ion Trap*. In: Journal of Physics B: Atomic, Molecular and Optical Physics **42**, 154013 (2009) (cit. on p. 13).

[Pos10a] U. G. Poschinger. *Quantum Optics Experiments in a Microstructured Ion Trap*. In: Ph.D. thesis, Universität Ulm, Fakultät für Naturwissenschaften (2010) (cit. on pp. 15, 47).

[Pos10b] U. Poschinger, A. Walther, K. Singer, and F. Schmidt-Kaler. *Observing the Phase Space Trajectory of an Entangled Matter Wave Packet*. In: Phys. Rev. Lett. **105**, 263602 (2010) (cit. on p. 134).

[Pou12] G. Poulsen, Y. Miroshnychenko, and M. Drewsen. *Efficient ground-state cooling of an ion in a large room-temperature linear Paul trap with a sub-Hertz heating rate*. In: Phys. Rev. A **86**, 051402 (2012) (cit. on p. 84).

[Rau01] R. Raussendorf and H. J. Briegel. *A One-Way Quantum Computer*. In: Phys. Rev. Lett. **86**, 5188–5191 (2001) (cit. on pp. 3, 119, 128).

[Rau07] R. Raussendorf, J. Harrington, and K. Goyal. *Topological fault-tolerance in cluster state quantum computation*. In: New Journal of Physics **9**, 199 (2007) (cit. on p. 119).

[Rea16] M. Reagor, W. Pfaff, C. Axline, R. W. Heeres, N. Ofek, K. Sliwa, E. Holland, C. Wang, J. Blumoff, K. Chou, M. J. Hatridge, L. Frunzio, M. H. Devoret, L. Jiang, and R. J. Schoelkopf. *Quantum memory with millisecond coherence in circuit QED*. In: Phys. Rev. B **94**, 014506 (2016) (cit. on p. 7).

[Rei06] R. Reichle, D. Leibfried, E. Knill, J. Britton, R. B. Blakestad, J. D. Jost, C. Langer, R. Ozeri, S. Seidelin, and D. J. Wineland. *Experimental purification of two-atom entanglement*. In: Nature **443**, 838–841 (2006) (cit. on p. 54).

[Rie04] M. Riebe, H. Häffner, C. F. Roos, W. Hänsel, J. Benhelm, G. P. T. Lancaster, T. W. Korber, C. Becher, F. Schmidt-Kaler, D. F. V. James, and R. Blatt. *Deterministic quantum teleportation with atoms*. In: Nature **429**, 734–737 (2004) (cit. on p. 4).

[Ril08] W. J. Riley. *Handbook of Frequency Stability Analysis*. In: NIST Special Publication 1065 (2008) (cit. on p. 86).

[Rom12] G. Romero, D. Ballester, Y. M. Wang, V. Scarani, and E. Solano. *Ultrafast Quantum Gates in Circuit QED*. In: Phys. Rev. Lett. **108**, 120501 (2012) (cit. on p. 138).

[Roo00] C. F. Roos. *Controlling the quantum state of trapped ions*. In: Ph.D. thesis, Leopold-Franzens-Universität Innsbruck (2000) (cit. on p. 47).

[Roo08] C. F. Roos. *Ion trap quantum gates with amplitude-modulated laser beams*. In: New Journal of Physics **10**, 013002 (2008) (cit. on p. 21).

[Rot03] D. Rotter. *Photoionisation von Kalzium*. In: Master's thesis, Leopold-Franzens-Universität Innsbruck (2003) (cit. on p. 39).

[Row02] M. Rowe, A. Ben-Kish, B. DeMarco, D. Leibfried, V. Meyer, J. Beall, J. Britton, J. Hughes, W. Itano, B. Jelenkovic, C. Langer, T. Rosenband, and D. Wineland. *Transport of quantum states and seperation of ions in a dual rf ion trap*. In: Quantum Inf. and Comput. **2**, 257 (2002) (cit. on p. 53).

[Rus12] T. Ruster. *Schneller Transport von kalten gefangenen Ionen*. In: Master's thesis, Johannes Gutenberg-Universität Mainz (2012) (cit. on p. 84).

[Rus14] T. Ruster, C. Warschburger, H. Kaufmann, C. T. Schmiegelow, A. Walther, M. Hettrich, A. Pfister, V. Kaushal, F. Schmidt-Kaler, and U. G. Poschinger. *Experimental realization of fast ion separation in segmented Paul traps*. In: Phys. Rev. A **90**, 033410 (2014) (cit. on pp. 10, 44, 53, 96, 97, 100, 105, 121, 141).

[Rus16] T. Ruster, C. T. Schmiegelow, H. Kaufmann, C. Warschburger, F. Schmidt-Kaler, and U. G. Poschinger. *A long-lived Zeeman trapped-ion qubit*. In: Applied Physics B **122**, 254 (2016) (cit. on pp. 5, 44, 46, 120, 129, 154, 164).

[Rus17] T. Ruster, H. Kaufmann, M. A. Luda, V. Kaushal, C. T. Schmiegelow, F. Schmidt-Kaler, and U. G. Poschinger. *Entanglement-based dc magnetometry with separated ions*. In: arXiv:1704.01793, accepted for publication in Phys. Rev. X (2017) (cit. on pp. 91, 113, 123, 127, 130).

[SK03] F. Schmidt-Kaler, H. Häffner, M. Riebe, S. Gulde, G. P. T. Lancaster, T. Deuschle, C. Becher, C. F. Roos, J. Eschner, and R. Blatt. *Realization of the Cirac-Zoller controlled-NOT quantum gate*. In: Nature **422**, 408–411 (2003) (cit. on pp. 2, 4, 7).

[Sac00] C. A. Sackett, D. Kielpinski, B. E. King, C. Langer, V. Meyer, C. J. Myatt, M. Rowe, Q. A. Turchette, W. M. Itano, D. J. Wineland, and C. Monroe. *Experimental entanglement of four particles*. In: Nature **404**, 256–259 (2000) (cit. on pp. 4, 119).

[Sch07] S. Schulz and F. Schmidt-Kaler. *Segmentierte Mikrochip-Falle für kalte Ionen*. In: Physik in unserer Zeit **38**, 162–163 (2007) (cit. on p. 25).

[Sch08] S. Schulz, U. Poschinger, F. Ziesel, and F. Schmidt-Kaler. *Sideband cooling and coherent dynamics in a microchip multi-segmented ion trap*. In: New Journal of Physics **10**, 045007 (2008) (cit. on pp. 62, 73).

[Sch09] S. Schulz. *Scalable microchip ion traps for quantum computation*. In: Ph.D. thesis, Universität Ulm (2009) (cit. on p. 25).

[Sch12] C. Schneider, D. Porras, and T. Schaetz. *Experimental quantum simulations of many-body physics with trapped ions*. In: Reports on Progress in Physics **75**, 024401 (2012) (cit. on p. 8).

[Sch13] P. Schindler, D. Nigg, T. Monz, J. T. Barreiro, E. Martinez, S. X. Wang, S. Quint, M. F. Brandl, V. Nebendahl, C. F. Roos, M. Chwalla, M. Hennrich, and R. Blatt. *A quantum information processor with trapped ions*. In: New Journal of Physics **15**, 123012 (2013) (cit. on p. 3).

[Sch16] C. T. Schmiegelow, H. Kaufmann, T. Ruster, J. Schulz, V. Kaushal, M. Hettrich, F. Schmidt-Kaler, and U. G. Poschinger. *Phase-Stable Free-Space Optical Lattices for Trapped Ions*. In: Phys. Rev. Lett. **116**, 033002 (2016) (cit. on pp. 22, 23).

[Sei06] S. Seidelin, J. Chiaverini, R. Reichle, J. J. Bollinger, D. Leibfried, J. Britton, J. H. Wesenberg, R. B. Blakestad, R. J. Epstein, D. B. Hume, W. M. Itano, J. D. Jost, C. Langer, R. Ozeri, N. Shiga, and D. J. Wineland. *Microfabricated Surface-Electrode Ion Trap for Scalable Quantum Information Processing*. In: Phys. Rev. Lett. **96**, 253003 (2006) (cit. on p. 8).

[Sho94] P. W. Shor. *Algorithms for quantum computation: Discrete logarithms and factoring*. In: Proceedings of the 35th Annual Symposium on Foundations of Computer Science, 124–134 (1994) (cit. on p. 3).

[Sho95] P. W. Shor. *Scheme for reducing decoherence in quantum computer memory.* In: Phys. Rev. A **52**, R2493–R2496 (1995) (cit. on pp. 4, 137, 140).

[Shu14] G. Shu, G. Vittorini, A. Buikema, C. S. Nichols, C. Volin, D. Stick, and K. R. Brown. *Heating rates and ion-motion control in a Y-junction surface-electrode trap.* In: Phys. Rev. A **89**, 062308 (2014) (cit. on p. 95).

[Sin10] K. Singer, U. Poschinger, M. Murphy, P. Ivanov, F. Ziesel, T. Calarco, and F. Schmidt-Kaler. *Colloquium: Trapped ions as quantum bits: Essential numerical tools.* In: Rev. Mod. Phys. **82**, 2609–2632 (2010) (cit. on pp. 16, 57, 62, 73, 101).

[Spl09] F. Splatt, M. Harlander, M. Brownnutt, F. Zähringer, R. Blatt, and W. Hänsel. *Deterministic reordering of $^{40}Ca^{+}$ ions in a linear segmented Paul trap.* In: New Journal of Physics **11**, 103008 (2009) (cit. on p. 96).

[Ste96] A. M. Steane. *Error Correcting Codes in Quantum Theory.* In: Phys. Rev. Lett. **77**, 793–797 (1996) (cit. on pp. 4, 137, 140).

[Tan15] T. R. Tan, J. P. Gaebler, Y. Lin, Y. Wan, R. Bowler, D. Leibfried, and D. J. Wineland. *Multi-element logic gates for trapped-ion qubits.* In: Nature **528**, 380–383 (2015) (cit. on p. 95).

[Tou16] A. d. Touzalin, C. Marcus, F. Heijman, R. Cirac Ignacio Murray, and T. Calarco. *Quantum Manifesto: A New Area of Technology (Quantum Information Processing and Communication in Europe).* In: http://qurope.eu/manifesto (2016) (cit. on p. 1).

[Tur00] Q. A. Turchette, C. J. Myatt, B. E. King, C. A. Sackett, D. Kielpinski, W. M. Itano, C. Monroe, and D. J. Wineland. *Decoherence and decay of motional quantum states of a trapped atom coupled to engineered reservoirs.* In: Phys. Rev. A **62**, 053807 (2000) (cit. on pp. 88, 135).

[Tur98] Q. A. Turchette, C. S. Wood, B. E. King, C. J. Myatt, D. Leibfried, W. M. Itano, C. Monroe, and D. J. Wineland. *Deterministic Entanglement of Two Trapped Ions.* In: Phys. Rev. Lett. **81**, 3631–3634 (1998) (cit. on p. 4).

[Ulm13] S. Ulm, J. Roßnagel, G. Jacob, C. Degünther, S. T. Dawkins, U. G. Poschinger, R. Nigmatullin, A. Retzker, M. B. Plenio, F. Schmidt-Kaler, and K. Singer. *Observation of the Kibble–Zurek scaling law for defect formation in ion crystals.* In: Nat. Commun. **4**, 2290 (2013) (cit. on pp. 8, 64).

[Van01] L. M. K. Vandersypen, M. Steffen, G. Breyta, C. S. Yannoni, M. H. Sherwood, and I. L. Chuang. *Experimental realization of Shor's quantum factoring algorithm using nuclear magnetic resonance.* In: Nature **414**, 883–887 (2001) (cit. on pp. 3, 7).

[Van05] L. M. K. Vandersypen and I. L. Chuang. *NMR techniques for quantum control and computation.* In: Rev. Mod. Phys. **76**, 1037–1069 (2005) (cit. on p. 127).

[Wal12] A. Walther, F. Ziesel, T. Ruster, S. T. Dawkins, K. Ott, M. Hettrich, K. Singer, F. Schmidt-Kaler, and U. Poschinger. *Controlling Fast Transport of Cold Trapped Ions*. In: Phys. Rev. Lett. **109**, 080501 (2012) (cit. on pp. 9, 44, 45, 53, 74, 97, 105, 141).

[Wal17] T. Walter, P. Kurpiers, S. Gasparinetti, P. Magnard, Y. Salathé, M. Pechal, M. Mondal, M. Oppliger, C. Eichler, and A. Wallraff. *Rapid High-Fidelity Single-Shot Dispersive Readout of Superconducting Qubits*. In: Phys. Rev. Applied **7**, 054020 (2017) (cit. on p. 6).

[Win87] D. J. Wineland, W. M. Itano, J. C. Bergquist, and R. G. Hulet. *Laser-cooling limits and single-ion spectroscopy*. In: Phys. Rev. A **36**, 2220–2232 (1987) (cit. on p. 12).

[Win98] D. J. Wineland, C. Monroe, W. M. Itano, D. Leibfried, B. E. King, and D. M. Meekhof. *Experimental issues in coherent quantum-state manipulation of trapped atomic ions*. In: Journal of Research of the National Institute of Standards and Technology **103**, 259 (1998) (cit. on p. 20).

[Woo82] W. K. Wootters and W. H. Zurek. *A single quantum cannot be cloned*. In: Nature **299**, 802–803 (1982) (cit. on p. 140).

[Wri13] K. Wright, J. M. Amini, D. L. Faircloth, C. Volin, S. C. Doret, H. Hayden, C.-S. Pai, D. W. Landgren, D. Denison, T. Killian, R. E. Slusher, and A. W. Harter. *Reliable transport through a microfabricated X-junction surface-electrode ion trap*. In: New Journal of Physics **15**, 033004 (2013) (cit. on p. 95).

[Yao93] A. C.-C. Yao. *Quantum circuit complexity*. In: Proceedings of 1993 IEEE 34th Annual Foundations of Computer Science, 352–361 (1993) (cit. on p. 2).

[Yok13] S. Yokoyama, R. Ukai, S. C. Armstrong, C. Sornphiphatphong, T. Kaji, S. Suzuki, J.-i. Yoshikawa, H. Yonezawa, N. C. Menicucci, and A. Furusawa. *Ultra-large-scale continuous-variable cluster states multiplexed in the time domain*. In: Nat Photon **7**, 982–986 (2013) (cit. on p. 119).

[Zwe17] M. Zwerger, B. P. Lanyon, T. E. Northup, C. A. Muschik, W. Dür, and N. Sangouard. *Quantum repeaters based on trapped ions with decoherence-free subspace encoding*. In: Quantum Science and Technology **2**, 044001 (2017) (cit. on p. 5).

[Řeh07] J. Řeháček, Z. Hradil, E. Knill, and A. I. Lvovsky. *Diluted maximum-likelihood algorithm for quantum tomography*. In: Phys. Rev. A **75**, 042108 (2007) (cit. on p. 125).